Computational modelling of perovskite-based materials for solid oxide fuel cell applications

Julia Savioli

A thesis submitted in the partial fulfilment of the requirements for the degree of Doctor of Philosophy

at the
School of Chemistry and CRANN,
University of Dublin, Trinity College

Supervisor: Prof. Graeme W. Watson

2022

Declaration of Authorship

I declare that this thesis has not been submitted as an exercise for a degree at this or any other university and it is entirely my own work, except for otherwise cited.

I agree to deposit this thesis in the University's open access institutional repository or allow the library to do so on my behalf, subject to Irish Copyright Legislation and Trinity College Library conditions of use and acknowledgement.

_____

Julia Savioli

2022

University of Dublin, Trinity College

Summary

The development and use of clean and renewable modes of power generation is essential to address the increasing environmental and health concerns associated with fossil fuel consumption. Solid oxide fuel cells (SOFCs) are promising technologies for clean and efficient energy generation, as they can directly convert chemical energy into electrical power overcoming combustion limitations and utilising a variety of fuels. High temperatures are currently required for satisfactory ionic conduction at the electrolyte and efficient catalytic activity for the oxygen reduction reaction at the cathode, decreasing the lifetime and increasing the device's cost. Hence, one of the main challenges associated with SOFC development is to decrease their operating temperatures to the intermediate temperature (IT) range (600-800 °C). Computational modelling is an essential tool in developing or improving IT-SOFC components, allowing researchers to predict, understand and explain the mechanisms behind experimentally observed properties. This thesis focus on the investigation of defect properties of perovskite-based materials and on the improvement of their ionic and/or electronic conduction properties, aiming their application as IT-SOFC components.

$LaGaO_3$-based materials have been suggested as suitable electrolytes, as they possess high conductivities at lower temperatures when compared to that of currently used yttria stabilized zirconia and samarium or gadolinium doped ceria. DFT calculations were performed to investigate the potential effects of a range of divalent dopants in the ionic conductivity and structure of $LaGaO_3$ aiming to ascertain which dopants are best suited for solid electrolyte applications. Quantities such as doping and association energies were evaluated, to determine how easily the distinct dopants were accepted into the lattice and if there is any tendency of vacancy segregation around them, which could be detrimental to ionic transport. Sr(II), Ba(II) and Mg(II) were identified as the most suitable dopants, with steric and electronic defects playing a role in how easily these cations are accepted into the lattice. The local structural distortion introduced upon doping was observed to be an indicator of the tendency of vacancies to be trapped around dopants, possibly hindering ionic conductivity.

The ionic conductivity of Sr and Mg doped $LaGaO_3$ (LSGM) was then examined by means of molecular dynamics simulations, as the investigation of the diffusion and

dynamics in doped $LaGaO_3$ requires larger simulation cells. An interatomic potential was derived from *ab initio* data, as the currently available force fields are empirically derived and lack transferability, and has shown good agreement with experimental structural results. The conduction and structural properties of LSGM systems with a range of dopant concentrations (between 5 and 50 mol%) were then investigated. The calculated ionic conductivity and activation energy values were in good agreement with the available experimental data, with a total dopant concentration of around 20 mol% being concluded to be optimal. Local structure analysis was carried out to evaluate the tendency of vacancy clustering around dopants and vacancy ordering throughout the lattice, and the influence of dopant content in such effects. Mg-doping was observed to be more beneficial to ionic conduction properties, as vacancies tend to be trapped around Sr cations, deteriorating ionic transport. Vacancy ordering occurs independently of dopant identity, more intensely in systems with higher dopant content.

Finally, the defect chemistry of La_2NiO_4, a layered Ruddlesden-Popper oxide and potential cathode material, was investigated. La_2NiO_4 is a mixed ionic and electronic conductor, with A- and B-site doping affecting the material's transport properties in different ways. Usually, a trade-off between ionic and electronic conductivity improvements needs to be achieved. Density functional theory calculations were carried out to investigate the effects of a range of A- and B-site dopants in the material's defect chemistry and conduction properties. Defect formation energies, transition level diagrams and preferable charge compensating mechanisms were investigated under distinct chemical environments so the optimal dopants for intermediate temperature cathode applications could be determined. The stability of oxygen defects was examined, as the Ruddlesden-Popper structure can accommodate both oxygen vacancies and interstitials; interstitials were predicted to be the dominant oxygen defect. The introduction of the selected A-site dopants is preferably charge compensated by the formation of electron holes, and hence could yield *p*-type electronic conductivity improvements. The calculated defect binding energies indicate that A-site dopants should not act as electron hole traps. The introduction B-site dopants, on the other hand, is preferably charge compensated with the introduction of oxygen interstitials, and hence could result in ionic conductivity improvements. Sr(II) and Co(III) were identified as the most suitable dopants for IT-SOFC applications.

Acknowledgments

Firstly, I would like to thank my supervisor, Prof. Graeme Watson, for giving me the opportunity to carry out this research and for his priceless help during the past few years. This project could not have been completed without his guidance, impressive expertise and endless patience. Thank you to all Watson group members for all the chats, knowledge sharing and for making the group a very enjoyable place to work. A special thanks to Dr. Aoife Lucid, for all the assistance during my first few years, and to Dr. Swetanshu Tandon, for the much-needed chats. I would also like to acknowledge Research IT in TCD for maintaining the Pople cluster, in which part of the calculations in this thesis were performed, and ICHEC for computing time on the Fionn and Kay supercomputers.

I would like to express my gratitude towards my family, especially my parents, which have supported me throughout my (very long) time in education. None of this would have been possible without their encouragement. Lastly, a huge thanks to Eamon. For his patience, unconditional support and never-ending encouragement.

Publications

Savioli, J. & Watson, G. W. Computational modelling of solid oxide fuel cells. *Current Opinion in Electrochemistry* **21**, 14-21 (2020)

Savioli, J., Gavin A. L., Lucid A. K. & Watson, G. W. The structure and electronic structure of tin oxides. in Tin Oxide Materials: Synthesis, Properties and Applications (ed. Orlandi, M. O.), 11-39 (Elsevier, 2020)

Savioli, J. & Watson, G. W. Defect chemistry of $LaGaO_3$ doped with divalent cations. *Solid State Ionics* **374**, 115828 (2022)

Conference Talks

1. Defect chemistry of $LaGaO_3$ doped with divalent cations, *Dublin Chemistry Postgraduate Conference*, Dublin, Ireland, September (2018)

2. Defect chemistry of $LaGaO_3$ doped with divalent cations, *European Materials Research Society Spring Meeting*, Nice, France, May (2019)

3. Defect modelling of $LaGaO_3$ for solid oxide fuel cell applications, *71st Annual Irish Universities Chemistry Research Colloquium*, Dublin, Ireland, June (2019) (*Winner: Best Analytical/Physical Chemistry Talk*)

4. Solid oxide fuel cells: energy for the future, *Trinity College Dublin Chemistry Colloquium*, Dublin, Ireland, September (2019) (*Runner up: Brian Dorgan Memorial Prize*)

5. Defect modelling of $LaGaO_3$ for solid oxide fuel cell applications, *Third year talks symposium*, Trinity College Dublin, September (2020)

Table of Contents

List of Figures

List of Tables

List of Abbreviations

AFM	**A**nti**f**erro**m**agnetic
BE	**B**inding **E**nergy
BIS	**B**remsstrahlung **I**sochromat **S**pectroscopy
BZ	**B**rillouin **Z**one
CBM	**C**onduction **B**and **M**inimum
CCV	**C**harge **C**ompensating **V**acancy
CPLAP	**C**hemical **P**otential **L**imits **A**nalysis **P**rogram
DFT	**D**ensity **F**unctional **T**heory
DIPPIM	**Dip**ole **P**olarizable **I**on **M**odel
EDOS	**E**lectronic **D**ensity **o**f **S**tates
FM	**F**erro**m**agnetic
GDC	**G**adolinium **D**oped **C**eria
GGA	**G**eneralized **G**radient **A**pproximation
HF	**H**artree-**F**ock
HSE	**H**eyd, **S**cuseria and **E**rnzerhof functional
IP	**I**nteratomic **P**otential
IT	**I**ntermediate **T**emperature
L(S)DA	**L**ocal (**S**pin) **D**ensity **A**pproximation
MLWF	**M**aximally **L**ocalized **W**annier **F**unctions
MD	**M**olecular **D**ynamics
MIEC	**M**ixed **I**onic-**E**lectronic **C**onductivity
MSD	**M**ean **S**quare **D**isplacement
NN	**N**earest **N**eighbour
NNN	**N**ext **N**earest **N**eighbour
NNNN	**N**ext **N**ext **N**earest **N**eighbour

ORR	**O**xygen **R**eduction **R**eaction
PAW	**P**rojector **A**ugmented **W**ave
PBE	**P**erdew-**B**urke-**E**rnzerhof functional
PBEsol	**P**erdew-**B**urke-**E**rnzerhof functional revised for solids
PEDOS	**P**artial **E**lectronic **D**ensity **o**f **S**tates
PES	**P**otential **E**nergy **S**urface
PIMAIM	**P**olarisable **I**on **M**odel **A**spherical **I**on **M**odel
RDF	**R**adial **D**istribution **F**unction
RP	**R**uddlesden-**P**opper
SCAN	**S**trongly **C**onstrained and **A**ppropriately **N**ormed functional
SCF	**S**elf-**C**onsistent **F**ield
ScSZ	**Sc**andia-**s**tabilized **Z**irconia
SDC	**S**amarium **D**oped **C**eria
SIE	**S**elf-**I**nteraction **E**rror
SOEC	**S**olid **O**xide **E**lectrolysis **C**ell
SOFC	**S**olid **O**xide **F**uel **C**ell
SORC	**S**olid **O**xide **R**eversible **C**ell
TEC	**T**hermal **E**xpansion **C**oefficient
TM	**T**ransition **M**etal
TPB	**T**riple **P**hase **B**oundary
VASP	**V**ienna ***ab initio*** **S**imulation **P**ackage
VBM	**V**alence **B**and **M**aximum
XPS	**X**-ray **P**hotoelectron **S**pectroscopy
YSZ	**Y**ttria-**s**tabilized **Z**irconia

Chapter 1

Introduction

In times of increasing environmental concern, fossil fuels, the current main energy source for industrial processes, electricity generation and transport, need to be replaced with sustainable and renewable alternatives [1]. Energy generation has been based on the use of finite fuel sources since the industrial revolution; the rate of fossil fuel consumption increases as the world population and its demand for energy services also does, as a direct result of improvements in quality of life and the industrialization of developing countries [2]. Considering that fossil fuels reserves are finite and renewable sources are naturally replenished in a human timescale, the latter are much more sustainable alternatives to power generation.

Air pollution, climate changes and health problems (such as cardiovascular diseases and respiratory illnesses, for example) are inevitably associated with the use of fossil fuels and the production of environmentally hazardous gases arising from it. While CO, CO_2, NO_2, SO_2 and CH_4 are just a few examples of by-products in the combustion of fossil fuels [1,2], renewable energy sources can generate power with no or very low emission of air pollutants and greenhouse gases. Therefore, the development and use of clean and renewable modes of power generation is essential to also address these increasing environmental and health concerns [1].

Despite their environmental benefits, some renewable energy sources such as solar and wind power are limited by their variable nature and thus require the use of efficient energy storage technologies. Hydro power has geographic limitations and can have tremendous impact on the lives of communities that are displaced and on the ecosystems that are flooded for the construction of dams. Solid oxide fuel cells (SOFCs), on the other hand, are highly efficient energy conversion devices, which can produce electricity anywhere and continuously as long as fuel is provided, being a very attractive alternative to fossil-fuel based technologies.

Computational modelling is an essential tool in developing or improving SOFC components, allowing researchers to predict, understand and explain the mechanisms behind experimentally observed properties. In this thesis, density functional theory and molecular

dynamics simulations are performed to investigate, understand and improve the properties of SOFC components, aiming to enhance the device's durability and performance.

1.1 Solid oxide fuel cells

Solid oxide fuel cells are highly efficient energy conversion devices and can produce electrical energy from a variety of fuels. They can directly convert chemical energy into electrical power with efficiencies higher than 60% (up to 90% when heat is recovered), as the process is not limited by the Carnot cycle [3]. Electricity can be generated from a variety of fuels (H_2, CO, CH_4, other hydrocarbons etc.) [2,3], allowing the SOFC technologies to easily adapt to current and future fuel demands. If carbon-based fuels are used, CO_2 is an inevitable product of power generation. If H_2 is the chosen fuel, a viable option in the future when problems such as its sustainable production, transportation and storage are overcome, water and heat are the only by-products and electricity is generated in an environmentally friendly way [2]. These devices consist of two electrodes, cathode and anode, separated by a solid-oxide electrolyte, through which ionic transport occurs [4] (Figure 1.1).

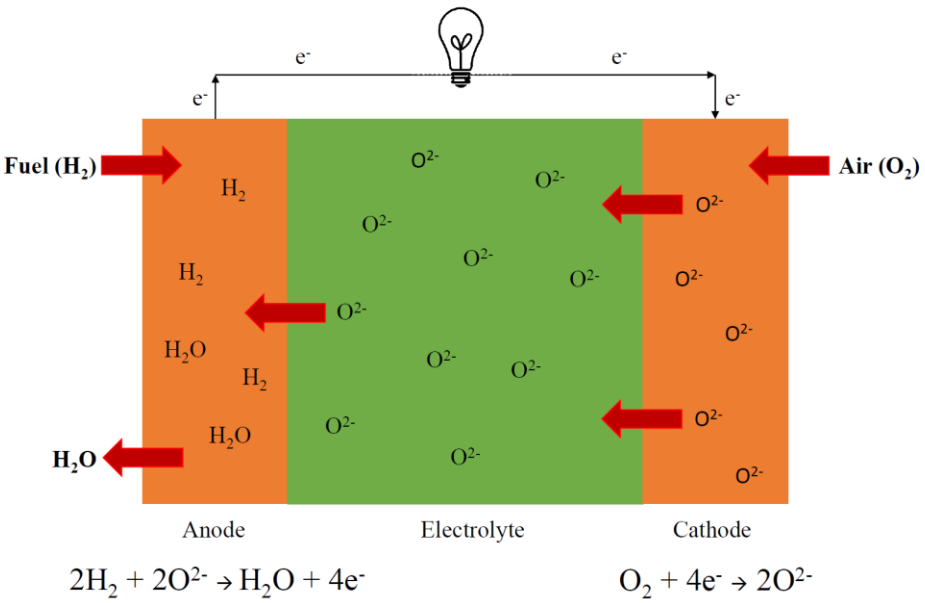

Figure 1.1 – Scheme illustrating SOFC operation. Oxygen gas is reduced at the cathode side and the resulting oxide ions are transported through the solid electrolyte. Fuel (H_2 in this case) is provided at the anode side and oxidized. The cathode and anode are electrically connected establishing an electron flux outside the cell.

At the cathode side, air (O_2) is electrochemically reduced to oxide ions (Equation 1.1), which are then transported through the electrolyte to the anode, to oxidise the fuel provided (Equation 1.2). The electrons generated in these redox reactions are transferred between the electrodes through an external circuit, generating electricity [5].

$$O_{2(g)} + 4\,e^- \rightarrow 2\,O^{2-} \tag{1.1}$$

$$2\,H_{2(g)} + 2\,O^{2-} \rightarrow 2\,H_2O_{(g)} + 4\,e^- \tag{1.2}$$

Cathode materials should present good catalytic activity to the oxygen reduction reaction (ORR), which consists of the adsorption and dissociation of O_2 molecules, followed by the transport of O^{2-} ions through the cathode to the solid electrolyte. These materials can be either pure electronic or mixed ionic-electronic conductors (MIEC). If only electronic conduction is present, the ORR will occur exclusively at the triple-phase boundary (TPB), i.e., the region where cathode, electrolyte and gas meet (Figure 1.2a). MIEC is therefore extremely beneficial as the ORR stops being restricted to the TPB and can occur at the electrode-air interface, since oxide ions are able to diffuse through the cathode [6,7] (Figure 1.2b). For both cases, the use of highly porous materials is an advantage, so oxygen gas can be efficiently transported throughout the cathode [8].

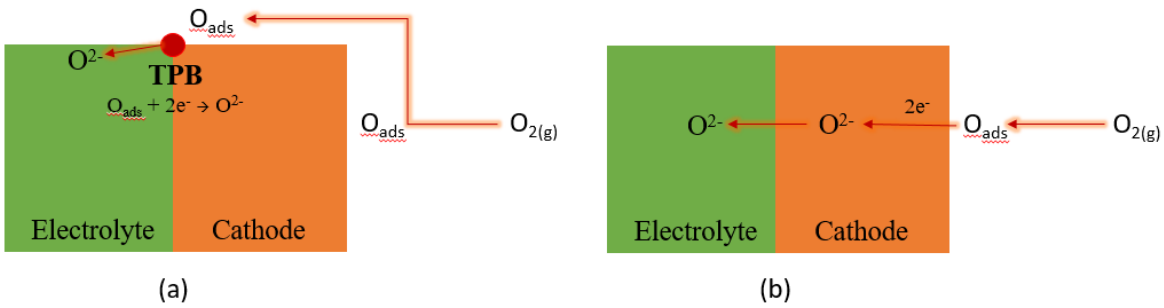

Figure 1.2 - ORR at (a) the TPB of a pure electronic conducting cathode, and (b) at the surface of a mixed ionic-electronic conducting cathode.

Electrolyte materials, through which ionic transport occurs, must possess high oxide ion conductivity and negligible electronic conduction to avoid the short circuit of the cell [5]. An ideal solid electrolyte must be stable in both oxidising and reducing environments, as it is in direct contact with both electrodes. Anode materials should present good catalytic activity for fuel oxidation, along with good electronic conduction. Ideally, the anode should

also be porous, with suitable candidates having a minimum of 30% porosity to guarantee sufficient catalytic activity [9].

In a SOFC, all components are solid and hence should have similar thermal expansion coefficients to avoid mechanical fracture due to volume changes. Electrodes and electrolyte should also be chemically inert to each other to avoid decomposition and formation of secondary phases. These properties must be observed under SOFC operating conditions, i.e., over a wide range of oxygen partial pressures (10^{-21} to 1 atm) and temperatures (673-1273 K) [10]. High temperatures (1073-1273 K) are currently required for satisfactory ionic conduction in the electrolyte and efficient catalytic activity to the ORR on the cathode [10,11], increasing the cost, since expensive materials are required as components, and decreasing the life-time of the device due to its fast degradation [12–14]. Therefore, one of the main challenges in SOFC design is to decrease the operating temperatures through the optimization or development of electrolyte and electrode materials with satisfactory conduction and catalytic properties in the intermediate temperature (IT) range (673 to 1073 K) [15,16].

1.2 Solid oxide electrolysis cells

Solid oxide electrolysis cells (SOECs) operate reversibly to SOFCs, converting electricity into chemical energy [17,18]. Steam (H_2O) provided at the cathode side is electrolysed to H_2 and O^{2-} (Equation 1.3). Hydrogen, a clean fuel, can act as energy carrier, while oxide ions can travel through the electrolyte and reach the anode, to be oxidised to air (Equation 1.4). While in SOFCs cathode and anode are the oxygen and fuel electrodes, respectively, in SOECs fuel is supplied at the cathode side, while oxygen is produced at the anode side.

$$2\,H_2O_{(g)} + 4\,e^- \rightarrow 2\,H_{2(g)} + 2\,O^{2-} \quad (1.3)$$

$$2\,O^{2-} \rightarrow O_{2(g)} + 4e^- \quad (1.4)$$

Ideally, SOFC and SOEC technologies would be coupled in solid oxide reversible cells (SORCs), devices which can act as both fuel cell and electrolyser [19], being able to convert chemical energy (fuel) into electricity and vice-versa. SORCs could be integrated

with other (intermittent) renewable technologies, to store their produced energy as H_2 and convert it back to electricity when required [19,20]. The main problem associated with SORCs is developing suitable materials that can act as both fuel and oxygen electrodes under the two operation modes. Still, electrolyte materials would have the same function in SOFC and SOECs, i.e., to efficiently transport oxide-ions between the electrodes. Hence, any developments in electrolyte materials aiming SOFC applications would also apply to SORCs.

1.3 Mechanisms for oxide ion diffusion

Ionic diffusion is the movement of ions away from their equilibrium lattice positions. Oxide ion diffusion, a central theme in this thesis, is a fundamental mechanism in SOFC operation and the main barrier to decreasing operation temperatures to the IT range. This section discusses three different mechanisms for oxide ion transport – the vacancy, interstitial, and interstitialcy mechanisms – commonly observed in electrolyte and cathode materials. The mechanism through which ionic diffusion occur will depend on the material's structure and composition (e.g. oxygen stoichiometry and which type of point defects are present within the lattice) [21].

For oxygen deficient materials possessing intrinsic or extrinsic mobile oxygen vacancies, ionic diffusion generally occurs via a vacancy mechanism, in which oxide ions jump to a neighbouring vacancy, leaving another vacancy behind, as depicted in Figure 1.3a. This mechanism is thermally activated and the high temperatures currently needed for SOFC operation are partly due to the high energy barriers for oxide ion hopping. Temperatures above 873 K are necessary for satisfactory ionic conduction ($\sigma > 0.01$ S cm^{-1}) [21].

Oxygen transport via a vacancy mechanism can be improved through aliovalent doping, which can add extrinsic vacancies to a system as a charge compensation mechanism. The ionic conductivity will increase with vacancy concentration up to a limit, after which long-range vacancy ordering or vacancy trapping around dopants will occur, hindering their mobility and significantly increasing the activation energy of oxide ion diffusion. Vacancy ordering also occurs at low temperatures [22], and hence is another reason for the high temperatures needed during SOFC operation. The vacancy mechanism is commonly

observed in fluorite- and perovskite-structured materials, which will be discussed in the following sections.

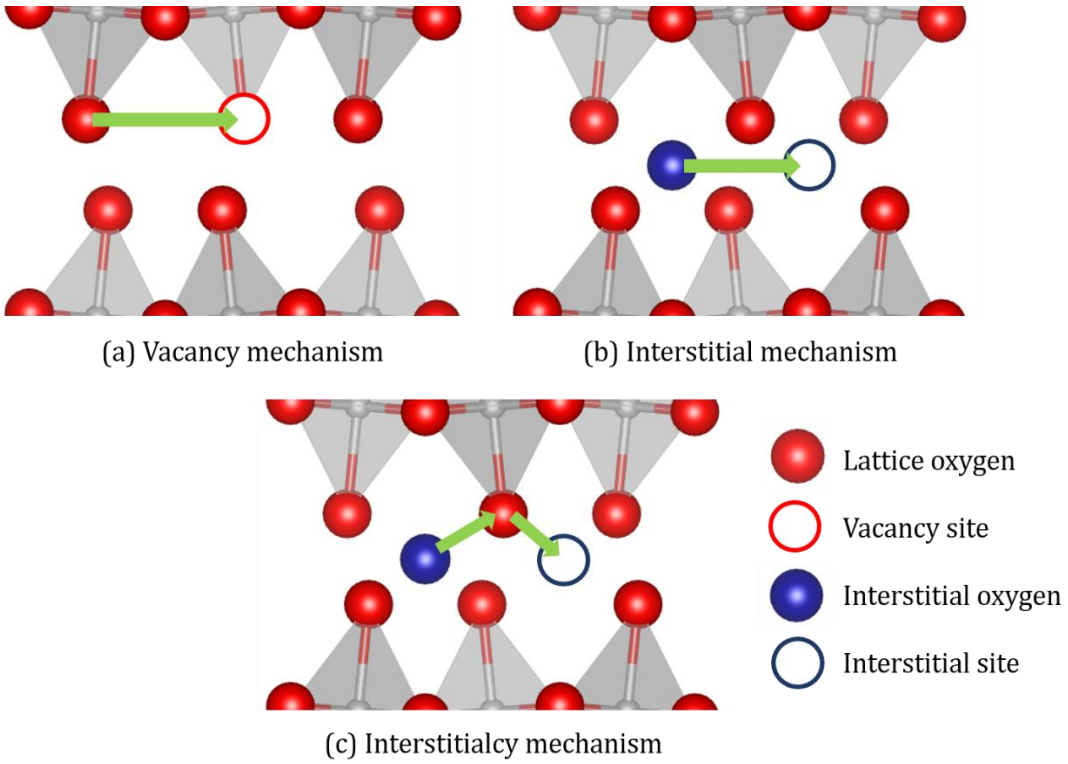

Figure 1.3 – (a) Vacancy, (b) interstitial and (c) interstitialcy oxide ion diffusion mechanisms

In chemical systems possessing excess oxygen, oxide ion diffusion can occur via the interstitial or the interstitialcy mechanisms. In the interstitial mechanism, interstitial oxide ions will jump to a neighbouring interstitial site, without permanently displacing any other ionic species from their lattice sites (Figure 1.3b) [21]. In the interstitialcy mechanism, the interstitial oxygen will displace a lattice oxygen from its site, which will then move to a neighbouring interstitial site (Figure 1.3c) [21]. These mechanisms are commonly observed in Ruddlesden-Popper oxides (Section 1.5.2), which can easily accommodate over-stoichiometric oxygen in interstitial sites due to their layered structure.

Fluorite- and perovskite-structured materials can be excellent pure oxide ion conductors or mixed ionic and electronic conductors, and hence are commonly used as electrolyte and cathode materials in SOFCs. Sections 1.4 and 1.5 will discuss their main structural properties, which allow their use as SOFC components.

1.4 Fluorite-structured materials

Fluorite-structured oxides have general formula AO_2, with A being a large tetravalent cation, such as Zr^{4+} or Ce^{4+} [23]. Zirconia, however, is too small to sustain the cubic fluorite structure at low temperatures, which can be stabilized via doping with larger species. The fluorite structure consists of oxygen atoms arranged in a cubic lattice, tetrahedrally coordinated to the cations, which assume a face-centred cubic arrangement (Figure 1.4) [16].

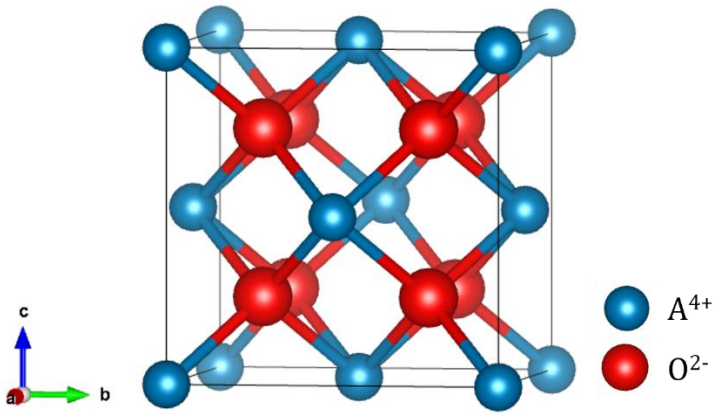

Figure 1.4 – The cubic fluorite structure, with general formula AO_2 and *Fm-3m* cubic space group. Blue and red spheres represent A^{4+} and O^{2-} ions.

Ionic diffusion in fluorite-structured materials occurs via a vacancy mechanism; oxygen vacancies are positioned in energetically equivalent lattice sites, decreasing the energy barrier for oxide ion transport. In less symmetric phases, ionic diffusion is hindered by the presence of energetically different oxygen sites; the energy difference might too high to overcome, resulting in the trapping of oxygen vacancies in lower energy sites [23].

Extrinsic vacancies can be introduced to the fluorite-structured materials via aliovalent doping, with dopant concentrations as high as 40% being accommodated due to the structure's openness and high tolerance [23]. However, lattice distortions arising from doping cause deviations from the cubic symmetry, which can hinder ionic conductivity. Dopants with an optimal size, the so-called critical radius (r_c), have higher solubility into the lattice and yield the highest improvements to ionic conduction properties, as they introduce the least amount of structural distortion. For ZrO_2 and CeO_2, the r_c for trivalent ions was determined as 0.95 Å and 1.04 Å, respectively [24,25]. Accordingly, the best ionic conductivity improvements are observed for scandia- and yttria-stabilized zirconia (ScSZ

and YSZ), with the ionic radii of 8-coordinated Sc^{3+} and Y^{3+} being 0.87 Å and 1.019 Å [26], respectively, and gadolinium or samarium doped ceria (GDC and SDC), with the ionic radii of Gd^{3+} and Sm^{3+} being 1.053 Å and 1.079 Å [26], respectively. YSZ, GDC and SDC are the commercially used SOFC electrolytes and will be discussed in more detail in Section 1.6.1.

1.5 Perovskite-based materials

Perovskite-structured materials are described by the general ABX_3 formula; A-site cations are 12-coordinated and larger in size, while B-site cations are 6-coordinated and possess smaller ionic radii. The perovskite structure (Figure 1.5) consists of B-site ions located in the middle of corner-sharing BX_6 octahedra, which in turn surround A-site cations (the A-site is in the centre of a cube formed by eight corner-sharing octahedra) [16]. X is usually oxygen or fluorine; still, perovskite chlorides, bromides, hydrides and sulphides have been reported [27]. X anions have a coordination number of 6, being 4- and 2-coordinated to A and B, respectively. A and B have a combined charge of +6, allowing a variety ionic charge combinations to exist, such as A^{1+} and B^{5+}, A^{2+} and B^{4+} or A^{3+} and B^{3+}. Therefore, most metallic elements can be accommodated within the perovskite lattice, resulting in a range of compositions and structures, which leads to a variety of dielectric, magnetic, electric and optical properties [16,27].

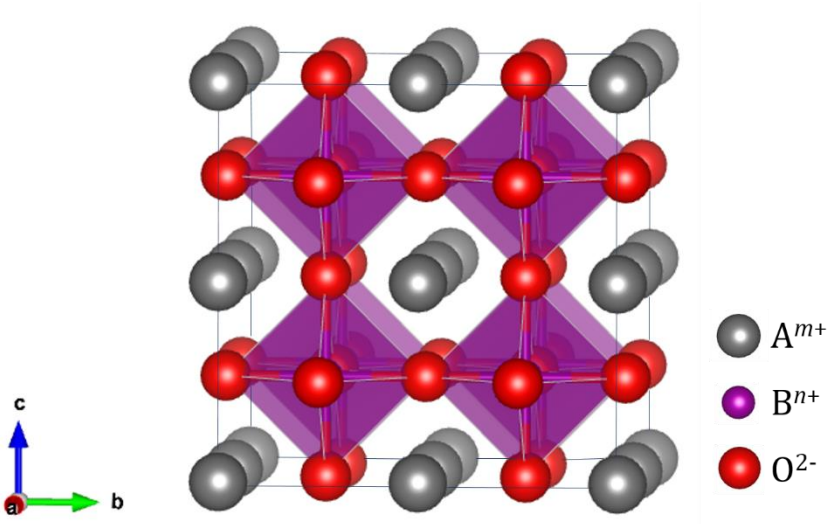

Figure 1.5 – Ideal cubic perovskite structure, with space group *Pm3m*. Grey, purple and red spheres represent A, B and O ions.

Perovskites oxides (ABO_3) are generally used as SOFC components [16] due to their high structural stability and oxygen transport properties. These ceramics are more flexible to doping than other systems due to the existence of two host sites and to their balanced geometrical array of atoms, which allows deviation of its stoichiometric composition to a considerable extent without the loss of the original perovskite structure [16,28]. If the host cations are substituted with lower valence species, oxygen vacancies can be generated as a charge compensating mechanism to preserve electroneutrality [29], leading to oxide-ion diffusion through the lattice. Electronic conduction can also be improved through aliovalent doping due to an increase in the number of charge carriers as a result of an electronic charge compensation mechanism [30]. Changes in the ratio between the ionic radii of A and B cations lead to structural distortions, lowering the ideal cubic symmetry to hexagonal or orthorhombic, which can originate ferromagnetic and ferroelectric properties [16,27]. Most deviations from the ideal perovskite structure are due to the tilting of the BX_6 octahedra, commonly observed for smaller A-site cations [27]. Other possible causes for structural distortions are related to electronic instabilities of the B-site cation, such as Jahn-Teller distortion of the BX_6 octahedral structure (observed in $KCuF_3$, for example) or the ferroelectric displacement of the B cation within the octahedron, as seen in $BaTiO_3$ [27].

1.5.1 The Goldschmidt tolerance factor

The stability of perovskites and deviations from the cubic symmetry can be predicted and evaluated from the Goldschmidt tolerance factor (t), given in Equation 1.5, where r_i is the ionic radii of species i. Goldschmidt [31] suggested that in the ideal cubic perovskite structure, the ratio between the A-O and B-O bond lengths should be $\sqrt{2}$: 1. If the bond length is assumed to be a sum of the ionic radii of the bonded species, a t value of 1 is obtained for the ideal cubic lattice [32].

$$t = \frac{r_A + r_O}{\sqrt{2}(r_B + r_O)} \tag{1.5}$$

Perovskite-structured compounds can possess t values between 0.89 and 1.10. Even though by definition the ideal cubic structure has t = 1, compounds with 0.89 < t < 1.01 can still be in the cubic phase (e.g. $SrTiO_3$, with t = 1.002). For t > 1, there is usually an increased

stability of the hexagonal (e.g. $BaMnO_3$, with t =1.075) and tetragonal ($BaTiO_3$, with t = 1.062) symmetries, due to the bigger size of A-site cations (or to the smaller size of the B-site species). For smaller t values (≈ 0.9), the BO_6 octahedra are tilted, resulting in orthorhombic or rhombohedral symmetries. The tilting of the octahedra, also known as $GdFeO_3$-type distortion, is observed in a number of compounds (e.g. $GdFeO_3$, with t = 0.909, and $YFeO_3$, with t = 0.897) [32]. Oxides with t < 0.89 usually crystallize in the ilmenite structure, possessing the same ABO_3 composition, but with similar-sized A and B-site cations, which both occupy octahedral sites [16].

The tolerance factor can be a useful indicator of the stability of perovskite-structured compounds and can be used to roughly predict the material's structure; however, many examples deviate from its predictions (e.g. $LaGaO_3$ is orthorhombic at room temperature and has t = 0.966). Other factors, such as the presence of intrinsic or extrinsic vacancies, for example, can change the expected symmetry due to the incompleteness of the octahedra. Furthermore, the nature of the cations, such as their preferable coordination number, electronic structure and chemical environment, also plays an important role, in both structural and transport properties.

Similarly to fluorite-structured oxides, ionic transport in perovskites is also related to lattice stress, with a higher degree of distortions hindering diffusion. In the ideal (stress-free) cubic perovskite structure, A-site cations possess the same size as oxide ions (1.40 Å). Thus, La^{3+}- (1.36 Å) and Sr^{2+}-containing (1.44 Å) perovskites have the highest oxide-ion conductivities among perovskite compounds. Similarly, B-site cations also have an ideal size (0.58 Å), which perfectly "fits" within the octahedral hole and hence decreases lattice stresses; Ti^{4+} (0.605 Å) and Ga^{3+} (0.62 Å) closely match this radius [23]. Besides steric factors, electronic effects also influence conduction properties; as previously mentioned, the Jahn-Teller effect and ferroelectric displacements can induce lattice distortions. Furthermore, the charge of B-site cations also plays a role; the interaction between B^{n+} and O^{2-} is expected to increase with n, hindering oxide ion conduction. As a result, $A^{3+}B^{3+}O^{2-}_3$ perovskites would possess higher conductivities than $A^{2+}B^{4+}O^{2-}_3$, which in turn would present higher conductivities than $A^{1+}B^{5+}O^{2-}_3$ [23].

1.5.2 Ruddlesden-Popper oxides

The Ruddlesden-Popper (RP) series of layered oxides are perovskite-related materials with anisotropic lattices leading to interesting oxygen diffusion and superconducting properties. Their general formula is $A_{n+1}B_nO_{3n+1}$, with the first members of the series (n = 1) possessing K_2NiF_4-type structures (Figure 1.6). These oxides consist perovskite (ABO_3) and rock salt (AO) layers, intercalated along the *c*-axis, resulting in strong anisotropic properties. Their structure can accommodate a wide range of oxygen stoichiometries (δ), with extrinsic oxide ions being accommodated in interstitial sites. Oxygen deficiency, on the other hand, results in oxygen vacancies. Diffusion occurs via the interstitial sites, in contrast to the vacancy mechanism predominantly observed in perovskites [16]. Even though the K_2NiF_4 structure is tetragonal, RP oxides usually present orthorhombic distortion to alleviate stresses arising from the intercalation of layers and oxygen excess [33]. The most extensively studied members of the first series are $La_2CuO_{4+\delta}$ and $La_2NiO_{4+\delta}$ [34–43], with other lanthanide-based nickelates also having attracted interest for energy applications, such as $Pr_2NiO_{4+\delta}$ and $Nd_2NiO_{4+\delta}$ [44–49].

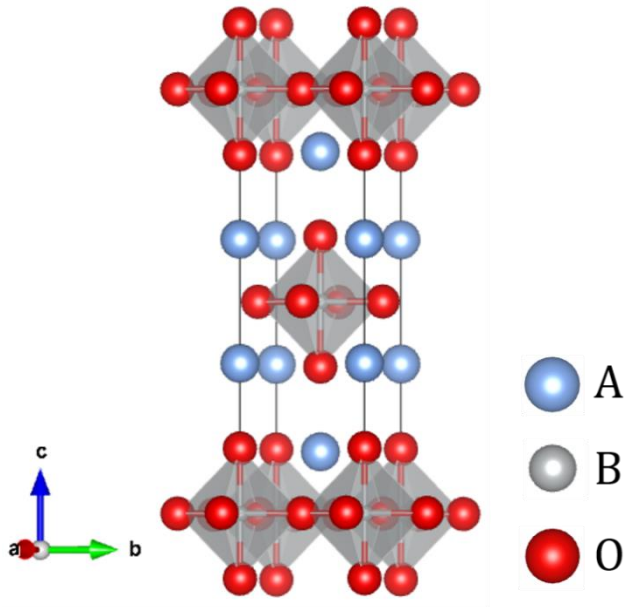

Figure 1.6 – K_2NiF_4-type structure (tetragonal symmetry with space group *I4/mmm*), adopted by the first members of the Ruddlesden-Popper series (n = 1), with general formula $A_{n+1}B_nO_{3n+1}$. Blue, grey and red spheres represent A, B and oxygen ions.

1.6 SOFC components

SOFC research focuses on optimising the conduction and catalytic properties of the current high-temperature components, or on the development of new materials, which can potentially lower operating temperatures to the IT range. The combination of first principle calculations and molecular dynamics (MD) simulations can provide an accurate and complete description of the chemical systems being investigated — from their electronic structure and related properties to the thermodynamic and kinetics behind catalytic reactions or diffusion processes. Computational modelling is, therefore, a fundamental asset in the development or improvement of SOFC components. The following sections will review the recent literature (experimental and theoretical) investigating current and potential SOFC components, focusing on the computational modelling of these materials.

1.6.1 Electrolyte materials

Fluorite-structured zirconia-based ceramics, especially yttria- (YSZ) and scandia-stabilized zirconia (ScSZ) present excellent ionic conductivities at high temperatures and negligible electronic conduction. Optimized compositions with 8 mol% [50–53] Sc_2O_3 or Y_2O_3 present the highest conductivity values at 1273 K, with ScSZ having ionic conductivity more than two times higher than that of YSZ. ScSZ also has satisfactory ionic conduction at lower temperatures (1073 K) [54], but problems regarding its low availability, high cost and poor stability impair its use. As a result, YSZ is the most widely used high-temperature SOFC electrolyte, with theoretical investigations still being done to further optimise its conduction properties at lower temperatures. MD simulations suggest that heterolayered YSZ/ScSZ show enhanced ionic conductivity when compared to heterogeneously doped YScSZ. This is mainly due to the introduction of in-plane biaxial strain [51] although the conductivities are still lower than those of YSZ or ScSZ. Regardless, heterointerface engineering could still be an interesting alternative to improve conduction properties. Reactive force field potential (ReaxFF) [55] MD simulations showed that Fe_2O_3-doping can significantly improve the ionic conductivity of YSZ in the 773-1073 K range, and it is better than BaO-, CuO-, ZnO- or MgO-doping. Maximum ionic conductivity was predicted to be achieved with a 4 mol% Fe_2O_3 concentration [56,57].

Core-shell structures composed of YSZ cores and carbonate shells present good ionic conductivities at IT (773-873 K) and possess multi-ionic nature, meaning that besides oxide-ion conduction, the diffusion of intrinsic (Li^+ and CO_3^{2-}) or extrinsic (H^+) species can also occur. PBE0 [58,59] calculations indicate that the presence of a space-charge layer at the interface appears to be a key element in these materials, facilitating defect formation and migration of Li^+ as well as extrinsic O atoms [60]. The energy barrier for H^+ migration is also lowered at the interface, since the formation of proton species is favoured in this region, due to their interaction with O atoms in the YSZ surface.

Ceria doped with trivalent cations, mainly Sm^{3+} (SDC) and Gd^{3+} (GDC), present ionic conductivities comparable to that of YSZ (0.1 S cm^{-1}) but at lower temperatures [2,15,61,62] (1073 K), being one of the main alternatives for its substitution. However, CeO_2-based systems are not purely ionic conductors – the reduction of CeO_2 as a result of the formation of intrinsic vacancies can generate unwanted electronic conduction due to the presence of Ce(III) ions [63,64], impairing cell performance as a result of electronic leakage [2,15,16,64]. From PBE+*U* calculations, Gd^{3+} (GDC), Sm^{3+} (SDC), Nd^{3+} and Pr^{3+} were predicted to be the best dopant options, with low doping energies, defect association energies and do not facilitate reduction. For Sm^{3+}, Nd^{3+}, Pr^{3+} and La^{3+} doping, the reduction energy is considerably higher than that of pure CeO_2, suggesting that reduction would be unlikely in the presence of these cations. Yb^{3+}, Tm^{3+}, Er^{3+}, Ho^{3+}, Dy^{3+} and Tb^{3+} are also suggested as dopants, for the same reasons but to a lesser extent [64]. Kinetic Monte Carlo simulations suggest the ionic conductivity to be linearly dependent on the dopant ionic radii, indicating that lattice distortions are closely related to oxide-ion conduction [65]. Maximum values were obtained for Sm^{3+} doping.

PBE calculations suggest that the application of biaxial tensile strain increases the lattice spacing in CeO_2 and reduces the oxide-ion migration barrier by up to 9%; local lattice strain can also promote changes in the local volume, allowing co-doping with bigger cations, which can further reduce the migration barrier (down by 26% for La^{3+} co-doping) [66]. However, even though such strain can improve oxide ion conduction, large cations can also increase defect association [64] and hence be detrimental to the ionic conductivity.

$LaGaO_3$-based materials possess high oxide-ion conductivity in lower temperatures (973-1073 K) [23,67–69] when compared to traditional fluorite-structured materials, with negligible electronic conduction and good chemical stability over a wide range of oxygen

partial pressures (10^{-20} to 1 atm) [68]. LSGM, a $LaGaO_3$-based electrolyte doped with Sr^{2+} (La-site) and Mg^{2+} (Ga-site), is a pure ionic conductor in the IT range; previous studies are in agreement that optimized compositions of LSGM can present ionic conductivity in the 0.11-0.17 S cm^{-1} range at 1073 K [2,70–74], higher than those observed for ceramics with a fluorite-type structure in the IT range. Islam *et al.* [75] used interatomic potentials to calculate the binding energies between dopants and vacancies in $LaGaO_3$ and determined that Ga-site dopants (Mg^{2+}, Co^{2+}, Ni^{2+} and Cu^{2+}) present considerably higher binding energies than La-site dopants (Sr^{2+} and Ca^{2+}), indicating that charge-compensating vacancies would tend to be trapped around Ga-site dopants. Defect interaction can therefore directly influence ionic conductivity and hence the suitability of a material as solid-oxide electrolyte.

1.6.2 Cathode materials

Perovskites oxides and related materials are generally chosen as cathodes [16] due to the variety of elements that can occupy the A and B sites as hosts or dopants, and the resulting wide range of properties. $LaMnO_3$-based perovskites present good electronic conductivity, chemical stability and catalytic activity for the ORR, with Sr-doped $LaMnO_3$ (LSM) being the most commonly used high temperature SOFC cathode [76]. However, its negligible ionic conductivity impairs its use in the IT range. Modelling $LaMnO_3$ is a challenge; both Jahn-Teller and $GdFeO_3$-type distortion of the [MnO_6] octahedra play a role in this perovskite's structure, and Mn^{3+} partially filled *d*-shell leads to the self-interaction error (SIE). Accordingly, a range of functionals (PBE [77], PBE+*U*, PBEsol [78], PBEsol+*U*, B3LYP, HSE [79], B3LYP [80] and HSE06 calculations [7,81–85]) have been used in simulations, with PBEsol+*U* ($U_{(\mathrm{Mn}\ 3d)}$ = 4.5 eV and $U_{(\mathrm{O}\ 2p)}$ = 5.5 eV using the Dudarev approach [86]) providing the best description of the structural and electronic properties of the orthorhombic perovskite [76].

Surface calculations indicate that the stability of $LaMnO_3$ surfaces increases in the order (010) < (100) < (111) < (110) < (101) < (011) < (001) [7,8,87], with low coordination around surface La/Mn atoms resulting in higher surface energies and greater reactivity. Oxygen vacancy formation energy was lower at the surfaces [7,8], which results in segregation. Sr doping has been shown to enhance this segregation [8] which can be of benefit to the ORR. PBE calculations investigating chromium poisoning from the $LaCrO_3$

interconnect suggest that the (La,Sr)O-terminated (001) surface [88] is particularly vulnerable when compared to the MnO_2-terminated one, although the lack of a self-interaction correction (SIC) method in these calculations call the obtained results into question.

$La_{0.6}Sr_{0.4}Co_{0.2}Fe_{0.8}O_{3-\delta}$ (LSCF) is a MIEC used as cathode in IT-SOFCs, possessing power densities similar to that of LSM, but at operating temperatures 100 K lower [89,90]. PBE+*U* calculations of $LaFeO_3$ predict Sr^{2+}, Ca^{2+} and Mn^{2+} (A-site) and Co^{2+}, Fe^{2+} and Mn^{2+} (B-site) to be the best dopants. These defects present low solution energies, vacancy compensation at oxygen poor conditions and no preference at oxygen rich conditions. B-site dopants present higher binding energies to oxygen vacancies which could result in defect clustering [91]. However, the relationship between the unspecified oxygen poor and rich conditions and experiment is unclear.

Sr surface segregation is observed in LSCF under SOFC operating conditions with contradictory effects having been reported [92–95]; both performance degradation and improvement have been attributed to the formation of Sr-O compounds (SrO, $Sr(OH)_2$ and $SrCO_3$). DFT calculations suggest that the presence of $SrCO_3$ nanoparticles enhances O_2 adsorption and dissociation [96]. However, since carbonate formation under CO_2-containing atmospheres degrades performance [97], $SrCO_3$ might not be the best candidate to exemplify the Sr surface segregation phenomenon.

The spin state in Co-based systems has been shown to impact vacancy formation at the surface with DFT calculations favouring the creation of these defects in the 2nd (Co^{3+} high spin) and 3rd layers (low spin) of the LaO-terminated (001) surface, preventing their interaction with O_2 [98]. DFT phonon calculations also suggest that transition metal doping ($LaCo_{0.5}A_{0.5}O_3$, A = Fe, Ni) can be used as strategy to decrease the TEC increasing the compatibility of the cathode with electrolytes such as YSZ and GDC [99]. However, a SIC was not included in these calculations, calling the results into question.

PBE+*U* calculations examining the minimization of the elastic energy of the A-site dopants suggest that replacing Sr (1.44 Å [26]) with Ca (1.34 Å [26]) should suppress dopant segregation. Larger fractional free volumes are suggested to result in smaller elastic energies [100], which may be extended to other perovskite oxides. However, other factors such as steric effects due to size mismatch, charging compensating mechanisms, defect-defect

interactions, SOFC operating temperatures and partial pressures should have also be taken into consideration.

$Ln_2NiO_{4+\delta}$ (Ln = La^{3+}, Pr^{3+}, Nd^{3+}) Ruddlesden-Popper oxides have attracted interest as cathode materials for IT-SOFCs due to their mixed ionic and electronic conductivity, good reactivity with oxygen and compatibility with commonly used electrolyte materials [6]. Their *p*-type electronic conductivity can be associated with nickel's mixed valence and occurs via a polaron hopping mechanism. $La_2NiO_{4+\delta}$ phases present conductivity of ≈100 S cm^{-1} at 1073 K under high oxygen partial pressures. Furthermore, at lower $p(O_2)$ values, their electronic conductivities decrease much slower than what is observed in traditional perovskite oxides [101]**.** The ability of these RP oxides to accommodate oxygen interstitial ions can lead to an improvement in the ionic conductivity compared to some perovskite materials, which could be beneficial to the ORR. MD simulations suggest that the oxide-ion transport in tetragonal $La_2NiO_{4+\delta}$ occurs via an interstitialcy mechanism and is highly anisotropic, occurring predominantly along the *a*-*b* plane. Furthermore, it was observed that oxygen excess did not significantly change the activation energy of oxide-ion diffusion, which remained at approximately 0.51 eV [102].

A-site doping (A = Ca, Sr, Ba) in Ln_2NiO_4 increases electrical conductivity due to the increased number of charge carriers [103–105]. In $Pr_{2-x}Sr_xNiO_{4+\delta}$ the highest conductivity (≈120 S cm^{-1} in the 773-1173 K range) is obtained for samples with $x = 0.5$, the ones to possess the highest $[Ni^{3+}]/[Ni^{2+}]$ ratio and thus the highest average Ni oxidation state (≈2.5+) [106]. However, a decrease in interstitial oxygen content (δ) occurs with the increase in dopant concentration, hindering oxygen mobility and hence the ionic conductivity – the highest values are observed for undoped $Ln_2NiO_{4+\delta}$ samples [103–105,107].

B-site doping has distinct effects in the material's properties; cobalt substitution can increase oxygen content and enhance both the oxygen diffusion and exchange coefficients in La_2NiO_4 [108]. Cu-doping led to an increase in electrical conductivity and a decrease in polarization resistance [108,109]. Cu-doped Pr_2NiO_4 possess higher electrical conductivity than Mg-, Zn- or Fe-substituted samples [109], as the Ni/Cu-O bond length in the *ab* plane is shortened, resulting in lattice contraction and hence facilitating polaron hopping from Ni^{3+} to Ni^{2+}/Cu^{2+} [110]. Lattice expansion along the *c* direction is observed under Cu-doping and facilitates interstitial O^{2-} diffusion to nearby sites, especially in the rocksalt layer via an interstitialcy mechanism, increasing ionic conductivity [110]. Iron doping, on the other hand,

can be detrimental to the electronic conductivity. Fe^{3+} is more stable than Ni^{3+}, and hence Fe-doped samples have a smaller amount of trivalent Ni when compared to other dopants [111]. Therefore, the stability of the trivalent cation with respect to its divalent form also plays a role in the conduction properties.

1.6.3 Anode materials

Ni-based electrodes are the most widely used anodes in SOFCs – a Ni/YSZ electrode is paired with YSZ electrolytes, while Ni-doped CeO_2 is used with ceria-based electrolytes. Even though Ni-systems present excellent catalytic properties for H_2 (fuel) dissociation, good electronic conductivity and low cost, problems such as low stability towards impurities present in the fuel, and low coking resistance [52] still need to be overcome. PBE calculations investigating sulphur poisoning of the Ni catalyst suggest that Rh, Pd, Ag, Pt and especially Au-doping can weaken the metal/adsorbate interaction, decreasing the adsorption strength of HS, H and S species (products of H_2S dissociation) on the M/Ni (111) surface and supressing the H_2S decomposition [112]. PBE also suggests that the presence of adsorbed OH lowers the energy barrier for the oxidation of sulphur by O atoms on the surface [113].

Anodes can also suffer from carbon deposition, which can lead to cell fracture due to volume changes [114]. MD simulations show that carbon atoms formed on the Ni (100) surface when methane is used as fuel can diffuse into the bulk, with the resulting lattice distortion causing volume changes and crystal fracture, impairing SOFC performance [115]. PBE calculations indicate that an oxygen-containing reaction media can prevent carbon deposition by converting CH (an intermediate of the CH_4 decomposition) to CO_2. This process can be favoured at the TPB due to the presence of oxide ions from the electrolyte, but coke formation away from this region can be an issue. A possible solution is to increase the concentration of oxy species on the Ni surface away from the TPB [116]. PBE calculations also suggest that carbon adsorption is disfavoured when Ni is alloyed with Fe, indicating a higher tolerance to carbon deposition. In addition, high H and O binding energies are calculated for the Ni/Fe surface, suggesting excellent catalytic performance [117].

1.7 Thesis Aims and Outline

SOFCs are attractive alternatives to fossil fuel-based technologies due to their high efficiency and fuel flexibility. The main issue is the fact that high temperatures (above 1073 K) are necessary for the satisfactory ionic transport in the electrolyte and catalytic activity to the ORR in the cathode, increasing the cost and decreasing the lifetime of these devices. Over the past few years, DFT (mainly PBE+*U*) and MD methods have been the preferred approaches to investigate and understand the properties of SOFC components, aiming to decrease SOFC operation temperature to the IT range (673 to 1073 K). Traditional materials continue to receive most of the attention – computational modelling has been used to further improve their properties and enhance SOFC durability and performance.

The research presented in this thesis aims to aid in the development of suitable electrolyte and cathode materials to IT-SOFCs, by investigating how conduction properties can be improved via aliovalent doping. The main objective is to determine which dopants yield the best ionic and/or electronic conductivity improvements in $LaGaO_3$ and La_2NiO_4, potential electrolyte and cathode materials, respectively, and investigate the reasons and mechanisms behind such improvements. This thesis aims to address the lack of comprehensive literature studies on these materials, by systematically investigating a range of dopants and hence obtaining consistent results. Furthermore, existing theoretical work does not take different chemical environments into consideration; hence their comparison to experiment can be called into question.

The principles behind the operation of SOFCs, the mechanisms of oxygen transport, and previous studies investigating materials used as SOFCs components have been presented in Chapter 1. In Chapter 2, the theoretical framework behind the computational methods used in this thesis are described, such as basic quantum chemistry principles, Hartree-Fock theory, density functional theory and interatomic potential methods. Chapter 3 outlines how these methods were implemented to calculate and investigate the structural, electronic and transport properties of the materials of interest.

In Chapter 4, DFT calculations are performed to investigate the effects of divalent metals (Mg, Zn, Co, Fe, Sn, Ni, Mn, Pt, Pd, Ca, Sr, Pb and Ba) as dopants in $LaGaO_3$ and understand their influence in the defect chemistry and ionic conductivity of the perovskite, aiming SOFC electrolyte applications. The lowest energy structure for each doped system was determined in order to investigate key features that affect the ionic conductivity of the

perovskite – the doping energy, the preferable dopant position (La or Ga site) and the association energy between vacancies and dopants – as a function of dopant identity and chemical environment, aiming to determine which dopants are the most beneficial to improve the ionic conductivity of $LaGaO_3$-based perovskites and to understand which aspect has the ultimate influence in the ionic transport properties of the perovskite considering IT-SOFC applications.

Previous molecular mechanics studies on $LaGaO_3$ are based on empirically derived force fields, which are often composed of parameters extracted from different sources. As a result, such force fields are non-transferrable and do not satisfactorily describe the system's behaviour in different conditions and thermodynamics states. Chapter 5 outlines the theoretical parametrization and validation of an accurate and transferrable DIPole Polarizable Ion Model (DIPPIM) interatomic potential, in order to investigate the ionic conductivity, the activation energies for oxide ion diffusion and changes in the local structure of Sr- ($La_{1-x}Sr_xGaO_{3-\delta}$), Mg- ($LaGa_{1-y}Mg_yO_{3-\delta}$) and co-doped ($La_{1-x}Sr_xGa_{1-y}Mg_yO_{3-\delta}$) lanthanum gallate systems by means of molecular dynamics simulations. In Chapter 6, the structural, electronic and defect properties of La_2NiO_4, a potential IT-SOFC cathode, are investigated by means of DFT+*U* and hybrid DFT (HSE06) calculations, aiming to improve its mixed ionic and electronic conductivity. The potential effects of aliovalent doping in La_2NiO_4 A- and B- sites (A = Ca(II), Sr(II), Ba(II) and B = Mn(III), Fe(III) and Co(III)) on the ionic and electronic conductivity will be analysed, by investigating properties such as the formation energies of defects, their thermodynamic transition levels, and their preferable charge compensation mechanism, considering both ionic (formation of oxygen vacancies or interstitials) and electronic (localisation of electrons or holes at Ni ions) compensation. This will allow us to identify which dopants can improve the performance of the La_2NiO_4-based cathodes and fundamentally understand the mechanisms through which such improvements occur. Finally, Chapter 7 outlines the conclusions and summarizes all the work presented in this thesis, besides discussing future work to be carried out.

Chapter 2

Theoretical Background

2.1 Introduction

Computational modelling is an essential tool to gain insight and rationalize experimentally observed properties, or to predict the behaviour of materials which are challenging to be synthesised or have not been discovered yet. The choice of a suitable computational method depends on the level of accuracy required for calculations and on which chemical and physical properties are of interest.

Quantum mechanics describes the behaviour of microscopic systems, composed of electrons or other subatomic particles that have both particle- and wave-like characteristics [118], and behave differently than classical systems obeying Newton's laws. While in classical systems energy can vary continuously, in quantum systems, energy is quantized (e.g. in atoms, electrons are limited to discrete energy levels) [2]. Therefore, quantum mechanical methods are suitable to investigate electronic properties, such as density of states, band structures, charge densities etc., but are limited to smaller systems due to their elevated computational cost. Molecular mechanics methods, also known as interatomic potential (IP) methods, on the other hand, do not explicitly consider electrons, but employ analytical or numerical force fields to describe particle interaction. As a result, they are less computationally expensive and can be used to study larger systems.

First-principles calculations and molecular mechanics methods are complimentary; their combination can provide an accurate and complete description of a chemical system – from their electronic structure and related properties, to the thermodynamic and kinetics behind catalytic reactions or diffusion processes. In this chapter, some widely used quantum and molecular mechanics computational methods are discussed – a brief discussion on quantum chemistry and the Schrödinger equation is followed by the description of Hartree-Fock (HF) theory, Density Functional Theory (DFT), hybrid-DFT and interatomic potential methods.

2.2 Quantum Chemistry

2.2.1 The Schrödinger equation

Quantum chemistry methods aims to calculate approximate solutions to the non-relativistic time-independent Schrödinger equation (Equation 2.1), which describes the quantum mechanical behaviour of a system and its particles. A wave function, Ψ, operates upon the Hamiltonian, H, returning the system's allowed energy levels, E, as multiple eigenvalues to Ψ [119,120].

$$H\Psi = E\Psi \tag{2.1}$$

The Hamiltonian (Equation 2.2) includes kinetic and potential energy components. The first two terms on the right-hand side of Equation 2.2 represent the contribution of the kinetic energy of electrons (*i*, *j*) and nuclei (*n*, *m*) to the energy, respectively, with ħ being Planck's constant divided by 2π, m_e the mass of the electron and m_n the mass of the nucleus. The Laplacian ∇^2 is a second-derivative operator that acts in all directions (three-dimensionally), i.e., it returns the sum of three second-derivatives of the function it acts upon, as shown in Equation 2.3. As a result, Ψ is a function of the three Cartesian coordinates of all the particles in the system. The last three terms in Equation 2.2 are potential energy components; the first two represent the total interaction between electrons, i.e. attraction (electron-nucleus) and repulsion (electron-electron and nucleus-nucleus) between pairs of charged particles, while the final term, describes the nuclear-nuclear interaction, and hence the potential field within which a particle is moving [118]. *e* is the electron charge, Z_n the atomic number of nucleus *n*, and r_{xy} the distance between particles *x* and *y*.

$$H = -\sum_i \frac{\hbar^2}{2m_e}\nabla_i^2 - \sum_n \frac{\hbar^2}{2m_n}\nabla_n^2 - \sum_i \sum_n \frac{e^2 Z_n}{r_{in}} + \sum_{i<j} \frac{e^2}{r_{ij}} + \sum_{n<m} \frac{e^2 Z_n Z_m}{r_{nm}} \tag{2.2}$$

$$\nabla^2 = \frac{\partial^2}{\partial x_i^2} + \frac{\partial^2}{\partial y_i^2} + \frac{\partial^2}{\partial z_i^2} \tag{2.3}$$

The exact solution of the Schrödinger equation can only be calculated for a single electron, as the electron-electron repulsion term cannot be solved analytically.

2.2.2 The Born-Oppenheimer approximation

Protons (1.673×10^{-27} kg) and neutrons (1.675×10^{-27} kg) are more than 1800 times heavier than electrons (9.109×10^{-31} kg) [119]. The significantly heavier nuclei move slower than the negatively charged particles, and any electronic motion resulting from nuclear motion occurs practically instantaneously [119]. Taking that into account, the Born-Oppenheimer approximation considers electrons to move within a field of fixed nuclei; the electron distribution will depend on the nuclear coordinates, which are treated classically, but not on the nuclear velocities. This approximation simplifies the solution of the Schrödinger equation; in Equation 2.2, the kinetic energy of the nuclei (2nd term on the right-hand side) can be ignored and the nuclear repulsion term (5th term on the right-hand side) becomes a constant for a given electronic configuration. As a result, electronic and nuclear terms can be separated and Equation 2.2 can be rewritten as 2.4, in which the electronic Hamiltonian (H_{elec}), the operator describing the movement of electrons *i* and *j* in a field of *n* point charges, has only three components – the electronic kinetic energy, the potential energy for the electron-nuclei attraction, and the potential energy for the electron-electron interaction, respectively.

$$H_{elec} = -\sum_{i} \frac{\hbar^2}{2m_e} \nabla_i^2 - \sum_{i} \sum_{n} \frac{e^2 Z_n}{r_{in}} + \sum_{i<j} \frac{e^2}{r_{ij}} \tag{2.4}$$

The solutions of the electronic Schrödinger equation using H_{elec} as the operator are the electronic energies (E_{elec}) for a set of fixed nuclear positions, as in Equation 2.5, in which V_n is the constant potential energy for nuclear repulsion.

$$(H_{elec} + V_n)\Psi_{elec}(r_i; r_n) = E_{elec}\Psi_{elec}(r_i; r_n) \tag{2.5}$$

From Equation 2.5, the electronic wave function (Ψ_{elec}) and energy (E_{elec}) depend both on the electronic (r_i) and nuclear (r_n) coordinates, with the latter being fixed parameters. Hence, the Born-Oppenheimer approximation allows the construction of a potential energy surface (PES) for any chemical system [119]; solving Equation 2.5 for the motion of the nuclei, i.e., calculating E for different sets of nuclear positions yields a PES evaluating the energy over all possible sets of fixed nuclear coordinates.

2.2.3 The Hartree model

The Hartree model further simplifies the Schrödinger equation by considering a system of non-interacting electrons. As a result, electron repulsion is ignored and the only components of the Hamiltonian are the electronic kinetic energy and the potential energy for the electron-nuclei attraction [119]. The one-electron Hamiltonian, $h(i)$, can be written as in Equation 2.6, in atomic units, resulting in the fundamental physical constants (Planck's constant, electron charge and electron mass) disappearing.

$$h(i) = -\frac{1}{2}\nabla_i^2 - \sum_n \frac{Z_n}{r_{in}} \tag{2.6}$$

The Hamiltonian operator of a molecular system composed of non-interacting electrons, H, is separable, and can be constructed from the sum of the one-electron Hamiltonians (Equation 2.7) [119].

$$H = \sum_i h(i) \tag{2.7}$$

The corresponding many-electron wave function (Equation 2.8) can then be built from one-electron molecular orbitals, ψ, and is called the Hartree Product, Ψ_{HP} [119]. The molecular orbitals in the equation below are a function of the electron position, *r*, and hence are called spatial orbitals.

$$\Psi_{HP}(r_1, r, \dots, r_n) = \psi_1(r_1)\psi_2(r_2) \dots \psi_i(r_i) \tag{2.8}$$

In addition to the electronic coordinates, electron spin can also be taken into account; If the spatial orbitals are multiplied by the different spin functions ($\alpha(\omega)$ for spin up and $\beta(\omega)$ for spin down), spin orbitals $\chi(x)$ are obtained (Equation 2.9), which are a function of *x*, describing both spatial (*r*) and spin (ω) coordinates. Since there are only two possibilities for the electron spin, N spatial orbitals can form 2N spin orbitals [120].

$$\chi_i(x_1) = \psi(r)\alpha(\omega)$$

$$\chi_j(x_2) = \psi(r)\beta(\omega) \tag{2.9}$$

The Hartree Product of two electrons occupying spin orbitals χ_i and χ_j is given by Equation 2.10. If the spatial and spin coordinates of these electrons are interchanged, the new Hartree Product can be written as in Equation 2.11.

$$\Psi^{HP}(x_1, x_2) = \chi_i(x_1)\chi_j(x_2) \tag{2.10}$$

$$\Psi^{HP}(x_1, x_2) = \chi_i(x_2)\chi_j(x_1) \tag{2.11}$$

2.2.4 Limitations of the Hartree Model and Hartree-Fock theory

The first limitation of the Hartree model is that it considers a system of non-interacting electrons; hence the multi-electron wave function described by the Hartree Product is physically unrealistic. Ψ_{HP} is then an uncorrelated electronic wave function, i.e., the probability of finding an electron at a given position does not depend on the coordinates of other electrons [120]. However, in a real system, electrons do interact and repel each other – one electron will avoid areas already occupied by other electrons and two electrons with parallel spins will have a correlated motion. Since the inclusion of electron-electron interactions make it impossible to solve the Schrödinger equation analytically, such limitation can be overcome by assuming that electrons are moving under an average potential created by all particles in the system – both nuclei and electrons. For a two-electron system (with electrons e_i and e_j), for example, a one-electron Schrödinger equation can be written for e_i, considering that e_i moves under the influence of e_j. On the other hand, e_j can be treated as a charge distribution, following the Born interpretation of quantum mechanics, which is that the probability density is proportional to the square of the wave function. The average interaction between e_i and all other electrons occupying the molecular orbitals χ_j can be written as in Equation 2.12, in which ρ_j is the charge density associated with e_j, integrated over all space [119]. This interaction potential, $V_i(j)$, can be added to the one-electron Hamiltonian of Equation 2.6, resulting in Equation 2.13, which defines the Fock operator, $f(i)$.

$$V_i(j) = \sum_{j \neq i} \int \frac{\rho_j}{r_{ij}} dr \tag{2.12}$$

$$f(i) = -\frac{1}{2}\nabla_i^2 - \sum_n \frac{Z_n}{r_{in}} + V_i(j) \quad (2.13)$$

The resulting one-electron Schrödinger equation can be solved with the Hartree self-consistent field (SCF) method [121–123], which consists of guessing the wave functions for all occupied molecular orbitals as a first step, making it possible to calculate the electron-electron interactions and hence obtain the Fock operator and the HF equations (Equation 2.14).

$$f(i)\chi(x_i) = E\chi(x_i) \quad (2.14)$$

After solving the equations, a new set of wave functions is obtained, which is used to calculate $f(i)$ more accurately. The iterative cycle goes on until the difference between a new calculated set of wave functions and the previous one falls within a certain difference, i.e. until the equations are self-consistent. Hence, convergence is reached when the total electronic energy reaches a minimum within a certain threshold [118]. Computationally, the use of smaller convergence criteria results in more SCF cycles being needed, increasing the cost of the calculation [119].

The second limitation of the Hartree model is that the wave functions presented in Equations 2.10 and 2.11 do not obey the antisymmetry principle, which states that a many-electron wave function must be antisymmetric and change sign if the positions of two electrons are interchanged [118]. They also do not reflect the indistinguishability of electrons, but instead assign each electron i to an specific spin orbital χ_i [120]. Such limitations can be solved by linearly combining the Hartree Products in Equations 2.10 and 2.11, which results in an antisymmetric wave function [120], as in Equation 2.15,

$$\Psi(x_1, x_2) = 2^{-1/2}(\chi_i(x_1)\chi_j(x_2) - \chi_i(x_2)\chi_j(x_1)) \quad (2.15)$$

where $2^{-1/2}$ is a normalization factor and the negative sign guarantees that the antisymmetry principle is obeyed (Equation 2.16).

$$\Psi(x_1, x_2) = -\Psi(x_2, x_1) \quad (2.16)$$

For an N-electron system, in which N electrons occupy N spin orbitals, a Slater determinant in the form of Equation 2.17 can be written to represent the antisymmetric wave

function; the use of Slater determinants and the resulting linear combination of spin orbitals guarantees that the wave function changes sign when the space and spin coordinates of two electrons are swapped [120].

$$\Psi(x_1, x_2, \dots, x_N) = \frac{1}{\sqrt{N!}} \begin{vmatrix} \chi_1(x_1) & \chi_2(x_1) & \cdots & \chi_N(x_1) \\ \chi_1(x_2) & \chi_2(x_2) & \cdots & \chi_N(x_2) \\ \vdots & \vdots & \ddots & \vdots \\ \chi_1(x_N) & \chi_2(x_N) & \cdots & \chi_N(x_N) \end{vmatrix} \tag{2.17}$$

In a Slater determinant, rows describe electrons (first row for electron one, second row for electron two etc.) and columns represent spin orbitals (first column for spin orbital one, second column for spin orbital two etc.). As a consequence, interchanging two electrons is the same as swapping two rows, which changes the sign of the determinant and ensures antisymmetry [120]. The obtained wave function also obeys the Pauli Exclusion Principle, which states that any two electrons cannot have all same four quantum numbers, i.e., two electrons can occupy the same molecular orbital, in which all quantum numbers except spin are defined, but cannot possess the same spin; in a Slater determinant, if two electrons occupy the same spin orbital, two columns in the determinant will be the same, resulting in a determinant (and a wave function) equal to zero [120]. Furthermore, all electrons are 'mixed' with every orbital within the determinant, accounting for their indistinguishability and the fact that their location is given by a probability density, which is an improvement from Hartree Product wave functions [118,119].

In Hartree-Fock (HF) theory, both corrections to the limitations of the Hartree model are taken into account; an average potential is considered to account for the electron-electron interactions and the spin orbitals are linearly combined through the use of Slater determinants to ensure that the wavefunction is antisymmetric and electrons are indistinguishable. The goal of HF theory is to find approximate solutions to the electronic Schrödinger equation, i.e. to find the best possible wave function to describe an N-electron system, given by a Slater determinant, that yields the lowest possible energy. Accordingly, the calculation of the expectation value for the N-electron Hamiltonian operator through the HF self-consistent field method obeys a variational principle: the best set of spin orbitals minimize the total electronic energy, which will always be greater than the energy yielded from the exact wave function [118,120].

The main limitation in HF theory is that since the electron-electron interactions in a system are treated as an average effect, instantaneous electron-electron interactions are neglected. Hence, correlation effects, arising from the correlated motion of electrons, are ignored. As a result, electrons tend to avoid each other more than they would in a real system, increasing the system's energy. If the HF equations were to be solved using an infinite basis set, the calculated energy would reach the HF limit i.e., a minimum energy value in which the only associated error would be due to correlation effects. Hence, the difference between the energy in the HF limit and the true system's energy yields the correlation energy [118,119]. Despite its limitations, HF theory serves as starting point for more sophisticated and accurate approximations including correlation effects, the so-called post-HF methods, such as configuration interaction (CI), coupled cluster (CC) and perturbation theory, for example, which are beyond the scope of this thesis.

2.2.5 Density functional theory

Modern density functional theory (DFT) is an *ab initio* simulation method based on Hohenberg and Kohn [124] mathematical formalism, which describes the interacting electron gas under the influence of an external potential in terms of the ground state electron density, $\rho(r)$. While in HF theory the N-electron wave function is a central quantity, determined through the construction of a Slater determinant from N single-electron wave functions, DFT uses $\rho(r)$ to calculate the overall electronic distribution and total electronic energy [119]. The electron density still contains information about the total number of electrons – its integration all over space results in N – and is also a function of the three spatial coordinates [125]. Its use makes the explicit calculation of the many-electron wave function unnecessary, reducing the number of variables to be dealt with.

In the electron gas, electrons interact with one another and with an external potential defined by the charge and position of the nuclei. The first Hohenberg and Kohn theorem shows that the electron density uniquely determines the ground state energy of a many-electron system. The non-degenerate ground state electron density determines the external potential, which in turn allows for the Hamiltonian and the electronic wave function to be calculated [119], and hence for the ground state total energy to be computed. Their second theorem demonstrates that the electronic density obeys a variational principle; the electron

density is the variable function, and for the correct $\rho(r)$, the energy functional of density $E[\rho(r)]$ corresponds to the total ground state energy of the system [119]. In other words, if a well-behaved electronic density – that when integrated over space results in the correct number of electrons – is considered, a candidate wave function can be related to it, and the energy value associated with that wave function will be equal to or greater than the ground state energy. Therefore, if different electron densities are considered, the one resulting in the lowest energy is closer to the exact ground state electron density [119].

The first theorem can be summarized by Equation 2.18, in which the ground state energy of a system, $E[\rho(r)]$, is written in terms of the external potential acting on the electrons, V_{ext}, and a unique functional of the electron density, $F[\rho(r)]$, which contains information about the electronic kinetic energy and electron-electron interactions, but has an unknown form [125]. If this universal density functional was known, the total energy of the system could be calculated exactly.

$$E[\rho(r)] = \int V_{ext}(r)\rho(r)dr + F[\rho(r)] \tag{2.18}$$

Kohn and Sham [126] further developed Hohenberg and Kohn formalism to obtain self-consistent equations that include exchange and correlation effects. In an interacting system, electrons repel each other and have a correlated motion, which lowers the system's energy. Kohn and Sham included these effects in the universal functional, proposing $F[\rho(r)]$ to be written as in Equation 2.19, in terms of the electronic kinetic energy (T), classical coulombic interactions, containing information on the nuclear-electron attraction (V_{ve}) and the electron-repulsion (V_{ee}), and a non-classical portion (E_{nc}) accounting for electronic exchange and correlation [118].

$$F[\rho(r)] = T[\rho(r)] + V_{ve}[\rho(r)] + V_{ee}[\rho(r)] + E_{nc}[\rho(r)] \tag{2.19}$$

The practical implementation of DFT is achieved by considering a fictitious system of non-interacting electrons as the starting point to calculate the ground state energy. The electronic Hamiltonian is simply the sum of one-electron operators, as there are no electron-electron interactions to be considered. The non-interacting system possess the same ground state electron density as the real interacting system of interest – if two systems possess the same densities, it follows from the first Hohenberg and Kohn theorem that they will also have the same external potential, i.e., the same nuclear positions and atomic numbers, and

hence the same ground state energy. Therefore, the total kinetic energy in Equation 2.19 can be split in two: the kinetic energy of the theoretical non-interacting electron system (T_{ni}), and a correction (ΔT) accounting for the electron-electron interactions, as in Equation 2.20. This allows the wave function to be reintroduced to the mathematical formalism, as in the conventional HF approach; even though such reintroduction makes the calculation more costly, a set of one-electron wave functions can now be used to describe the non-interacting electrons, allowing T_{ni} to be computationally calculated, and transferring the unknown form of $F[\rho(r)]$ to other terms.

$$F[\rho(r)] = T_{ni} + V_{ve}[\rho(r)] + V_{ee}[\rho(r)] + \Delta T[\rho(r)] + \Delta V_{ee}[\rho(r)] \qquad (2.20)$$

The last two terms on the right hand side of Equation 2.20 consist of corrections, one for the difference in kinetic energy between the non-interacting and interacting systems (ΔT), and one to account for the difference between electronic repulsion in classical and quantum mechanics, ΔV_{ee}, which contains exchange and correlation effects [119]. These correction terms, which cannot be exactly determined (ΔT and ΔV_{ee}) are grouped under $E_{XC}[\rho(r)]$, the exchange-correlation functional, which has an unknown form (Equation 2.21) [119].

$$F[\rho(r)] = T_{ni} + V_{ve}[\rho(r)] + V_{ee}[\rho(r)] + E_{XC}[\rho(r)] \qquad (2.21)$$

In summary, Kohn-Sham equations reintroduce the wave function to DFT's mathematical formalism and transfer the unknown form of Hohenberg-Kohn universal functional, $F[\rho(r)]$, to $E_{XC}[\rho(r)]$. Since exchange and correlation effects are key to accurately describe the behaviour of interacting particles, approximations to $E_{XC}[\rho(r)]$ are necessary to make DFT applicable. DFT is an exact theory, but its equations are solved approximately, since approximations define the form of $E_{XC}[\rho(r)]$. In contrast, HF theory is essentially approximate, since correlation is ignored, but its equations are solved exactly [119]. The Kohn-Sham equations can be solved self-consistently similarly to HF theory, i.e., from an initial guess of the electronic density, a set of orbitals can be derived. From that, an improved value for $\rho(r)$ can be obtained and is used in the second iteration, until the total ground state energy of the system is calculated within the selected convergence criteria [125]. The accuracy of DFT methods depends on the adequate determination of the exchange-correlation energy functional.

2.2.6 Exchange-correlation functional

As the exact form of the exchange-correlation functional is not known, approximations must be made. The simplest one is known as the local density approximation (LDA), also derived by considering the uniform electron gas, which has a uniform electronic density at every position in space. The electron density and energy density (ε_{XC}) are computed locally, hence the name 'local density approximation', with the value of $\rho(r)$ changing for different points in space [119,125]; in Equation 2.22 these quantities are integrated to yield E_{XC}.

$$E_{XC} = \int \rho(r)\varepsilon_{XC}(\rho(r))dr \tag{2.22}$$

LDA's main limitation comes from the fact that it considers the exchange-correlation energy to depend only on the local electron density. As a result, this approximation is only suitable to describe $E_{XC}[\rho(r)]$ for slowly varying densities, which is not the case for strongly correlated systems [119]. To account for the inhomogeneity of $\rho(r)$, the exchange-correlation energy in more sophisticated functionals does not depend only on local values of the electron density, but also on its gradient, which reflects how the density is locally changing and, sometimes, on higher derivatives of the density [118,125], as given in Equation 2.23

$$E_{XC} = \int (\rho(r), \nabla\rho(r), \nabla^2\rho(r) \ldots)\varepsilon_{XC}(\rho(r))dr \tag{2.23}$$

The approximation proposed by Perdew and Wang (PW91 [127]) and its simplified and improved version by Perdew, Burke and Ernzerhof (PBE [77]) are the most commonly used gradient-corrected or generalized gradient approximation (GGA) based functionals for solid state calculations. Meta-generalized gradient approximations (meta-GGAs) include, besides the electron density and its gradient, the kinetic energy density to the exchange-correlation energy functional, i.e. the second derivative of the density (the Laplacian). While most meta-GGAs are semi-empirical, with at least part of their derivation fitted to experimental properties [128], Sun *et al.* [129] developed a meta-GGA functional with no empirical terms; the non-empirical Strongly Constrained and Appropriately Normed meta-

GGA (SCAN functional) presents a superior description of geometries and energies of diversely bonded systems when compared to LDA and standard PBE GGA results.

2.2.7 The self-interaction error

The Coulomb electrostatic component of the universal functional (V_{ee} in Equation 2.21) accounts for all the coulombic electron-electron interactions, including the interaction of an electron with itself. In HF methods, this self-interaction is cancelled by the existence of an exact exchange term. In DFT, on the other hand, the exchange term is approximate and this cancellation is not exact, which results in a self-interaction error (SIE). As a result, the electronic structure of a system, especially those containing highly localised electrons or partly filled *d* and *f* shells, may not be accurately described by DFT methods, which might predict electron delocalisation where localised electrons are expected. To overcome the SIE, two approaches are usually adopted. In DFT+*U* calculations, an empirical correction parameter, the Hubbard *U*, can be added to *d* or *f* valence states along with an exchange parameter, *J*, as an attempt to localise the electrons. Another approach consists of the use of hybrid functionals, in which a portion of the exact HF exchange is added to the approximate DFT exchange-correlation functional. The hybrid approach partially corrects for the SIE in some cases, but it ultimately depends on the amount of HF exchange that is included.

2.2.8 DFT+*U*

For some transition metal oxides, a LSDA (the spin polarized version of LDA) or GGA approach predicts a metallic ground state for systems experimentally observed to be insulators [130] – with NiO being the classical example – as a result of the poor description of the strong Coulomb repulsion between highly localized electrons by DFT. For uranium dioxide, the same problem is observed; while UO_2 is experimentally known to be an insulator, LSDA predicts the oxide to be metallic, due to uranium's partially filled *f* shells [131,132]. Dudarev *et al*. [133] demonstrated that this problem can be solved for NiO by combining DFT LSDA with the unrestricted Hartree-Fock (UHF) approximation. Dudarev's approach has the form of Equation 2.24, in which a +*U* correction (U_{eff} = *U* – J) is applied to specific orbitals (e.g. *d* orbitals) in specific atoms (e.g. Ni in NiO). $\lambda_i^{j\sigma}$ is the orbital

occupation for an orthogonal set of localised orbitals *i* on atom *j*, with angular momentum σ. In DFT, if an extra electron is added to the system, partial orbital occupation resulting in charge delocalisation is usually more favourable than the electron being localized in a single particle.; the +*U* correction in Equation 2.24 encourages integer orbital occupation.

$$E_{DFT+U} = E_{DFT} + \frac{U_{eff}}{2} \sum_{j,\sigma} \sum_{i} \lambda_i^{j\sigma} (1 - \lambda_i^{j\sigma}) \tag{2.24}$$

The amount of self-interaction in a system also depends on the chemical environment, which determines the degree of mixing of ionic states with their surroundings. To determine appropriate Hubbard *U* values for a given system, one possible approach is to compare valence band features calculated for a range of +*U* values to experimental data, such as X-ray/Ultraviolet Photoelectron Spectroscopy (XPS/UPS). While band gaps are frequently used to fit U_{eff}, that approach is only appropriate for Mott insulators such as NiO, since in those the band gap is a result of how orbitals are split. As a result, while LSDA predicts NiO to have a band gap of 0.6 eV, LSDA+*U* calculates a value of 3.0 eV, comparable to the experimental value of 4.2 eV [133].

2.2.9 Hybrid DFT

While HF theory treats exchange contributions exactly, DFT introduces correlation effects. Since both methods calculate the system's energy self-consistently, the exchange and correlation energies derived from DFT can be linearly combined with the HF energy, giving rise to hybrid DFT methods. Hybrid DFT is an improvement of traditional methods, as it deals with the SIE by mixing a portion of the HF exact exchange with DFT exchange and correlation effects.

Becke proposed the exchange-correlation energy to be written as in Equation 2.25, where λ is a coupling parameter with values between 0 and 1 and U_{XC} represents the electronic Coulomb repulsion. The value of λ controls the extent of electron-electron interactions in a given system; for λ = 0, U_{XC} is also zero, indicating no electronic repulsion and hence a non-interacting system. In that case, U_{XC} consists of exchange effects only, resulting from the antisymmetric nature of the wave function [119]. As λ increases, so does the electronic repulsion; for λ = 1, a real interacting system is represented [125].

$$E_{XC} = \int_0^1 U_{XC}^{\lambda} d\lambda \quad (2.25)$$

Equation 2.26 exemplifies the linear combination of HF (E_{HF}^{X}) exchange and DFT (E_{DFT}^{XC}) exchange-correlation effects observed in hybrid methods [118]. A range of exchange-correlation functionals can be used and different amounts of HF exchange (a) can be included [119]. PBE0, for example, uses the standard GGA PBE functional and contains 25% of HF exchange, percentage chosen based on perturbation theory calculations. Its name comes from the fact that the hybrid functional was not empirically derived and hence 'zero' empirical parameters were included. [119]

$$E_{XC} = (1 - a)E_{XC}^{DFT} + aE_{X}^{HF} \quad (2.26)$$

2.3 Interatomic potential methods

Some systems are too large to be treated by quantum mechanical methods, which depend on electronic distribution. Large simulation cells have too many particles to be treated by electronic structure approaches, resulting in impractical and computationally expensive calculations. Instead, interatomic potential (IP) methods, also known as force field methods, can be used to simulate and analyse these large systems for long simulation times, with the system's properties being calculated considering the nuclear positions and the attraction/repulsion among particles.

In IP methods, particle interactions are described by an analytical (or numerical) force field, which can be empirically or theoretically derived [134]. It is crucial for these force fields to be transferrable, i.e., to be able to satisfactorily describe a system's behaviour in different conditions and thermodynamic states (mixtures, distinct phases of the same material, bulk, surface or grain boundary calculations etc.) [135]. Empirical derivation consists of parameters being chosen to reproduce specific experimental properties. Therefore, the main drawback of the empirical approach is that the derived interatomic potentials are not necessarily predictive; the simple reproduction of available experimental data diminishes the transferability of the force field if multiple structures and environments are not taken into account. Furthermore, reliable experimental data is only available for a

limited amount of thermodynamic states [125]. Alternatively, first principles DFT calculations allow the theoretical parametrization of a force field, in which observables calculated by the interatomic potential (such as forces, stresses and multipoles, for example), are fitted to DFT values. This theoretical approach yields force fields of *ab initio* accuracy, with a higher degree of transferability [136,137].

2.3.1 Form of the interatomic potential

A force field describes how independent particles interact with each other due to non-bonded forces, which can be divided into electrostatic and van der Waals interactions. These interactions occur through space and are influenced by the proximity between two particles; as a result, a force field contain terms depending on the inverse power of distance [125]. The interaction potential used in this work is the DIPole Polarisable Ion Model (DIPPIM) [138]. Its functional form (Equation 2.27) possess charge-charge ($U^{Coulomb}$), overlap repulsion (U^{rep}), dispersion (U^{disp}) and polarization (U^{pol}) contributions [134].

$$U^{total} = U^{Coulomb} + U^{rep} + U^{disp} + U^{pol} \tag{2.27}$$

2.3.2 Long-range interactions

The first term in Equation 2.27 is defined by Coulomb's Law, which describes the interaction of two point charges, q, as a function of their separation distance, r (Equation 2.28). It is a long-range interaction, in which the inverse power of distance (r^{-1}) express the slow decay of the interaction with distance [139]. An Ewald summation [140,141], as opposed to a direct summation, is needed to compute these long-range interactions efficiently, by dividing the interaction into short- and long-range components, which are evaluated in real and reciprocal space, respectively.

$$U^{Coulomb} = \sum_{i<j} \frac{q_i q_j}{r_{ij}} \tag{2.28}$$

2.3.3 Short-range interactions

2.3.3.1 Overlap repulsion

The overlap repulsion (U^{rep}) arises from the quantum nature of electrons and the Pauli exclusion principle – if two electrons in a system cannot be in the same quantum state, exchange forces come into effect to forbid pairs of electrons to simultaneously occupy the same point in space [125]. U^{rep} possess a Yukawa form [134], as shown in Equation 2.29.

$$U^{rep} = \sum_{i<j} \frac{A_{ij} e^{-a_{ij} r_{ij}}}{r_{ij}} + \sum_{i<j} B_{ij} e^{-b_{ij} r_{ij}^2} \tag{2.29}$$

A_{ij} correlates the amount of overlap to the magnitude of the repulsive energy. The second exponential term in Equation 2.29 acts as a steep repulsive wall for lower separation distances, and is especially important for anion interactions with highly polarisable cations at small separation distances due to the anion hard core [64]. B_{ij} controls the magnitude of the anion-cation interaction, while b_{ij} defines how quickly that interaction decays with separation distance, r_{ij}.

2.3.3.2 Dispersion interactions

The second-last term in the interatomic potential from Equation 2.27 (U^{disp}) accounts for dispersion interactions, arising from the correlated motion of electrons [134]. When two particles come closer together, their correlated electronic motion results in mutually induced instantaneous multipoles. These dispersion interactions are modelled by Equation 2.30, where C_6 and C_8 are the dipole-dipole and the dipole-quadrupole dispersion coefficients, f_6 and f_8 are the Tang-Toennies damping functions, shown in Equation 2.31, with *n* set as 6 and 8 for dipole-dipole and dipole-quadrupole dispersion, respectively.

$$U^{disp} = -\sum_{i \leq j} \left[\frac{C_{6,ij} f_6}{r_{ij}^6} + \frac{C_{8,ij} f_8}{r_{ij}^8} \right] \tag{2.30}$$

$$f_n^{ij} = 1 - c_{ij} e^{-b_{ij} r_{ij}} \sum_{k=0}^{n} \frac{\left(b_{ij} r_{ij}\right)^k}{k!} \tag{2.31}$$

The Tang-Toennies damping function (f_n^{ij}) [142,143] (Equation 2.31) accounts for the overlap of charge densities, reducing the over-attraction at short interionic distances [134]. The range of the damping and the intensity of the ionic response to the charge overlap are given by b_{ij} and c_{ij}, respectively [134]. At large separation distances, the value of damping function converges to 1, while at small separation distances it tends to $(1 - c_{ij})$. The form of the damping function is controlled by n. The behaviour of the Tang-Toennies damping function is shown in Figure 2.1, setting b_{ij} = c_{ij} = 1 a.u.

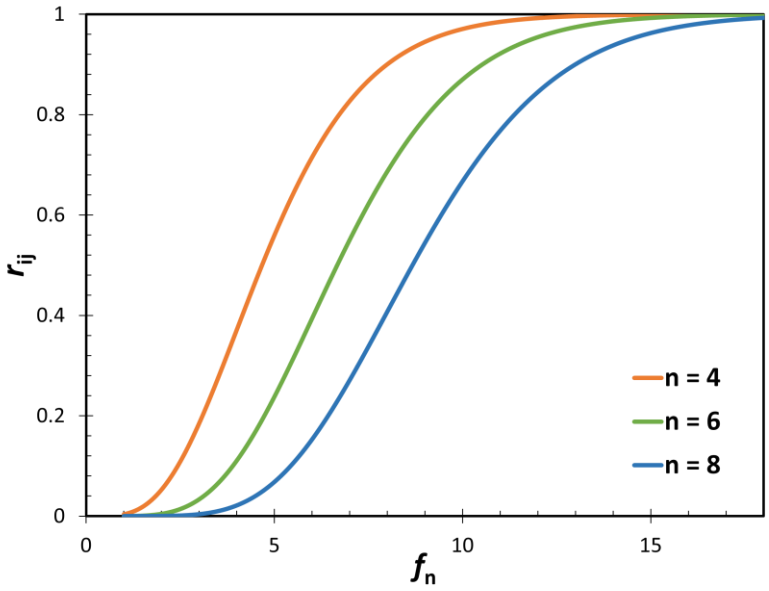

Figure 2.1 – The Tang-Toennies damping function (f_n^{ij}) as a function of the separation distance (r_{ij}), as described in Equation 2.32, for n = 4 (orange), 6 (green) and 8 (blue), and b_{ij} = c_{ij} = 1 a.u.

2.3.4 Many-body effects

Electrostatic and van der Waals interactions are usually evaluated between pairs of particles, and hence the total system's energy possesses a pairwise additive form. This simplistic view treats particles as charged hard-spheres, i.e., closed-shell ions with integer charge. In reality this is not true – the electron density of a particle can be deformed by their local environment, i.e., ions can be polarised (induction effect) or have their size (compression) and shape (deformation) affected by their interaction with neighbouring particles. In fact, the electron density of anions is more greatly affected by their neighbouring

particles in comparison to cations, with their polarizability within a crystal being much lower than that of the gaseous ion [144]. The oxide ion, for example, a crucial species in solid-state chemistry, is unstable in the gas phase, but exists in the condensed phase, as a result of the confining potential applied by neighbouring particles upon its electrons, stabilizing it [134]. The magnitude of this confining potential changes among different phases of the same material or among different systems, which affects the transferability of force fields not taking into account many-body effects [134,135]. Therefore, the inclusion of terms accounting for these effects is extremely important for modelling structural and dynamical phenomena in ionic systems [136]. Many-body effects are even more important in the evaluation of defective systems, which possess a less symmetrical environment when compared to bulk, defect-free phases, resulting in distortions of confining potentials and induced multipole moments [137]. As a result, an extended force field model including effects arising from the many-body character of real systems is more realistic and might be necessary to adequately describe a system's behaviour and increase the transferability of a given IP [135].

Extended models can include dipole polarization (as in DIPPIM), quadrupole polarization (as in the QUADrupole Polarisable Ion Model, QUADPIM), compression (as in the Compressible Ion Model, CIM) or deformation (as in the QUadrupole Aspherical Ion Model, QUAIM) effects [134]. These are all improvements to the Rigid Ion Model (RIM), due to the inclusion of environmental effects to their formalisms.

Polarisation effects are included in a force field to describe changes in the electron density distribution of a system's particles due to the presence of an external electric field, i.e., a particle's neighbouring particles. Therefore, they are a result of the uneven charge distribution within a system due to distinct species having different electronegativity values [125]. This effect is called induction, since a dipole, μ, is induced in the system by its environment. The dipole's magnitude is directly proportional to the intensity of the electric field, *E*, and the polarizability, α, of the neighbouring species (Equation 2.32).

$$\mu = \alpha E \tag{2.32}$$

DIPPIM includes dipolar effects exclusively to account for the particle's environment. Dipole effects (U^{pol} in Equation 2.27) are given by

$$U^{pol} = \sum_{j \neq i}^{N} \left[f_4^{ij} T^{(1)}(r_{ij})(q_j \mu_i - q_i \mu_j) \right] + \sum_{j \neq i}^{N} \mu_i T^{(2)}(r_{ij}) \mu_j + \sum_{i=1}^{N} \frac{1}{2\alpha_i} |\mu_i|^2 \qquad (2.33)$$

where the first term on the right-hand side accounts for the charge-dipole interactions between atoms *i* and *j*, by considering their charges (q), dipoles (μ) and separation distance (r_{ij}), the charge-dipole interaction tensor ($T^{(1)}$), and a Tang-Toennies function (f_4^{ij}, from Equation 2.31). The second term represents the dipole-dipole interactions between atoms *i* and *j*, with $T^{(2)}$ being the dipole-dipole interaction tensor. Finally, the third term represents the energy required to polarise the ion.

Chapter 3
Computational Methodology

This chapter outlines the computational methods used in this thesis and is divided in four parts. In Section 3.1, periodic boundary conditions are discussed, followed by Section 3.2, where fundamental concepts to solid state simulations using DFT, such as plane wave basis sets, pseudopotentials, and the geometric optimisation procedure are introduced. The analysis of the electronic structure of a chemical system through band structures and density of states is also discussed. All DFT, DFT+*U* and hybrid DFT calculations were carried out using VASP (Vienna Ab initio Simulation Package) [145–147]. Section 3.3 discusses the fundamentals of molecular dynamics (MD) simulations, such as integration algorithms and thermodynamic ensembles, and methods for analysis of MD data, such as mean square displacements and radial distribution functions. All MD simulations were carried out using TCD-PIMAIM (Polarisable Ion Model Aspherical Ion Model) [136].

3.1 Periodic boundary conditions

In a chemical system, the forces operating on an atom located at the surface are different from those experienced by atoms in the bulk, as the latter are completely surrounded by neighbouring particles. Not taking these surface effects into account when modelling a bulk or defective chemical system could result in optimisation problems. To overcome this limitation, periodic boundary conditions can be implemented, allowing a smaller simulation cell to be modelled as if it was part of a much larger system [149]. A "box" containing the smaller cell is replicated three-dimensionally in space, resulting in an infinite lattice and hence removing surface effects. When a particle moves within the simulation box, its periodic image, present in all neighbouring boxes, moves in the same way. If a particle leaves the simulation cell, it is immediately replaced by another particle entering the box from its opposite face. As a result, the number of particles within the simulation cell is kept constant and the forces acting upon surface atoms are removed.

Periodic boundary conditions are implemented in both the DFT and IP based methods used in this thesis. A suitable simulation cell size needs to be chosen, depending on the method being used. In DFT, unit cells are usually enough for geometry optimisation;

however, for modelling defective systems, larger supercells (usually containing between 100-400 atoms) might be necessary to avoid defect-defect interactions (between a defect and its periodic image), or to simulate lower defect concentrations. In molecular dynamics, even larger supercells are required to properly evaluate time-dependent trajectories and hence the system's dynamics.

3.2 Plane wave DFT simulations

3.2.1 Plane wave basis sets

In solid state calculations, periodic crystalline systems can have their wave functions mathematically represented by a plane wave basis set, i.e. linearly combined periodic waves with varying frequencies. The three-dimensional representation of the wave function, $\psi_{i\mathbf{k}}(r)$, in a plane wave basis set is given by Equation 3.1. Plane waves of the form $e^{i(\mathbf{k}+\mathbf{G})\cdot\boldsymbol{r}}$ differ by a reciprocal vector, G, consisting of a combination of the reciprocal lattice vectors, and a **k**-point. $c_{j\mathbf{k}}(G)$ are plane wave coefficients that need to be optimised to solve the Schrödinger equation.

$$\psi_{j\mathbf{k}}(r) = \sum_{G} c_{j\mathbf{k}}(G) e^{i(\mathbf{k}+\mathbf{G})\cdot\boldsymbol{r}} \tag{3.1}$$

The Fourier transformation of plane waves in reciprocal space yields an infinite Fourier series and hence provides a complete description of the solid-state system. However, an infinite description cannot be computationally treated. If a plane wave cutoff energy (E_{cut}) is set, a finite and treatable Fourier series (and hence a finite basis set) is obtained. The cutoff energy is related to the reciprocal lattice vectors ($|G_{max}|^2 \propto E_{cut}$); large E_{cut}values increase the number of reciprocal space lattice vectors (and basis functions) included in the basis set and hence adds more terms to the Fourier series, resulting in a more accurate description. E_{cut} needs to be large enough to properly describe the rapid spatial changes in the wave function due to the varying kinetic energies of the plane waves, which rapidly oscillate close to the nucleus (high kinetic energy) and assume a smoother form further away. Therefore, the choice of an E_{cut} value is a trade-off between accuracy and computational cost.

Besides its periodicity, another advantage of a plane wave basis set is that they depend only on the size of the simulation cell and not on atomic positions or number of atoms, in contrast with localised atomic basis sets, which are system size-dependent. This overcomes the basis set superimposition error (BSSE) arising from the incompleteness of localised basis sets, which yield a more complex and flexible description to molecules than to individual atoms resulting in a poor evaluation of interaction energies. Another advantage is that plane wave basis sets are uniquely defined by the cutoff energy, and hence their optimisation is more straightforward.

3.2.2 *K*-points

There is a set of **k** values (Equation 3.1) that fully describes the electrons in the system and can be found within the 1st Brillouin zone (BZ), i.e. within the system's uniquely defined primitive cell in reciprocal space. These unique and equally spaced representative points, used to sample the 1st BZ and approximate the ground state energy of the system, are also called *k*-points and are repeated outside of the 1st BZ throughout reciprocal space due to the system's periodicity. In theory, the wave function should be integrated over reciprocal space (the *k*-space), which is computationally impractical. However, due to the smooth variation of the wave function over reciprocal space, a smaller, representative set of *k*-points can be chosen [150]. The amount of *k*-points needed depends on the system size, with bigger systems needing less *k*-points. Non-metallic materials need a smaller set of *k*-points, since electron occupation is the same across the entire band structure, while for metallic systems, a denser *k*-point mesh is necessary, as the number of occupied bands varies across the BZ. In this thesis, *k*-point meshes for non-metallic systems were calculated by dividing the inverse of the lattice vectors by a sampling density of 0.04 A^{-1}, which was previously calculated by the Watson group as suitable for large band-gap materials and semiconducting oxides. *K*-point meshes immediately smaller or bigger than the calculated one were also tested, to ensure convergence to 0.005 eV per atom.

Common *k*-point meshes are composed of sample points that are equally spaced from the origin and should be representative of the BZ. They can include Γ (the centre of the 1st BZ) or not. Ideally, high-symmetry points would not be included, as they are not representative [151]. Still, the inclusion of high-symmetry points might be necessary in some situations, such as when the system's conduction band maximum or the valence band

minimum fall on those points. In this work, non-gamma centred Monkhorst-Pack [152] *k*-point meshes were used.

3.2.3 Pseudopotentials

Plane waves behave differently in distinct regions of space; for electron states in the nuclear vicinity, the wave function is expected to oscillate rapidly due to the attractive potential electrons experience and due to its orthogonality requirement to core electrons. To model a rapidly oscillating wave function, a very large number of high kinetic energy plane waves (and hence a large basis set with a high E_{cut}) is needed to efficiently describe these effects, increasing the computational cost of the calculations.

Pseudopotentials can be used to describe the interaction between valence electrons and the combination of nucleus and core electrons, lowering plane wave cutoff energies; the contribution of core electrons is pre-calculated in an atomic environment, and their effects remain frozen for all calculations. This is done by solving the Kohn-Sham equations, i.e., the all-electron system, and deciding which states will be considered as core or valence states. Inside the assigned core radius, the all-electron wave function is replaced with a smoother non-oscillating wavefunction. Outside the chosen radius, the all-electron wave function can be used [153]. This approximation is possible because core electrons do not participate in the most relevant chemical processes, such as bonding or ionic diffusion, for example, and hence can be effectively removed from the calculation.

VASP implements the projector-augmented wave (PAW) method [154], which projects the effect of core states, represented by localised basis sets, onto the valence electrons. As a result, PAW has the numerical advantages of pseudopotential calculations, but it is effectively an all-electron approach. VASP possess its own set of PAW pseudopotentials, derived to reproduce the behaviour of valence electrons observed in relativistic all-electron simulations, and indicates the minimum plane wave cutoff required for each element according to the considered electronic configuration of valence states.

3.2.4 Structural optimisation

Experimental structures obtained from crystallographic data are structurally optimised before a more detailed study on the system's properties is carried out. Structural optimisation calculations are performed under the constraint of constant volume, with atomic positions and cell shape (angles and vectors) allowed to change. Volumes ranging from approximately 98% to 102% of experimental values are used. From the variational principle, the ground state of a system possesses the lowest energy. Accordingly, the energies for each simulation at a given volume are noted and the obtained energy-volume curve (illustrated in Figure 3.1) is fitted to the Murnaghan equation of state (Equation 3.2) [155], yielding the equilibrium cell volume (V_0). This process is done to minimise errors in the calculated stress tensors, associated with Pulay stress on plane wave DFT calculations on volume change due to the incompleteness of the finite basis set. These errors can also be minimised through the use of high plane wave cutoff values, which can be computationally expensive. If left unaddressed, Pulay forces will result in an underestimation of volumes.

$$E(V) = E_0 + \frac{B_0 V}{B_0'}\left[\left(\frac{V_0}{V}\right)^{B_0'}\frac{1}{B_0' - 1} + 1\right] - \frac{B_0 V_0}{B_0' - 1} \tag{3.2}$$

In Equation 3.2, the calculated energies, $E(V)$, are related to the bulk modulus of the material (B_0), its pressure derivative (B_0'), the equilibrium cell volume (V_0) and the ground state energy (E_0). A series of energy-volume curves can be plotted using distinct plane wave cutoff energies and *k*-point meshes, to test for basis set resolution and *k*-point sampling density. The minimum of an appropriate energy-volume curve should converge to within 0.005 eV per atom. Once the equilibrium cell volume is calculated from Equation 3.2, a final geometry relaxation at the equilibrium lattice constant is performed, yielding the optimised structure for the system, which then can then be used to investigate the electronic properties of the material, as outlined in the following section.

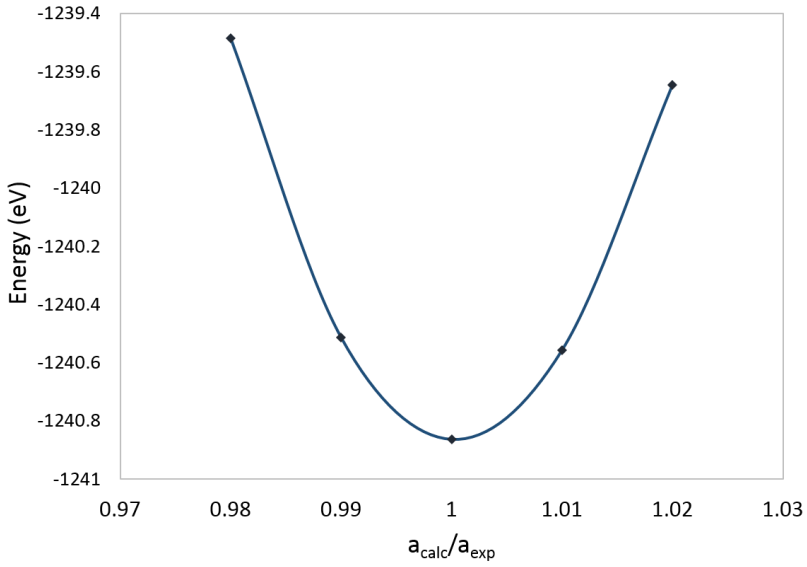

Figure 3.1 – Energy-volume curve for $La_4Ga_2O_9$ obtained from PBE calculations. The obtained points can be fitted to the Murnaghan equation of state (Equation 3.2). The *x* axis corresponds to the ratio between the tested (a_{calc}) the experimental (a_{exp}) lattice constants.

In this thesis, the structural parameters calculated from DFT are compared to experimental results, as a way of evaluating the quality and reliability of the chosen functionals. However, it is important to note that DFT results are calculated at 0 K, which is not the reality of experimentally determined data; hence, some disagreement is expected in such comparison as a result of the temperature difference.

3.2.5 Electronic structure analysis

Band structure

In a band structure, energies (Kohn-Sham eigenvalues) are plotted along *k*-point paths within the 1st Brillouin zone. Such diagrams illustrate the range of energies that the electrons in a system can have, and hence contain important information regarding the electronic structure of a material. Determining the position (*k*-point) of the valence and conduction band edges yields information about the magnitude and nature (direct or indirect) of the band gap, which can be related to the metallic, semiconductor or insulator character of a system. These can be directly compared to experimental results and reveal the quality

of the theoretical method in evaluating the electronic properties of a system. Data regarding the electronic conduction properties (assuming band conduction, and not electron hopping) can also be extracted from the band structure; the band curvature is related to the effective mass of charge carriers and hence to carrier mobility, which is directly proportional to the material's conductivity. Highly dispersed bands at the top of the valence band (or at the top of the conduction band) are related to small electron hole (or electron) effective masses, and hence high charge carrier mobility, resulting in good *p*-type (or *n*-type) conductivity. The variation in the energy of the bands yields information about the type and strength of orbital interactions; disperse bands arise from diffuse orbitals and hence stronger interactions, while flatter bands are related to localised orbitals, resulting in little mixing and weaker interactions. Orbital projected band structures can also be calculated, in which the contribution of specific atomic orbitals to a given band is evaluated separately, yielding information about orbital hybridization or about the bond character in a system (ionic, covalent or mixed), for example.

The DFT calculation of the band structure includes two steps; a self-consistent calculation on the system's optimised structure using a homogenous *k*-point mesh to accurately calculate the charge density and the wave function. The second step consists of a non-self-consistent calculation, during which the obtained charge density in the first step is kept constant. In this calculation, energy eigenvalues are obtained along a path between high-symmetry points in the Brillouin Zone, which depends on the space group of the system of interest [156].

Electronic density of states

If the band structure is integrated with respect to energy, the electronic density of states (EDOS) is obtained. Accordingly, an intense peak in the EDOS usually corresponds to an energy range in the band structure containing a large number of adjacent bands**.** Peak intensity depends on band curvature as well; flat bands also yield intense peaks in the EDOS. The total EDOS shows the density of eigenvalues (the number of available electron states per unit volume) as a function of energy, and hence is an alternative way to depict the electronic structure of a system. It contains information about the electronic structure of the valence and conduction bands, being useful to study defect systems and its resulting band gap states, or to evaluate the metallic, semiconductor or insulator character of the material.

The electronic states can be decomposed by element and quantum number (orbital type and spin), making it possible to identify which element or orbital contributes to each peak. These partial EDOS can be directly compared to experimental spectra – x-ray photoelectron spectroscopy (XPS) for valence band features, and bremsstrahlung isochromat spectroscopy (BIS) for conduction band features – and also gives information about the bonding in the system, which can possess ionic, covalent or mixed character depending on the degree of hybridization between states of different ionic species. To calculate the partial electronic density of states, spheres of specific radii (the Wigner-Seitz radius) are defined around each ionic species, with the electron density within the sphere being attributed to the ion. The wave function is projected onto the spherical harmonics within the spheres, to identify which orbital is associated with the electron density. Sphere size (usually defaulted to the PAW radii in VASP simulations) should be small enough to minimize overlap between adjacent spheres and avoid double counting of the electrons, and large enough to encase a considerable amount of the charge density.

3.2.6 Defect systems

The performance of electrolyte and electrode components in SOFCs can be improved by the creation and transport of point defects. Aliovalent doping generates charge compensating defects, such as oxygen vacancies, oxygen interstitials, electrons or electron holes, which can affect the material's ionic and electronic conductivity. Therefore, investigating the formation of such defects is key to understand how the system's properties can be improved considering SOFC applications. In this thesis, supercell expansions of the materials' unit cells were used in DFT calculations, ensuring at least a 15 Å separation between defects and their periodic images, aiming to minimize defect-defect interactions.

3.2.6.1 Neutral defect formation

The formation energies of charge neutral defects, $E_f(D)$, can be calculated from the defect calculations and the chemical potential of the species, according to Equation 3.3.

$$E_f(D) = (E^D - E^P) + \sum_i \pm n_i(E_i + \Delta\mu_i) \quad (3.3)$$

E^D and E^P are the DFT energies of the defective and pure stoichiometric systems, and *n* is the number of atoms of type *i* taken from or added to an external reservoir. The + and – signs are used when species are being taken from (e.g. the addition of dopants or O upon the formation of oxygen interstitials) or added to (e.g. O removal upon the formation of oxygen vacancies) an external reservoir, respectively. E_i is the elemental reference energy, which is the energy of the constituent elements in their standard states (e.g. $La_{(s)}$, $Ga_{(s)}$, $O_{2(g)}$). $\Delta\mu_i$ is the chemical potential of species *i* under equilibrium growth conditions.

3.2.6.2 Charged defect formation

A defect can possess a range of charge states when introduced to a system. The formation energy of defect D with charge q, $E_f(D,q)$, is calculated as in Equation 3.4, which modifies Equation 3.3 by the addition of new parameters that account for the defect charge.

$$E_f(D,q) = (E^{D,q} - E^P) + \sum_i \pm n_i(E_i + \Delta\mu_i) + q(E_{Fermi} + \varepsilon^P_{VBM}) + E_{align} \quad (3.4)$$

E_{Fermi} is the electron chemical potential, ranging from the valence band edge (E_{Fermi} = 0) to the conduction band minimum (E_{Fermi} = the value of the system's band gap), and ε^P_{VBM} is the valence band maximum eigenvalue for the pure system. The artificial interactions between localized charged defects and their periodic images introduces errors to the calculation of their formation enthalpy [157]. E_{align} aligns the valence band maximum of the pure and defective systems and is calculated using the SXDEFECTALIGN code by Freysoldt *et al.* [157]. The code calculates the interaction of a defect with its periodic images using a charge model and the dielectric constant matrix of the pure material, which in turn is obtained from Density Functional Perturbation Theory as implemented in VASP.

3.2.6.3 Oxygen partial pressure and chemical potentials

Defect properties can be analysed under a range of distinct chemical conditions, such as oxygen-poor and oxygen-rich environments, or anywhere in between. Taking $LaGaO_3$ as an example, its formation enthalpy (ΔH_f) can be calculated from the difference

between its DFT energy ($E[LaGaO_3]$) and the sum of the DFT elemental energies (in this case, metallic La and Ga, and molecular O_2), as exemplified in Equation 3.5.

$$\Delta H_f(LaGaO_3) = E[LaGaO_3] - E[La] - E[Ga] - \frac{3}{2}E[O_2] \tag{3.5}$$

The formation energy obtained from Equation 3.5 can then be related to the sum of the elemental chemical potentials, $\Delta\mu_i$ (Equation 3.6), which set the conditions under which the material is formed. $\Delta\mu_i$ values are limited by the formation energies of $LaGaO_3$ competing phases (La_2O_3, Ga_2O_3 and $La_4Ga_2O_9$), yielding a set of linear equations (3.6-3.9), which can be solved to determine the intersection points of the material's thermodynamic stability field. These intersection points correspond to the range of elemental chemical potentials within which the material is stable and hence to the O-rich, O-poor and any other relevant chemical conditions under which defect properties should be investigated.

$$\Delta H_f(LaGaO_3) = \Delta\mu_{La} + \Delta\mu_{Ga} + 3\Delta\mu_O \tag{3.6}$$

$$\Delta H_f(La_2O_3) \leq 2\Delta\mu_{La} + 3\Delta\mu_O \tag{3.7}$$

$$\Delta H_f(Ga_2O_3) \leq 2\Delta\mu_{Ga} + 3\Delta\mu_O \tag{3.8}$$

$$\Delta H_f(La_4Ga_2O_9) \leq 4\Delta\mu_{La} + 2\Delta\mu_{Ga} + 9\Delta\mu_O \tag{3.9}$$

Temperature effects are not considered when chemical potentials are calculated as outlined in Equations 3.6-3.9. The temperature and partial pressure dependence of the oxygen chemical potential ($\Delta\mu_o$), allowing its calculation for distinct chemical environments representing IT-SOFC operating conditions, reflecting the different experimental conditions experienced by electrolytes and electrodes, is given by Equation 3.10.

$$\Delta\mu_o(T,p) = \Delta\mu_O(T,p^o) + \frac{1}{2}kTln\left(\frac{p}{p^o}\right) \tag{3.10}$$

The first term on the right-hand side of Equation 3.10 can be calculated with respect to the zero reference state of the oxygen chemical potential, $\Delta\mu_O(0\ K, p^o)$, which corresponds to the total energy of an isolated oxygen molecule at 0 K, and hence is equal to zero:

$$\Delta\mu_O(T,p^o) = \Delta\mu_O(0\ K,p^o) + \frac{1}{2}\Delta G(\Delta T,p^o,O_2) \tag{3.11}$$

$$= \frac{1}{2}[H(T,p^o,O_2) - H(0\ K,p^o,O_2)] - \frac{1}{2}[S(T,p^o,O_2) - S(0\ K,p^o,O_2)]$$

The temperature-dependent enthalpy (H) and entropy (S) values can be extracted from thermochemical tables [158] to calculate the oxygen chemical potential under a range of conditions, while taking temperature and pressure effects into account. Table 3.1 lists the calculated oxygen chemical potentials corresponding to IT-SOFC operation (600 K ≤ T ≤ 1000 K) and typical cathodic pressure (p^o = 1 atm and $p(O_2)$ = 0.21 atm).

Table 3.1 – Oxygen chemical potential at IT-SOFC operating conditions (600 K ≤ T ≤ 1000 K, p^o = 1 atm and $p(O_2)$ = 0.21 atm), calculated from Equations 3.10 and 3.11.

T (K)	600	700	800	900	1000
$\Delta\mu_o$ (eV)	-0.65	-0.78	-0.90	-1.03	-1.17

3.2.6.4 Thermodynamic transition levels

The formation of intrinsic and extrinsic defects in a system can create charge states within the band gap and shift the position of the system's Fermi level. The thermodynamic transition (or ionisation) levels between distinct charge states, $\varepsilon_E(q/q')$, can be calculated from Equation 3.12 and correspond to the Fermi energy at which the defect goes from one charge state to another, i.e., the Fermi energy at which the energies of the two charge states, q and q', are equal.

$$\varepsilon_E\left(\frac{q'}{q}\right) = \frac{\Delta H_f(D,q) - \Delta H_f(D,q')}{q' - q} \tag{3.12}$$

Transition level diagrams possess information about the formation energies of intrinsic and extrinsic defects, showing at which Fermi energy the transition between charge states occur. Changes in slope represent the transition/ionisation levels, where q and q' states have equal formation energies and hence are in equilibrium. The transition level diagrams of *p*-type defects will have negative slope, with the slope being equal to the defect charge state. Accordingly, *n*-type defects will have a positive slope, while charge neutral defects will have zero slope. These diagrams contain important information about the individual and combined contribution of these defects to the electronic conductivity of the host material; if a defect is a contributor to *p*-type conductivity, its first transition level will be located close

to the valence band (VB), allowing holes to easily move from acceptor levels to the VB. Similarly, if a defect is to contribute to *n*-type conductivity, its first transition level will be close to the conduction band (CB), allowing electrons to readily move from donor levels to the CB. On the other hand, the interception of the thermodynamic transition levels of two defects with opposite polarity suggests the occurrence of charge compensation i.e., if both defects are present in the system, the Fermi level would be pinned at the point of intersection, hindering any *p*- or *n*-type conductivity that could potentially arise from such impurities. Figure 3.2 illustrates the transition level diagrams for (a) *p*-type and (b) *n*-type defects. The dashed lines represent the distinct charge states for each defect, while the solid lines represent the most stable charge state at a given Fermi energy.

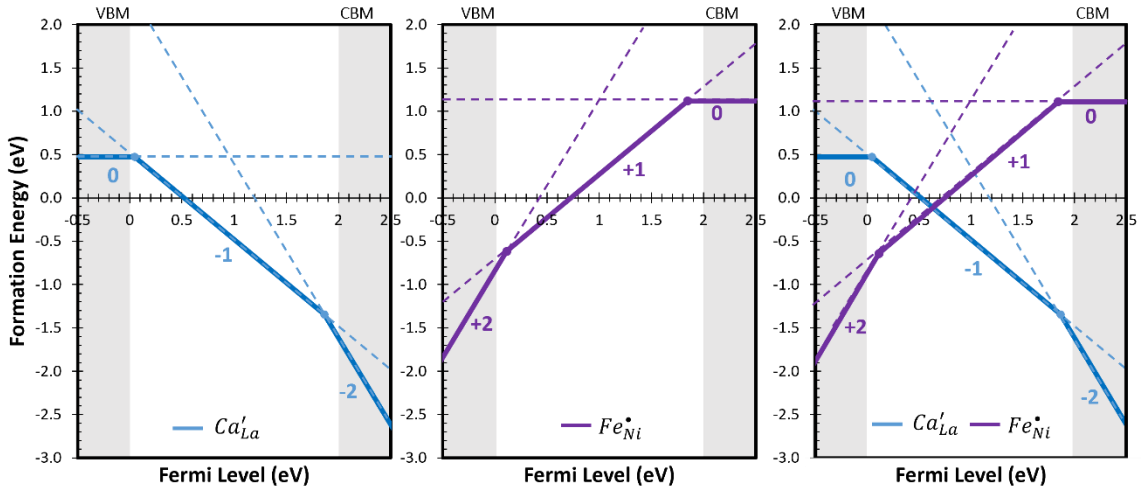

Figure 3.2 – Transition level diagrams of (a) *p*-type (Ca'_{La}) and (b) *n*-type ($Fe^{\bullet}_{Ni}$) defects. Part (c) illustrates Fermi level pinning when the ± 1 charge states of *p*-type and *n*-type defects cross.

In Figure 3.2a the transition level diagram of extrinsic calcium as an aliovalent A-site dopant (Ca'_{La} in Kröger-Vink notation) in La_2NiO_4 is shown. As Ca(II) and La(III), the host cation, possess +2 and +3 charges, respectively, calcium is introduced to the lattice in a -1 charge state, producing an electron hole, which can potentially contribute to *p*-type conductivity. If the first transition level of such defect is close to the VBM, the dopant is said to have a shallow 0/-1 transition level, indicating that its ionisation occurs close to the valence band maximum. As the Fermi level is shifted to the VB, electrons can be easily excited into the holes associated with the defect, allowing such holes to move into the

valence band, contributing to *p*-type conduction. Indeed, from Figure 3.2a, the first transition level of Ca'_{La} (i.e., the first change of slope, from q = 0 to q = -1) lies very close to the VBM.

In Figure 3.2b, the transition level diagram of extrinsic Fe(III) ($Fe^{\bullet}_{Ni}$) acting as a B-site aliovalent dopant in La_2NiO_4 is shown. This trivalent defect will substitute divalent nickel, and hence will be introduced in the lattice in a +1 charge state, with an electron associated to it. As a result, the charge states of this *n*-type defect will have positive slope. $Fe^{\bullet}_{Ni}$ also possess shallow 0/+1 transition level, close to the CBM, suggesting that electrons formed upon ionisation can readily move from donor levels to the conduction band. Hence, Fe-doping potentially contributes to *n*-type conductivity in the host material. Figure 3.2c depicts the transition level diagrams of extrinsic calcium and extrinsic iron (Ca'_{La} and $Fe^{\bullet}_{Ni}$), *p*- and *n*-type defects, respectively, so their combined contribution to the electronic conduction properties of the host material can be evaluated. The intersection of Ca'_{La} -1 state with the +1 charge state of $Fe^{\bullet}_{Ni}$ will cause pinning of the Fermi level at 0.65 eV into the band gap (i.e. further away from the VBM or CBM), hindering any *p*- or *n*-type conduction that could arise from Ca- or Fe-substitution, respectively, in the co-doped material.

3.3 Molecular dynamics

In molecular dynamics simulations, Newton's equations of motion, which describe the classical interaction between particles as a function of time, are integrated for the atoms in a molecular system, aiming to calculate their time-correlated motion i.e., their trajectory. Newton's second law is presented in Equation 3.13, where the force acting on particle *i*, F_i, is directly proportional to the particle's mass, m_i and acceleration, a_i, which in turn is related to changes in the particle's position over time.

$$F_i = m_i a_i = m_i \frac{\partial^2 r_i}{\partial t^2} \tag{3.13}$$

Statistical mechanical methods allow the calculation of the particles' positions, velocities, forces, energies and other dynamic variables at each timestep in the simulation. The obtained information is used to recalculate these same variables at a later time, $t + \delta t$, allowing the structural, thermodynamic and transport properties of a chemical system to be investigated [159]. A variety of algorithms can be used to integrate Newton's equations of

motion, with the Verlet, the Verlet leapfrog and the velocity Verlet algorithms being discussed in this section. These three algorithms are numerically equivalent, with the latter being used in TCD-PIMAIM. The thermodynamic ensembles that can be used in molecular dynamics simulations are also presented, followed by the general methodology used in this thesis to generate molecular dynamics data.

3.3.1 Integration algorithms

After the forces between the atoms in a chemical system have been calculated, Newton's equations of motion can be integrated from time t to $(t + \partial t)$, to obtain the particles' time-dependent trajectory. The algorithms used in this integration are usually derived from the Taylor series of the function of interest. The Verlet algorithm [160] is obtained from two Taylor expansions of the particle's position, r_i, from time t to $(t + \partial t)$ and from time t to $(t - \partial t)$, which are then added together. It considers that the particle's acceleration, a_i, is constant over timestep ∂t. The Taylor series expansion of $r_i(t + \partial t)$ is given in Equation 3.14, while the backwards expansion $r_i(t - \partial t)$ is given by Equation 3.15.

$$r_i(t + \partial t) = r_i(t) + v_i(t)\partial t + \frac{a_i(t)}{2!}\delta t^2 + \frac{b(t)}{3!}\delta t^3 + \cdots \quad (3.14)$$

$$r_i(t - \partial t) = r_i(t) - v_i(t)\partial t + \frac{a_i(t)}{2!}\delta t^2 - \frac{b(t)}{3!}\delta t^3 + \cdots \quad (3.15)$$

The addition of Equations 3.14 and 3.15 removes all odd-order terms and is truncated at δt^2, yielding the functional form of the Verlet algorithm, as in Equation 3.16.

$$r_i(t + \partial t) = 2r_i(t) - r_i(t - \partial t) + a_i\delta t^2 \quad (3.16)$$

One limitation of the Verlet algorithm is that the addition of Equations 3.14 and 3.15 eliminates the velocity term (and hence kinetic energy information), which cannot be explicitly calculated. Velocities can be approximately calculated as given in Equation 3.17.

$$v_i(t) = \frac{r_i(t + \partial t) - r_i(t - \partial t)}{2\partial t} \quad (3.17)$$

To overcome this limitation and calculate the velocity and kinetic energy more precisely, the Verlet leapfrog algorithm (Equation 3.18) [161] is derived from Taylor series

expansion of the particles' velocities (instead of positions) at every half timestep (½ ∂t), updating v_i before the positions (calculated as in Equation 3.19) change.

$$v_i\left(t+\frac{\partial t}{2}\right)=v_i\left(t-\frac{\partial t}{2}\right)+a_i(t)\delta t \tag{3.18}$$

$$r_i(t+\partial t)=r_i(t)+v_i\left(t+\frac{\partial t}{2}\right)\partial t \tag{3.19}$$

The system's total energy conservation cannot be efficiently evaluated throughout the simulation with the Verlet leapfrog algorith, as velocities (and hence kinetic energy) and positions (and potential energy) are computed at different times due to their distinct timesteps (½ ∂t and ∂t, respectively). The velocity Verlet algorithm [162], on the other hand, computes velocities, positions and accelerations at the same timestep. As a result, the total (potential + kinetic) energy can be evaluated throughout the simulations. The velocity Verlet algorithm is obtained from the Taylor expansions of position and velocity, given in Equations 3.20 and 3.21.

$$r_i(t+\partial t)=r_i(t)+v_i(t)\partial t+\frac{a_i(t)\partial t^2}{2} \tag{3.20}$$

$$v_i(t+\partial t)=v_i(t)+\frac{1}{2}[a_i(t)+a_i(t+\partial t)]\partial t \tag{3.21}$$

3.3.2 Timestep

Ideally, a timestep should be one order of magnitude smaller than the fastest process in the simulations (for numerical stability and accuracy in the conservation of energy) [163], and long enough to allow realistic time frames (and enough atomic motion) to be sampled. Still, there is a limit in the precision at which computed values can be stored; this round-off error increases with the number of timesteps and the true particle's trajectory cannot be ever traced. Therefore, the choice of a suitable timestep is generally a trade-off between tractability and accuracy, and can be done by evaluating energy conservation to a given degree of accuracy for different ∂t. In this thesis, a timestep of 4 fs was calculated to be ideal. Even though it is not possible to completely eliminate errors associated with the

timestep choice, such errors could be seen as uncontrolled perturbations that are also observed experimentally [164].

3.3.3 Thermodynamic ensembles

The choice of an adequate thermodynamic ensemble determines how macroscopic observables, such as volume, temperature or pressure will relate to the microscopic data obtained in MD simulations from the particles' positions and momentum. In the microcanonical (or NVE) ensemble, the number of particles N, the total energy E and the volume V are kept constant during the simulation, representing isolated systems, which do not exchange heat (energy) with their surroundings. Pressure and temperature can vary. Potential and kinetic energies also fluctuate, while the system's total energy is fixed as there is no heat flow. The Hamiltonian of the system (H_{NVE}) is a function of the N particles' momentum ($\mathbf{p}_N$) and position ($\mathbf{r}_N$), and hence their kinetic (K) and potential energy (U), respectively, as given by Equation 3.22. Since experimental systems are usually not isolated, the NVE ensemble is not commonly used in MD simulations.

$$H_{NVE}(\mathbf{p}_N, \mathbf{r}_N) = K(\mathbf{p}_N) + U(\mathbf{r}_N) \tag{3.22}$$

The canonical (or NVT) ensemble is more realistic; the number of particles N, the volume V and the temperature T are kept constant throughout the simulation, with the latter being controlled by a thermostat, usually the Nosé-Hoover thermostat [165–167], with modifications as proposed by Martyna *et al.*[168]. Such modifications extended the Nosé-Hoover single thermostat to a chain of thermostats, after demonstrating that the Nosé-Hoover dynamics did not necessarily result in a canonical distribution. The first thermostat is coupled and in equilibrium with the chemical system, while successive thermostats are in equilibrium with the previous one. In the canonical ensemble, the system's Hamiltonian (H_{NVT} in Equation 3.23) is a function of the potential energy (U) and the kinetic energy, which is given in terms of momentum ($\mathbf{p}_i$) and mass (m_i). N_{df} is the number of degrees of freedom, Q is the thermostat's effective mass, k_B is the Boltzmann constant and η and $\mathbf{p}_\eta$ are the position and momentum of the thermostat. The last term in Equation 3.23 defines the chain of thermostats proposed by Martyna. The demonstration of how Equation 3.23 is obtained and further definitions of each of its terms can be found elsewhere [165–168].

$$H_{NVT} = U + \sum_{i=1}^{N_{df}} \frac{\mathbf{p}_i^2}{2m_i} + \frac{\mathbf{p}_\eta^2}{2Q} + N_{df} k_B T \eta_1 + \sum_{j=2}^{M} k_B T \eta_j \quad (3.23)$$

Finally, in the isothermal-isobaric (NPT) ensemble, the number of particles N, the pressure P and the temperature T are kept constant. This ensemble is the closest to experimental settings, and hence is used in this thesis for simulations investigating ionic diffusion in bulk systems. Temperature and pressure are controlled by a thermostat and a barostat, as demonstrated by Martyna *et al*. [169] The extended Hamiltonian for the NPT ensemble is given by Equation 3.24, where $\mathbf{p}_\epsilon$ and W are the momentum and the effective mass of the barostat, and P_{ext} is the external pressure.

$$H_{NPT} = \sum_{i=1}^{N_{df}} \frac{\mathbf{p}_i^2}{2m_i} + \frac{\mathbf{p}_\in^2}{2W} + \frac{\mathbf{p}_\eta^2}{2Q} + U + (N_{df} + 1) k_B T \eta + P_{ext} V \quad (3.24)$$

3.3.4 Short-range cutoff radius

Since molecular dynamics depends on the forces acting upon the systems' particles, surface effects would affect the calculations and obtained results if they are not accounted for. To solve this limitation, periodic boundary conditions are implemented (Section 3.1) and allow a smaller cell to be simulated as if it was part of a much larger system [149]. When periodic boundary conditions or very large simulation cells are used, a cutoff radius (r_c) needs to be set; an atom will only interact with neighbouring particles that are within the determined r_c, i.e. the cutoff radius sets the limit within which pairwise interactions are evaluated. The cutoff radius should be smaller than half of the width of the cell for cubic systems, or less than half of the smallest lattice vector for orthorhombic cells. For rhombohedral systems, on the other hand, the length across the cell is less than the lattice vector. Hence, this should be taken into account when choosing r_c for hexagonal systems. Setting a cutoff radius guarantees that the minimum image convention is obeyed, i.e., that an atom interacts only with one equivalent image of any given particle in the periodic system and do not interact with itself [149].

3.3.5 Molecular dynamics procedure

In MD simulations, an equilibration period during which the system reaches the desired thermodynamic state needs to be simulated. First, the system undergoes temperature scaling, where velocities (and hence kinetic energies) are periodically scaled, guaranteeing that the systems' temperature stays around the target temperature. The initial particle's positions can be taken from experimental structural data. Initial velocities are randomly assigned to each particle, obeying the Maxwell-Boltzmann distribution, and resulting in appropriate kinetic energies to achieve the desired simulation temperature. Equilibrium runs are then performed prior to data collection, so the system can reach thermodynamical equilibrium, and usually last for a few hundred picoseconds. Data starts to be collected for analysis only after equilibration is over. These data collection (or production) runs are long enough (in the order of nanoseconds) to converge the dynamic properties of interest.

3.3.6 MD analysis

Mean square displacement and ionic conductivity

Ionic motion can be described as a 'random walk'; the ion's path is not a straight line, as the particle collides with other ions during its movement. The mean square displacement (MSD) of species i, $\langle \Delta r_i(t)^2 \rangle$, is the measurement of the average square distance travelled by it within the system (Equation 3.25) and contains information about its diffusion.

$$\langle \Delta r_i(t)^2 \rangle = \frac{1}{N_i} \sum_{i=1}^{N_i} [r_i(t) - r_i(0)]^2 \tag{3.25}$$

In Equation 3.25, $\langle \Delta r_i(t)^2 \rangle$ measures the displacement of i at time t (as $r_i(t)$ is the particle's position at time t), with N_i being the number of ions of species i. An MSD vs. time plot depicts the average displacement of atoms as a function of time, and hence indicates how fast is the ionic diffusion process within a system, with a linear increase in the MSD suggesting the presence of ionic diffusion through the solid. MD simulations allow the determination of the trajectory of different ionic species, and hence diffusion properties can be calculated and analysed individually for anions and cations, for example.

Fick's Law relates diffusion processes to the random ionic motion. It states that the flux of the diffusing species is proportional to its gradient of concentration. The proportionality constant relating these two quantities is the diffusion coefficient, D; it measures the mobility of the diffusing species [170] and can be related to the MSD, as given by Equation 3.26,

$$\langle r_i(t)^2 \rangle = 2N\,Dt + k \tag{3.26}$$

where N is the dimensionality of the diffusion and k is the Debye-Waller factor. While three dimensonal diffusion occurs in bulk systems, one-dimensional processes can happen in dislocations, and two-dimensional diffusion can occur parallel to surfaces or interfaces, for example. Equation 3.26 suggests that for three dimensional systems, a plot of $\langle r_i(t)^2 \rangle$ against time should result in a straight line with slope 6*D*.

The diffusion coefficient can be related to the activation energy of diffusion (E_a), according to the Arrhenius equation (Equation 3.27) [171], which can also be written in terms of natural logarithms (Equation 3.28).

$$D = D_0 \exp\left(-\frac{E_a}{RT}\right) \tag{3.27}$$

$$lnD = lnD_0 - \frac{E_a}{RT} \tag{3.28}$$

From Equation 3.28, the activation energy of diffusion can be obtained from the Arrhenius plot (lnD against 1/T), which yields a straight line of slope $-E_a/R$.

The diffusion coefficient can also be related to the ionic conductivity (σ), which indicates how fast charge carriers move through the system under the influence of an external electric field. The ionic conductivity is defined by the Nernst-Einstein equation (Equation 3.29) [172], where ρ is the number of charge carriers per unit volume, q is their effective charge, i.e., their ionic charge multiplied by the elementary charge (e = 1.602 x 10^{-16} C), k_B is the Boltzmann constant, T is the temperature at the system and f is the Haven coefficient, related to the lattice type and diffusion mechanism, usually set as 1 [173].

$$\sigma = \frac{\rho q^2 D}{f k_B T} \tag{3.29}$$

In this work, the displacement of particles over time is analysed using multiple time origins MSDs. Traditionally, a single time origin is used when computing MSDs, meaning that every point in the particle's trajectory contributes one single time to the calculation of ionic conduction properties. To avoid this inefficient use of data points, multiple time origins can be considered when calculating the MSD, which also improves statistics, since multiple reference states are being considered. Any frame in the particle's trajectory can be taken as an origin, as long as enough frames come after it. However, the averaging of the MSD over all possible time origins yields highly correlated data. To avoid this, in this thesis time origins are taken every 100 ps, and the final part of the computed MSDs is discarded before calculating ionic diffusion properties, since each point should be averaged over the same number of data points.

Radial distribution function

The radial distribution function (RDF), $g_{ij}(r)$, is a pair correlation function. It indicates the probability of finding an atom at a given distance from another atom compared to the ideal gas distribution, which is a random distribution of particles with $g(r) = 1$. Local structural information about the investigated system can be extracted from the RDF, which is calculated from the particle's trajectory and averaged over the MD simulation. The RDF describes how atoms are distributed around each other by showing the atomic density variation as a function of distance from a given particle, as shown in Equation 3.30

$$g_{ij}(r) = \frac{n_{ij}(r)}{\rho_j 4\pi r^2 \Delta r} \tag{3.30}$$

where n_{ij} is the number of particles j located at a distance between r and $(r + \Delta r)$ from particles i. The RDF can be calculated between the same $(j = i)$ or different $(j \neq i)$ species. ρ_j is the number density of particles j.

The average coordination number (c_{ij}) of an atom in the material can also be calculated from RDFs, as in Equation 3.31, obtained from the integration of the RDF up to distance r_c.

$$c_{ij} = 4\pi\rho_j \int_0^{r_c} r^2 g_{ij} dr \tag{3.31}$$

Vacancy analysis

Oxide-ion conductivity can take place via a vacancy mechanism. Hence, investigating the distribution of these defects in a system can be of paramount importance to evaluate ionic conduction properties. To locate the vacancies within the simulation cell, the bulk pure system, without any dopants or vacancies, is used as a template to designate the original lattice sites. Each ionic species in the MD simulation frames are then allocated to one of these original lattice sites. Vacancies are assigned to the remaining vacant lattice sites, allowing the calculation of vacancy RDFs. Vacancy-vacancy and cation-vacancy RDFs can be calculated to investigate the tendency to vacancy trapping around dopant cations (suggesting which dopants are beneficial to ionic conduction properties) or to vacancy ordering and segregation.

Chapter 4

Defect chemistry of $LaGaO_3$ doped with divalent cations

4.1 Introduction

Perovskite-based systems are attractive alternatives to fluorite-structured materials as solid oxide fuel cell electrolytes, as outlined in Section 1.5. If the host cations are substituted with lower valence species, oxygen vacancies can be generated as a charge compensating mechanism to preserve electroneutrality [29], leading to oxide-ion diffusion through the lattice. $LaGaO_3$-based perovskites have been shown to present high oxide-ion conductivity at intermediate temperatures (973-1073 K) [23,67–69], with negligible electronic conduction and good chemical stability over a wide range of oxygen partial pressures (10^{-20} to 1 atm) [68]. The electronic insulating properties are a result of both La and Ga having only one stable oxidation state and of the large band gap of the material – the orthorhombic phase of the perovskite has an optical band gap of 4.4 eV [174]. $LaGaO_3$ undergoes phase transition from orthorhombic (*Pbnm*, space group 62) to rhombohedral (*R3c*, space group 161) around 420 K (Figure 4.1).

LSGM, a $LaGaO_3$-based electrolyte doped with Sr(II) (La-site) and Mg(II) (Ga-site), is an ionic conductor in the IT range and over a wide oxygen partial pressure range (from 10^5 to 10^{-25} atm) [16,70–74]. Traina *et al*. [72] measured an ionic conductivity of 0.11 S cm^{-1} at 1073 K for the $La_{1-x}Sr_xGa_{1-y}Mg_yO_{3-\delta}$ (x = 0.10 and y = 0.20) perovskite. More recently, Huang *et al.* [74] studied the ionic conductivity of LSGM by testing 38 different dopant concentrations and determined that oxygen vacancies are mobile above 873 K, but condense into clusters at lower temperatures. The highest ionic conductivity of 0.166 S cm^{-1} was measured for x = 0.2 and y = 0.17 at 1073 K. Wu and Lee [73] came to a similar conclusion with their highest ionic conductivity (0.173 S cm^{-1}) observed when x = 0.15 and y = 0.20 at 1073 K. Therefore, previous studies are in agreement that optimized compositions of LSGM can present ionic conductivity in the 0.11-0.17 S cm^{-1} range at 1073 K, higher than those observed for ceramics with a fluorite-type structure in the IT range [2,70–74].

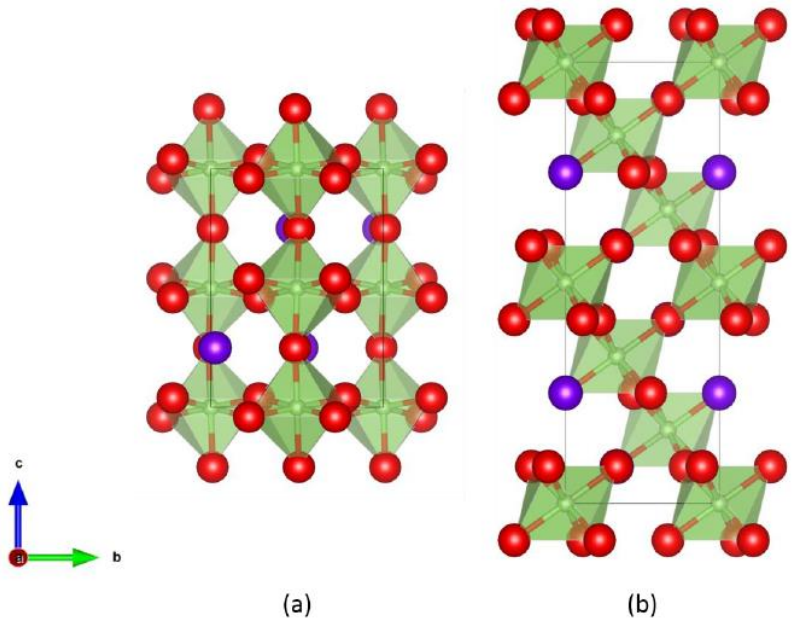

Figure 4.1– The (a) orthorhombic (*Pbnm*) and (b) rhombohedral (*R-3c*) $LaGaO_3$ phases. O atoms are shown in red, La atoms are shown in purple and the GaO_6 octahedra in green.

Due to their distinct ionic radii when compared to host cations, dopants can introduce small distortions to the local perovskite structure and can interact with the generated charge compensating vacancies. This leads to the formation of defect clusters, i.e., vacancies can be trapped around the dopants, which hinders their mobility and hence oxide-ion conductivity [73]. Each perovskite system has an optimum vacancy concentration for which ionic conductivity is maximum [175,176] and concentrations above the critical value lead to defect ordering, decreasing the amount of vacancies available for ionic transport and thus the mobility of oxide ions [28]. Islam *et al.* [75] used interatomic potentials to calculate the binding energies between dopants and vacancy in $LaGaO_3$ and concluded that Ga-site dopants (Mg(II), Co(II), Ni(II) and Cu(II)) present considerably higher binding energies than La-site dopants (Sr(II) and Ca(II)), suggesting that charge-compensating vacancies would tend to be trapped around Ga-site dopants. Defect interactions can therefore directly influence ionic conduction properties and thus the suitability of a material as SOFC electrolyte.

Another constraint when selecting suitable materials as SOFC components is that the electrolyte and electrodes should be compatible both physically, with similar thermal expansion coefficients to avoid thermal stresses and mechanical fracture, and chemically, being chemically inert to each other [177]. While Ni-YSZ and Ni-CeO_2 cermets are

commonly used as anodes with YSZ- and CeO_2-based electrolytes, Ni reacts with LSGM, forming secondary phases at the electrode-electrolyte interface or during synthesis of the Ni-LSGM cermet, hindering ionic conduction and increasing anode polarization [178,179]. Both $La_{1-x}Sr_xCoO_3$ (LSC) and $La_{1-x}Sr_xMnO_3$ (LSM) have been suggested as cathodes for LSGM-based SOFCs. The first, however, reacts with LSGM and does not have a compatible thermal expansion coefficient to that of the electrolyte. LSM, on the other hand, is chemically and thermally compatible with LSGM, but possesses negligible ionic conduction [180]. Pure electronic conduction limits the oxygen reduction reaction on the cathode to the triple phase boundary (TPB), i.e., the regions where cathode, electrolyte and gaseous O_2 are in contact. Therefore, mixed ionic and electronic conduction is desirable, since it allows the ORR to occur at the entire cathode/O_2 gas interface due to O^{2-} ions being efficiently transported from the cathode's surface to the electrolyte [180].

Transition metal (TM) doped $LaGaO_3$ has been suggested as both cathode and anode for $LaGaO_3$-based IT-SOFCs, as this would bypass the chemical and physical compatibility problems between electrode and electrolyte, TM doping also increases electronic conduction in the perovskite, resulting in MIEC [178]. $La_{0.9}Sr_{0.1}Ga_{0.8}M_{0.2}O_{3-\delta}$ (M = Co, Mn) [178,180] is suitable as cathode (LSGCo) and anode (LSGMn) in $LaGaO_3$-based IT-SOFCs. Single cells using these materials as electrodes possess maximum power density of 88 mW cm^{-2} at 1073 K, higher than those presented by cells containing Pt electrodes (20 mW cm^{-2}), or LSC and Ni-CeO_2 as cathode and anode, respectively (61 mW cm^{-2}). TM doped $LaGaO_3$ can have their electronic conduction further improved by increasing dopant concentration within the solubility limit of the transition metal in the perovskite [178,180]. In LSGMn, for example, ionic conduction dominates in lower Mn concentrations (20 mol%), but electronic conduction increases five times with an increase in Mn concentration from 20 to 43 mol% [180]. $LaGaO_3$ systems doped with other transition metals such as Cr, Fe and V were also investigated as anode materials, but they either presented poor chemical stability under reducing conditions or low electronic conduction.

In this chapter, DFT calculations have been performed to investigate the effects of divalent metals (Ni(II), Sn(II), Mg(II), Zn(II), Co(II), Fe(II), Pt(II), Mn(II), Pd(II), Ca(II), Sr(II), Pb(II) and Ba(II)) as dopants in $LaGaO_3$ to understand their influence on the defect chemistry and ionic conductivity of the perovskite. The lowest energy structure for each doped system was determined in order to investigate key features that affect the ionic

conductivity of the material – the doping energy, the preferable dopant position (La or Ga site) and the association energy between vacancies and dopants – as a function of dopant identity and chemical environment. This chapter aims to determine which dopants are the most beneficial when improving the ionic conductivity of $LaGaO_3$-based systems and to understand which aspect has the ultimate influence in the ionic transport properties of the perovskite considering IT-SOFC applications.

4.2 Methodology

DFT and DFT+*U* calculations using the SCAN [129] functional were carried out with VASP [145–147]. SCAN is a meta-GGA functional which has been suggested to yield better results regarding the geometry and energy of diversely bonded materials when compared to PBE. A plane wave basis set was used to describe valence electrons, while projector augmented wave (PAW) pseudopotentials were used to describe the interactions between core (La:[Kr], Ga:[Ar,$3d^{10}$], O:[He], Mg:[Ne], Zn:[Ar], Co:[Ar], Fe:[Ar], Sn:[Kr], Ni:[Ar], Mn:[Ne,$3s^2$], Pt:[Xe,$4f^{14}$], Pd:[Kr], Ca:[Ne], Sr:[Ar,$3d^{10}$], Pb:[Xe,$4f^{14}$], Ba:[Kr,$4d^{10}$]) and valence electrons [181,182]. The ionic and electronic convergence criteria were 0.01 eV $Å^{-1}$ and 10^{-6} eV, respectively, with a plane-wave cutoff energy of 500 eV, converging the energy to 0.003 eV/atom. A +*U* correction of 4 eV was applied to the 3*d* (Co(II), Fe(II), Ni(II) and Mn(II)), 4*d* (Pt(II)) and 5*d* (Pd(II)) states of the transition metals using the Dudarev approach [86] to reduce the self-interaction error which favours the partial occupation of these states. When using U = 4 eV, the high spin state (partially filled t_{2g} orbitals) of Mn^{2+}, Fe^{2+}, Co^{2+} and Ni^{2+} in their native oxides [183–188] was accurately predicted, as well as the semiconductor character of PdO and PtO (standard GGA-DFT erroneously predicts metallic character and no band gap) [189,190]. The suitability of U = 4 eV was determined after comparison between the obtained SCAN valence band features in the electronic density of states and experimental XPS data [191–199]. Furthermore, similar *U* values were previously reported for DFT+*U* calculations on transition metal oxides utilising a range of functionals [200–211]. Table 4.1 summarizes previous theoretically calculated *U* corrections for TM monoxides with a range of different values (2.5–6.1 eV) depending on the derivation method. A comparison between the calculated SCAN+*U* (U = 4 eV) band gaps and experimental results for these oxides can be found in Table 4.2, while Figure 4.2 shows the obtained SCAN+*U* band structures and electronic density of states for

the TM monoxides. VESTA [212] was used to perform visual and structural analysis of the systems.

Table 4.1 – Previous theoretical studies deriving a Hubbard *U* correction ($U_{eff} = U - J$ in eV) to transition metal (Mn^{2+}, Fe^{2+}, Co^{2+}, Ni^{2+}, Pd^{2+} and Pt^{2+}) 3*d*/4*d* states in their monoxides.

TM Oxide	U_{eff} **(eV)**	**Functional**	**Method**	**Ref.**
MnO	2.7	SCAN+U	Oxidation energy, lattice constants, electronic structure	[213]
	3.6	LDA+*U*	Constrained LDA	[207]
	3.9	LDA+*U*	Constrained LDA	[208]
	4.0	PBE+*U*	Magnetic ordering, μ_B, formation energy	[214]
	4.0	PW91+*U*	Oxidation energy, μ_B	[206]
	4.5	LDA+*U*	Linear response	[209]
	4.9	PBE+*U*	Linear response	[210]
FeO	3.1	SCAN+U	Oxidation energy, lattice constants, electronic structure	[213]
	3.7	PBE+U	Unrestricted Hartree-Fock molecular orbitals	[204]
	3.9	LDA+*U*	Constrained LDA	[208]
	4.0	PW91+*U*	Oxidation energy, μ_B	[206]
	4.0	PBE+*U*	Magnetic ordering, μ_B, B_0, band gap, lattice parameters	[201]
	4.1	PBE+*U*	Linear response	[210]
	4.3	LDA+*U*	Linear response	[211]
	4.6	LDA+*U*	Constrained LDA	[207]
CoO	3.0	SCAN+U	Oxidation energy, lattice constants, electronic structure	[215]
	3.3	PW91+*U*	Oxidation energy, μ_B	[206]
	4.2	LDA+*U*	Constrained LDA	[208]
	4.4	PBE+*U*	Linear response (Co^{2+} in Co_3O_4)	[200]
	4.9	PBE+*U*	Linear response	[210]
	5.0	LDA+*U*	Constrained LDA	[207]
NiO	2.5	SCAN+U	Oxidation energy, lattice constants, electronic structure	[215]
	4.3	LDA+*U*	Constrained LDA	[208]
	4.6	LDA+*U*	Linear response	[211]
	5.0	LDA+*U*	μ_B and optical properties	[202]
	5.1	LDA+*U*	Constrained LDA	[207]
	5.3	PW91+*U*	Electronic structure, μ_B and lattice parameters	[203]
PdO	5.0	PBE+U	μ_B, electronic structure, band gap	[216]
	6.1	PBE+U	Linear response	[217]
PtO	5.9	PBE+U	Linear response	[217]

μ_B: magnetic moment, B_0: bulk modulus

Table 4.2 – Comparison between the SCAN+*U* (*U* = 4 eV applied on transition metal 3*d*/4*d*/5*d* states) band gaps values (in eV) obtained in this chapter, with previous theoretical (utilising DFT+*U* [206,208,213,217] and hybrid functional frameworks [218–222]) and experimental [192,195,199,223–236] results. Previous studies using DFT+*U* do not distinguish between indirect/direct band gaps, but simply report the fundamental band gap value.

TM oxide	SCAN+U (eV)		DFT+U (eV)		Hybrid DFT (eV)		Exp.
	Indirect	Direct	Indirect	Direct	Indirect	Direct	(eV)
MnO	2.45	2.71	-	1.2[a], 2.2[b], 3.2[c]	2.6[d], 2.8[e]	3.2[d], 3.3[e]	3.6-4.2
FeO	2.34	2.40	-	0.7[a], 2.1[b], 2.2[c]	2.1[d], 2.4[e]	2.2[d], 2.7[e]	2.4
CoO	-	3.16	-	1.9[b], 2.0[c]	3.2[d], 2.4[e]	4.0[d], 3.4[e]	2.5-3.0
NiO	2.55	2.85	-	3.2[b], 3.4[c]	4.1[d], 3.8[e]	4.5[d], 4.1[e]	3.5-4.3
PdO	-	0.76	-	1.4[b]	-	0.9[f]	0.8-2.67
PtO	1.30	1.35	-	metallic[b], 0.4[c]	0.85[f]	0.86[f]	-

[a] SCAN+*U* [213] (U_{Mn} = 2.7 eV, U_{Fe} = 3.1 eV)
[b] PBE+*U* [217] (U_{Mn} = 6.4 eV, U_{Fe} = 6.3 eV, U_{Co} = 6.3 eV, U_{Ni} = 7.7 eV, U_{Pd} = 6.1 eV, U_{Pt} = 5.9 eV)
[c] PW91+*U* [206] (U_{Mn} = 4 eV, U_{Fe} = 4 eV, U_{Co} = 3.3 eV, U_{Ni} = 6.4 eV and U_{Pt} = 9 eV [237])
[d] HSE03 [218]
[e] sX-LDA [219]
[f] HSE06 [220–222]

The unit cells of orthorhombic (*Pbnm*, space group 62) and rhombohedral (*R3c*, space group 161) $LaGaO_3$ (*o*-$LaGaO_3$ and *r*-$LaGaO_3$, respectively) were structurally optimized using SCAN, considering lattice constants ranging from 98% to 102% of experimental values [238–242] and under the constraint of constant volume with atomic positions and cell shape being allowed to change. The equilibrium cell volume was determined after fitting the resulting energy-volume curve to the Murnaghan [243] equation of state, minimising errors associated with Pulay stress and plane-wave DFT calculations on volume change due to the incompleteness of the finite basis set [244].

Defect calculations were performed in 3x3x2 and 3x2x1 expansions (360 atoms) of the optimized *o*-$LaGaO_3$ and *r*-$LaGaO_3$ unit cells, respectively, ensuring a minimum distance of 15 Å between vacancies to minimize vacancy-vacancy interactions. Doped supercells were created by replacing two La(III) or Ga(III) ions with two divalent dopant cations (Ni(II), Sn(II), Mg(II), Zn(II), Co(II), Fe(II), Pt(II), Mn(II), Pd(II), Ca(II), Sr(II), Pb(II) and Ba(II)), resulting in the creation of one charge compensating vacancy (CCV) to preserve the

electroneutrality of the system. In Kröger-Vink notation, the formation of a CCV due to M-doping of the La-site is given by Equation 4.1.

$$2MO + 2La_{La}^{X} + O_{O}^{X} \rightarrow 2M'_{La} + V_{\ddot{O}} + La_2O_3 \quad (4.1)$$

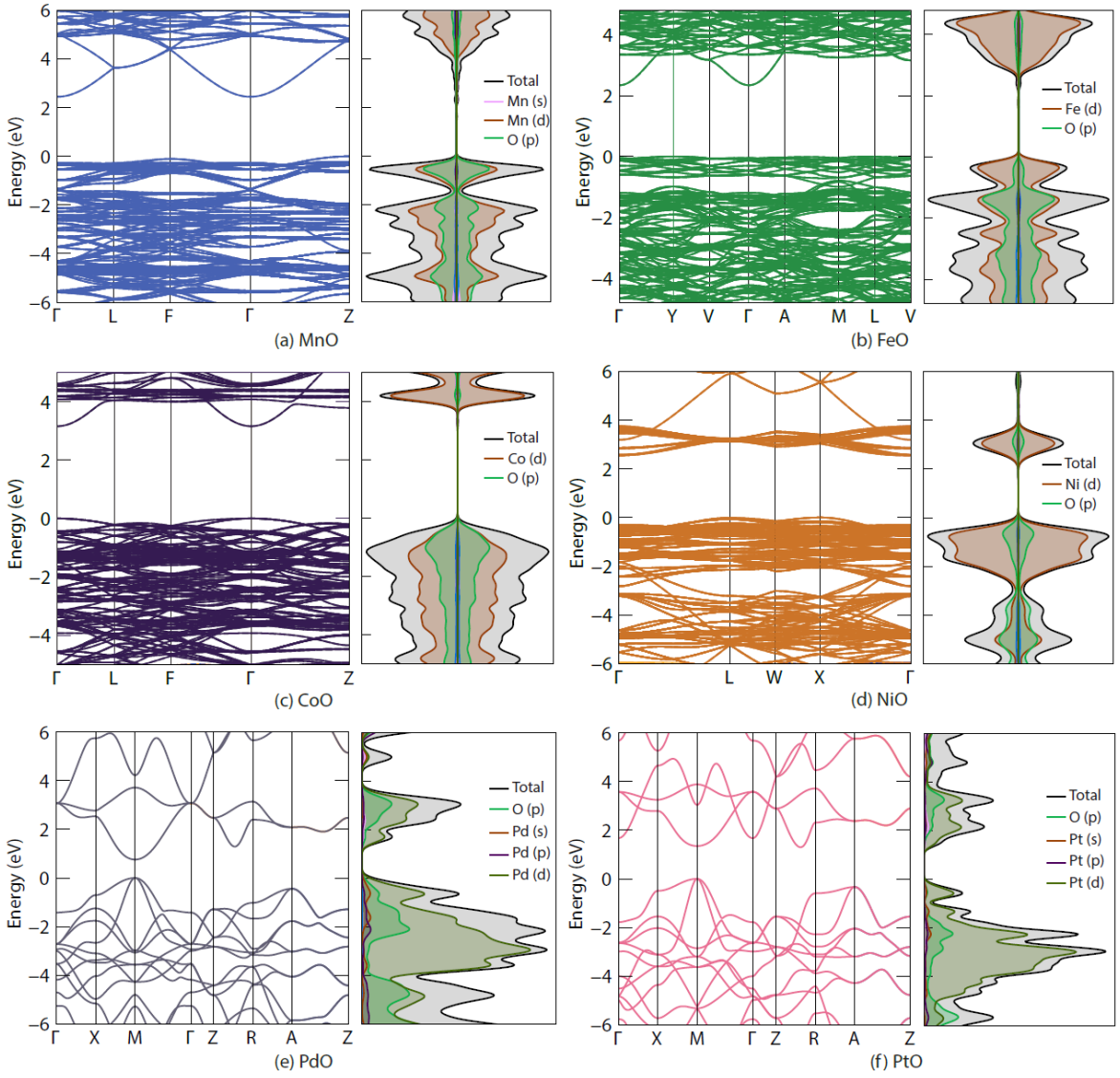

Figure 4.2 – (a) MnO, (b) FeO, (c) CoO, (d) NiO (e) PdO and (f) PtO band structures and electronic density of states calculated with SCAN+*U* (*U* = 4 eV applied on transition metal 3*d*, 4*d* or 5*d* states). The valence band maximum is set to zero. Indirect and direct band gap values are given in Table 4.2.

A range of different locations for the CCV were analysed to determine where it would preferentially lie – nearest-neighbour to both dopants (NN), next-nearest-neighbour to both dopants (NNN), NN to one of the dopants and NNN to the other (NN/NNN), and far away from both dopants (far). When more than one configuration within the same definition exists, a subscript (A and B) was used to distinguish them (NN_A and NN_B, for example).

In *o*-$LaGaO_3$, the La sites are not equivalent and the La-La nearest neighbour distance changes depending on the crystallographic direction. Two nearest-neighbours La atoms can be positioned along the [001] and [110] crystallographic directions, distant 3.906 Å from each other along the [001] direction, and 3.844 or 3.948 Å along the [110] direction. Therefore, two dopant-dopant configurations, corresponding to the two smallest NN distances (3.844 and 3.906 Å), were considered and are referred to as La_A (dopants positioned along [110]) and La_B (dopants positioned along [001]). The tested configurations for La-site doping in *o*-$LaGaO_3$ (La_A and La_B dopant arrangements, with the CCV located at NN, NNN, NN/NNN and far away sites) are shown in Figure 4.3.

Similarly, for Ga-site doping in *o*-$LaGaO_3$, the dopants can also be located in two different arrangements; the Ga-Ga distances are 3.896 Å and 3.898 Å when Ga atoms are in the centre of two octahedra along the [010] (Ga_A) and [001] crystallographic directions, respectively. In addition, Ga-O distances are also different along the axial and equatorial plane of the GaO_6 octahedra, being 1.983/1.987 and 1.994 Å respectively). Tested configurations for Ga-site doping in *o*-$LaGaO_3$ (Ga_A and Ga_B dopant arrangements, with the CCV located at NN, NNN, NN/NNN and far away sites) are shown in Figure 4.4.

When compared to the orthorhombic structure, the rhombohedral lattice has more symmetry; all La sites are equivalent (the La-La distance is 3.897 Å). The same is observed for Ga and O atoms (the Ga-Ga and the Ga-O distances are 3.897 and 1.985 Å, respectively). Consequently, only one dopant-dopant configuration was investigated for each La and Ga-site doping, as presented in Figure 4.5.

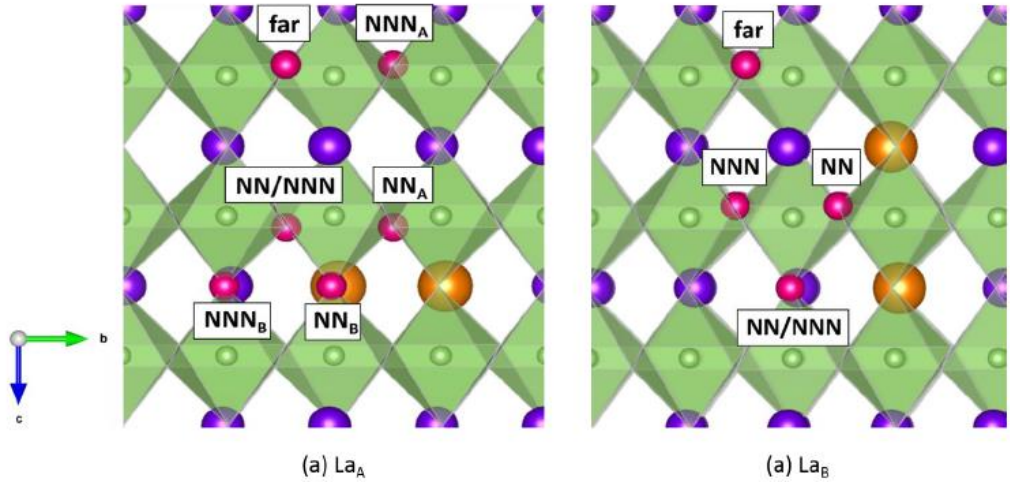

Figure 4.3 – Starting configurations for La-site doping of *o*-$LaGaO_3$. La, Ga, dopants and CCVs are shown in purple, green, orange and pink, respectively. Vacancies are located in NN, NNN, NN/NNN and far positions. Figures show a subsection of the lattice and O atoms are not shown for clarity.

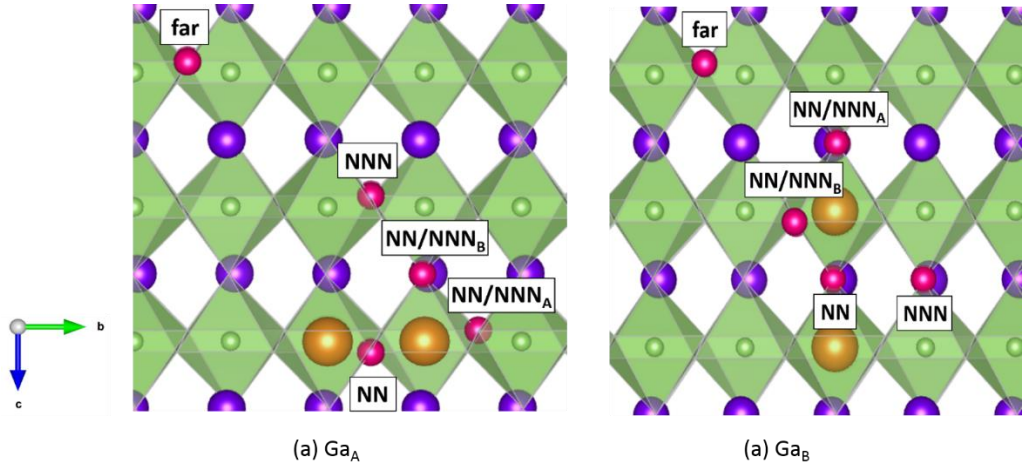

Figure 4.4 – Starting configurations for Ga-site doping of *o*-$LaGaO_3$. La, Ga, dopants and CCVs are shown in purple, green, orange and pink, respectively. Vacancies are located in NN, NNN, NN/NNN and far positions. Figures show a subsection of the lattice and O atoms are not shown for clarity.

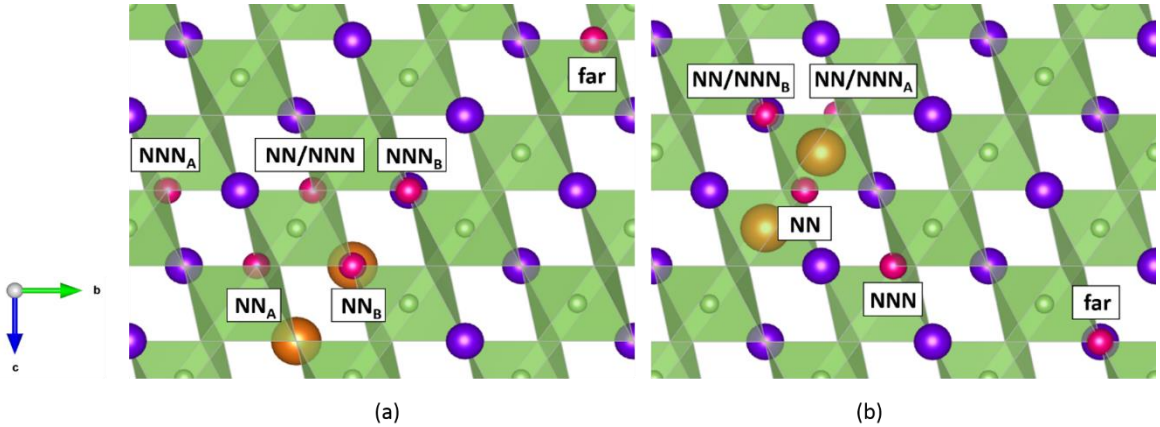

Figure 4.5 – Starting configurations for (a) La- and (b) Ga-site doping of *r*-$LaGaO_3$. La, Ga, dopants and CCVs are shown in purple, green, orange and pink, respectively. Vacancies are located in NN, NNN, NN/NNN and far positions. Figures show a subsection of the lattice and O atoms are not shown for clarity.

The doping energy, E_{dop}, which indicates how easily a dopant cation would be accepted in the lattice [64], was calculated from the defect calculations and the chemical potentials of the species, as described in Equation 3.3. E_{dop} values were analysed under distinct chemical environments, as outlined in Section 3.2.6.3.

To quantify how easily the CCV can move from a NN to a NNN site, we define the short-range association energy, E_{ass}^{SR}, to be the energy difference between the structures in which the CCV is in the NN and in the NNN positions with respect to the dopants [64]. In real systems with high dopant concentrations (above 35 mol% for LSGM for optimum ionic conductivity values, for example), the majority of charge compensating vacancies would be in a NN or NNN position with respect to a dopant. Therefore, E_{ass}^{SR} indicates the tendency of vacancies to be trapped around the dopants in regions of realistic and uniform dopant concentration. Similarly, the long-range association energy (E_{ass}^{LR}) between the oxygen vacancy and the dopant ions was obtained from the energy difference between the structure in which the vacancy is positioned far away from the dopants and the lowest energy structure. E_{ass}^{LR} evaluate the tendency of vacancies being trapped around the dopants in regions of non-uniform or low dopant concentration [64]. Therefore, both E_{ass}^{SR} and E_{ass}^{LR} values should be as low as possible, since large values would indicate that vacancies tend to be ordered due to defect interactions.

4.3 The electronic structure of $LaGaO_3$

The electronic band structure and the electronic density of states for *o*-$LaGaO_3$ obtained with PBE, SCAN and HSE06 are presented in Figure 4.6. The valence band is dominated by oxygen 2*p* orbitals, with some small contribution from La *5d*, Ga *4s* and *4p* states. La *f* orbitals are the main contributors to unoccupied states with some La 5*d*, Ga 4*s*4*p* and O 2*p* contributions. The interaction between Ga *s* and Ga *p* states with O *p* orbitals at the bottom (from -5 to -7.5 eV) and middle (-2.5 to -5 eV) parts of the valence band, respectively, indicates some covalent character in the Ga-O bonding. The contribution of La states to the conduction band and of O states to the valence band indicates the occurrence of electron-charge transfer between La and O ions, and thus the ionic character of the La-O interaction. Furthermore, there is some level of mixing between La and O states along the entire range, indicating some covalency in the La-O interaction. The perovskite's mixed bonding character is in agreement with other theoretical work [245]. These features can also be observed in the orbital projected band structures is presented in Figure 4.7.

The valence band maximum is located at the high-symmetry *S* point (-0.5, 0.5, 0.0), while the conduction band minimum is located at Γ, resulting in an indirect band gap of 3.70 eV. The VBM and CBM are mainly composed of O *2p* occupied levels and Ga 5*s* unoccupied states, respectively (Figure 4.7). The smallest direct energy gap is located at Γ (3.80 eV) and is optically active allowing direct comparison with the experimental optical adsorption (4.4 eV [174]). SCAN therefore underestimates the optical band gap by 13.6%, as expected from meta-GGAs, but it is still considerable better than PBE and HSE06; PBE calculates indirect and direct band gaps of 3.14 and 3.24 eV (26.4% underestimation), respectively, while HSE06 significantly overestimates the indirect and direct band gaps with values of 5.30 and 5.44 eV (23.6% overestimation), respectively. Even though the three methods yield similar features in the electronic band structure and density of states (Figure 4.6), the meta-GGA SCAN functional gives rise to superior results when describing the geometry and electronic structure of the investigated perovskite when compared to the GGA PBE functional and hybrid-DFT (HSE06), and therefore will be used for defect calculations. A direct comparison of structural parameters and formation energies of $LaGaO_3$ and related phases calculated with SCAN, PBE and HSE06 are presented in Tables 4.3 and 4.4.

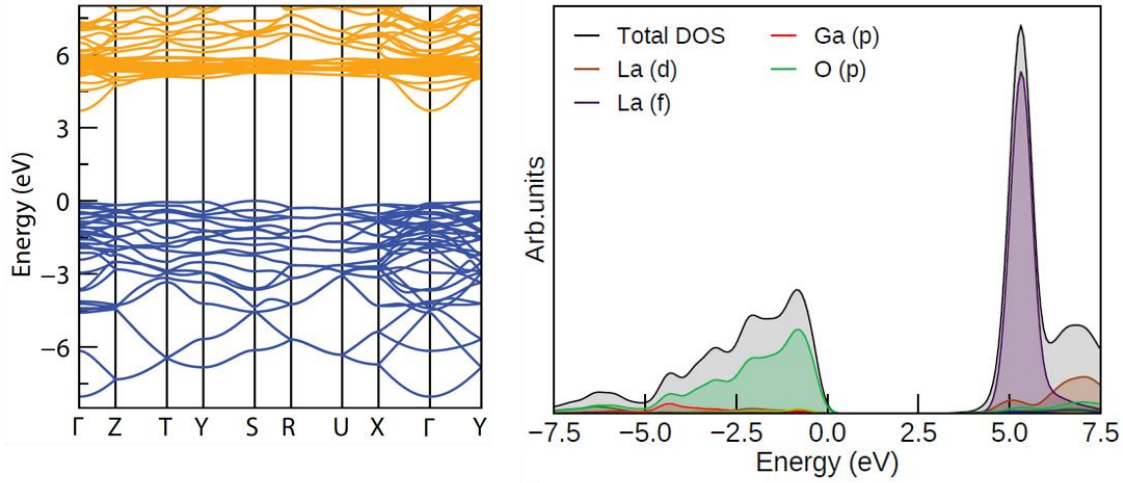

(a) SCAN

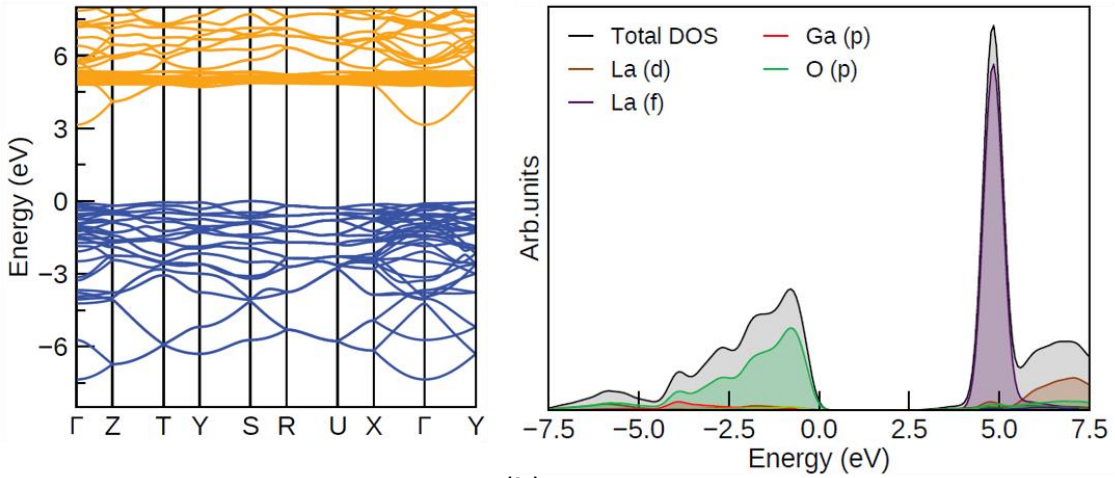

(b) PBE

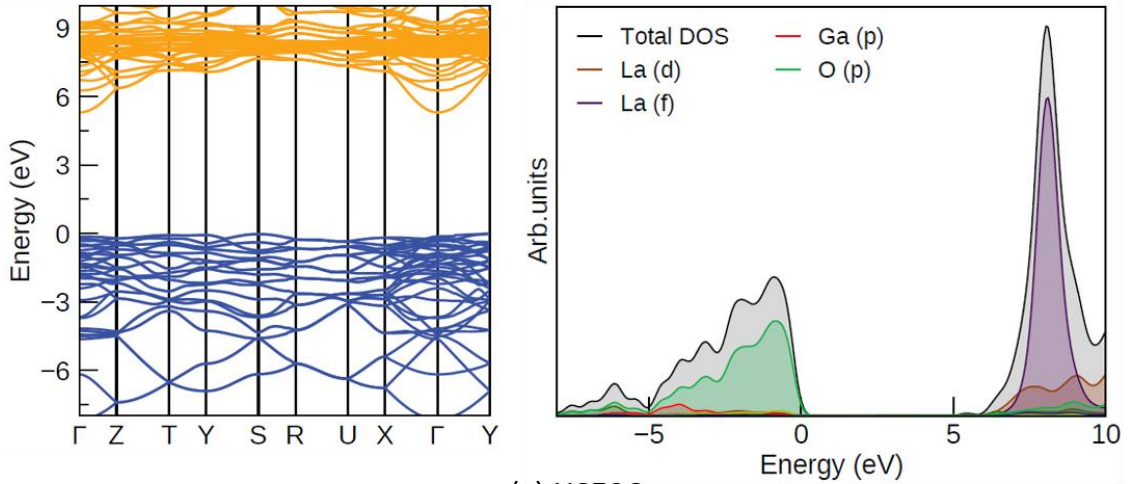

(c) HSE06

Figure 4.6 – Electronic band structure and electronic density of states of *o*-$LaGaO_3$, obtained with (a) SCAN, (b) PBE and (c) HSE06, plotted using the sumo [246] package. The valence band maximum is set to zero.

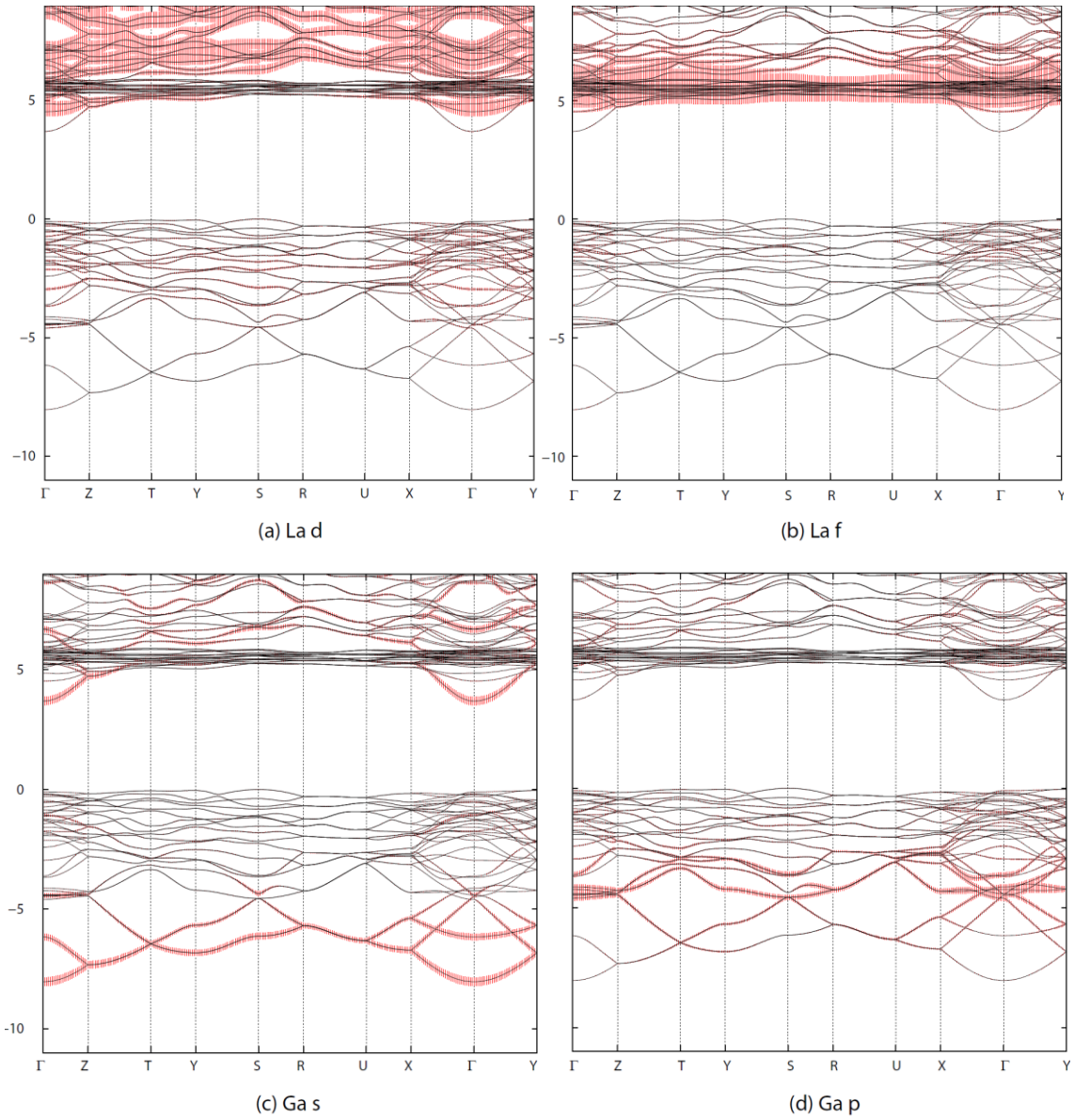

Figure 4.7 – Orbital projected band structures of *o*-$LaGaO_3$ to investigate the mixing of (a) La *f*, (b) La *d*, (c) Ga *s*, (d) Ga *p* and (e) O *p* states in the electronic structure of the perovskite.

Table 4.3 – Optimized lattice parameters of orthorhombic (*Pbnm*) and rhombohedral (*R3c*) $LaGaO_3$ (*o*-$LaGaO_3$ and *r*-$LaGaO_3$, respectively) and formation enthalpies obtained from theoretical calculations (SCAN, PBE and HSE06) and experiment [240,247,248]. O1 and O2 are the axial and equatorial oxygen atoms in the [GaO_6] octahedron, respectively. Experimental results in ref. [247] were measured at 298 K and 523 K for the orthorhombic and rhombohedral phases, respectively. Parameters in ref. [248] were measured at 11 K. The percentage difference between calculated results and experimental values is given in parenthesis.

Phase	**Parameter**	**SCAN**	**PBE**	**HSE06**	**Exp.**
o-$LaGaO_3$	*a* (Å)	5.520 (-0.07)	5.567 (+0.78)	5.512 (-0.22)	5.524 [247]
	b (Å)	5.511 (+0.35)	5.606 (+2.08)	5.523 (+0.56)	5.492 [247]
	c (Å)	7.795 (+0.27)	7.895 (+1.56)	7.793 (+0.24)	7.774 [247]
	V (Å^3)	237.16 (+0.54)	246.41 (+4.46)	273.27 (+15.85)	235.89 [247]
	Ga-O1 (Å)	1.990 (+0.61)	2.024 (+2.33)	1.992 (+0.71)	1.978 [248]
	Ga-O2 (Å)	1.984 (+0.56)	2.019 (+2.33)	1.987 (+0.71)	1.973 [248]
	Ga-O2 (Å)	1.987 (+0.61)	2.028 (+2.68)	1.992 (+0.86)	1.975 [248]
	La-O1 (Å)	2.399 (-0.42)	2.411 (+0.08)	2.400 (-0.37)	2.409 [248]
	La-O1 (Å)	2.605 (-0.72)	2.557 (-2.55)	2.562 (-2.36)	2.624 [248]
	La-O2 (Å)	2.442 (-1.05)	2.443 (-1.01)	2.440 (-1.13)	2.468 [248]
	La-O2 (Å)	2.627 (-0.08)	2.650 (+0.80)	2.619 (-0.38)	2.629 [248]
	La-O2 (Å)	2.808 (+0.36)	2.808 (+0.36)	2.788 (-0.36)	2.798 [248]
	ΔH_f (eV)	-15.50 (+1.37)	-13.63 (-10.86)	-	-15.29 [240]
r-$LaGaO_3$	*a* (Å)	5.537 (+0.02)	5.610 (+1.34)	5.545 (+0.16)	5.536 [247]
	c (Å)	13.361 (-0.28)	13.492 (+0.70)	13.347 (-0.38)	13.398 [247]
	V (Å^3)	354.72 (-0.75)	367.78 (+2.90)	355.41 (-0.56)	357.41 [247]
	ΔH_f (eV)	-15.50	-13.60	-	-

Table 4.4 – Optimized lattice parameters and formation enthalpies of monoclinic Ga_2O_3 ($C12/m1$, space group 12), hexagonal La_2O_3 ($P6_3/mmc$, space group 194) and monoclinic $La_4Ga_2O_9$ ($P12_1/c1$, space group 14) obtained from theoretical calculations (PBE and SCAN) and experiment. The percentage difference between calculated results and experimental values is given in parenthesis.

Compound	**Parameter**	**PBE**	**SCAN**	**Exp.**
Ga_2O_3	*a* (Å)	12.507 (+2.40)	12.276 (+0.51)	12.214 [240]
	b (Å)	3.103 (+2.17)	3.052 (+0.49)	3.037 [240]
	c (Å)	5.920 (+2.10)	5.838 (+0.69)	5.798 [240]
	V (Å^3)	223.24 (+6.90)	212.35 (+1.68)	208.84 [240]
	β (º)	103.73 (-0.10)	103.84 (+0.01)	103.83 [240]
	ΔH_f	-9.44 (-16.53)	-10.94 (-3.27)	-11.31 [240]
La_2O_3	*a* (Å)	3.939 (+0.05)	3.923 (-0.36)	3.937 [249]
	c (Å)	6.183 (+0.86)	6.121 (-0.15)	6.130 [249]
	V (Å^3)	83.13 (+1.01)	81.60 (-0.85)	82.30 [249]
	ΔH_f	-17.23 (-7.37)	-19.03 (2.31)	-18.60 [240]
$La_4Ga_2O_9$	*a* (Å)	8.017 (+0.56)	7.966 (-0.08)	7.972 [250]
	b (Å)	11.296 (+0.89)	11.209 (+0.12)	11.196 [250]
	c (Å)	11.781 (+1.40)	11.633 (+0.13)	11.618 [250]
	V (Å^3)	1007.3 (+3.02)	980.18 (+0.24)	977.80 [250]
	β (º)	109.25 (-0.19)	109.33 (-0.12)	109.46 [250]
	ΔH_f	-45.02 (-8.42)	-49.77 (+1.24)	-49.16 [240]

4.4 Thermodynamic stability field of $LaGaO_3$

The chemical potential limits, which determine the region of thermodynamic stability for the two crystallographic phases of $LaGaO_3$ (Figure 4.8, plotted using the code developed by Jackson [251]), were calculated using CPLAP [252], as outlined in Section 3.2.6.3. The coloured lines in Figure 4.8 represent the limits of the $LaGaO_3$ stability field, set by the formation energies of the perovskite and its competing phases (La_2O_3, Ga_2O_3 and $La_4Ga_2O_9$). A-D are the intersection points of the region of stability determined by these limits. The oxygen, lanthanum and gallium chemical potentials and the competing phases in each of the intersection points of the stability field for *o*-$LaGaO_3$ and *r*-$LaGaO_3$ are presented

in Table 4.5 and will be used to calculate the doping energies (Equation 3.3) for the considered divalent dopants in different chemical environments.

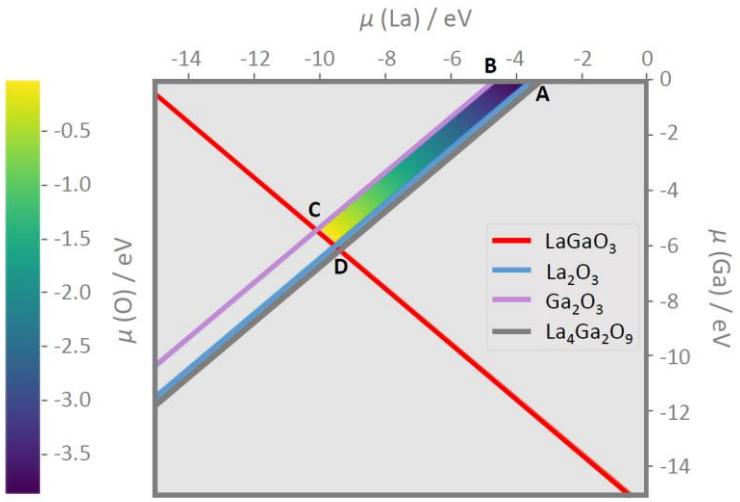

Figure 4.8 – Region of stability (coloured area) for *o*-$LaGaO_3$ spanned by $\Delta\mu_{La}$ and $\Delta\mu_{Ga}$ obtained from the formation energies calculated using the SCAN functional. A-D are the intersection points of the stability field determined by the limits set by the competing phases. Due to the similarity of *o*-$LaGaO_3$ and *r*-$LaGaO_3$ results, only the *o*-$LaGaO_3$ stability field is shown. The coloured bar on the left indicates how the oxygen chemical potential varies in different regions of the stability field.

Table 4.5 – Elemental chemical potentials for O, La and Ga, and competing phases at the A-D intersection points of the thermodynamic stability field of $LaGaO_3$, determined by the formation of its competing phases (Figure 4.8).

Competing Phases		***o*-$LaGaO_3$**			***r*-$LaGaO_3$**		
		$\Delta\mu_O$ (eV)	$\Delta\mu_{La}$ (eV)	$\Delta\mu_{Ga}$ (eV)	$\Delta\mu_O$ (eV)	$\Delta\mu_{La}$ (eV)	$\Delta\mu_{Ga}$ (eV)
A	La_2O_3	-3.989	-3.530	0.00	-3.991	-3.528	0.00
B	Ga_2O_3	-3.647	-4.557	0.00	-3.647	-4.559	0.00
C	Ga_2O_3, $LaGaO_3$	0.00	-10.027	-5.470	0.00	-10.029	-5.470
D	La_2O_3, $LaGaO_3$	0.00	-9.514	-5.983	0.00	-9.514	-5.986

4.5 Doping energy

E_{dop} (Equation 3.3) can be calculated at any point within the stability field of $LaGaO_3$ (Figure 4.8). Along the red line diagonal (C-D), $\Delta\mu_O$ and, consequently, $\Delta\mu_M$ are constant, (since $\Delta H_f(MO) = \Delta\mu_M + \Delta\mu_O$, as outlined in Section 3.2.6.3). E_{dop}, however, changes, depending on the variation of $\Delta\mu_{La}$ and $\Delta\mu_{Ga}$. Along the blue and purple lines (A-D and B-C directions), $\Delta\mu_O$ varies proportionally to changes in the $\Delta\mu_{La}$ and $\Delta\mu_{Ga}$ and hence E_{dop} is constant as the difference between $\Delta\mu_{La}$ and $\Delta\mu_{Ga}$ is constant along A-D (-5.98 eV) and B-C (-5.47 eV), indicating that the defect energy does not depend on $\Delta\mu_O$ (vacancy formation is not a redox process).

E_{dop} was calculated for the two sets of conditions determined by the formation of La_2O_3 (A-D direction) and Ga_2O_3 (B-C direction) as secondary phases, representing the limits of the perovskite's stability field. These chemical conditions will be referred to as La- and Ga-rich, respectively. By calculating the lowest energy configurations, it is possible to determine the preferable doping site, i.e., if a dopant will preferably go to the La or Ga site, and the most stable vacancy configuration with respect to the dopants. Accordingly, the lowest obtained E_{dop} values for both *o*-$LaGaO_3$ and *r*-$LaGaO_3$ in the distinct chemical environments are presented in Tables 4.6 and 4.7, respectively.

The CCV preferably occupies a NN position for most of the analysed dopants. The oxygen vacancy is effectively positively charged, since an anion is missing from the lattice, while the divalent dopants are 'less positive' than the trivalent host cations. Therefore, the vacancy would experience less electrostatic repulsion from the divalent dopant in a NN position, than it would from trivalent host cations. Consequently, the NN configuration is the most stable due to Coulombic effects. The exception is Ba-doping in *o*-$LaGaO_3$; the vacancy is NN to one of the dopants and NNN to the other. Ba(II) possess the biggest ionic radius (1.61 Å) among the analysed dopants, hence the CCV is pushed from a NN to a NN/NNN position due to steric effects overcoming electrostatic effects. A similar behaviour was observed by Lucid *et al.*[64] when investigating the doping of CeO_2 with trivalent cations; the CCV would preferably be in a NN position, except for dopants with ionic radii bigger than 1.09 Å. For those, the CCV would preferably be NNN to the dopants, as steric effects overcome coulombic effects.

Table 4.6 – Doping energies (eV) for *o*-$LaGaO_3$ under La- and Ga-rich chemical environments as a function of ionic radius (Å) [26] for La-site and Ga-site doping, along with the preferable doping site and most stable vacancy configuration. The ionic radii for Ga(III) (6-coordinated) and La(III) (12-coordinated) are 0.62 and 1.36 Å, respectively.

Dopant	**Ionic Radius (Å) 6-/12-coord.**		**E_{dop} (La-site dop.)**		**E_{dop} (Ga-site dop.)**		**Doping Site**	**CCV config.**
			La-rich	**Ga-rich**	**La-rich**	**Ga-rich**		
Ni(II)	0.69	-	7.09	6.06	2.98	4.01	Ga	NN
Sn(II)	0.69	-	4.48	3.45	3.43	4.46	Ga (La-rich) La (Ga-rich)	NN NN_A
Mg(II)	0.72	-	4.92	3.89	1.38	2.40	Ga	NN
Zn(II)	0.74	-	4.61	3.59	1.26	2.28	Ga	NN
Co(II)	0.74	-	4.68	3.65	1.12	2.15	Ga	NN
Fe(II)	0.78	-	4.30	3.28	1.08	2.11	Ga	NN
Pt(II)	0.80	-	6.74	5.71	1.56	2.59	Ga	NN
Mn(II)	0.83	-	3.83	2.80	1.45	2.48	Ga	NN
Pd(II)	0.86	-	6.30	5.27	1.67	2.70	Ga	NN
Ca(II)	1.00	1.34	2.25	1.22	3.92	4.95	La	NN_A
Sr(II)	1.18	1.44	1.33	0.30	6.32	7.34	La	NN_A
Pb(II)	1.19	1.49	3.13	2.11	4.76	5.78	La	NN_A
Ba(II)	1.35	1.61	1.34	0.31	8.63	9.66	La	NN/NNN

Steric effects also influence the preferential doping site; for both *o*-$LaGaO_3$ and *r*-$LaGaO_3$, dopants with smaller ionic radii (up to 0.86 Å) go to the Ga(III) (0.62 Å) site and dopants with bigger ionic radii go to the La(III) (1.36 Å) site. According to these criteria, Sn(II), with ionic radius of 0.81 Å, should preferably occupy the Ga site. However, the cation presents a distinct behaviour with its preferable doping site depending on the chemical environment, i.e., Sn(II) goes to the Ga site in La-rich environments, and to the La site under Ga-rich conditions. Even though tuning the thermodynamic conditions could influence its site selectivity, the observed E_{dop} values for Sn(II) are comparatively high, indicating the cation is not easily accepted into the perovskite lattice, which will lead to dopant segregation and hence would not be a good dopant choice.

Table 4.7 – Doping energies (eV) for *r*-$LaGaO_3$ under La- and Ga-rich chemical environments as a function of ionic radius (Å) [26] for La-site and Ga-site doping, along with the preferable doping site and most stable vacancy configuration. The ionic radii for Ga(III) (6-coordinated) and La(III) (12-coordinated) are 0.62 and 1.36 Å, respectively.

Dopant	**Ionic Radius (Å)**		**E_{dop} (La-site dop.)**		**E_{dop} (Ga-site dop.)**		**Doping**	**CCV**
	6-/12-coord.		**La-rich**	**Ga-rich**	**La-rich**	**Ga-rich**	**Site**	**config.**
Ni(II)	0.69	-	7.17	6.13	2.96	3.99	Ga	NN
Sn(II)	0.69	-	3.72	2.69	3.30	4.33	Ga (La-rich) La (Ga-rich)	NN NN_B
Mg(II)	0.72	-	4.83	3.79	1.33	2.36	Ga	NN
Zn(II)	0.74	-	4.67	3.63	1.24	2.27	Ga	NN
Co(II)	0.74	-	4.70	3.67	1.09	2.13	Ga	NN
Fe(II)	0.78	-	4.12	3.09	1.08	2.11	Ga	NN
Pt(II)	0.80	-	6.89	5.85	1.62	2.65	Ga	NN
Mn(II)	0.83	-	3.73	2.70	1.47	2.50	Ga	NN
Pd(II)	0.86	-	6.10	5.07	1.70	2.73	Ga	NN
Ca(II)	1.00	1.34	2.23	1.20	3.95	4.98	La	NN_B
Sr(II)	1.18	1.44	1.23	0.19	6.43	7.46	La	NN_B
Pb(II)	1.19	1.49	2.96	1.93	4.66	5.70	La	NN_B
Ba(II)	1.35	1.61	1.19	0.16	8.40	9.43	La	NN_B

The existence of an ideal ionic radius for dopants in perovskites and fluorite-structured materials has been previously suggested in literature [24,25,253]. Ideally sized dopants do not necessarily have the same ionic radius as the host cation, but rather a critical value, which is system dependent. For example, Kim [253] determined 1.04 Å as the critical ionic radius (r_c) for dopants in CeO_2, which would result neither in the contraction nor in the expansion of the host lattice. This value is larger than the ionic radii of 8-coordinated Ce(IV) (0.97 Å), showing that the critical value indeed differs from the size of the host cation. For ZrO_2, r_c = 0.95 Å, which is also bigger than the ionic radius of 8-coordinated Zr(IV) (0.84 Å) [24,25]. Accordingly, the magnitude of the doping energies presented in Tables 4.6 and 4.7 can be related to dopant size and the resulting distortions to the local structure.

For A-site dopants, the doping energy increases in the order Ba(II) < Sr(II) < Ca(II), with their ionic radii decreasing in the same order, confirming the relationship between doping energy and dopant size. Sr(II) and Ba(II) possess the lowest E_{dop} values, suggesting that the critical radius for A-site dopants in $LaGaO_3$ lies between 1.44 and 1.61 Å. Pb(II)

does not follow the observed steric trends due to electronic effects; while alkaline earth metals are spherical, Pb(II) has an asymmetric electron density. In fact, Pb(II) and Sn(II) present the highest doping energies among A- and B-site dopants, respectively. Their asymmetric electron density arises from the formation of a sterically active "lone pair" of electrons (ns^2 electron configuration). This effect is not actually a lone pair, but a result of the mixing between Sn 5*s*, 5*p* (or Pb 6*s*, 6*p*) and O 2*p* states, which can be observed in the total and partial electronic density of states for Sn-doped *o*-$LaGaO_3$ (Figure 4.9). Sn(II) 5*s* orbital at the top of the valence band interacts with O 2*p* states of same energy, resulting in bonding and antibonding combinations. The antibonding Sn(5*s*)-O(2*p*) orbital, can undergo further hybridization with Sn p_z states, resulting in the projection of the density one side of the Sn(II) forming the so called lone-pair [254–257]. The resulting asymmetric electron density contributes to the distortion of the lattice structure, and hence higher doping energies. This effect can be also observed in the valence charge density of a Sn(II) ion (Figure 4.10), where the asymmetric electron density around the Sn(II) cation points towards the vacancy.

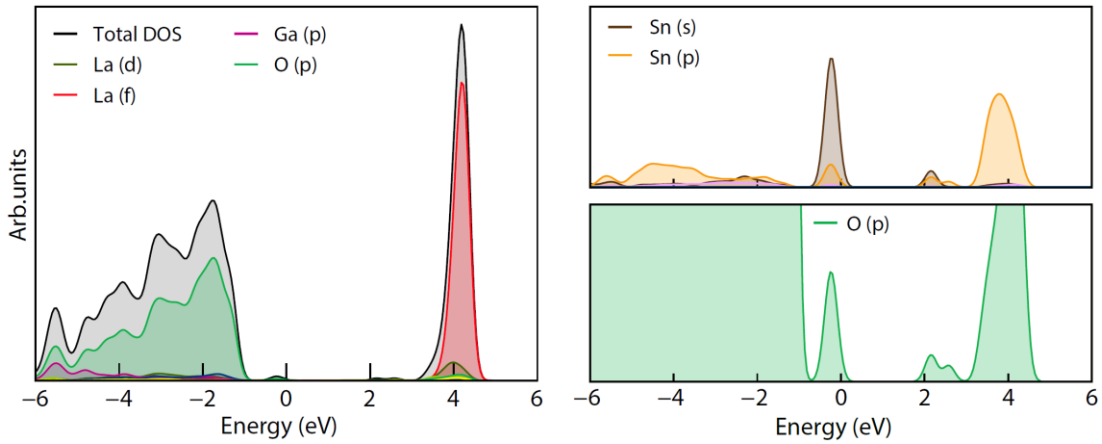

Figure 4.9 – (a) Total and partial electronic density of states for Sn-doped *o*-$LaGaO_3$ and (b) partial EDOS for Sn and O. Sn(II) 5*s* states are positioned at the top of the valence band, hybridizing with O 2*p* states of same energy, forming bonding and antibonding states. The mixing of these antibonding states with Sn(II) 5*p* orbitals results in lone pair formation and asymmetric electron density.

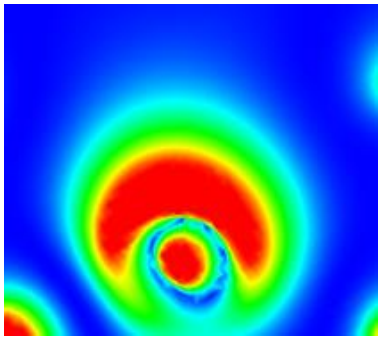

Figure 4.10 – Charge density at the top 1.5 eV of the valence band around a Sn(II) cation occupying a La-site in doped *o*-$LaGaO_3$. The vacancy is positioned right above the ion and the dopant asymmetric electron density due to lone-pair formation points towards the CCV. The charge density plot ranges from 0 (blue) to 0.15 e/Å^3 (red).

For B-site dopants, a steric trend in the doping energy magnitude is observed for some of the dopant ions; E_{dop} increases in the order Fe(II) < Co(II) < Zn(II) < Mg(II) < Ni(II), with their ionic radii decreasing in the same order. Since Fe(II) and Co(II) possess the lowest E_{dop} values, the ideal ionic radii for B-site dopants should be close to 0.74-0.78 Å. Mn(II), however, is larger than Fe(II) and hence possess ionic radius larger than r_c, presenting a higher doping energy as a result. Transition metals are not spherical due to their partially filled *d* orbitals, and hence small deviations from E_{dop} size dependence would be expected, as different metals have different *d* orbital filling. Even though Zn(II) and Co(II) have the same ionic radius (0.74 Å), different orbital occupations (they are d^{10} and d^7 ions, respectively) result in distinct doping energies. Furthermore, high E_{dop} values are observed for Pd(II) and Pt(II); they are d^8 ions which favourably adopt square planar structures due to crystal field effects (as previously seen in doped CeO_2 [258,259]) and hence would not favour octahedral coordination. Therefore, our results suggest that while steric effects are important, they do not fully describe the E_{dop} magnitude for B-site dopants, as these 3*d* metals are not perfectly spherical and doping energies are also influenced by electronic structure effects.

In summary, from the values presented in Tables 4.6 and 4.7, Sr(II) and Ba(II) possess the lowest E_{dop} values among La-site dopants, while Fe(II) and Co(II) present the lowest energies among Ga-site dopants, indicating that these cations would be easily accepted into the lattice and dopant segregation would be low. However, a low doping

energy alone does not characterize a good dopant, since doping also affects the mobility of CCVs, i.e., the metal cations could still trap vacancies around them due to defect-defect interactions and hence negatively affect vacancy mobility. Therefore, the short- and long-range association energies (E_{ass}^{SR} and E_{ass}^{LR}, respectively) were calculated to evaluate the tendency of the CCVs to be trapped around the dopants.

4.6 Association energy

The short- (E_{ass}^{SR}) and long-range (E_{ass}^{LR}) association energies indicate the tendency of CCVs to be trapped around the dopants in regions of uniform or non-uniform/low dopant concentrations, respectively [64]. While E_{ass}^{SR} quantifies how easily the CCV can move from a NN to a NNN site, E_{ass}^{LR} is calculated from the energy difference between the structure in which the vacancy is positioned far away from the dopants, i.e. in a pure $LaGaO_3$ region, and the lowest energy NN configuration (NNN for Ba). The obtained E_{ass}^{SR} and E_{ass}^{LR} values for *o*-$LaGaO_3$ and *r*-$LaGaO_3$ are presented in Table 4.8. Since E_{ass}^{SR} and E_{ass}^{LR} are calculated by the difference between E_{dop} values for distinct vacancy configurations, they do not depend on chemical environment, i.e., they are the same for both La- and Ga-rich environments.

E_{ass}^{SR} and E_{ass}^{LR} values do not necessarily increase/decrease with ionic radii, i.e., no trend related to steric effects was observed. For La-site doping, Sr(II), Ba(II) and Ca(II) possess the lowest E_{ass}^{SR} and E_{ass}^{LR}, indicating that vacancies do not tend to be trapped around these metals. Short-range association energies are lower than the long-range values, revealing that vacancies are more likely to be trapped around dopants in regions of non-uniform or low dopant concentration. Pb(II) and Sn(II) possess the highest E_{ass}^{SR} and E_{ass}^{LR} values, meaning that vacancies would be trapped, which could negatively affect the ionic conductivity of the perovskite. For Ga-site doping, Mg(II) possess the lowest E_{ass}^{SR} and E_{ass}^{LR}values, followed by Ni(II), Co(II), Fe(II), Zn(II) and Mn(II). Those could all be good Ga-site dopant choices, since they are not expected to negatively affect the mobility of vacancies. Sn(II), Pd(II) and Pt(II) have the highest E_{ass}^{SR} and E_{ass}^{LR}values, indicating a higher tendency to vacancy trapping.

Table 4.8 – Short- and long-range association energies (E_{ass}^{SR} and E_{ass}^{LR}, respectively) in eV for the considered dopants in *o*-$LaGaO_3$ and *r*-$LaGaO_3$

	Dopant	***o*-LaGaO₃**		***r*-LaGaO₃**	
		E_{ass}^{SR}	E_{ass}^{LR}	E_{ass}^{SR}	E_{ass}^{LR}
Ga-site dopants	Ni(II)	0.39	0.58	0.38	0.65
	Sn(II)	2.92	3.28	3.11	3.43
	Mg(II)	0.25	0.44	0.25	0.52
	Zn(II)	0.95	1.22	0.99	1.33
	Co(II)	0.63	0.86	0.69	0.98
	Fe(II)	0.90	0.90	0.90	0.89
	Pt(II)	4.67	4.66	4.70	4.67
	Mn(II)	0.91	1.28	1.31	1.76
	Pd(II)	4.68	4.65	4.67	4.66
La-site dopants	Sn(II)	1.06	1.08	1.70	1.77
	Ca(II)	0.46	0.53	0.51	0.60
	Sr(II)	0.36	0.42	0.35	0.41
	Pb(II)	0.74	0.80	0.75	0.82
	Ba(II)	0.40	0.43	0.36	0.38

4.7 Structural distortions

Doping introduces distortions to the local structure of the perovskite as a result of both steric and electronic effects, which can affect the magnitude of the calculated doping and association energies. Lucid *et al.* [64] observed that distortions in the local structure of doped CeO_2 are mainly a result of dopants trying to reach similar M(III)-O bond lengths and coordination environments to those observed in their native oxides. Here, comparable structural distortion occurs, which can result in higher E_{ass}^{SR} and E_{ass}^{LR} values, increasing the likelihood of vacancies being trapped. Figure 4.11 shows the distortion in the local structure around the dopants due to changes in the M-O bond length when compared to the pure *o*-$LaGaO_3$ structure. The calculated M(II)-O distances for Ga-site dopants in a NN configuration in *o*-$LaGaO_3$ are presented in Table 4.9, along with the bond distances observed in the metals' native oxides. Figure 4.11a clarifies the nomenclature used in Table 4.9.

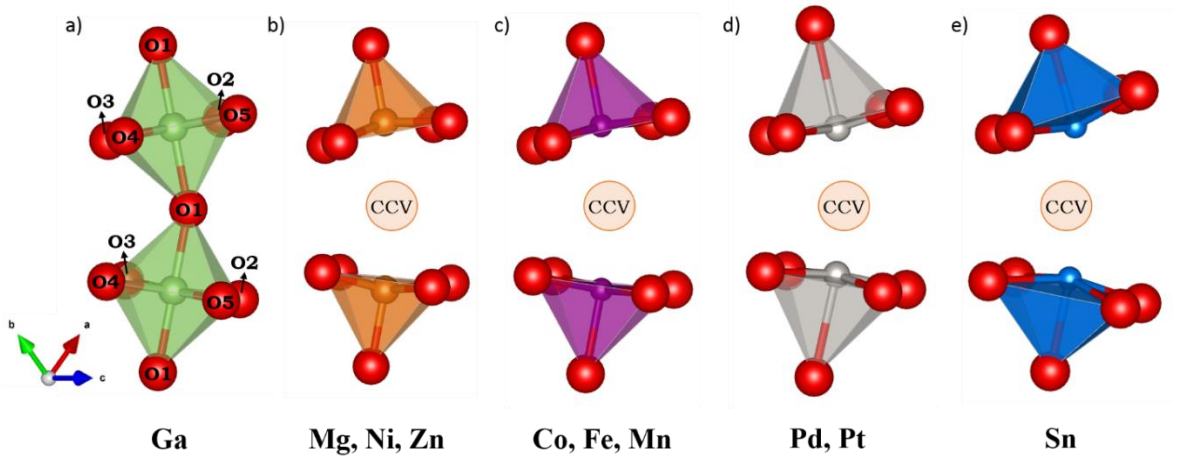

Figure 4.11– a) Local GaO_6 structure in pure *o*-$LaGaO_3$, with Ga(III) ions in green and oxygen ions in red, and schematic representation of the structural distortion when b) Mg(II), Ni(II), Zn(II) (in orange), c) Co(II), Fe(II), Mn(II) (in purple), d) Pd(II), Pt(II) (in grey) and e) Sn(II) (in blue) are used as dopants. The schemes display the NN vacancy configuration, in which the charge compensating vacancy is located between two dopant cations.

Mg(II) and Ni(II) are the dopants that introduce the least amount of distortion in the local structure of the perovskite, and hence present the lowest association energies. The equatorial M-O bond lengths in these systems are similar to those observed for Ga-O, while the axial M-O bond length decreases (1.92 Å and 1.94 Å for Mg(II) and Ni(II), respectively) when compared to the original Ga-O distance, as a way of compensating for the oxygen vacancy in the opposite axial position of the octahedron. The shortening of the axial bond in these systems can be observed in Figure 4.11b. Zn(II), on the other hand, despite possessing similar ionic radius to Mg(II) and Ni(II), presents higher association energy values; while both Mg(II) and Ni(II) have the octahedral coordination environment of their native oxides reproduced in the perovskite, zinc is tetrahedrally coordinated in ZnO. The distortion around Co(II) and Fe(II) is more substantial; their longest M-O distances are 2.04 Å and 2.06 Å (Figure 4.11c) resulting in slightly bigger E_{ass}^{SR} and E_{ass}^{LR}. Nonetheless, their association energy values are still lower than 1.00 eV, since the octahedral geometry expected for d^6 (Fe(II)) and d^7 (Co(II)) metals is being reproduced in this system. Mn(II) is a d^5 ion and hence does not favour a particular coordination arrangement – the observed distortions are similar to those in Fe- and Co-doped systems (Figure 4.11c). However, Mn(II) presents

higher association energies, likely due to the difference in size in comparison to the host cation.

Table 4.9 – M-O bond lengths within the MO_6 octahedra (in Å) for Ga-site dopants in a NN configuration in *o*-$LaGaO_3$, along with experimental bond lengths in their native MO oxides.

Dopant	**O1**	**O2**	**O3**	**O4**	**O5**	**M-O bond length in native oxide**	**M(II) coordination in MO**
Ga	1.98	1.98	1.99	1.98	1.99	-	-
Ni_1	1.94	1.99	2.00	2.00	2.00	2.09 Å [260]	6-coordinated
Ni_2	1.94	2.00	2.01	1.99	1.99		octahedral
Sn_1	2.18	2.18	2.21	2.19	2.17	2.21 Å [261]	4-coordinated
Sn_2	2.17	2.17	2.19	2.16	2.16		pyramidal
Mg_1	1.92	2.00	2.00	2.00	2.01	2.11 Å [262]	6-coordinated
Mg_2	1.92	2.00	2.01	2.00	2.00		octahedral
Zn_1	1.96	2.01	2.02	2.02	2.03	1.98 Å [263]	4-coordinated
Zn_2	1.96	2.03	2.04	2.02	2.02		tetrahedral
Co_1	2.00	1.99	2.02	2.03	2.00	2.12 Å [264]	6-coordinated
Co_2	2.02	2.00	2.04	2.00	1.98		octahedral
Fe_1	2.05	2.06	2.02	2.04	2.00	2.15 Å [265]	6-coordinated
Fe_2	2.10	1.99	2.00	1.99	1.99		octahedral
Pt_1	2.45	2.01	2.03	2.03	2.01	2.02 Å [261]	4-coordinated
Pt_2	2.45	2.01	2.03	2.02	2.01		square planar
Mn_1	2.04	2.05	2.06	2.06	2.06	2.25 Å [266,267]	6-coordinated
Mn_2	2.04	2.05	2.06	2.06	2.06		octahedral
Pd_1	2.39	2.00	2.02	2.01	2.01	2.02 Å [268,269]	4-coordinated
Pd_2	2.39	2.00	2.02	2.01	2.01		square planar

Pd(II), Pt(II) and Sn(II), which possess the highest association energy values, are the dopants that introduce the biggest local distortions to the perovskite lattice. While the longest Ga-O distance within the GaO_6 octahedron in pure *o*-$LaGaO_3$ is 1.99 Å, the Pd-O, Pt-O and Sn-O distances can be as high as 2.39, 2.45 and 2.21 Å, respectively (Table 4.9). The observed structural distortions in Pd- and Pt-doped *o*-$LaGaO_3$ are due to the elongation of the axial M-O bonds, a result of Pt/Pd ions moving out of the plane towards the CCV as an attempt to assume a square planar geometry (Figure 4.11d). For these systems, the NNN and

far configurations are energetically unfavourable, since the presence of all NN oxygen ions in the octahedra impedes the formation of the stable square planar structure commonly observed for the d^8 metal cations. The equatorial Pt/Pd-O bond distances remain at around 2.00-2.03 Å (Table 4.9), similar to those observed in their native oxides, PtO and PdO (2.02 Å [261,266,267]).

The local structure around Sn(II) ions (Figure 8e) have similar bond lengths to that observed in its native oxide, SnO (2.21 Å [261,270]); the cation moves considerably within the octahedron towards the CCV, resulting in the elongation of the Sn-O bond. The observed lattice distortion and the decreased mobility of vacancies is also due to electronic effects; Sn(II) possesses an asymmetric electron density pointing towards the vacancy (Figure 4.10), which stabilizes the Sn-O bonds and decreases the mobility of the oxygen vacancy, resulting in comparatively high association energies. Our results suggest that the distortion of the local structure, displayed in Figure 4.11, which in turn is related to the metal's electronic structure and preferential coordination environment, can be a good indicator of the magnitude of E_{ass}^{SR} and E_{ass}^{LR} values and hence the tendency for vacancies to be trapped.

At the 12-coordinated La-site, the spherical alkaline earth metals, Sr(II), Ca(II) and Ba(II) introduce similar and small distortions to the local structure of the perovskite with the M-O bond lengths slightly elongated when compared to the original La-O bonds, due to their difference in size to the host cation. Pb(II) ($6s^2$ electron configuration), on the other hand, possesses an asymmetric electron density due to lone pair formation pointing towards the CCV, resulting in bigger distortions and hence high association energy values in comparison to other La-site dopants.

Tables 4.10 and 4.11 summarize the obtained results for *o*-$LaGaO_3$ and *r*-$LaGaO_3$, respectively. The doping energy indicates how easily a dopant cation would be accepted in the perovskite lattice and was calculated under distinct chemical environments. The short- and long-range association energies quantify how easily the CCV can move from NN to NNN or to a far away site, respectively, indicating the tendency of vacancies to be trapped around the dopants. Accordingly, the best-suited dopants are those with low E_{dop}, E_{ass}^{SR} and E_{ass}^{LR} values. Cations with E_{dop} smaller than 1.4 eV, associated with E_{ass}^{SR} and E_{ass}^{LR} smaller than 0.6 eV were considered the best dopant choices when considering SOFC applications. These criteria were selected to provide a suitable framework for comparing the analysed dopants.

Table 4.10 – Summary of the ionic radii (in Å), doping energies (E_{dop}, in eV), short- and long-range association energies (in eV) for *o*-$LaGaO_3$. Values in bold correspond to results within selected criteria. The ionic radii for Ga(III) (6-coordinated) and La(III) (12-coordinated) are 0.62 and 1.36 Å [26], respectively.

Dopant site	**Dopant**	**Ionic Radius 6-/12-coord.**		**E_{dop} La-Rich**	**E_{dop} Ga-Rich**	E_{ass}^{SR}	E_{ass}^{LR}
Ga-site	Ni(II)	0.69	-	2.98	4.01	**0.39**	**0.58**
dopants	Sn(II)	0.69	-	3.43	4.46	2.92	3.28
	Mg(II)	0.72	-	**1.38**	2.40	**0.25**	**0.44**
	Zn(II)	0.74	-	**1.26**	2.28	0.95	1.22
	Co(II)	0.74	-	**1.12**	2.15	0.63	0.86
	Fe(II)	0.78	-	**1.08**	2.11	0.9	0.9
	Pt(II)	0.80	-	1.56	2.59	4.67	4.66
	Mn(II)	0.83	-	1.45	2.48	0.98	1.28
	Pd(II)	0.86	-	1.67	2.70	1.94	4.65
La-site	Sn(II)	0.69	-	4.48	3.45	1.06	1.08
dopants	Ca(II)	1.00	1.34	2.25	**1.22**	**0.46**	**0.53**
	Sr(II)	1.18	1.44	**1.33**	**0.30**	**0.36**	**0.42**
	Pb(II)	1.19	1.49	3.13	2.11	0.74	0.8
	Ba(II)	1.35	1.61	**1.34**	**0.31**	**0.40**	**0.43**

Table 4.11 – Summary of the ionic radii (in Å), doping energies (E_{dop}, in eV), short- and long-range association energies (in eV) for *r*-$LaGaO_3$. Values in bold correspond to results within selected criteria. The ionic radii for Ga(III) (6-coordinated) and La(III) (12-coordinated) are 0.62 and 1.36 Å [26], respectively.

Dopant site	**Dopant**	**Ionic Radius 6-/12-coord.**		**E_{dop} La-Rich**	**E_{dop} Ga-Rich**	**E_{ass}^{SR}**	**E_{ass}^{LR}**
Ga-site dopants	Ni(II)	0.69	-	2.96	3.99	**0.38**	0.65
	Sn(II)	0.69	-	3.30	4.33	3.11	3.43
	Mg(II)	0.72	-	**1.33**	2.36	**0.25**	**0.52**
	Zn(II)	0.74	-	**1.24**	2.27	0.99	1.33
	Co(II)	0.74	-	**1.09**	2.13	0.69	0.98
	Fe(II)	0.78	-	**1.08**	2.11	0.9	0.89
	Pt(II)	0.80	-	1.62	2.65	4.70	4.67
	Mn(II)	0.83	-	1.47	2.50	1.31	1.76
	Pd(II)	0.86	-	1.70	2.73	4.67	4.66
La-site dopants	Sn(II)	0.69	-	3.72	2.69	1.70	1.77
	Ca(II)	1.00	1.34	2.23	**1.20**	**0.51**	**0.6**
	Sr(II)	1.18	1.44	**1.23**	**0.19**	**0.35**	**0.41**
	Pb(II)	1.19	1.49	2.96	1.93	0.75	0.82
	Ba(II)	1.35	1.61	**1.19**	**0.16**	**0.36**	**0.38**

The best Ga-site dopant for both perovskite lattices according to the selected criteria would be Mg(II). This is the only dopant to present low E_{dop} (under Ga-poor conditions) associated with small E_{ass}^{SR} and E_{ass}^{LR} values, indicating that it would be easily incorporated into the Ga site of the lattice and that vacancies would not be trapped around the cation. Ni(II), Co(II), Fe(II) and Zn(II) also possess low association energies. This indicates low tendency to vacancy trapping and hence could yield some improvement to the ionic conduction properties of the perovskite considering electrode applications, since transition metal doping in $LaGaO_3$ has been reported to generate mixed ionic and electronic conduction [178,180]. These metals possess lower doping and association energy values when compared to Mn(II), which has been previously suggested as a suitable co-dopant (LSGMn) for anode applications [178]. Zn(II) and Fe(II) also possess doping energies lower than those of Mg(II). Ni(II), however, presents high E_{dop} values when compared to the other transition metals.

Sn(II), Pt(II) and Pd(II) are the dopants to introduce the biggest distortions to the perovskite lattice, hence possessing high E_{dop}, E_{ass}^{SR} and E_{ass}^{LR}, and being poor dopant choices.

The best La-site dopants would be Ca(II), Sr(II) and Ba(II), with Sr(II) and Ba(II) presenting the lowest E_{dop}, E_{ass}^{SR} and E_{ass}^{LR} values for *o*-$LaGaO_3$ and *r*-$LaGaO_3$, respectively. Sr(II) and Ba(II) are also the only dopants observed to have low E_{dop} under both La-rich and Ga-rich chemical environments. Since the chosen environments correspond to the extremes in the $LaGaO_3$ stability field, these cations would be good dopant choices in all chemical conditions under which the perovskite is stable.

4.8 A-site co-doping

Co-doping of the same cation site has been suggested to improve the ionic conductivity in CeO_2-based systems [271–276] when compared to singly doped phases. This co-doping effect has been related to the correspondence between the average ionic radius of the chosen dopants to an ideal dopant ionic radius [272,274,276,277], i.e., dopants are chosen purposefully to reproduce r_c, which minimizes local strains, distortions and hence defect interactions, driving the improvement of ionic conduction properties [278,279]. To gain more insight into the critical radius for La-doping in the $LaGaO_3$ system, SCAN calculations were performed for both the Ca/Sr co-doped system, considering the ionic radii of the dopants are smaller/bigger than that of La(III), and the Sr/Ba co-doped perovskite, as these resulted in the lowest E_{dop}, E_{ass}^{SR} and E_{ass}^{LR} values for singly doped systems. The calculated doping and association energies for both *o*- and *r*-$LaGaO_3$ are presented in Table 4.12.

The doping and association energies of Ca/Sr phases are in between Sr-doped and Ca-doped values. Therefore, Ca/Sr co-doping does not yield significant improvements, confirming that selecting dopants according to the closeness of their average ionic radii to the host cations is not the most appropriate strategy for the improvement of ionic conduction properties of $LaGaO_3$-based systems. Sr/Ba co-doped *o*-$LaGaO_3$ adopts the same vacancy configuration as the Ba-doped perovskite (NN/NNN) rather than that of the Sr-doped system, due to steric effects, i.e., the bigger size of Ba(II) pushes the vacancy away. No significant

difference was observed among doping energies for the Sr/Ba-, Sr- and Ba-doped *o*-$LaGaO_3$ systems; E_{dop} values remained in the already low 0.30-0.32 eV range for co-doped systems.

Table 4.12 – Ionic radii (in Å), doping energies (E_{dop}, in eV), short- and long-range association energies (in eV) for singly and co-doped *o*-$LaGaO_3$ and *r*-$LaGaO_3$. The ionic radii for La(III) (12-coordinated) is 1.36 Å [26].

System	Dopant	Ionic Radius 12-coordinated	E_{dop} Ga-Rich	Vacancy Position	E_{ass}^{SR}	E_{ass}^{LR}
o-$LaGaO_3$	Ca(II)	1.34	1.22	NN_A	0.46	0.53
	Sr(II)	1.44	0.30	NN_A	0.36	0.42
	Ba(II)	1.61	0.31	NN/NNN	0.40	0.43
	Ca(II)/Sr(II)	1.39 (average)	0.74	NN_A	0.44	0.51
	Sr(II)/Ba(II)	1.52 (average)	0.32	NN/NNN	0.27	0.36
r-$LaGaO_3$	Ca(II)	1.34	1.20	NN_B	0.51	0.60
	Sr(II)	1.44	0.19	NN_B	0.35	0.41
	Ba(II)	1.61	0.16	NN_B	0.36	0.38
	Ca(II)/Sr(II)	1.39 (average)	0.74	NN_B	0.38	0.46
	Sr(II)/Ba(II)	1.52 (average)	0.09	NN_B	0.45	0.50

For *r*-$LaGaO_3$, the same vacancy configuration (the NN_B position) is the most energetically stable for Sr/Ba-, Sr- and Ba-doped systems, and a significant decrease in the doping energy was observed for the co-doped perovskite. The calculated association energies for the Sr/Ba co-doped *o*-$LaGaO_3$ system are smaller than the values observed for the singly doped phases, indicating less tendency to trap vacancies in the co-doped perovskite in comparison to Sr- and Ba-doped systems. This suggests that the critical ionic radius for La-site doping in the *o*-$LaGaO_3$ system is close to the average size between Sr(II) and Ba(II) (1.52 Å). The same trend was not observed for E_{ass}^{SR} and E_{ass}^{LR} values in Sr/Ba co-doped *r*-$LaGaO_3$, indicating that the rhombohedral system might possess a different critical ionic radius for doping.

These results indicate that simply reproducing the ionic radius of the host cation through co-doping does not improve ionic conduction; a larger ionic radius might be ideal, due to the presence of an oxygen vacancy nearest neighbour to the dopants. Our results suggest that if the average size of the chosen dopants does not match the ideal ionic radius,

a simple average of the properties of singly doped systems will be observed, as in the Ca/Sr co-doped perovskite. However, if the average dopant size is indeed close to the ideal value, as in Sr/Ba co-doped *o*-$LaGaO_3$, association energies should be improved in comparison to singly doped systems, improving ionic conduction properties.

4.9 Conclusion

DFT calculations were performed to investigate the effects of a range of divalent dopants (Ni(II), Sn(II), Mg(II), Zn(II), Co(II), Fe(II), Pt(II), Mn(II), Pd(II), Ca(II), Sr(II), Pb(II) and Ba(II)) in the defect chemistry of the $LaGaO_3$, aiming to determine which dopants would yield the greatest ionic conductivity improvements in the perovskite and the reasons behind such improvements. The lowest energy structure for each doped system was used to determine the preferable dopant position (La or Ga site), the preferable vacancy position, and calculate the association energy between vacancies and dopants. Steric effects determine the preferential doping site for most dopants, with Ca(II), Sr(II), Pb(II) and Ba(II) preferably occupying the La site of the perovskite, and Mg(II), Zn(II), Co(II), Fe(II), Ni(II), Mn(II), Pt(II) and Pt(II) preferably going to the smaller Ga site. Sn(II) presents dual behaviour, i.e. it can go to both La and Ga sites depending on the chemical environment due to electronic effects. The preferred vacancy configuration for the investigated divalent dopants is a NN position, as a result of coulombic effects. For A-site dopants, the majority of the doping energies were observed to vary according to the dopants' ionic radii, with the lowest values being observed for Sr(II) and Ba(II). In the case of Pb(II), electronic factors associated with its lone pair result in a higher doping energy. For B-site dopants, the magnitude of the doping energies is strongly influenced by steric effects; however, electronic effects also play a role, as transition metals are not perfectly spherical due to their partially filled *d* orbitals. In particular, Sn(II) lone pair formation results in much higher doping energies than its size would suggest. For Pd(II) and Pt(II), their electronic structure strongly favours a square planar configuration, which results in a high doping energy as the lattice is strongly distorted. Among the B-site dopants, Fe(II) and Co(II) presented the lowest values. Pd(II), Sn(II) and Pt(II) are the dopants to introduce the most significant local distortions to the perovskite lattice and hence present the highest association energies, indicating that vacancies would be trapped around these metals, maintaining the stabilizing distortion around the dopant. Transition metal doping (Ni(II), Co(II), Fe(II) and Zn(II)) can potentially generate mixed

ionic and electronic conduction in the perovskite, making it suitable as electrode instead of electrolyte. However, despite its good association energies, Ni(II) presents high doping energy values. Among the investigated cations, Sr(II), Ba(II) and Mg(II) doping should result in the greatest improvements to the ionic conductivity of $LaGaO_3$ according to the selected criteria, considering electrolyte applications. Sr/Ba co-doping was observed to further decrease the tendency of *o*-$LaGaO_3$ systems to vacancy trapping, which might be beneficial to ionic conduction properties. To the best of our knowledge, co-doping of a single site in $LaGaO_3$ has not been previously investigated by means of DFT calculations. Even though the most utilized dopants in literature are Sr and Mg, our results indicate that Sr and Ba co-doping of the A-site, along with Mg-doping on the B-site could potentially have a more positive influence in ionic conduction properties.

Chapter 5
Molecular dynamics study of Sr- and Mg-doped $LaGaO_3$

5.1 Introduction

$LaGaO_3$-based systems are an attractive alternative to fluorite-structured electrolyte materials in SOFCs (such as YSZ and doped CeO_2), as outlined in Chapter 4. $LaGaO_3$ co-doped with Sr(II) and Mg(II) in the La- and Ga-sites (LSGM), respectively, is a pure ionic conductor in the intermediate temperature SOFC operation range (873-1073 K) and over a wide oxygen partial pressure interval (from 1 to 10^{-22} atm) [16,70–74]. Molecular dynamics can provide a detailed understanding of LSGM dynamical properties, such as ionic conductivity, activation energies of diffusion and defect interactions, in contrast to quantum mechanical methods, which investigate attributes arising from the system's electronic structure. MD simulations generally rely on the use of interatomic potentials (IPs, also known as force fields), i.e. a mathematical model that describes the interactions between the system's particles, as described in Section 2.3. Hence, the accuracy of molecular dynamics results strongly depends on the IP's functional form and on how well it describes the interaction between distinct atomic species.

The force fields available in literature to study $LaGaO_3$-based systems are empirically derived, i.e. parameters are chosen to reproduce specific experimental properties, such as lattice constants within a specific temperature range [280], and take into account a single crystallographic phase of the material, usually the orthorhombic (*Pbnm*) [11]. Furthermore, these IPs are often composed of parameters extracted from different sources [281], resulting in force fields that are inconsistent and incapable of correctly reproducing effects arising from the different coordination environments experienced by the atoms. Due to their lack of transferability, such IPs do not satisfactorily describe the system's behaviour in different conditions and thermodynamics states, such as distinct crystallographic phases ($LaGaO_3$ undergoes phase transition from orthorhombic to rhombohedral around 420 K and from rhombohedral to cubic above 1200 K, with space groups *Pbnm*, *R3c* and *Pm3m*, respectively), bulk systems, surfaces or grain boundaries, for

example. Alternatively, first principles DFT calculations can be used to theoretically parametrize a force field through a force-matching procedure, in which the forces, stresses and multipoles calculated by the interatomic potential are fitted to DFT values. The inclusion of DFT dipoles from maximally localised Wannier functions in the IP parametrization, allows the incorporation of polarizability effects to the force field. Furthermore, the consideration of non-equilibrium DFT structures can account for the range of coordination environments present within the system. This theoretical parametrization approach yields force fields of *ab initio* accuracy, with a higher degree of transferability [136,137].

5.1.1 Previous studies

Experimentally, there is some debate regarding which dopant concentration yields the highest ionic conductivity (σ) values for $LaGaO_3$-based systems. Still, LSGM presents the highest conductivities among oxide-ion conductors for solid electrolyte applications. There is also some disagreement regarding LSGM crystal structure, which has been reported as orthorhombic [68,282–286], cubic [74,282,287,288], rhombohedral [282,286] and monoclinic [285,289] under IT-SOFC operating conditions. Even though no clear correlation between dopant concentration and crystal structure has been consistently observed, some studies have proposed that increasing dopant (and hence vacancy) concentration changes the structure from orthorhombic to rhombohedral and from rhombohedral to cubic [282], as an increased dopant content results in the presence of more oxygen deficient GaO_6 octahedra, affecting their tilting and hence the perovskite's crystallographic phase. ^{17}O NMR chemical shifts are sensitive enough to distinguish between oxygen atoms in equatorial and axial positions, revealing that oxygen deficient octahedra adopt a heavily distorted square pyramidal geometry (with the Ga-O axial bond length opposite to the vacancy being shortened), which might influence on structural transitions [282].

The ionic conductivity of LSGM is experimentally observed to increase with dopant content [290]. Drops in σ values are due to the formation of secondary phases at higher dopant concentrations; the formation of $LaSrGaO_4$ [74,283] and $LaSrGa_3O_7$ [74,284,290,291] have been reported for Sr-doped samples, while $La_4Ga_2O_9$ [284] has been observed for Mg-doped samples. In contrast, the ionic conduction properties of fluorite-structured materials is known to be influenced by vacancy ordering [11,68,292]. The

solubility limit of Sr(II) and Mg(II) in the A- and B-site sublattices of singly-doped $LaGaO_3$ is 10 mol% and 20 mol%, respectively. Sr(II) solubility is enhanced to 20 mol% through co-doping with Mg(II) due to the lattice expansion resulting from Mg-substitution [291]; single phase LSGM2020 was successfully synthesized [290]. Optimized compositions of LSGM present ionic conductivity in the 93-166 S cm^{-1} range at 1073 K, higher than those observed for ceramics with a fluorite-type structure at the same temperature [2,70–74]. The magnitude of σ values is strongly influenced by the variety of synthetic methods and sintering temperatures used in literature [283]. Sintering temperatures in the 1573-1873 K interval yield LSGM1020 samples with densities in the 5.01-6.58 g cm^{-3} range (lower than the theoretical density of 6.849 g cm^{-3}), which in turn present ionic conductivity values between 33.9 and 107 mS cm^{-1} at 1073 K, with higher σ values being obtained for higher sample densities [293].

The dopant concentrations yielding the highest ionic conductivity values are observed to change with temperature. At 1073 K, the highest σ values are obtained for both *x* and *y* ranging between 12.5 and 25 mol% [74]. When the temperature is lowered to 973 K, the optimal dopant concentration range shrinks differently for Sr and Mg; optimal *x* values are between 15 and 20 mol%, while optimal *y* values are between 12.5 and 17.5 mol%. At 878 K, these ranges diminish further, with optimal *x* ranging between 14.5 and 16 mol%, and *y* between 0 and 6 mol%. Such anisotropic shrinkage reveals that the ionic conductivity and the activation energy of diffusion depend differently on *x* and *y* [74]. Activation energy (E_a) values are believed to depend on the ionic radius of dopant cations, which can change the space available to oxide-ion transport [290]. Higher values are usually measured for higher dopant concentrations, as their bigger ionic radius with respect to the host cations decrease the space available for oxide-ion transport [290]. E_a is observed to increase with increasing Mg content, due to the larger ionic radius of 6-coordinated Mg(II) (0.72 Å [26]) when compared to Ga(III) (0.62 Å [26]) [290,291]. For a fixed Mg concentration, E_a did not change significantly with varying Sr content (less than 0.06 eV variation among samples with x = 0.00, 0.10 and 0.20). This is a result of the smaller difference between the ionic radii of 12-coordinated Sr(II) (1.44 Å [26]) and La(III) (1.36 Å [26]) [74,290], and to the fact that a bigger A-site cation increases the perovskite's Goldschmidt tolerance factor (Equation 1.5), influencing octahedra tilting and relieving the compressive strain on nearest neighbour Ga-O-Ga bonds.

There are two distinct activation energy regimes, below and above a critical temperature (T*), which has been reported to be within the 700-873 K range [74,282]. It was believed that below T*, vacancies were condensed into clusters, which would be detrimental to the ionic conductivity and increase the activation energy, with both LSGM dopants having been reported to act as nucleating centres to the formation of such clusters with decreasing temperature [74]. However, a more recent study [282] analysing the first order quadrupole splitting of ^{71}Ga, ^{25}Mg and ^{17}O NMR spectra in the 100-670 K range for LSGM (with $x = y$ = 0, 5, 10, 15, 20 mol%) has revealed that below T* vacancies (V_O) are preferentially trapped in Ga-V_O-Ga sites, with the presence of two adjacent vacancies being highly unlikely. Hence, vacancy clustering does not occur, but instead they are trapped between oxygen deficient octahedra [282]. Another combined experimental (^{15}Mg and ^{71}Ga NMR) and theoretical (DFT PBE doping energies) study confirmed that at room temperature, vacancies are preferably located in nearest neighbour sites to Ga atoms, with the Ga-V_O-Ga environment being more favourable than Ga-V_O-Mg and Mg-V_O-Mg arrangements for LGM with 6.25, 12.5 and 25 mol% of Mg. In those systems, more than 70% of the vacancies in all systems only got as close as NNN position to Mg ions [294]. The difference in E_a between the low and high temperature regimes is 0.3 eV; with values between 0.60 and 1.40 eV having been reported depending on temperature and dopant concentration [71,74,282,283,287,290,295,296].

Khan et al. [11] used a shell model in static lattice simulations to investigate the formation of dopant-vacancy clusters for doped $LaGaO_3$ systems, considering Sr-doping in the La-site, and Cu-, Mg- and Hg-doping on the Ga-site. The shell model parameters were empirically fitted to lattice parameters of the orthorhombic $LaGaO_3$ structure, with La-O and O-O potential parameters being the same as those used in a range of perovskite studies, such as $LaCrO_3$, $LaMnO_3$, $LaFeO_3$ and $LaCoO_3$. The IP parameters for the dopant ions were reproduced from studies on their binary oxides. The lowest binding energy was calculated for the Sr-V_O pair, while the migration energy of oxygen vacancies was calculated to be 0.73 eV. For the orthorhombic perovskite, dopant-vacancy binding energies increase in the dopant order Sr (-0.37 eV) < Cu (-1.50 eV) < Mg (-1.77 eV) < Hg (-1.90 eV). Even though the shell model parameters were derived for the orthorhombic $LaGaO_3$ structure, the authors also used the IP to calculate binding energies for the cubic perovskite, which increased in the dopant order Sr (-0.02 eV) < Cu (-1.34 eV) < Hg (-1.76 eV) < Mg (-1.83 eV) [11,75].

Another study using the same IP calculated the binding energy for the Sr-vacancy pair to be nearly zero and for the Ga-site dopants (Mg, Ni, Cu, Zn, Co, Fe) to be significant, indicating the trapping of oxygen vacancies around them [297]. This, however, is in disagreement with recent ^{71}Ga, ^{25}Mg and ^{17}O NMR studies revealing that vacancies are preferably localized near Ga(III) ions, forming oxygen deficient GaO_6 octahedra, while Mg(II) ions retain their octahedral coordination [282].

In this chapter, we parametrize a highly accurate DIPole Polarizable Ion Model (DIPPIM) force field (as outlined in Section 2.3), which will be used to predict the ionic conduction behaviour of two LSGM crystallographic phases (orthorhombic and rhombohedral). The force fields that are currently available in literature to study $LaGaO_3$-based systems [11, 280, 281] were empirically derived and have parameters extracted from different sources; hence, they lack transferability to accurately study the material in its different crystallographic phases and thermodynamic states. DIPPIM is less computationally expensive than *ab initio* MD, allowing bigger cells and/or time scales to be simulated. It has also been shown to depict an accurate description of defects and their effect on the ionic transport in doped ceria [139]. Section 5.5 consists of a classical molecular dynamics study of the bulk properties of $La_{1-x}Sr_xGa_{1-y}Mg_yO_{3-\delta}$ systems, referred to as LSGMXY, where X and Y are the mole percentages (mol%) of Sr(II) and Mg(II), i.e. a sample with x = 10 mol% and y = 15 mol% will be referred to as LSGM1015. The influence of dopant concentration on ionic conduction properties will be investigated, aiming to address the disagreement between experimentalists on which dopant content yields the best ionic conductivity values. The separate contributions of dopants to ionic conductivity will also be evaluated, by comparing the properties of singly doped and co-doped systems. To the best of our knowledge, there is no previous work in literature presenting a comprehensive and systematic analysis on the ionic conduction properties (diffusion coefficients, ionic conductivities, activation energies of diffusion and structural analysis) of LSGM systems, using the same methodology and hence obtaining consistent results, considering a range of temperatures (873-1273 K) and total dopant concentrations varying from 5 to 50%.

5.2 Derivation of the force field

This section describes the methodology employed to theoretically derive a DIPPIM force field aiming to investigate ionic conduction properties of LSGM systems by means of molecular dynamics simulations, and is divided in three parts:

(1) The generation of non-equilibrium configurations of orthorhombic (*Pbnm*), rhombohedral (*R3c*) and cubic (*Pm3m*) $LaGaO_3$-based systems using *ab initio* MD simulations (aiMD);

(2) DFT (using the SCAN functional) calculations on the obtained structures and extraction of the *ab initio* observables (forces, dipoles and stresses);

(3) Parametrization of the IP using a force-matching procedure, through minimization of an objective function (χ^2).

After that, details about the molecular dynamics simulations using PIMAIM, performed to validate the IP and investigate the ionic conduction properties of the material, will be presented.

5.2.1 *Ab initio* MD simulations

The force field was fitted to non-equilibrium structures generated from *ab initio* molecular dynamics simulations, allowing for a variety of geometries corresponding to different points in the system's potential energy surface to be considered. aiMD simulations were carried out using VASP and the meta-GGA SCAN functional, at constant volume and temperature (NVT ensemble), with the latter being controlled by the Nosé–Hoover thermostat (Section 3.3.3). The target temperatures were set as 300 K, 600 K and 900 K for the *Pbnm*, *R3c* and *Pm3m* cells, respectively, and the simulations were carried out for 20 ps with a timestep of 5 fs. The supercells contained 160 (*Pbnm*), 120 (*R3c*) and 135 (*Pm3m*) atoms, corresponding to 2x2x2, 2x1x1 and 3x3x3 expansions of the respective unit cells. The *R3c* supercell consisted of an orthogonal representation of the hexagonal cell. Calculations were performed in the pure and doped $LaGaO_3$ systems. Doped systems were randomly substituted with equal concentrations of Sr and Mg at the La- and Ga-sites

(LSGM), respectively, with four total dopant concentrations being considered (~25%, ~35%, ~45% and ~55%, varying slightly among the three phases due to the different cell sizes). Projector augmented wave (PAW) pseudopotentials were used (La:[Kr,$4d^{10}$], Ga:[Ar], O:[He], Sr:[Ar,$3d^{10}$] and Mg:[He]), with plane wave cut-off energy of 400 eV.

5.2.2 Generation and extraction of *ab initio* observables

Four structural frames were extracted from each *ab initio* MD simulation. Single-point DFT calculations using the SCAN functional were performed on these frames, with plane wave cut-off energy of 600 eV and electronic convergence criteria of 10^{-6} eV, so the *ab initio* observables used for the IP parametrization could be obtained. The forces acting upon each atom and the stresses were directly extracted from the DFT calculations, while Wannier analysis of the wave function was carried out for calculating the dipoles.

Wannier analysis, performed using the Wannier90 package [298], transforms the delocalized Kohn-Sham orbitals into a localised representation of the electron distribution. This is done by the generation of maximally localized Wannier functions (MLWFs) [299,300], which are a more suitable representation of the electronic density for dipole extraction, since it associates the Wannier functions to individual atoms. MLWFs are obtained from unitary transformations of the Kohn-Sham eigenvectors, as in Equation 5.1.

$$|\psi_{nR}^{w}\rangle = \frac{V}{(2\pi)^3}\int_{BZ}\sum_{m=1}^{N} U_{mn}^{(\boldsymbol{k})}|\psi_{m\boldsymbol{k}}\rangle e^{-i\boldsymbol{k}.\boldsymbol{R}}d\boldsymbol{k} \qquad (5.1)$$

In Equation 5.1, a Wannier function (ψ_{nR}^{w}) associated with the lattice site **R**, is determined for every wave vector **k**, from the transformation of *N* Kohn-Sham orbitals ($\psi_{m\boldsymbol{k}}$) by a unitary operator ($U_{mn}^{(\boldsymbol{k})}$). The evaluation is done over the Brillouin zone (BZ), with V being the volume of the primitive cell. $U_{mn}^{(\boldsymbol{k})}$ is determined from the minimization of the Wannier spread (Ω), i.e., from the spread of the Wannier function about its centre that yields "maximum localisation", as given in Equation 5.2 [301], where $\langle r^2\rangle_n$ and $|\bar{r}_n|^2$ are related to the position of Wannier centres, which in turn can be associated to the dipole moment (Equation 5.3). In Equation 5.3, the α Cartesian component of the dipole moment of ion *i* (μ_i^{α}) is calculated from the position of the Wannier centres (r_n^{α}).

$$\Omega = \sum_{n=1}^{N} (\langle r^2 \rangle_n - |\bar{r}_n|^2) \tag{5.2}$$

$$\mu_i^{\alpha} = -2 \sum_{n \in i} r_n^{\alpha} \tag{5.3}$$

5.2.3 Fitting Process

In the fitting process, an educated guess at the interatomic potential parameters is initially taken, based on previous experimental results or theoretical literature values, generating a trial potential. PIMAIM is then used to perform single-point MD calculations at 0 K on the $LaGaO_3$-based systems using such trial potential. The obtained observables (forces, dipoles and stresses) can be fitted to *ab initio* values extracted from single-point SCAN calculations on the *Pbnm*, *R3c* and *Pm3m* phases of pure and doped $LaGaO_3$, with the quality of the fit being evaluated by an objective function (χ^2), as given in Equation 5.4.

$$\chi^2 = \frac{1}{X} \sum_{i \in \{observables\}} \left\{ \frac{x_i}{N_i} \left[\sum_{j=1}^{N_i} \frac{|f_{pot}(j,i) - f_{ref}(j,i)|^2}{f_{ref}(j,i)^2} \right] \right\} \tag{5.4}$$

In the calculation of the weighted objective function (χ^2), each type of observable can have a different weight, x_i, with X being the sum of weights and N_i being the number of values considered for each observable. The objective function reflects the difference between the observable value calculated from DFT ($f_{ref}(j,i)$) and the value obtained from the trial potential ($f_{pot}(j,i)$), with each i observable being evaluated for every j element. Hence, small χ^2 values are an indication of a good fit.

In this thesis, the minimization of χ^2 was initially done using a modified evolutionary algorithm (ESCH) [302,303] for global optimization as implemented in NLopt [304]. The resulting χ^2 was then minimized using a non-gradient simplex method [305] followed by a MIGRAD method [306,307], as implemented in MINUIT [308], bringing the system to a local minimum, i.e. the algorithm searches for a local minima in the potential energy surface, in a region that was previously narrowed down during a global optimization. The forces, dipoles and stresses obtained after the local minimization can be compared to the DFT

values; if the objective function is small enough, meaning that the trial potential provided a good description of the *ab initio* data, the fitting process is considered complete. The considered parameters in the fitting process are listed in Table 5.1, along with the Equations where they can be found.

Table 5.1 – Parameters included in the force field parametrization and reference equations.

Parameter	Description	Ref. equation
A_{ij}	Yukawa pre-exponential factor for short-range repulsion	2.29
a_{ij}	Yukawa exponential factor for short-range repulsion	2.29
B_{ij}	Gaussian pre-exponential factor for short-range repulsion	2.29
b_{ij}	Gaussian exponential factor for short-range repulsion	2.29
$b_{6,ij}$	Dispersion (Tang-Toennies) damping factor for $C_{6,ij}$*	2.32
$\alpha_{O^{2-}}$	Oxide-ion dipole polarizability	2.30 and 2.31
$b_{D,ij}$	Dipole damping exponent	2.32
$c_{D,ij}$	Dipole damping coefficient for *ij* interaction	2.32
$c_{D,ji}$	Dipole damping coefficient for *ji* interaction	2.32

*$C_{6,ij}$ are the dipole-dipole dispersion coefficients, given in Equation 2.33.

Global optimization becomes exponentially harder with an increase in the number of parameters being considered [304]. Since the objective function (Equation 5.4) can be separately calculated for each observable, dipole-related terms were parametrized first (global optimization followed by local optimization), as a way of facilitating the optimization process. Educated guesses for $b_{D,ij}$, $c_{D,ij}$ and $c_{D,ji}$ parameters were taken, considering all cation-anion interactions (cation-cation terms were not included in the fit, as cations-cation short-range interactions are not significant). As the dipole polarizability of anions is environment dependent, a starting value for $\alpha_{O^{2-}}$ was calculated from the material's refractive index (or the high frequency dielectric constant) as described by Dimitrov and Sakka [309], and is listed in Table 5.2. The dipole polarizabilities of cations (α_i) were not fitted, with experimental values being used (Table 5.2) and being kept fixed throughout the fitting process. Dipole-dipole dispersion coefficients (the $C_{6,ij}$ term in Equation 2.33) were also not fitted, but calculated during the fit from the Slater-Kirkwood relationship [310], given in Equation 5.5; since the oxygen polarizability was allowed to vary during the fit, $C_{6,ij}$ was then indirectly fitted, as it was calculated from it. In Equation

5.5, p_i and p_j are the effective electron numbers of interacting ions *i* and *j*, obtained from isoelectronic literature values [311,312] for the ionic species, also presented in Table 5.2.

Table 5.2 – Dipole polarizabilities (α_i) used in the fitting process (cation values were kept fixed throughout the process, while $\alpha_{O^{2-}}$ is simply a starting guess calculated from $LaGaO_3$ refractive index) and effective electron numbers (p_i) used to calculate the dipole-dipole dispersion coefficient ($C_{6,ij}$).

Species	α_i (Bohr^3)	p_i
O^{2-}	13.210	4.455 [311]
La^{3+}	7.018 [313]	7.901 [311]
Ga^{3+}	1.316 [309,313]	5.477 [312]
Sr^{2+}	5.800 [309,313]	7.305 [311]
Mg^{2+}	0.630 [309,313]	4.455 [311]

$$C_6(i,j) = \frac{\frac{3}{2}\alpha_i\alpha_j}{\sqrt{\frac{\alpha_i}{p_i}} + \sqrt{\frac{\alpha_j}{p_j}}} \tag{5.5}$$

It is important to note that DFT does not accurately describe van der Waals interactions [314], with only approximately 25% of dispersion being accounted for [315]. Even though these interactions contribute to a small fraction of the system's total energy, they have a substantial influence on the stress tensor and the material's density. Therefore, the calculated $C_{6,ij}$ values were scaled back by 25% during the parametrization and scaled back up for subsequent MD simulations. All $C_{6,ij}$ values presented in this chapter correspond to the full value of dispersion coefficients (100%). Finally, the initial guess for the dispersion and the dipole damping factors ($b_{6,ij}$ and $b_{D,ij}$, respectively) was taken to yield a value of 0.5 for the Tang-Toennies function (Equation 2.31, for n = 6) at the bond distance for the considered *ij* atom pair, estimated from the ionic radii of *i* and *j*.

After the objective function for dipoles was minimized, dipole parameters were kept fixed and short-range repulsion terms (A_{ij}, a_{ij}) were fitted (global followed by local optimization), so objective functions for forces and stresses could be obtained. Finally, after reasonable values, close to the local minima of the potential energy surface, were obtained

for the short-range repulsion terms, all parameters listed in Table 5.1 were allowed to vary, yielding the force field used in the remainder of the chapter.

5.3 Interatomic potential for pure $LaGaO_3$ and LSGM phases

The force field was fitted to DFT data calculated for pure and co-doped $LaGaO_3$ phases (*Pbnm*, *R3c* and *Pm3m*). Eight frames were analysed for each crystallographic phase; from those, four frames corresponded to pure $LaGaO_3$ systems, with cells containing 160, 240 and 135 atoms for *Pbnm*, *R3c* and *Pm3m* $LaGaO_3$, respectively. The remaining four frames corresponded to doped LSGM phases with equal amounts of Sr and Mg, representing total dopant concentrations of ~25%, ~35%, ~45% and ~50%. As a result, a total sample size of 4197 atoms was used to fit dipoles and forces. These observables were evaluated for each ion, on the *x*, *y* and *z* directions. Stress tensors, on the other hand, have six components per frame, resulting in a sample size of 144. The objective functions obtained for each observable (dipoles, forces and stresses) and the total χ^2 value, along with the sample sizes for the LSGM system are presented in Table 5.3.

Table 5.3 – Objective functions for each observable taken in isolation and overall χ^2 value, obtained for LSGM systems, considering *Pbnm*, *R3c* and *Pm3m* phases.

Observable	**LSGM**	
	$\boldsymbol{\chi^2}$	**Sample size**
Dipoles	0.344	4197
Forces	0.264	4197
Stresses	0.112	144
Total $\boldsymbol{\chi^2}$	0.240	

The χ^2 value for the LSGM system is low (Total $\chi^2 = 0.24$), suggesting the good quality of the fit to DFT data. For comparison, objective functions of 0.383 [139] and 0.217 [164] were obtained for doped CeO_2 using rigid-ion model (RIM) and DIPPIM interaction potentials, respectively. The quality of the force field could likely be improved by the addition of SrO and MgO phases to the parametrization process, to include other Sr/Mg-O environments than those encountered in LSGM and hence achieve a better description of the interaction between dopants and oxide ions.

The obtained short-range, dispersion and polarizability parameters are listed in Tables 5.4 and 5.5, in atomic units. All symbols correspond to those listed in Table 5.1. A_{ij} was set as zero for all cation-cation pairs.

Table 5.4 – Short-range repulsion and dispersion parameters of the DIPPIM potential obtained for pure LSGM phases (*Pbnm*, *R3c* and *Pm3m*). All values are in atomic units.

Interaction	A_{ij}	a_{ij}	B_{ij}	b_{ij}	$C_{6,ij}$	$b_{6,ij}$
O^{2-} – O^{2-}	0.00	0.00	0.00	0.00	66.67	2.49
La^{3+} – O^{2-}	167.04	1.40	0.00	0.00	49.19	1.17
Ga^{3+} – O^{2-}	44.17	1.26	50000	1.60	11.17	4.00
Sr^{2+} – O^{2-}	256.78	1.59	0.00	0.00	41.47	1.26
Mg^{2+} – O^{2-}	140.97	1.72	0.00	0.00	5.65	2.00
La^{3+} – La^{3+}	0.00	0.00	0.00	0.00	39.20	1.50
La^{3+} – Ga^{3+}	0.00	0.00	0.00	0.00	9.67	1.83
La^{3+} – Sr^{2+}	0.00	0.00	0.00	0.00	33.30	1.42
La^{3+} – Mg^{2+}	0.00	0.00	0.00	0.00	5.03	1.74
Ga^{3+} – Ga^{3+}	0.00	0.00	0.00	0.00	2.65	2.32
Ga^{3+} – Sr^{2+}	0.00	0.00	0.00	0.00	8.29	1.70
Ga^{3+} – Mg^{2+}	0.00	0.00	0.00	0.00	1.44	2.18
Sr^{2+} – Sr^{2+}	0.00	0.00	0.00	0.00	28.31	1.34
Sr^{2+} – Mg^{2+}	0.00	0.00	0.00	0.00	4.32	1.62
Mg^{2+} – Mg^{2+}	0.00	0.00	0.00	0.00	0.79	2.05

Table 5.5 – Polarisability parameters of DIPPIM potential obtained from LSGM phases (*Pbnm*, *R3c*, *Pm3m*). All values are in atomic units.

Species	α	$b_{D,(O^{2-}-X)}$	$c_{D,(O^{2-}-X)}$	$c_{D,(X-O^{2-})}$
O^{2-}	12.10	2.48	3.00	0.00
La^{3+}	7.018	1.63	0.00	1.59
Ga^{3+}	1.316	2.04	1.46	2.03
Sr^{2+}	5.80	1.60	0.26	1.67
Mg^{2+}	0.63	2.09	0.53	2.59

We tried to fit A_{ij} and a_{ij} for the O^{2-}– O^{2-} interaction, however, no sensible values were obtained, so these terms were set to zero; although short-range parameters have been previously published for O^{2-}– O^{2-}, their examination (through calculation of U^{rep} as in Equation 2.29) reveals that such parameters yield no significant interactions at normal interatomic separations. Figure 5.1 shows that the A_{ij} and a_{ij} parameters empirically derived by Cherry *et al.* to study $LaBO_3$ (B = Cr, Mn, Fe and Co) oxides [148] yield no physically significant interaction for separation distances higher than 0.8 Å. Such parameters were also used by Khan *et al*. [11] to investigate oxide-ion migration in $LaGaO_3$. Furthermore, Burbano *et al.* [385] has parametrized a DIPPIM potential to investigate the solid lithium-ion electrolyte $Li_7La_3Zr_2O_{12}$ (LLZO) using a similar methodology to that presented in this chapter, fitting forces, dipoles and stresses to Hybrid DFT data. In their work, the short-range A_{ij} and a_{ij} parameters for the O^{2-}– O^{2-} interaction were also set to zero. The obtained value for $\alpha_{O^{2-}}$ in LSGM systems (12.10 $Bohr^3$) is close to the initial guess of 13.21 $Bohr^3$ calculated from the material's refractive index, indicating that this force-matching procedure can satisfactorily determine anion dipole polarizabilities.

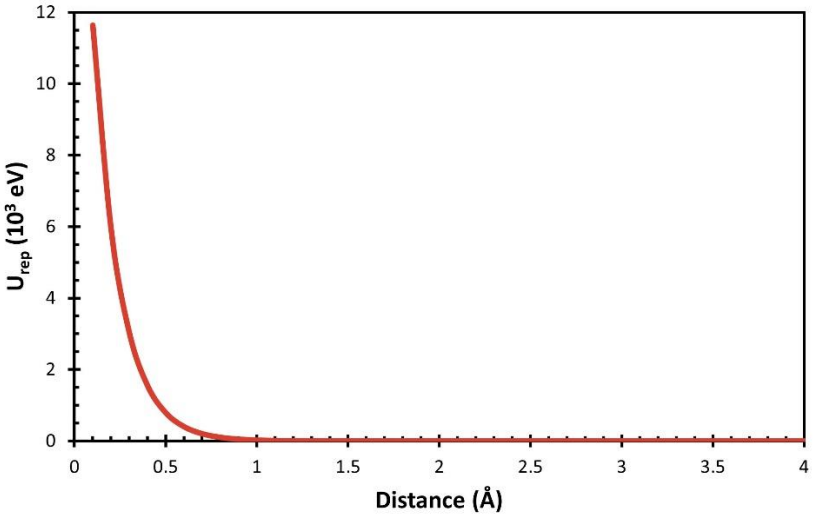

Figure 5.1 – Graphical representation of the short-range repulsion term (U_{rep}) for the for O^{2-} – O^{2-} interaction, calculated as in Equation 2.29, utilising the A_{ij} and a_{ij} (22764.3 eV and 0.149 Å, respectively) parameters empirically derived by Cherry *et al.* [148] to study $LaBO_3$ (B = Cr, Mn, Fe and Co) oxides. As no interactions are calculated for separation distances higher than 0.8 Å, such parameters are not physically significant.

A visual representation of the quality of the fit is given in Figure 5.2, which shows the match between forces, dipoles and stresses obtained from DIPPIM and DFT. The general agreement between DFT and PIMAIM values indicates that the force field can satisfactorily reproduce *ab initio* data for all three $LaGaO_3$ phases, suggesting good transferability of the IP. The biggest discrepancies occur for forces, dipoles and stresses of larger magnitudes. DIPPIM overestimates the absolute values of forces and stresses of higher magnitudes. Such overestimation of forces was also observed by Burbano [164] and Lucid [139], when parametrizing force fields for CeO_2-based systems using a similar force-matching approach, and might be related to the fitting procedure or to a more intricate force field being necessary to accurately describe forces. The absolute values of dipoles of higher magnitudes, on the other hand, are underestimated by DIPPIM. Despite this, the observables' objective functions (Table 5.3) are still low and the transferability of the potential between phases was achieved.

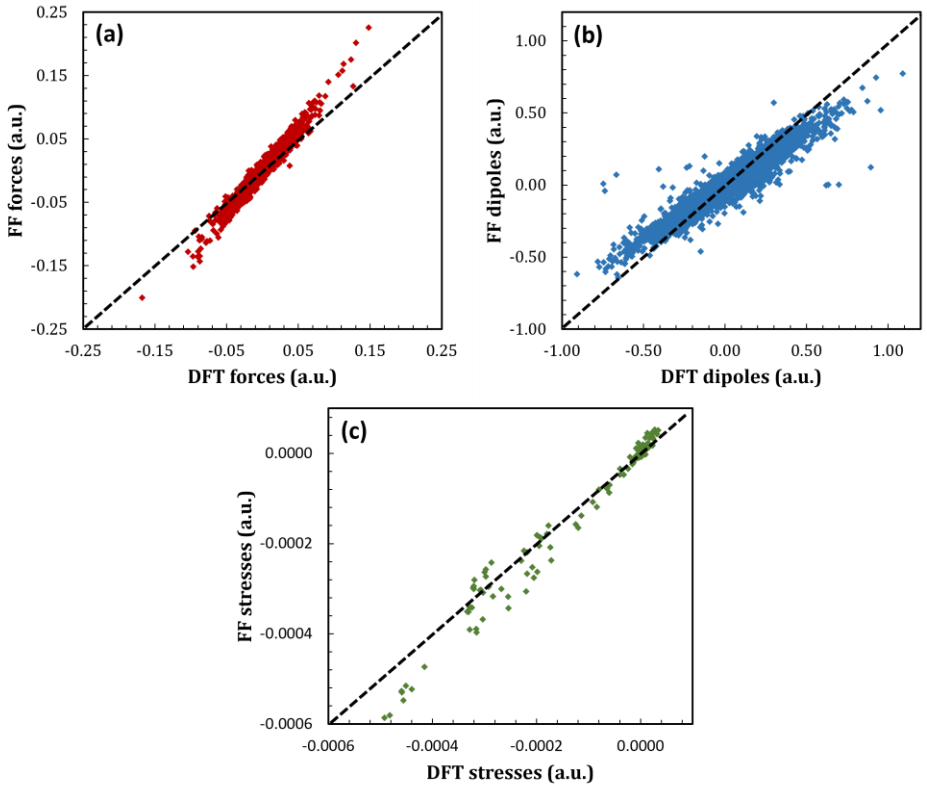

Figure 5.2 – Comparison between (a) forces, (b) dipoles[1] and (c) stresses values (in atomic units) calculated from DFT (*x* axis) and the DIPPIM force field (FF, *y* axis).

5.4 Potential validation

To evaluate the validity of the parametrized force field, the reproduction of experimental properties (such as thermal expansion coefficients and structural parameters) was evaluated. The linear and volumetric thermal expansion coefficients were investigated for the pure $LaGaO_3$ phases in the 300-2100 K temperature range, while the structural parameters of the *Pbnm*, *R3c* and *Pm3m* phases, were evaluated at 300 K, 600 K and 1200 K, respectively.

[1] The match between DFT and FF dipoles for *Pbnm* and *Pm3m* frames with total dopant content of 50 mol% are not included in Figure 5.2b, as unrealistic dipole values were obtained from the DFT data, most likely due to an error during Wannier analysis. The dipoles values obtained for these frames are shown in Figure A.1 (see Appendix) and compared to the *R3c* 50 mol% phase, which possesses more realistic values.

5.4.1 Structural parameters of pure $LaGaO_3$ phases

The crystal structures of the *Pbnm*, *R3c* and *Pm3m* phases were optimized at 300 K, 600 K and 1200 K, respectively and the obtained structural parameters (*a*, *b*, *c*, *V*) are listed in Table 5.6, and compared to experimental results at 298 K (*Pbnm*), 573 K (*R3c*) and 1200 K (*Pm3m*). DFT lattice parameters calculated using the SCAN functional are also presented.

Table 5.6 – Optimized lattice parameters of orthorhombic (*Pbnm*), rhombohedral (*R3c*) and cubic (*Pm3m*) $LaGaO_3$ obtained from theoretical calculations (DFT/SCAN and DIPPIM) and neutron powder diffraction results. DIPPIM calculations were performed at 300 K, 600 K and 1200 K for the *Pbnm*, *R3c* and *Pm3m* phases, respectively. The percentage difference between the calculated results and experimental values is in parenthesis. DFT and DIPPIM results for the *Pbnm* phase where compared to experimental values at 11 K [248] and 298 K [316], respectively, while results for the *R3c* system were compared to experimental data measured at 573 K [316]. It is not clear at which temperature measurements from reference [317] were taken.

Phase	Parameter	DFT (SCAN)	DIPPIM	Experiment
Pbnm	*a* (Å)	5.520 (0.09%)	5.474 (-0.96%)	5.515 [248], 5.527 [316]
	b (Å)	5.511 (0.44%)	5.456 (-0.69%)	5.487 [248], 5.494 [316]
	c (Å)	7.795 (0.37%)	7.718 (-0.75%)	7.766 [248], 7.777 [316]
	V (Å^3)	237.16 (0.90%)	230.55 (-2.38%)	235.04 [248], 236.17 [316]
R3c	*a* (Å)	5.537 (-0.04%)	5.474 (-1.17%)	5.539 [316]
	c (Å)	13.361 (-0.35%)	13.399 (-0.07%)	13.409 [316]
	V (Å^3)	354.72 (-0.43%)	347.496 (-2.45%)	356.25 [316]
Pm3m	*a* (Å)	3.888 (0.05%)	3.893 (0.18%)	3.886 [317]
	V (Å^3)	58.77 (0.15%)	58.70 (0.03%)	58.68 [317]

DIPPIM underestimates *Pbnm* and *R3c* lattice parameters when compared to experimental results, while DFT overestimates the first and underestimates the latter. DFT results are closer to experimental values, especially considering that DFT calculates parameters at 0 K, while the experimental information for *R3c* and *Pm3m* phases were measured at high temperatures. Both methods slightly overestimate *Pm3m* parameters.

Overall, the percentage differences of the DIPPIM and DFT results from experimental values are small, indicating excellent agreement from both methods to experiment, and indicating the high quality of the IP. DIPPIM yields lattice parameters within ~1% of experimental results, and volumes with deviation lower than 2.5%.

The La-O, Ga-O and O-O radial distribution functions of orthorhombic (*Pbnm*) $LaGaO_3$ at 300 K were also calculated and are presented in Figure 5.3. DIPPIM calculates the nearest neighbour (NN) La-O distance to be within the 2.45-3.08 Å range, and the Ga-O and O-O NN distances to be 1.95 Å and 2.75 Å, respectively. Neutron powder diffraction measurements at 298 K [248] reveal the existence of five NN La-O (2.409, 2.468, 2.624, 2.629 and 2.7982 Å) and three NN Ga-O distances (1.973, 1.975 and 1.978 Å), as presented in Table 4.3. Therefore, DIPPIM predicts bond distances to be within the expected range, overestimating La-O distances in 1.7-10.0%, and underestimating the Ga-O distance in 1.02%.

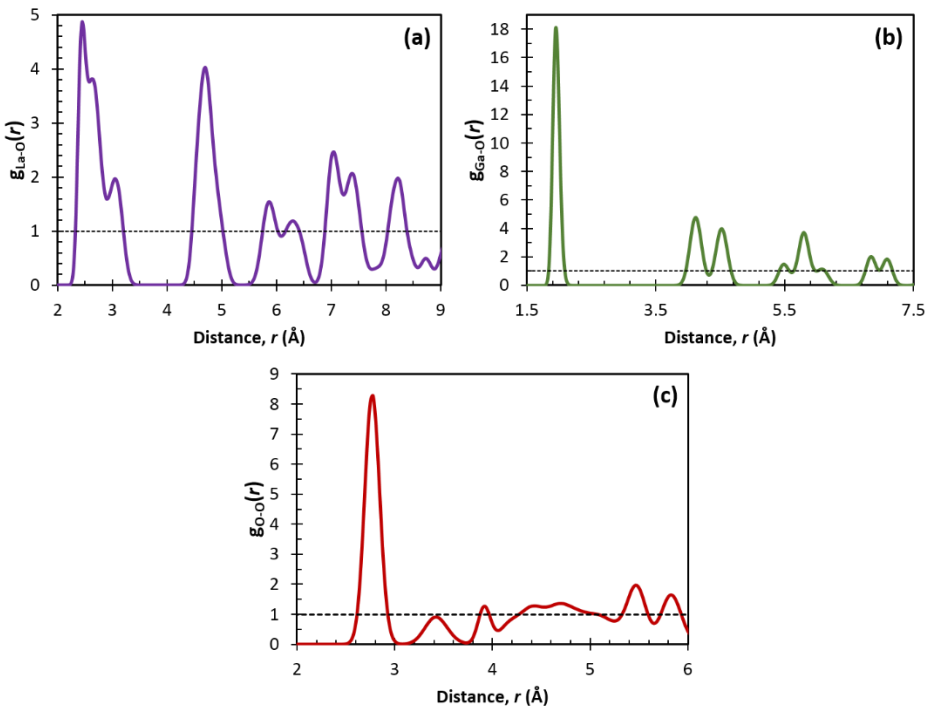

Figure 5.3 – (a) La-O, (b) Ga-O and (c) O-O DIPPIM radial distribution functions of orthorhombic (*Pbnm*) $LaGaO_3$ calculated at 300 K.

5.4.2 Thermal expansion of pure $LaGaO_3$ phases

The DIPPIM was used to investigate the thermal expansion of the three crystallographic phases of pure $LaGaO_3$, which was compared to experimental results as a way of validating and evaluating the quality of the IP. Thermal expansion can be investigated with respect to the material's lattice constants, along the three crystallographic directions, as shown in Equation 5.6, where changes in the cell length, L, are proportional to the linear thermal expansion coefficient (TEC), α, and temperature variations.

$$\Delta L = \alpha L \Delta T \tag{5.6}$$

Thermal expansion can also be evaluated with respect to the cell volume (V), as shown in Equation 5.7; changes in V with temperature are proportional to the volumetric TEC, β. The linear and volumetric TECs, which have units of reciprocal temperature, can be approximately correlated as shown in Equation 5.8.

$$\Delta V = \beta V \Delta T \tag{5.7}$$

$$\beta \approx 3\alpha \tag{5.8}$$

Equations 5.6 and 5.7 can be rearranged, and rewritten as Equations 5.9 and 5.10, where L_0 (V_0) is the cell length (volume) at the initial temperature T_0, and L (V) is the cell length (volume) at the final temperature T, under which the TEC is being evaluated. Therefore, a plot of $(L - L_0)/L$ (or $(V - V_0)/V$) vs $(T - T_0)$ (or ΔT) should result in a straight line of slope α (or β), in units of reciprocal temperature

$$\frac{(L - L_0)}{L} = \alpha(T - T_0) \tag{5.9}$$

$$\frac{(V - V_0)}{V} = \beta(T - T_0) \tag{5.10}$$

MD simulations were performed at six different temperatures (300, 600, 900, 1200, 1500 and 1800 K), with the average volume being used to estimate the volumetric TECs for the different phases. The plot of $(L - L_0)/L$ vs T and of $(V - V_0)/V$ vs T for the three phases of $LaGaO_3$ (*Pbnm, R3c* and *Pm3m*) is presented in Figures 5.4 and 5.5, respectively. For the cubic structure, only the lattice parameter *a* was considered, as in the cubic phase *a* = *b* = *c*. Similarly, for the rhombohedral phase, the lattice parameter *b* is not shown, as *a* = *b*. The

linear and volumetric TECs calculated from the linear fit of these plots in the 300-1800 K temperature range, along with the available experimental data, are listed in Table 5.7.

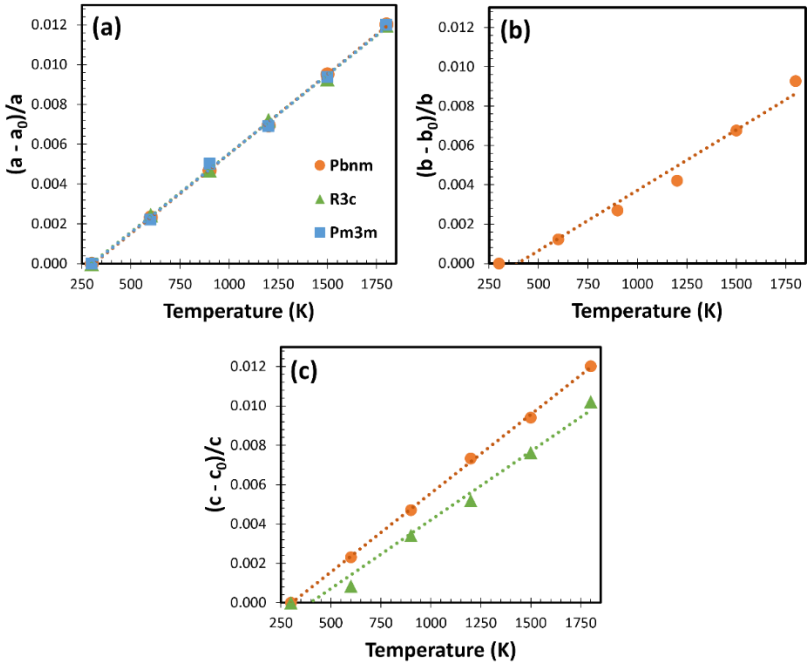

Figure 5.4 – Plot of $(L - L_0)/L$ vs T for the orthorhombic (*Pbnm*, in orange), rhombohedral (*R3c*, in green) and cubic (*Pm3m*, in blue) perovskite in the 300-1800 K temperature range, considering the (a) *a*, (b) *b* and (c) *c* crystallographic directions. The linear thermal expansion coefficients (α_a, α_b, α_c) is equal to the slope of these plots as given by Equation 5.9.

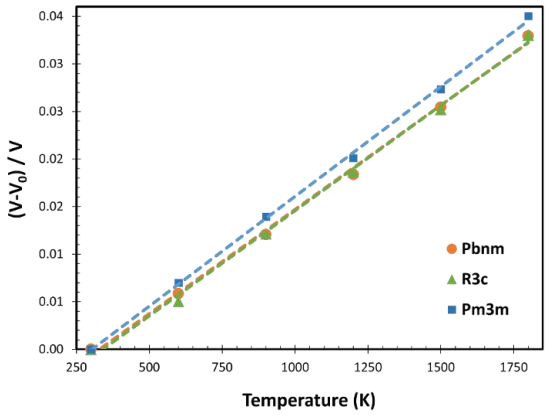

Figure 5.5 – Plot of $(V - V_0)/V$ vs T for the orthorhombic (*Pbnm*, in orange), rhombohedral (*R3c*, in green) and cubic (*Pm3m*, in blue) perovskite in the 300-1800 K temperature range. The volumetric thermal expansion coefficients (β_a, β_b, β_c) is equal to the slope of these plots as given by Equation 5.10.

Table 5.7 – Linear (α) and volumetric (β) thermal expansion coefficients for the three $LaGaO_3$ phases, calculated from the linear fits of the plots presented in Figure 5.4 and 5.5. Experimental data measured in the 11-413 K (*Pbnm* phase) and 420-1200 K (*R3c* phase) temperature range are also listed. There are no experimental results available for the *Pm3m* phase.

Space Group	***Pbnm***	***R3c***	***Pm3m***	**Exp. (*Pbnm*)**	**Exp. (*R3c*)**
α_a (10^{-6} K^{-1})	7.99	7.89	7.94	10.2 [248], 11.16 [318], 12.1 [316]	10.3 [316]
α_b (10^{-6} K^{-1})	6.14	7.48	-	7.0 [248], 6.98 [318], 9.7 [316]	-
α_c (10^{-6} K^{-1})	8.00	6.97	-	7.2 [248], 7.66 [318], 11.0 [316]	18.4 [316]
β (10^{-6} K^{-1})	21.89	22.10	23.07	24.9 [248], 25.8 [318], 33.0 [316]	32.6 [318], 39.5 [316]

There is significant variation among the available experimental parameters. In general, DIPPIM underestimates the linear TECs. For orthorhombic $LaGaO_3$, α_a and α_b are underestimated with respect to experimental results, while α_c is an overestimation of some of the available experimental data. Still, DIPPIM predicts α_b to be smaller than α_a, in agreement to experimental observations. The volumetric thermal expansion coefficient for the orthorhombic phase is in good agreement with the lower range of experimentally reported values. The volumetric thermal expansion coefficient obtained in other molecular dynamics study ($\beta = 22.8 \times 10^{-6}$ K^{-1} [319]) using an interatomic potential including charge-charge, overlap repulsion and dispersion contributions were also an underestimation of experimental results. For the rhombohedral phase, while the DIPPIM α_a value is in agreement with experimental data, α_c is strongly underestimated. As a result, so is the volumetric TEC. Hence, the description of the orthorhombic phase's thermal expansion is superior to that of the rhombohedral structure, while no experimental data is available for the cubic phase. DIPPIM was also observed to underestimate the thermal expansion coefficients of doped ceria in 15-20% [164]; however, it still yields a smaller underestimation in comparison to other IPs available in literature, which calculate TECs 37-89% lower than experimental values [320–322]. Therefore, the discrepancy between our results and literature values are within expected, especially considering that out IP was theoretically parametrized, i.e. it was fitted to DFT results calculated at 0 K without the inclusion of any empirical data, and was not manually optimized to reproduce the material's thermal expansion behaviour.

5.5 Molecular dynamics simulations

Sr ($La_{1-x}Sr_xGaO_{3-\delta}$), Mg ($LaGa_{1-y}Mg_yO_{3-\delta}$) and co-doped ($La_{1-x}Sr_xGa_{1-y}Mg_yO_{3-\delta}$) $LaGaO_3$ systems were investigated by means of molecular dynamics simulations, using the DIPPIM force field presented in Section 5.3. *x* and *y* values between 0 and 0.35 (35 mol%) were considered, with dopants and vacancies being randomly added to the structure. All MD simulations were performed using TCD-PIMAIM [96]. 6x6x6, 6x6x4 and 8x8x8 unit cell expansions were used for the *Pbnm* (4320 atoms), *R3c* (4320 atoms) and *Pm3m* (2560 atoms) phases, respectively, resulting in ~33x33x46 Å, ~33x28x56 Å and ~31x31x31 Å supercell dimensions. The number of atoms slightly vary for different dopant and vacancy concentrations. Calculations to investigate the ionic conduction properties were carried out at three temperatures (873 K, 1073 K and 1273 K), chosen to represent intermediate (873 and 1073 K) and high temperature (1273 K) SOFC conditions. Diffusion coefficients, activation energies of diffusion and ionic conductivity values were calculated from multiple time origin MSDs, as described in Section 3.3.6.

All systems were first simulated at 200 K for 0.4 ps, with temperature scaling being carried out every 0.04 fs, to remove any excess potential energy in the lattice, especially for systems with higher dopant concentrations. Temperature scaling at the target T (873 K, 1073 K or 1273 K) was then carried out every 0.1 ps for 10 ps. The supercells were allowed 500 ps to reach equilibrium before data collection began. Data collection runs were 2 ns (873 K), 1.5 ns (1073 K) or 1 ns (1273 K) long. All runs used an isothermal-isobaric ensemble (NPT) [169], with time step of 4 fs, and short-range and real space Ewald cut-offs of 13 Å. Two randomized defect configurations were considered for each dopant concentration to account for the statistical nature of molecular dynamics. Therefore, the diffusion coefficients, ionic conductivities and activation energies presented here are average values with their standard errors.

5.5.1 Singly doped $LaGaO_3$ systems

5.5.1.1 Ionic conductivity in LSG and LGM

The oxide ion-conductivity of $La_{1-x}Sr_xGaO_{3-\delta}$ (LSG) with x = 0.10, 0.15, 0.20, 0.25, 0.30, 0.35 and $LaGa_{1-y}Mg_yO_{3-\delta}$ (LGM) with y = 0.05, 0.10, 0.15, 0.20, 0.25, 0.30, 0.35 were investigated from the analysis of their mean square displacements at three different temperatures (873, 1073 and 1273 K). Here, smaller y values (0.05) were considered when compared to x, as in experimental studies, Mg addition to $LaGaO_3$ systems has the primary objective of expanding the perovskite lattice and facilitate Sr incorporation, with smaller y being sufficient to achieve such results [74,290,291]. Diffusion coefficients were calculated from the slope of the linear fit of the MSD (Equation 3.26) and can be used to calculate the ionic conductivity from the Nernst-Einstein Equation (Equation 3.29). The obtained diffusion coefficients (D, in 10^{-8} cm^2 s^{-1}) and ionic conductivities (σ, in mS cm^{-1}) for orthorhombic and rhombohedral Sr-doped $LaGaO_3$ (LSG) for all dopant concentrations and temperatures are presented in Tables A.1-A.4 (see Appendix). The variation in ionic conductivity values with Sr (x) and Mg content (y) for the orthorhombic and rhombohedral phases is shown in Figure 5.6, where the errors bars are given as standard error. Error bars are quite large in some cases; the simulation of extra configurations to improve statistics was not possible due to time constraints.

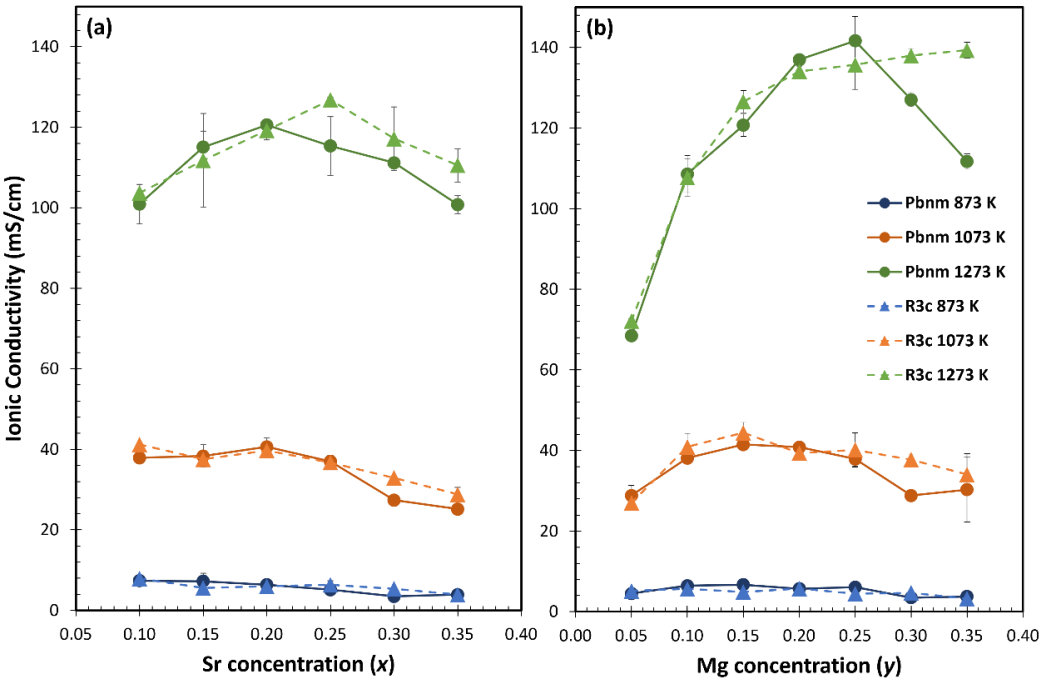

Figure 5.6 – Ionic conductivity variation with (a) Sr (x = 0.10, 0.15, 0.20, 0.25, 0.30 and 0.35) or (b) Mg (y = 0.05, 0.10, 0.15, 0.20, 0.25, 0.30 and 0.35) content at 873 K (blue), 1073 K (orange) and 1273 K (green), for orthorhombic (*Pbnm*) and rhombohedral (*R3c*) doped $LaGaO_3$ phases, which are represented by solid and dashed lines, respectively.

The Sr and Mg concentrations at which maximum ionic conductivity is achieved increase with temperature; for orthorhombic LSG (solid lines in Figure 5.6a), maximum conductivity occurs for LSG10 at 873 K. For higher temperatures (1073 K and 1273 K), maximum σ is obtained for LSG20, decreasing for higher dopant contents. Even though systems with 30 and 35 mol% of Sr have an elevated vacancy concentration, defect interactions might start to play a more significant role at higher dopant content, hindering ionic diffusion and resulting in the observed σ decrease. If the calculated standard errors are considered, maximum values of ionic conductivity in orthorhombic LSG are achieved at $0.10 \leq x \leq 0.20$ at 873 K, $0.15 \leq x \leq 0.20$ at 1073 K and $0.20 \leq x \leq 0.25$ at 1273 K. Hence, x = 0.20, which is within the optimal range for all analysed temperatures, is likely to be the optimal Sr concentration for singly doped orthorhombic systems. For rhombohedral LSG (dashed lines in Figure 5.6a), maximum conductivity is observed for LSG10 at 873 K and 1073 K, and for LSG25 at 1273 K. As the calculated standard errors are smaller when compared to the orthorhombic phase, there is no 'optimal range' of x values.

For orthorhombic LGM (solid lines in Figure 5.6b), on the other hand, maximum σ is observed for LGM15 at 873 and 1073 K, and for LGM25 at 1273 K. Interestingly, for all analysed concentrations, ionic conductivity is higher in LGM than in LSG samples for the same dopant content. If standard errors are taken into account, optimal dopant concentration in LGM lies within $0.10 \leq y \leq 0.15$ at 873 K, $0.15 \leq y \leq 0.20$ at 1073 K, and $0.20 \leq y \leq 0.25$ at 1273 K. Hence, we can suggest that for orthorhombic LGM, $y = 0.20$ is also the optimal dopant concentration, and that oxide-ion mobility is just not high enough at 873 K for an accurate prediction of optimal values. For rhombohedral LGM (dashed lines in Figure 5.6b), ionic conductivity is maximum at $y = 0.20$, 0.15 and 0.35 at 873 K, 1073 K and 1273 K, respectively. Considering the calculated standard errors, optimal dopant concentration should be between $0.05 \leq y \leq 0.20$ at 873 K, $0.15 \leq y \leq 0.25$ at 1073 K and $0.20 \leq y \leq 0.35$ at 1273 K. Therefore, similarly to that which was observed for the orthorhombic phase, optimal dopant concentration in rhombohedral LGM should also be around $y = 0.20$.

In summary, for both orthorhombic and rhombohedral LSG and LGM systems, ionic conductivity increases with dopant concentration until it reaches its limit at around 20 mol%, decreasing after that, with LGM systems possessing higher σ values. These results indicate that vacancies might be somewhat trapped in systems with higher dopant content, resulting in the observed decrease in ionic conductivity, even though there are more vacancies present in such systems. Furthermore, dopant-vacancy interactions are probably different in LSG and LGM systems, as the latter possess higher σ values than the first for the same dopant content. Vacancy trapping at higher dopant contents might also lead to an increase in activation energy with dopant concentration. These higher activation energies result in larger slopes in the system's Arrhenius plots (lnD vs. 1/T, as outlined in Section 3.3.6), which in turn indicates that the effect of temperature on ionic diffusion in such systems is greater. Hence, for higher dopant content, the associated high activation energies result in a stronger temperature dependence of diffusion processes. As a result, the maximum in ionic conductivity as a function of dopant content moves to higher dopant concentrations as temperature increases. To confirm this effect, the activation energies of diffusion for LSG and LGM will be investigated in the following section.

Experimental data on diffusion coefficients, ionic conductivities and activation energies of diffusion can vary considerably due to different synthesis conditions (synthetic method, sintering times and temperatures), the variety of grain sizes and the presence of

impurities and secondary phases. Small variations can also be attributed to measurements being performed under different environments (usually air or N_2); the ionic conductivity of doped $LaGaO_3$, however, is practically the same under both chemical conditions [323]. Experimental data is also limited; not all dopant concentrations presented here have been tested. The ionic conductivity of Sr-doped $LaGaO_3$ has been reported to increase with dopant concentration until secondary phase formation ($LaSrGa_3O_7$ and $LaSrGaO_4$) at Sr concentrations higher than 10 mol% [74,290,291]. Other studies report the appearance of secondary phases only at 20 mol% [284], and hence optimal conductivity values at this dopant concentration, in agreement to DIPPIM results for the orthorhombic LSG phase. The solubility limit of SrO can be increased to 20 mol% through the addition of MgO, which results in lattice expansion and hence facilitates Sr incorporation [74,290,291]. Similarly, the ionic conductivity of Mg-doped $LaGaO_3$ has also been observed to increase with dopant concentration until the formation of secondary phases, which deteriorate conduction properties. For both LSG and LGM systems, the ionic conductivity decrease is always associated with secondary phase formation, and not with the increase in defect-defect interactions suggested from DIPPIM results. The appearance of secondary phases in LGM (mainly $La_4Ga_2O_9$) is reported only at $y > 0.20$, with 20 mol% being the solubility limit of MgO in $LaGaO_3$ [284,290,291]; hence, maximum ionic conductivity is achieved at this concentration. Therefore, DIPPIM results for LGM are also in agreement with experiment, especially considering that in MD simulations the formation of secondary phases is not considered, which explains the high σ values observed for $y > 0.20$ at 1273 K. Table 5.8 presents the experimentally measured ionic conductivities for LSG10 at 873 K, 1073 K and 1273 K, along to DIPPIM results. Table 5.9 lists the experimental ionic conductivities for LGM15 at 1073 K, and LGM20 at 873 K and 1073 K.

Table 5.8 – DIPPIM (*Pbnm* and *R3c* phases) and experimental ionic conductivities (in mS/cm) for $La_xSr_{1-x}GaO_{3-\delta}$ with x = 0.10 at 873 K, 1073 K and 1273 K. All experimental studies report an orthorhombic structure.

T (K)	This study - *Pbnm* (mS/cm)	This study – *R3c* (mS/cm)	Experiment (mS/cm)	Ref.
873	7.37 ± 0.42	7.92±0.12	4.2	[290]
			9	[324]
			18	[323]
1073	37.92 ± 0.12	41.19±0.36	25	[286]
			27	[290]
			30	[323]
			36.5	[324]
1273	100.92 ± 4.88	103.68±2.03	71	[286]
			79	[323]

Table 5.9 – DIPPIM (*Pbnm* and *R3c* phases) and experimental ionic conductivities (in mS/cm) for $LaGa_{1-y}Mg_yO_{3-\delta}$, with x = 0.15 at 1073 K and x = 0.20 at 873 K and 1073 K. Both experimental studies report an orthorhombic structure.

T (K)	*y*	This study – *Pbnm* (mS/cm)	This study – *R3c* (mS/cm)	Experiment (mS/cm)	Ref.
873	0.20	5.71±0.71	5.72±0.23	5	[290]
1073	0.15	41.48±0.82	44.40±2.60	45	[286]
	0.20	40.85±0.61	39.37±0.55	46	[290]

The DIPPIM ionic conductivities for LSG10 are in reasonable agreement with the available experimental data; DIPPIM σ values are slightly higher than experimental results. This is expected, since at x = 0.10 the formation of secondary phases is already observed experimentally, hindering ionic conduction. A better comparison between DIPPIM and experimental results cannot be made due to the lack of available experimental data at different temperatures and concentrations. DIPPIM predicts maximum conductivity for LSG20 at 1073 K and 1273 K, in agreement with the optimum concentration range ($0.10 < x < 0.20$) from experimental studies, depending on secondary phase formation. DIPPIM results for LGM, on the other hand, are in excellent agreement with experimental values.

5.5.1.2 Activation energy of diffusion in LSG and LGM

The Arrhenius equation (Equations 3.27 and 3.28) relates the diffusion coefficient to the activation energy of diffusion (E_a); from Equation 3.28, a plot of lnD against 1/T, i.e. an Arrhenius plot, should yield a straight line with slope $-E_a/R$. The presence of curvature and consequent change on slope in the Arrhenius plot indicates the existence of distinct ionic diffusion mechanisms on the different temperature regions. Experimentally, the observed change in slope in the Arrhenius plots of Sr- and Mg-doped $LaGaO_3$ systems has been related to the occurrence of defect clustering; the existence of a critical temperature (T*) above which defects (vacancies) are mobile has been suggested. Under T*, dopants might act as nucleation centres for the formation of vacancy clusters, resulting in vacancy ordering and hindering ionic conduction [74,325]. Accordingly, activation energies can be calculated under two regimes: T < T* and for T > T*. The critical temperature for LSGM is 873 K [74], i.e. vacancies are mobile above such temperature. Hence, since simulations were carried out in the 873-1273 K range (T > T* regime), DIPPIM results should yield linear Arrhenius plots.

The activation energies of $La_{1-x}Sr_xGaO_{3-\delta}$ (x = 0.10, 0.15, 0.20, 0.25, 0.30 and 0.35) and $LaGa_{1-y}Mg_yO_{3-\delta}$ (y = 0.05, 0.10, 0.15, 0.20, 0.25, 0.30 and 0.35) systems were calculated from the linear fit of the lnD against 1/T plots. The Arrhenius plot for orthorhombic LSG30 is shown in Figure 5.7 as an example. All obtained plots are linear, with r-squared values between 0.982 and 1.000, indicating that the ionic diffusion mechanism does not change in the 873-1273 K temperature range. The calculated activation energy values for orthorhombic and rhombohedral LSG and LGM phases are presented in Table 5.10 and Figure 5.8.

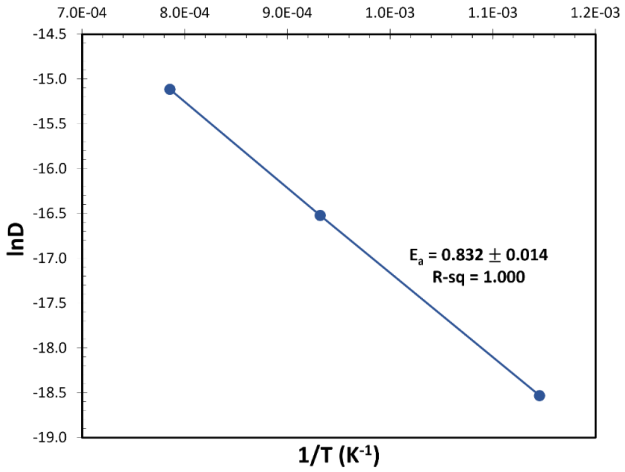

Figure 5.7 – Arrhenius plot (*lnD* against 1/T) for orthorhombic (*Pbnm*) $La_{0.7}Sr_{0.3}GaO_{3-\delta}$ within the 873-1273 K temperature range, with the calculated activation energy and r-squared of the linear fit displayed on the graph.

Table 5.10 – Activation energies (E_a) of oxide-ion diffusion (in eV) for orthorhombic (*Pbnm*) and rhombohedral (*R3c*) $La_{1-x}Sr_xGaO_{3-\delta}$ (LSG with x = 0.10, 0.15, 0.20, 0.25, 0.30 and 0.35) and $LaGa_{1-y}Mg_yO_{3-\delta}$ (LGM with y = 0.05, 0.10, 0.15, 0.20, 0.25, 0.30 and 0.35) systems, calculated from 873 K to 1273 K, along with the available experimental results. Errors are given as standard errors.

System	Dopant content	Ea (eV) - *Pbnm*	Ea (eV) - *R3c*	Experiment (eV)	Ref.
LSG	**0.10**	0.632±0.025	0.622±0.001	0.82, 0.71	[290], [291]
	0.15	0.675±0.061	0.725±0.019	-	-
	0.20	0.710±0.016	0.723±0.001	0.72	[290]
	0.25	0.754±0.046	0.723±0.042	-	-
	0.30	0.832±0.014	0.740±0.001	-	-
	0.35	0.780±0.001	0.805±0.014	-	-
LGM	**0.05**	0.665±0.042	0.638±0.030	-	-
	0.10	0.681±0.020	0.717±0.030	0.86	[290]
	0.15	0.697±0.015	0.794±0.056	0.75	[291]
	0.20	0.768±0.034	0.759±0.001	0.96	[290]
	0.25	0.755±0.017	0.823±0.013	-	-
	0.30	0.864±0.013	0.814±0.026	-	-
	0.35	0.819±0.052	0.904±0.015	-	-

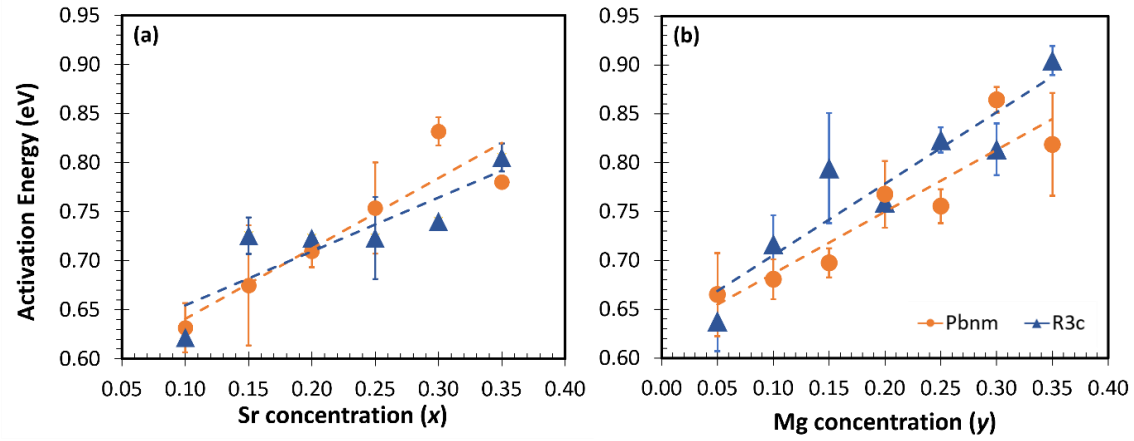

Figure 5.8 – Activation energy vs. dopant concentration in orthorhombic (*Pbnm*, in orange) and rhombohedral (*R3c*, in blue) (a) $La_{1-x}Sr_xGaO_{3-\delta}$ and (b) $LaGa_{1-y}Mg_yO_{3-\delta}$ systems. Activation energies were extracted from the Arrhenius plot of the DIPPIM diffusion coefficients at high temperatures (873-1273 K). The dashed lines are trendlines and error bars are given as standard errors.

It has been suggested that the magnitude of the activation energy for oxide-ion conduction in $LaGaO_3$-based systems depends on the ionic radii of dopants, which can affect the available space for oxide-ion transport [74]. Larger dopants tend to result in higher activation energies, while smaller dopants decrease the observed values. 12-coordinated Sr^{2+} (1.44 Å [26]) is bigger than La^{3+} (1.36 Å [26]), and hence an increase in dopant concentration should result in an increase in the activation energy for oxide-ion transport [290,291]. From Table 5.10 and Figure 5.8, it is possible to observe that activation energies indeed tend to increase with Sr concentration. Similarly, 6-coordinated Mg^{2+} (0.72 Å [26]) is bigger than Ga^{3+} (0.62 Å [26]), and hence an increase in dopant content would also decrease the available space for oxide-ion transport [290,291]. Because the difference in ionic radius to the host cation is bigger for the Mg(II)/Ga(III) pair than for the Sr(II)/La(III) pair, Mg-doping should introduce more lattice strain to the perovskite than Sr substitution. Furthermore, the bigger radius of Mg(II) decreases the value of the Goldschimidt tolerance factor (t) (Equation 1.5), increasing lattice tension. As a result, for the same dopant concentration, activation energies are bigger for LGM than for LSG. In addition, a bigger variation in activation energy values with dopant concentration is observed for Mg-doping [74,290]. This can be visualized from the trendlines in Figure 5.8 (a) and (b), for both orthorhombic and rhombohedral phases; the variation of E_a (y axis) for Sr-doped samples is smaller than what is observed for LGM.

For both LSG and LGM, similar E_a values were obtained for the orthorhombic and rhombohedral phases, with neither phase tending to possess higher/lower activation energies. Our results are also in good agreement to some of the available experimental data. Still, the available experimental data is limited, and a better understanding of the quality of the data calculated by DIPPIM will be achieved for co-doped samples, for which larger sets of experimental data are available.

5.5.1.3 Local structure of singly doped systems

The local structure in LSG and LGM, the defect interactions (dopant-vacancy and vacancy-vacancy), and their influence in the calculated ionic conductivity and activation energy values were investigated through the analysis of the partial radial distribution functions (RDFs). The two-configuration average Sr-oxygen vacancy (Sr-vac), La-oxygen vacancy (La-vac), Mg-oxygen vacancy (Mg-vac), Ga-oxygen vacancy (Ga-vac) and oxygen vacancy-oxygen vacancy (vac-vac) RDFs at 1073 K for the orthorhombic (*Pbnm*) and rhombohedral (*R3c*) LSG and LGM structures were calculated and compared to a random distribution of vacancies (La-O, Ga-O and O-O RDFs of the pure $LaGaO_3$ phases at the same temperature), where no defect ordering has occurred. The RDFs peaks were integrated, with the obtained values corresponding to the number of vacancies surrounding an A-site cation (for La-vac and Sr-vac RDFs), a B-site cation (for Ga-vac and Mg-vac RDFs) or another vacancy (for the vac-vac RDFs) from a given distance. RDFs were calculated using Equation 3.30 and its peaks were integrated as in Equation 3.31.

The A-site sublattice in LSG

The Sr-vac and La-vac partial RDFs were calculated for all dopant concentrations in orthorhombic and rhombohedral LSG. The obtained plots for *Pbnm* LSG20 at 1073 K are presented in Figure 5.9, along to the La-O RDF of pure $LaGaO_3$ at the same temperature, which represents a random distribution of the same number vacancies, where no defect ordering has occurred. The plots for the remaining dopant concentrations and for the rhombohedral structure are not shown, as the same features are observed in all of them, with the only difference being the intensity of the peaks.

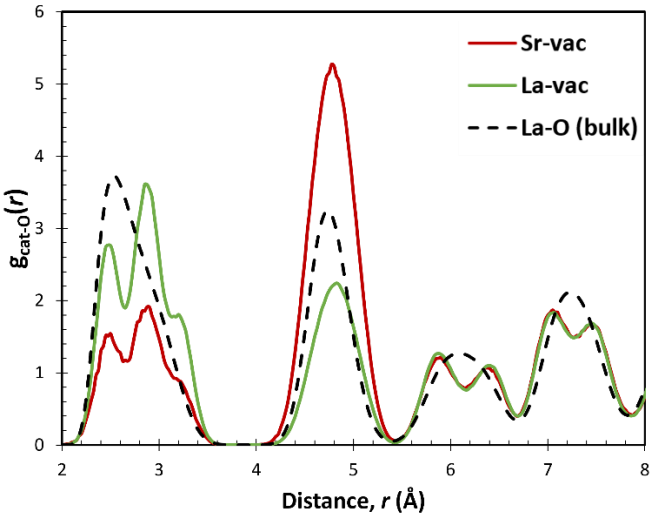

Figure 5.9 – Cation-vacancy partial radial distribution functions, $g_{cat\text{-}vac}(r)$, obtained from MD simulations at 1073 K for orthorhombic (*Pbnm*) LSG20. Sr-vacancy and La-vacancy RDFs are represented by red and green solid lines, respectively. The La-O RDF in the bulk $LaGaO_3$ structure at 1073 K is shown in black (dashed) for comparison.

The RDF features in Figure 5.10 can be related to the local structure around La(III) and Sr(II) ions; Figure 5.10 shows the oxygen coordination environment around A-site cations in the cubic (*Pm3m*) perovskite lattice, i.e. which oxide-ions are located at the cation's first (nearest-neighbour, NN), second (next-nearest-neighbour, NNN) and third (next-next-nearest-neighbour, NNNN) coordination shells. A *Pm3m* perovskite cell is also shown in Figure 5.10 for comparison. The cubic lattice (instead of the orthorhombic) was chosen to depict the local structure around La(III) and Sr(II), as the A-site sublattice and coordination environment is similar in both *Pm3m* and *Pbnm* phases, but more easily observed in the first. The tilting of the GaO_6 octahedra in the *Pbnm* and *R3c* structures simply increases the variety of La-O bond distances within the same coordination shell, which might split some of the RDF peaks.

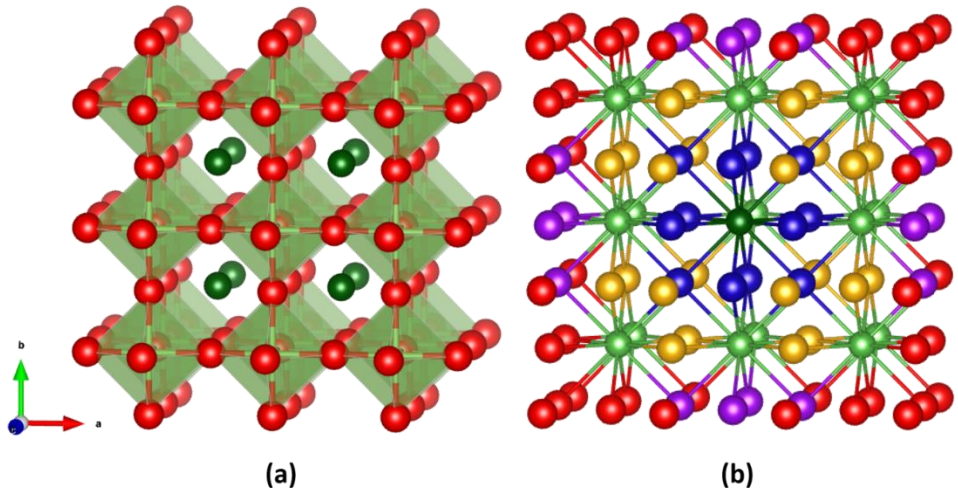

Figure 5.10 – (a) The cubic (*Pm3m*) perovskite lattice of $LaGaO_3$, with La and Ga ions in dark and light green (and the latter being located at the centre of the octahedra), respectively, and O ions in red. (b) The coordination environment around a La ion, represented as the dark green ion in the centre of the structure. The first (NN), second (NNN) and third (NNNN) coordination shells around the La ion are given by blue, yellow and purple oxide ions, respectively. The remaining La in the structure are light green, and oxygen ions that are further away than a NNNN position are in red. Ga ions were removed for clarity.

The three-peak feature in the Sr-Vac and the La-Vac RDFs, located between 2.0-3.5 Å, describes the occupation of NN sites and arises as thermal vibrations are not taken into account for the vacancy RDFs. La(III) and Sr(II) are 12-coordineated in the $LaGaO_3$ structure, and hence possess 12 NN sites in their surroundings, as shown by the blue oxygen ions in Figure 5.10b. While in the cubic lattice the La-O NN bond length is 2.74 Å, in the distorted orthorhombic structure there are eight distinct bond distances within La(III) 12-cordination sphere. The three-peak feature in the RDF reflects such bond lengths, which are (in Å) 2.40, 2.44, 2.60 and 2.62 (1^{st} peak), 2.81 and 2.98 (2^{nd} peak), 3.14 and 3.21 (3^{rd} peak). The same NN feature corresponds to one broad peak in the La-O RDF, as oxygen atoms thermally vibrate. No other significant discrepancies are observed among the three plots. The second RDF feature, with maximum around 4.7 Å, corresponds to 24 NNN sites, shown as yellow oxygen ions in Figure 5.10b. The intensity of the NNN feature in the Sr-vac and La-vac RDFs is higher and lower than the random distribution (La-O), respectively, indicating that there are more vacancies around Sr(II) in a NNN site than around La(III). The third feature, centred at approximately 6.2 Å, corresponds to the purple oxygen ions and the

24-coordinated NNNN shell in Figure 5.10b; the intensity of the NNNN peaks in the Sr-vac and the La-vac RDFs seems to be similar to that of a random distribution. The number of vacancies surrounding the A-site cations (in orthorhombic LSG) in NN, NNN and NNNN sites were calculated through the integration of the RDF peaks (as in Equation 3.31) and are presented in Table 5.11. Rhombohedral results, which follow the same trends that will be discussed for the orthorhombic structure, are presented in Table A.5 (see Appendix).

Table 5.11 – Number of oxygen vacancies surrounding A-site cations (La and Sr) in orthorhombic (*Pbnm*) $La_{1-x}Sr_xGaO_{3-\delta}$ (x = 0.10, 0.15, 0.20, 0.25, 0.30, 0.35) at 1073 K, occupying the nearest-neighbour (NN), next-nearest-neighbour (NNN) and next-next-nearest-neighbour (NNNN) positions. La-O corresponds to a random distribution of vacancies where no defect ordering has occurred.

x	**La-O**			**La-vac**			**Sr-vac**		
	NN	**NNN**	**NNNN**	**NN**	**NNN**	**NNNN**	**NN**	**NNN**	**NNNN**
# sites	12	24	24	12	24	24	12	24	24
0.10	0.198	0.399	0.395	0.208	0.337	0.394	0.122	0.949	0.407
0.15	0.300	0.604	0.597	0.320	0.483	0.595	0.193	1.274	0.627
0.20	0.396	0.799	0.790	0.437	0.627	0.797	0.240	1.480	0.781
0.25	0.498	1.003	0.992	0.570	0.760	1.005	0.290	1.722	0.980
0.30	0.599	1.207	1.194	0.701	0.881	1.224	0.372	1.954	1.158
0.35	0.696	1.402	1.386	0.820	1.008	1.416	0.473	2.127	1.370

La(III) ions are surrounded by more oxygen vacancies at a NN site than Sr(II) for all dopant concentrations. The number of vacancies around La(III) and Sr(II) in a NN position are slightly higher and lower, respectively, than that which is observed in a random distribution (La-O), where no defect ordering has occurred. Sr(II) is surrounded by considerably more oxygen vacancies at a NNN site, when compared to both La-vac and La-O, most likely as a result of its bigger ionic radius or of its lower charge, decreasing the electrostatic repulsion experienced by vacancies when compared to the host cation. The increase in the number of vacancies at NNN sites is significantly higher than the observed reduction at NN, suggesting that such NNN occupation is not a result of a simple redistribution of vacancies, but an indication of vacancy trapping. Such over-occupation could also be the reason for the observed depletion of vacancies around La. The amount of

vacancies at NNNN sites is close to that of a random distribution for both La and Sr cations. Hence, the total number of vacancies around Sr ions is higher than expected (from the sum of NN, NNN and NNNN), with substantially more vacancies in NNN sites, while there are less at NN sites and about the expected at NNN sites. These results confirm that vacancies are trapped around Sr cations at NNN sites and go against what was predicted in Chapter 4, where DFT results suggested that vacancies would be preferably located NN to dopants. Such disagreement could be a result of concentration or dynamic effects, considered in MD simulations but not taken into account in DFT. Vacancies being trapped at a NNN position to the dopant might be a contributing factor to the ionic conductivity drop observed for Sr content higher than 25 mol%; if vacancies are trapped at NNN sites and cannot get any closer to Sr ions, a conduction channel might be blocked. For higher Sr concentrations, a significant portion of the lattice might be blocked, as Sr ions are closer together, leading to a decrease in ionic conduction.

The B-site sublattice in LGM

The Mg-vac and Ga-vac partial RDFs were calculated for all dopant concentrations in orthorhombic and rhombohedral $LaGa_{1-y}Mg_yO_{3-\delta}$. The obtained plots for orthorhombic LGM10 at 1073 K are presented in Figure 5.11, along to the Ga-O RDF of pure $LaGaO_3$ at the same temperature, representing a random distribution of vacancies. The plots for the remaining dopant concentrations and for the rhombohedral structure are not shown, as the same features are observed in all of them. Figure 5.12 shows the oxygen coordination environment around a Ga(III) cations in a cubic (*Pm3m*) cell; the first RDF peak (between 1.5 to 2.5 Å) corresponds to 6 NN sites, shown as blue oxygen ions in Figure 5.12b, all part of the same GaO_6 octahedron. The second feature in the RDF (between 3.7 and 4.9 Å), corresponds to 24 NNN sites, shown as yellow oxide ions in Figure 5.12b. The third feature (between 5.2 and 6.5 Å) corresponds to the 30 NNNN sites, shown as purple oxide ions in Figure 5.12b.

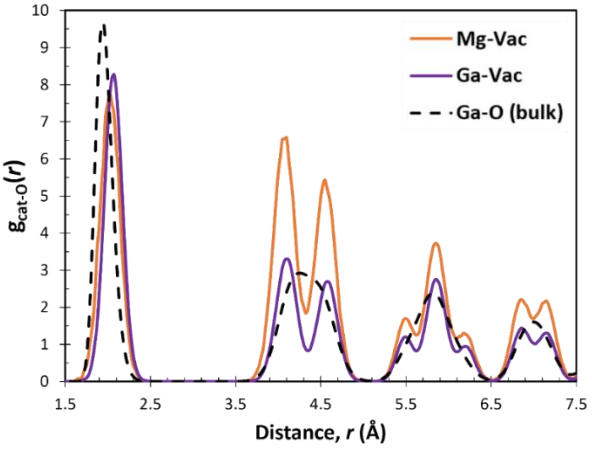

Figure 5.11 – Cation-vacancy partial distribution functions, $g_{cat-vac}(r)$, obtained from MD simulations at 1073 K for orthorhombic (*Pbnm*) $LaGa_{0.9}Mg_{0.10}O_{3-\delta}$. Mg-vacancy and Ga-vacancy RDFs are represented by orange and purple solid lines, respectively. The Ga-O RDF for the bulk $LaGaO_3$ structure at 1073 K is shown in black (dashed) for comparison

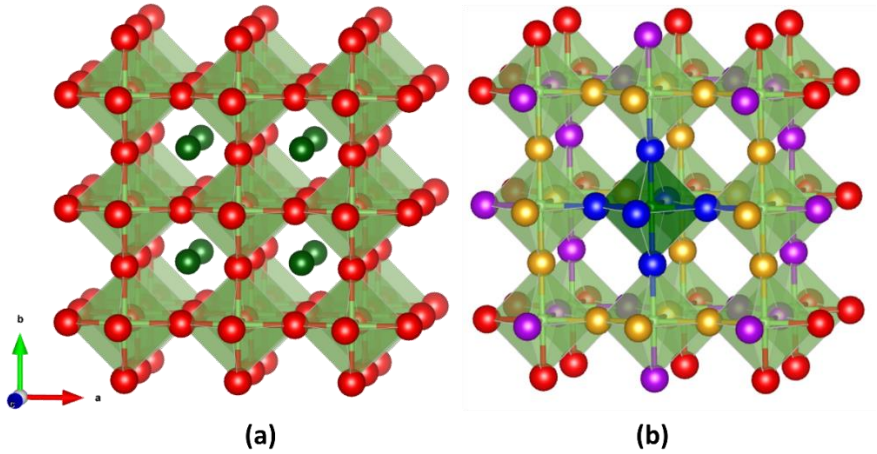

Figure 5.12 – (a) The cubic (*Pm3m*) perovskite lattice of $LaGaO_3$, with La and Ga ions in dark and light green (and the latter being located at the centre of the octahedra), respectively, and O ions in red. (b) The coordination environment around a Ga ion, represented as the dark green ion in the centre of the structure. The first (NN), second (NNN) and third (NNNN) coordination shells around the Ga ion are given by blue, yellow and purple oxide ions, respectively. The remaining Ga in the structure are light green, and oxygen ions that are further away than a NNNN position are in red. La ions were removed for clarity.

There are no significant discrepancies between the cation-vacancy and Ga-O partial RDFs, except for the splitting of the peaks composing the NNN and NNNN features, which

results in double and triple peaks in the Ga-vac and Mg-vac RDFs, as thermal vibrations are not included in such plots, and a single broad feature in the Ga-O RDF. Furthermore, Ga-vac and Mg-vac distances are a bit longer than the Ga-O distances in a random distribution, most likely as a result of the experimentally observed lattice expansion arising from Mg(II) doping [291] due to its larger ionic radius when compared to Ga(III). The number of oxygen vacancies surrounding a B-site cation (Ga or Mg) at NN (between 1.5 to 2.5 Å), NNN (between 3.7 and 4.9 Å) and NNNN positions (between 5.2 and 6.5 Å) in orthorhombic LGM, calculated through the integration of the RDF peaks are presented in Table 5.12. Rhombohedral LGM results follow the same trends that will be discussed for the orthorhombic structure and are presented in Table A.6 (see Appendix).

Table 5.12 – Number of oxygen vacancies surrounding a B-site cation (Ga or Mg) in orthorhombic (*Pbnm*) $LaGa_{1-y}Mg_yO_{3-\delta}$ (y = 0.05, 0.10, 0.15, 0.20, 0.25, 0.30, 0.35) at 1073 K, occupying the nearest-neighbour (NN), next-nearest-neighbour (NNN) and next-next-nearest neighbour (NNNN) positions. Ga-O corresponds to a random distribution of vacancies where no defect ordering has occurred.

y	**Ga-O (*Pbnm*)**			**Ga-vac (*Pbnm*)**			**Mg-vac (*Pbnm*)**		
	NN	**NNN**	**NNNN**	**NN**	**NNN**	**NNNN**	**NN**	**NNN**	**NNNN**
# sites	6	24	30	6	24	30	6	24	30
0.05	0.051	0.203	0.254	0.049	0.188	0.247	0.090	0.504	0.390
0.10	0.100	0.399	0.499	0.100	0.363	0.481	0.101	0.738	0.673
0.15	0.149	0.597	0.747	0.147	0.539	0.708	0.168	0.946	0.988
0.20	0.198	0.792	0.991	0.190	0.710	0.963	0.236	1.145	1.131
0.25	0.248	0.993	1.243	0.243	0.886	1.201	0.270	1.341	1.403
0.30	0.299	1.194	1.495	0.287	1.061	1.454	0.333	1.537	1.628
0.35	0.347	1.388	1.737	0.332	1.204	1.675	0.385	1.765	1.897

The number of oxygen vacancies located at the first coordination shell of Mg(II) is somewhat higher than that of Ga(III), probably due to a decreased electrostatic repulsion experienced by vacancies, which possess an effective +2 charge, from the divalent dopant. At a NNN site, there is a clear preference of vacancies to be around dopant cations instead of Ga(III), similarly to that which was observed in Sr-doped samples, where oxygen

vacancies are preferably located at the cation's second coordination shell. The occupation of NNNN sites around Mg cations is also higher than that of a random distribution. Since the occupation of all coordination shells around Mg is elevated, vacancies can still move among the different shells and are presumably not trapped, in contrast to Sr-doped samples, where vacancies at NNN sites are unlikely to escape to adjacent shells, as the concentration in NN and NNNN are the same or smaller than average, creating a barrier for NNN vacancies. Therefore, despite NNN being more elevated than NN and NNNN in LGM, these results could be interpreted as less trapping than what was observed in LSG, which could explain the higher conductivity values observed for Mg-doped samples.

The oxide-ion sublattice in singly doped phases

The vacancy-vacancy partial RDFs were also calculated for all dopant concentrations in orthorhombic and rhombohedral LSG and LGM. The obtained plots for orthorhombic and rhombohedral LSG20 at 1073 K are presented in Figure 5.13, along with the O-O RDF of pure $LaGaO_3$ at 300 K and 1073 K, representing a random distribution of vacancies. The plots for the remaining dopant concentrations and for LGM are not shown, as the same features are observed, with the only difference being the intensity of the peaks.

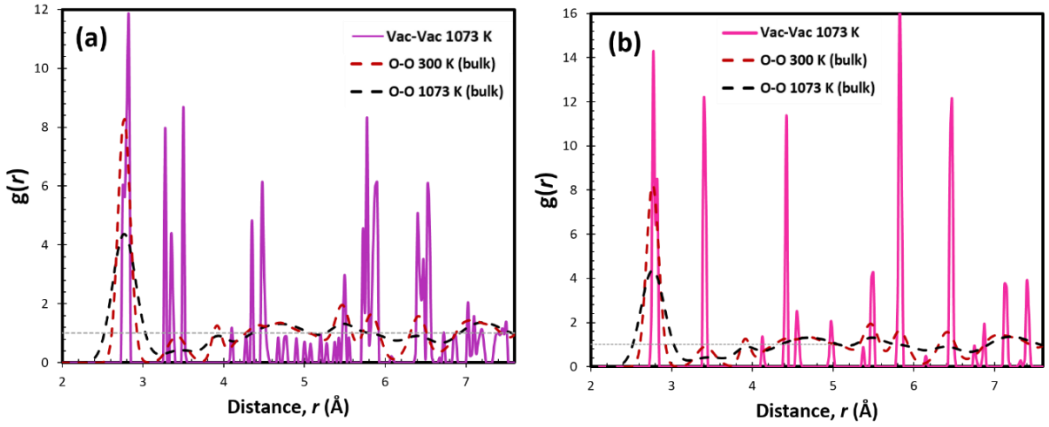

Figure 5.13 – Oxygen-vacancy and vacancy-vacancy partial radial distribution functions, g (*r*), obtained from MD simulations at 1073 K for (a) orthorhombic (*Pbnm*) and (b) rhombohedral (*R3c*) $La_{0.8}Sr_{0.2}GaO_{3-\delta}$. Vacancy-vacancy RDFs are represented by purple and pink solid lines. The O-O RDFs for the pure $LaGaO_3$ structure at 300 K and 1073 K are shown in red and black dashed lines for comparison.

The oxygen-oxygen coordination in the orthorhombic and rhombohedral phases is intricate and cannot be easily compared to that observed in the cubic structure. The RDF features between 2.4 and 3.2 Å correspond to NN sites, while all peaks between 3.2 and 5.6 Å are associated to NNN sites. NNNN positions are all above 5.7 Å. In the analysis of the vacancy-vacancy RDFs, six oxygen-oxygen bond distance intervals, and hence six coordination environments, will be evaluated: between 2.4 and 3.2 Å (1st coordination shell), 3.2 to 3.6 Å (2nd coordination shell), 3.8 to 5.6 Å (3rd coordination shell), 5.7 to 6.0 Å (4th coordination shell), 6.0 to 6.6 Å (5th coordination shell) and 6.6 to 7.6 Å (6th coordination shell). Hence, the 1st region corresponds to NN sites, the 2nd and 3rd regions represent NNN sites, while the 4th, 5th and 6th regions are related to NNNN sites. The number of oxygen vacancies surrounding another oxygen vacancy in the six distinct coordination environments were calculated through the integration of the RDF peaks and are presented in Tables 5.13 (orthorhombic LSG) and 5.14 (orthorhombic LGM). Results for the rhombohedral phases follow the same trends that will be discussed in this section and are presented in Tables A.7 and A.8 (see Appendix).

Table 5.13 – Number of oxygen vacancies surrounding another oxygen vacancy in orthorhombic (*Pbnm*) $La_{1-x}Sr_xGaO_{3-\delta}$ (x = 0.10, 0.15, 0.20, 0.25, 0.30, 0.35) at 1073 K, occupying sites in six different coordination shells. O-O corresponds to a random distribution of vacancies at the same temperature where no defect ordering has occurred.

x	O-O						vac-vac					
	1st	2nd	3rd	4th	5th	6th	1st	2nd	3rd	4th	5th	6th
0.10	0.136	0.018	0.508	0.175	0.138	0.569	0.046	0.067	0.177	0.322	0.333	0.262
0.15	0.205	0.027	0.769	0.264	0.208	0.860	0.083	0.084	0.293	0.490	0.485	0.384
0.20	0.271	0.036	1.017	0.349	0.275	1.138	0.130	0.135	0.369	0.636	0.573	0.493
0.25	0.341	0.045	1.278	0.439	0.346	1.429	0.168	0.161	0.447	0.723	0.691	0.621
0.30	0.410	0.055	1.539	0.529	0.416	1.721	0.208	0.208	0.481	0.794	0.863	0.591
0.35	0.476	0.064	1.786	0.614	0.483	1.998	0.327	0.229	0.590	0.876	0.988	0.788

Table 5.14 – Number of oxygen vacancies surrounding another oxygen vacancy in orthorhombic (*Pbnm*) $LaGa_{1-y}Mg_yO_{3-\delta}$ (y = 0.05, 0.10, 0.15, 0.20, 0.25, 0.30, 0.35) at 1073 K, occupying sites in six different coordination shells. O-O corresponds to a random distribution of vacancies at the same temperature where no defect ordering has occurred.

y	O-O						vac-vac					
	1st	**2nd**	**3rd**	**4th**	**5th**	**6th**	**1st**	**2nd**	**3rd**	**4th**	**5th**	**6th**
0.05	0.069	0.009	0.259	0.089	0.070	0.290	0.038	0.052	0.154	0.229	0.312	0.135
0.10	0.136	0.018	0.508	0.175	0.138	0.569	0.107	0.093	0.255	0.378	0.428	0.262
0.15	0.203	0.027	0.761	0.262	0.206	0.852	0.144	0.158	0.378	0.511	0.524	0.481
0.20	0.269	0.036	1.009	0.347	0.273	1.129	0.129	0.186	0.495	0.603	0.629	0.723
0.25	0.338	0.045	1.266	0.435	0.343	1.416	0.161	0.280	0.647	0.661	0.706	0.976
0.30	0.406	0.054	1.523	0.523	0.412	1.704	0.174	0.323	0.823	0.772	0.769	1.282
0.35	0.472	0.063	1.770	0.608	0.479	1.980	0.230	0.383	0.981	0.840	0.874	1.451

In both LSG and LGM systems, the number of vacancies surrounding another vacancy at the 1st and 2nd coordination shells is lower and higher than the random distribution, respectively. The 1st shell corresponds to vacancy sites that are located within the same GaO_6 octahedra, while the 2nd shell describes sites located in the adjacent octahedra. Hence, these results indicate that vacancies are effectively trying to avoid each other, most likely because of their effective positive charge. The shift at around 4 Å in the vac-vac RDF with respect to the O-O RDF occurs because the 0 K DFT $LaGaO_3$ structure was used to define the oxygen sites for the vacancy analysis (Section 3.3.6), which will then locate the oxygen vacancies at the oxygen lattice sites specified by DFT. As a result, some shifts in the vac-vac RDF are expected due to structural changes happening during the high temperature MD simulations. The 3rd coordination shell is underpopulated with respect to a random distribution, while the 4th and 5th shells are overpopulated, revealing that vacancies are indeed repelling each other. The number of vacancies in the 6th coordination shell in LSG and LGM is smaller than the random distribution, suggesting that vacancy ordering continues throughout the lattice in singly doped systems. Interestingly, the 1st, 3rd and 6th shells are more depleted in LSG when compared to LGM, while the 2nd, 4th and 5th shells are more populated in LSG than in LGM. These results indicate that vacancy ordering occurs to a higher extent in Sr-doped samples, which can be related to the lower ionic conductivity values observed for LSG.

5.5.2 Co-doped $LaGaO_3$ systems

5.5.2.1 Ionic conductivity in LSGM

The oxide ion-conductivity of $La_{1-x}Sr_xGa_{1-y}Mg_yO_{3-\delta}$ (x = 0.10, 0.15, 0.20, 0.25 and y = 0.05, 0.10, 0.15, 0.20, 0.25, 0.30, 0.35) was also investigated from the analysis of the mean square displacements at 873, 1073 and 1273 K. Figures 5.14 and 5.15 are heat maps for the ionic conductivity of orthorhombic and rhombohedral systems, respectively, showing the variation in σ with Sr and Mg content; higher conductivity values are in green, while the lowest results are in red. The diffusion coefficients and ionic conductivities used to build these heat maps are presented in Tables A.9-A.16 (see Appendix).

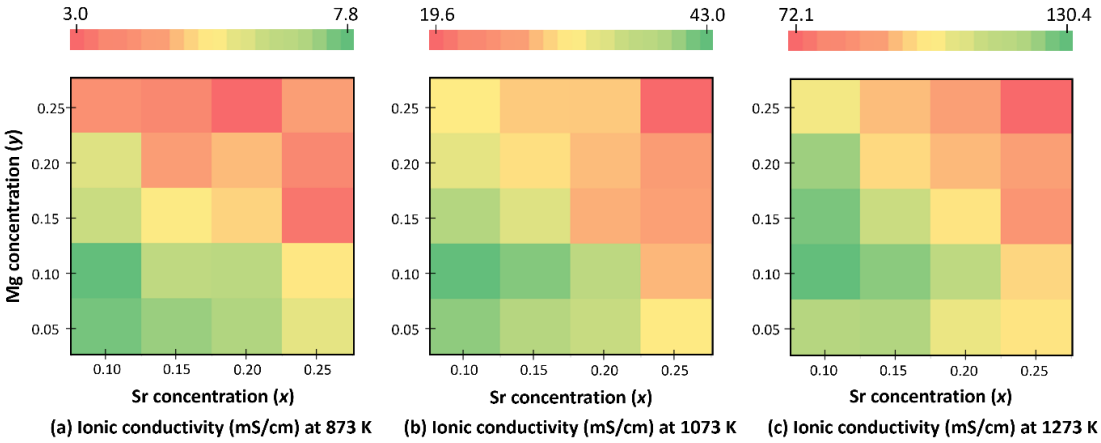

Figure 5.14 – Variation of ionic conductivity values in $La_{1-x}Sr_xGa_{1-y}Mg_yO_{3-\delta}$ systems with dopant concentration, x and y, at (a) 873 K, (b) 1073 K and (c) 1273 K for orthorhombic (*Pbnm*) $LaGaO_3$. Higher ionic conductivities are given in green, and the lowest values are in red.

The best improvements in the ionic conductivity of LSGM are observed for lower values of x and y; the highest σ value was obtained for LSGM1010 under all analysed temperatures, for both orthorhombic and rhombohedral phases. In orthorhombic LSGM, regardless of Sr content 10 mol% is the most favourable Mg concentration for ionic conduction, in contrast to singly doped systems in which y = 0.20 is optimal. Considering the calculated standard errors, the optimal range of Sr and Mg content is within $0.10 \leq x \leq 0.20$ and $0.05 \leq y \leq 0.10$.

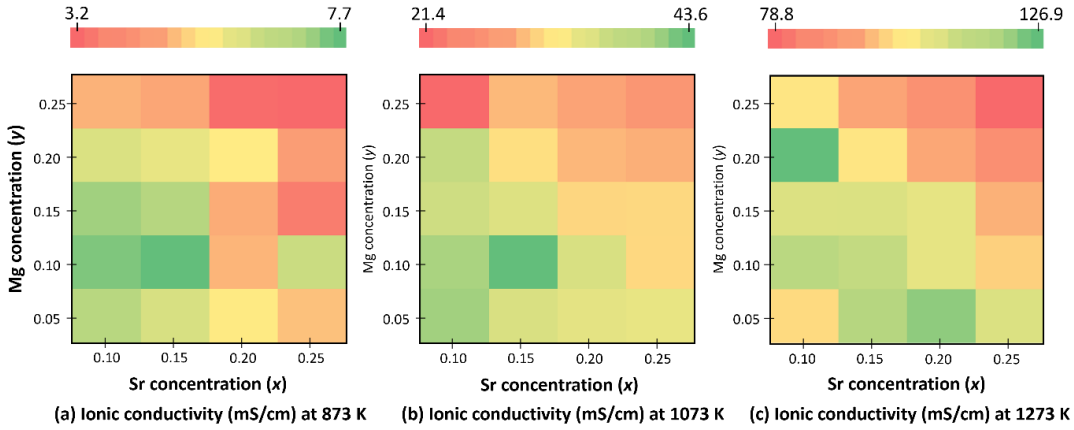

Figure 5.15 – Variation on ionic conductivity values with dopant concentration, *x* and *y*, at (a) 873 K, (b) 1073 K and (c) 1273 K for rhombohedral (*R3c*) $LaGaO_3$. Higher ionic conductivities are given in green, and the lowest values are in red.

For rhombohedral $LaGaO_3$, the optimal Mg content varies depending on Sr concentration; for lower Sr content (x = 0.10, 0.15), y = 10 is ideal. For higher Sr concentrations, on the other hand, the highest σ values are obtained for a slightly lower y at 0.05. If the calculated standard errors are taken into account, the optimal dopant concentration range is between $0.10 \leq x \leq 0.15$, with $x = 0.20$ presenting comparable σ values only at higher temperatures (1273 K), and between $0.05 \leq y \leq 0.15$.

The optimal range for dopant concentration (green regions in Figures 5.14 and 5.15) is observed to slightly change with temperature, for both orthorhombic and rhombohedral LSGM systems. Such anisotropic change might be related to the different dependence of the activation energy for oxide-ion conduction on x and y. The same behaviour was reported by Huang *et al*. [74], who observed that at 1073 K the optimal region was within the 0.125-0.25 range for both x and y, shrinking at lower temperatures (to $0.15 < x < 0.20$ and $0.125 < y < 0.175$ at 973 K and to $0.145 < x < 0.16$ and $0.0 < y < 0.06$ at 868 K).

Figure 5.16 summarizes the information presented in Tables A.9-A.16. It shows the similarity in ionic conductivity values calculated with DIPPIM for the orthorhombic and rhombohedral phases, suggesting that the structural differences upon phase transition do not influence σ significantly.

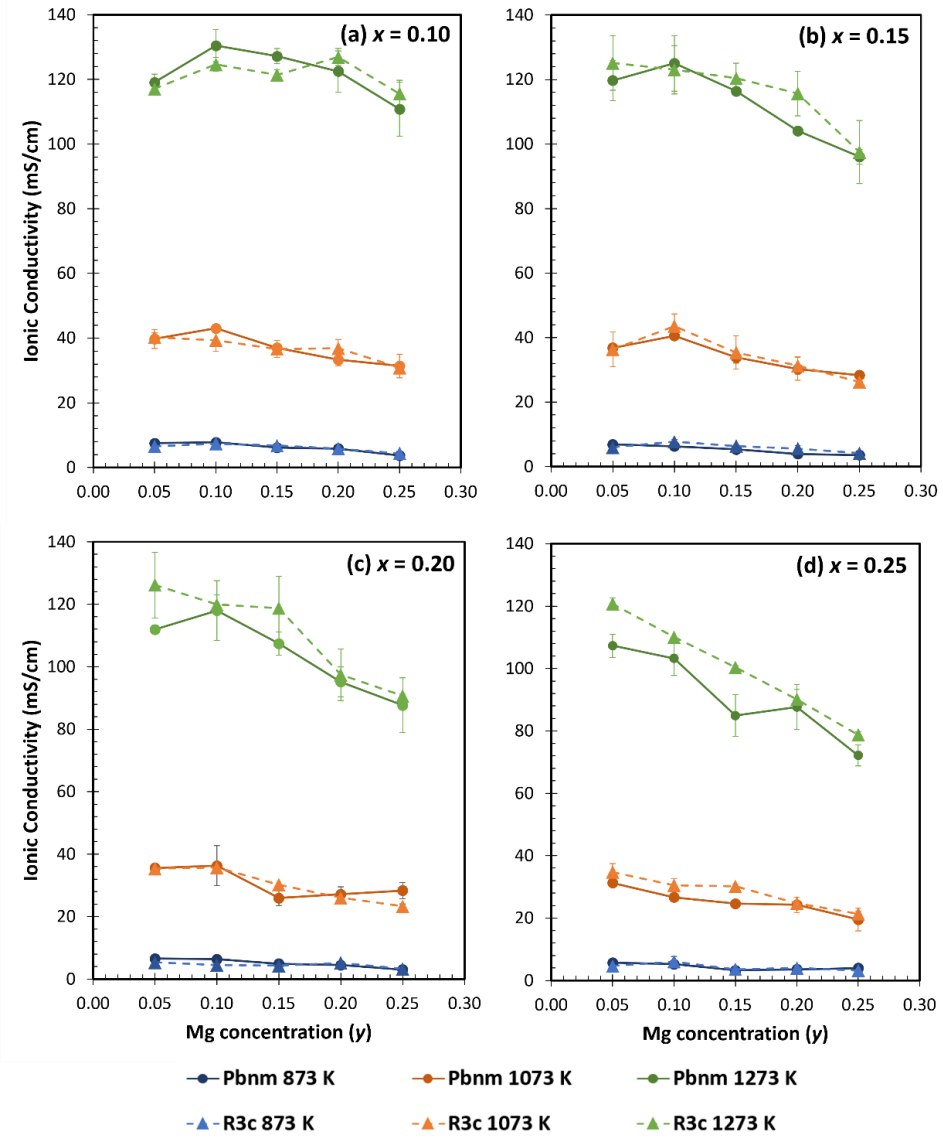

Figure 5.16 – Ionic conductivity in $La_{1-x}Sr_xGa_{1-y}Mg_yO_{3-\delta}$ as a function of Mg concentration, y, for (a) x = 0.10, (b) x = 0.15, (c) x = 0.20 and (d) x = 0.25. Blue (873 K), orange (1073 K) and green (1273 K) solid and dashed lines represent the orthorhombic (*Pbnm*) and rhombohedral (*R3c*) systems, respectively.

Experimentally, similarly to singly doped samples, the ionic conductivity in LSGM seems to be limited by the formation of secondary phases, i.e. σ increases with dopant content until the appearance of impurities, and drops after that. Chen and Fung [290] measured the highest ionic conductivity value for LSGM2020 (73 mS/cm at 1073 K), four times higher than that of YSZ. A decrease in Mg content (LSGM2010) results in the appearance of secondary phase, decreasing σ to 15 mS/cm. Huang *et al.* [74] analysed a wider range of dopant concentrations and determined LSGM2017 to be the optimal

composition for ionic transport, obtaining σ = 166 mS/cm at 1073 K. Secondary phase formation was observed for $y = 0.05$ and $y > 0.20$ regardless of Sr concentration, indicating that a small amount of Mg ($y = 0.05$) might not provide sufficient lattice expansion to increase the solubility of Sr. Even though the study conducted by Huang *et al*. [74] is the only complete set of experimental ionic conductivities for $0.05 \leq x, y \leq 0.30$, the reliability of their results can be put into question, as their obtained σ values are considerably higher than the other available results in literature. They measured high ionic conductivities even for samples containing secondary phases ($LaSrGaO_4$ and/or $LaSrGa_3O_7$), while other studies [290] report a five-fold decrease in σ for samples containing impurities when compared to pure phases. Furthermore, secondary phase formation was observed in more than 70% of their analysed samples. Table 5.15 summarizes the available experimental ionic conductivity data, along with DIPPIM calculated values. Huang *et al*. [74] results are also presented, as they are only complete set of ionic conductivities in LSGM systems with total dopant concentrations ranging from 10 to 60 mol%, and to show the discrepancy between their results and the available experimental data.

Table 5.15 – DIPPIM (*Pbnm* and *R3c* phases) and experimental ionic conductivities (in mS/cm) for $La_{1-x}Sr_xGa_{1-y}Mg_yO_{3-\delta}$, for various dopant concentrations and temperatures. All experimental studies report an orthorhombic structure, except for the work of Huang *et al*. [74], which reports a cubic (*Pm3m*) phase.

T (K)	***x***	***y***	**DIPPIM – *Pbnm* (mS/cm)**	**DIPPIM – *R3c* (mS/cm)**	**Huang *et al.*** [74]	**Exp. (mS/cm)**	**Ref.**
873	0.1	0.2	5.82±0.47	5.81±0.97	18[a]	1.6	[293]
	0.2	0.2	4.45±0.41	5.16±0.03	21	3	[290]
1073	0.1	0.1	43.02±0.56	39.35±3.38	116	95, 107	[283], [324]
	0.1	0.2	33.33±1.88	36.85±2.78	132[a]	107[b]	[293]
	0.2	0.1	36.29±6.42	35.72±1.60	133[a]	15[c]	[290]
	0.2	0.15	25.95±2.49	30.22±0.16	149[a]	140	[324]
	0.2	0.2	27.14±2.35	25.99±0.84	140	73	[290]
1273	0.1	0.1	130.44±4.91	124.61±2.18	-	190	[283]

[a] Samples containing $LaSrGaO_4$ and/or $LaSrGa_3O_7$ secondary phases.
[b] A range of σ values (33.9-107 mS/cm) were measured for distinct sample densities.
[c] Low σ value obtained due to formation of secondary phase.

The variation in the existing experimental data is evident and there is little agreement in literature on the ionic conductivity values of the LSGM system. Experimental studies consistently measure lower σ values when compared to Huang *et al.* [74], especially at 873 K. Hence, DIPPIM calculated results are in better agreement with the lower end of experimental data. A similar trend (DIPPIM values being in better agreement with the lower end of experimental results) was observed by Lucid [139] in a DIPPIM potential derived for CeO_2. The variability among experimental values could be explained by the fact that different experimental techniques yield samples with distinct densities; traditional ceramic techniques, for example, result in super-fine powders with higher surface energy, which tend to aggregate, while samples prepared by the sol-gel method have lower density [293]. Ionic conductivity values were experimentally shown to significantly vary with sample density [293]; six LSGM1020 samples prepared by distinct methods and/or at different sintering temperatures (ranging from 1573 K to 1823 K), yielded a range of sample densities, varying from 4.72 to 6.58 g/cm^3. These samples presented σ values within the 33.9-107.0 mS/cm range at 1073 K, with ionic conductivity increasing with sample density up to 6.17 g/cm^3, and decreasing after that, indicating that there is an optimal density for ionic transport, lower than the theoretical density for the cubic phase. DIPPIM calculates densities within the 6.96-7.10 g/cm^3 range for the orthorhombic and rhombohedral phases depending on temperature and dopant/vacancy content, which could explain the observed discrepancy between DIPPIM and experimental results.

5.5.2.2 Activation energy of diffusion in LSGM

The activation energies of $La_{1-x}Sr_xGa_{1-y}Mg_yO_{3-\delta}$ systems were calculated from the linear fit of the lnD against 1/T plots. The obtained plots are linear, with r-squared values between 0.980 and 1.000, suggesting that no change in the oxide-ion conduction mechanism occurs in the 873-1273 K range, similarly to what was observed in singly doped phases. The calculated activation energy values (E_a) for both orthorhombic and rhombohedral phases are presented in Table 5.16, along with experimental results, and Figure 5.17.

Table 5.16 – Activation energies (E_a) of oxide-ion diffusion (in eV) for orthorhombic (*Pbnm*) and rhombohedral (*R3c*) $La_{1-x}Sr_xGa_{1-y}Mg_yO_{3-\delta}$ systems with x = 0.10, 0.15, 0.20, 0.25 and y = 0.05, 0.10, 0.15, 0.20, 0.25, calculated from 873 K to 1273 K, along with experimental results.

x	***y***	**E_a (eV)** ***Pbnm***	**E_a (eV)** ***R3c***	**Huang *et al*. (eV)** [74]	**Other Exp. (eV)**	**Ref.**
0.10	0.05	0.666±0.004	0.708±0.078	0.783	0.60	[326]
	0.10	0.680±0.016	0.680±0.013	0.993	0.83, 1.20	[290], [283]
	0.15	0.730±0.035	0.694±0.021	1.050		
	0.20	0.731±0.033	0.745±0.049	1.111	1.00, 0.74	[290], [327]
	0.25	0.820±0.001	0.791±0.034	1.146		
0.15	0.05	0.687±0.021	0.730±0.002	0.803	0.52	[326]
	0.10	0.720±0.013	0.669±0.010	0.930		
	0.15	0.742±0.025	0.705±0.005	0.998	0.79	[328]
	0.20	0.790±0.007	0.731±0.029	1.073	0.73	[327]
	0.25	0.813±0.099	0.756±0.002	1.116		
0.20	0.05	0.686±0.035	0.761±0.014	0.815	0.61	[326]
	0.10	0.701±0.008	0.795±0.016	0.935	0.80, 0.61	[290], [326]
	0.15	0.738±0.010	0.804±0.079	0.999	0.62, 0.69	[326], [327]
	0.20	0.737±0.032	0.702±0.017	1.074	1.37, 0.74, 0.78	[290], [326], [327]
	0.25	0.819±0.058	0.800±0.036	1.140		
0.25	0.05	0.705±0.009	0.786±0.015	0.835	0.59	[326]
	0.10	0.716±0.054	0.705±0.070	0.976		
	0.15	0.787±0.007	0.807±0.001	1.067		
	0.20	0.769±0.014	0.750±0.026	1.118		
	0.25	0.696±0.044	0.771±0.004	1.167		

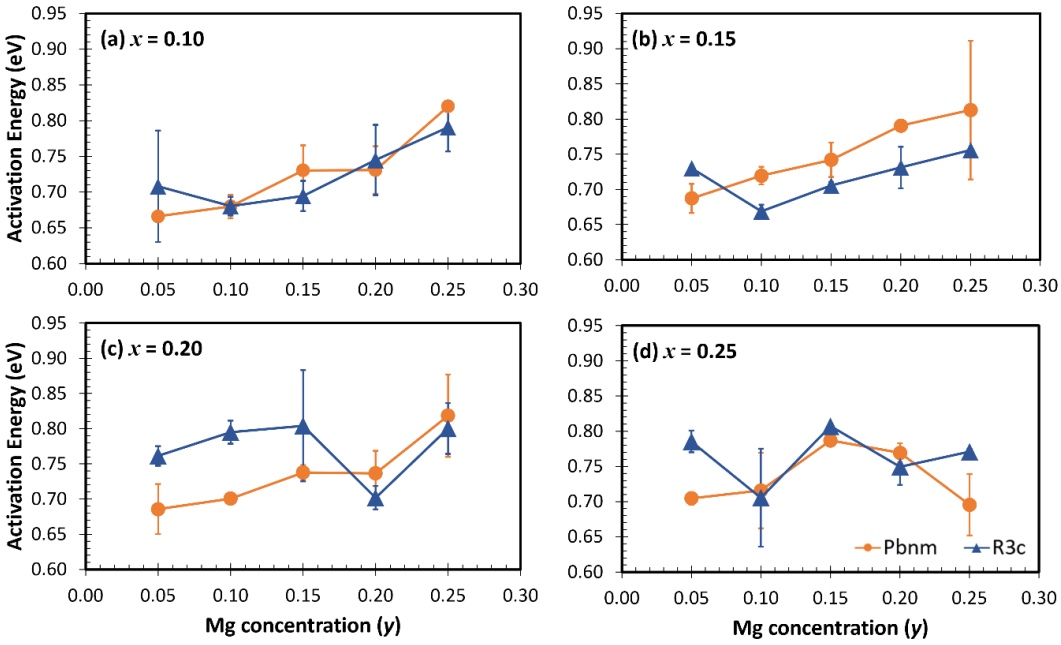

Figure 5.17 – Activation energy in orthorhombic (*Pbnm*, in orange) and rhombohedral (*R3c*, in blue) $La_{1-x}Sr_xGa_{1-y}Mg_yO_{3-\delta}$ systems vs. Mg concentration, *y*, for *x* = (a) 0.10, (b) 0.15, (c) 0.20 and (d) 0.25. Activation energies were extracted from the Arrhenius plot of the DIPPIM diffusion coefficients at high temperatures (873-1273 K).

Experimental values between 0.52-1.37 eV have been reported, while DIPPIM calculates activation energies to be within the 0.67-0.82 eV range. The discrepancy between experimentally reported activation energy values was expected due to the variety of experimental methods, sintering times and temperatures, yielding distinct grain sizes and sample densities. The presence of secondary phases might be the biggest factor contributing to the higher magnitude of experimental values, as impurities would likely hinder oxide-ion transport, hence increasing E_a. In general, DIPPIM results are in good agreement with the available experimental data.

From the values presented in Table 5.16 and from Figure 5.17, for a fixed Sr concentration, E_a increases with Mg content, up to 0.15 eV when the Mg concentration goes from 5 mol% to 25 mol%. For a fixed Mg content, E_a also increases with Sr concentration, but to a smaller extent; for fixed *y* values (0.05, 0.10 or 0.15), the magnitude of E_a increases by 0.04 eV in the orthorhombic system when Sr content goes from 10 mol% to 25 mol%. These trends are not followed by systems with high total dopant concentrations (above 40 mol%), as in such systems other effects such as dopant-vacancy interactions and vacancy

ordering might play a more significant effect. In summary, Mg doping is observed to have a bigger effect on the activation energy, which is also observed experimentally and suggested to result from the difference in size between dopant and host cation, and the resulting lattice strain for such radii mismatch [74,290,326]. The different dependence of the activation energy for oxide-ion conduction on *x* and *y* results in the anisotropic shrinkage of the optimal ionic conductivity regions in the heat maps presented in Figures 5.14 and 5.15.

5.4.2.3 Local structure of co-doped systems

To investigate the local structure and defect chemistry of co-doped systems, the number of oxygen vacancies surrounding A- (La and Sr) and B-site (Ga and Mg) cations at NN, NNN and NNN sites calculated through the integration of the RDF peaks are presented in Tables A.17-A.20 (see Appendix). The number of vacancies surrounding another vacancy, an indicative of vacancy ordering, was also calculated taking into consideration six O-O bond distance intervals, as presented in Tables A.21 and A.22. The Sr-vac, La-vac, Mg-vac, Ga-vac and vac-vac partial RDF plots are not shown, as the obtained features for the co-doped systems are similar to those observed in Figures 5.9, 5.11 and 5.13, with the only difference being the intensity of the peaks.

The obtained results for co-doped systems are in line to what was observed for singly-doped phases; for the A-site dopants, the number of vacancies at NN sites around La(III) ions is slightly higher than that of a random distribution; hence, these defects are preferably located at NN positions to La(III) ions instead of Sr(II). Oxygen vacancies are also preferably located at a NNN position to Sr(II) cations, which in turn have their NNNN coordination shell depleted, suggesting that vacancies are trapped at NNN sites and unlikely to escape to the underpopulated adjacent shells. For B-site dopants, the NN, NNN and NNNN sites around Mg ions are overpopulated with respect to a random vacancy distribution. However, despite NNN sites possessing the highest number of vacancies comparatively, these oxygen defects can still move around among NN, NNN and NNNN shells, as none of them is depleted, and are presumably not trapped. Finally, as observed for LSG and LGM phases, vacancy ordering also takes place in LSGM; vacancies repel each other due to their effective positive charge. Vacancy ordering in these materials consists of the 2^{nd}, 4^{th} and 5^{th} shells around a vacancy being overpopulated, while the 1^{st}, 3^{rd} and 6^{th}

shells are depleted. Vacancies are unlikely to be positioned within the same GaO_6 octahedra (1^{st} coordination shell). Such ordering might hinder vacancy movement and hence oxide-ion diffusion, which could be related to the ionic conductivity drop observed for samples with higher dopant/vacancy concentration.

In summary, while both dopants favour the presence of vacancies at their NNN sites, these oxygen defects are probably trapped around Sr, but able to move among the Mg coordination shells. Such results suggest that Mg-doping is presumably more effective than Sr-substitution for ionic conduction properties via a vacancy mechanism; LGM samples indeed possess higher ionic conductivities and hence diffusion when compared to LSG for the same dopant content. Therefore, vacancy trapping is observed to be directly influenced by dopant identity. On the other hand, vacancy ordering seems to be independent of dopant identity, as it is observed to happen for LSG, LGM and LSGM samples. Our results indicate that the ionic conductivity in $LaGaO_3$-based systems can be influenced by dopant identity and their tendency to trap vacancies, or by the occurrence of vacancy ordering, which seems to occur regardless of which dopant is being added to the system. To further investigate which of these effects have the uttermost influence in ionic conduction properties, the ionic conductivity, activation energies and local structure of average $LaGaO_3$ systems will be investigated in the next sections, where dopant effects are neglected.

5.5.3 Average cation $LaGaO_3$ systems

In addition to the DIPPIM calculations on singly and co-doped $LaGaO_3$, we also performed simulations on average cation $LaGaO_{3-\delta}$ systems (ac-$LaGaO_3$), where the charges of both La and Ga cations are equally adjusted to account for the charge of all O^{2-} ions (and hence vacancies) present in the material. Therefore, it is possible to consider a range of vacancy concentrations, δ, corresponding to distinct dopant amounts. This eliminates any dopant effects on the material's conduction properties, such as the influence of their lower charges when compared to the host cations or any lattice distortions arising from their distinct ionic radii, for example. Hence, dopant-vacancy interactions and ordering effects caused by the dopants' presence are eliminated, and ionic conductivity and vacancy-vacancy interactions can be evaluated simply as a result of vacancy content. As a result, it might be possible to determine if the ionic conduction properties in $LaGaO_3$-based systems are mostly

influenced by dopant identity and the resulting dopant-vacancy interactions, or by vacancy ordering (and if such ordering process occurs regardless of dopant identity).

5.5.3.1 Ionic conductivity in ac-$LaGaO_3$ systems

In $LaGaO_3$ systems, vacancy concentration is equal to half of dopant content, i.e. $\delta = (x + y)/2$. Hence, the analysed δ values (0.075, 0.10, 0.125, 0.15, 0.175, 0.20, 0.225 and 0.25) correspond to total dopant concentrations of $x + y$ = 0.15, 0.20, 0.25, 0.30, 0.25, 0.40, 0.45 and 0.50. The $0.15 \leq (x + y) \leq 0.50$ range was chosen, as the minimum total dopant content investigated in co-doped systems was 15 mol% and the maximum ionic conductivity in singly doped phases was obtained for 20 mol% of Sr and Mg. Hence, lower dopant contents (5 and 10 mol%) were not considered, as vacancy interactions might not be as significant in such systems. The diffusion coefficients and ionic conductivities of orthorhombic and rhombohedral ac-$LaGaO_3$ systems are given in Tables A.23 and A.24 (see Appendix). Figure 5.18 shows the variation in ionic conductivity values with vacancy content (δ) for both phases.

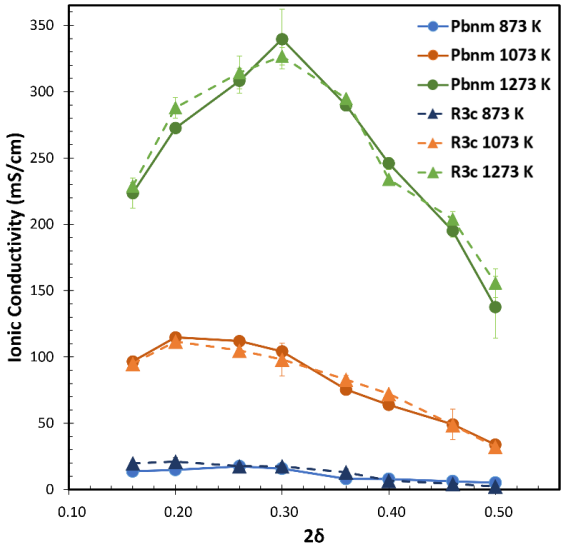

Figure 5.18 – Ionic conductivity variation with total dopant content (2δ = 0.15, 0.20, 0.25, 0.30, 0.35, 0.40, 0.45 and 0.50) at 873 K (blue), 1073 K (orange) and 1273 K (green), for orthorhombic (*Pbnm*) and rhombohedral (*R3c*) $LaGaO_{3-\delta}$ phases, represented by solid and dashed lines, respectively.

A more pronounced conductivity peak is observed for the average cations systems when compared to singly and co-doped phases. DIPPIM σ values for ac-$LaGaO_3$ systems are also considerably higher than experimental or simulated results for real LSGM systems at the same temperatures, as result of the exclusion of dopant-vacancy interactions. Considering the calculated standard errors, for both orthorhombic and rhombohedral ac-$LaGaO_3$ the optimal vacancy concentration for maximum σ ranges between $0.20 \leq 2\delta \leq 0.30$ at 873 K, is $2\delta = 0.20$ at 1073 K and is within $0.25 \leq 2\delta \leq 0.30$ at 1273 K. The conductivity peak in Figure 5.18 at 1273 K occurs at a total dopant concentration of 30 mol%, in contrast to singly and co-doped systems, which possess optimal total dopant concentration around 20 mol%; in LSG, LGM and LSGM, dopant-vacancy interactions at higher dopant content might result in a decrease in ionic conductivity above 20 mol%, despite the increased vacancy concentration at $x + y > 0.20$.

5.5.3.2 Activation energy of diffusion in ac-$LaGaO_3$ systems

In the previous sections, Sr and Mg have been observed to affect the activation energy of diffusion in $LaGaO_3$-based systems in different ways, with Mg doping resulting in higher activation energy values when compared to Sr substitution. To evaluate the effect of vacancy concentration without taking into account dopant effects and dopant-vacancy interactions, the activation energies of ac-$LaGaO_{3-\delta}$ systems were also calculated from the linear fit of the lnD against 1/T plots. All plots are linear, with r-squared values between 0.989 and 0.999, suggesting that no change in the ionic diffusion mechanism occurs in the 873-1273 K range, when dopant effects are eliminated. The calculated activation energy values (E_a) for both orthorhombic and rhombohedral phases are presented in Figure 5.19 and Table 5.17.

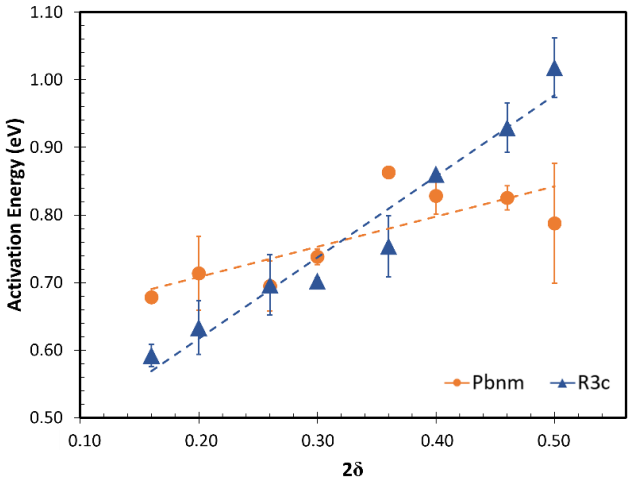

Figure 5.19 – Activation energy in orthorhombic (*Pbnm*, in orange) and rhombohedral (*R3c*, in blue) ac-$LaGaO_{3-\delta}$ systems with 2δ = 0.15, 0.20, 0.25, 0.30, 0.35 0.40, 0.45 and 0.50. Activation energies were extracted from the Arrhenius plot of the DIPPIM diffusion coefficients at high temperatures (873-1273 K).

Table 5.17 – Activation energies (E_a) of oxide-ion diffusion in eV for orthorhombic (*Pbnm*) and rhombohedral (*R3c*) ac-$LaGaO_{3-\delta}$ systems with 2δ = 0.15, 0.20, 0.25, 0.30, 0.35 0.40, 0.45 and 0.50, calculated from 873 K to 1273 K.

2δ	**Ea (eV) - *Pbnm***	**Ea (eV) - *R3c***
0.15	0.678±0.001	0.592±0.016
0.20	0.714±0.055	0.633±0.040
0.25	0.695±0.037	0.697±0.045
0.30	0.738±0.012	0.702±0.005
0.35	0.863±0.001	0.754±0.045
0.40	0.828±0.027	0.860±0.002
0.45	0.825±0.018	0.929±0.037
0.50	0.788±0.089	1.018±0.044

Activation energy increases with vacancy content, suggesting that the ionic radii mismatch between dopants and host cations and the resulting lattice strains are not the only factor contributing for the observed increase in E_a with vacancy concentration for LSG, LGM and LSGM systems, i.e. vacancy ordering might also play a role. From Figure 5.19, a bigger variation in E_a values is observed for the rhombohedral phase, suggesting that

vacancy ordering might occur more intensely in the *R3c* phase. To further investigate the influence of vacancy interactions on the ionic conductivity of the perovskite, structural analysis was carried out by the investigation of radial distribution functions and coordination environments.

5.5.3.3 Local structure in ac-$LaGaO_3$ systems

The A- and B-site sublattices in ac-$LaGaO_3$

The number of oxygen vacancies surrounding La(III) and Ga (III) ions at NN, NNN and NNNN sites in ac-$LaGaO_{3-\delta}$ systems at 1073 K, calculated through the integration of the RDF peaks, are presented in Table A.25 and A.26 (see Appendix). The partial RDF plots are now shown here, as the same features presented in Figures 5.9 and 5.11 were obtained here, with the only difference being the intensity of the peaks.

The number of vacancies surrounding La cations at the 12-coordinated NN site and the 24-coordinated NNN and NNNN sites is very similar to that of a random distribution, indicating that there is no tendency to vacancy trapping or vacancy ordering around La ions. This indicates that the results obtained for singly and co-doped systems, where La ions have their NN sites slightly overpopulated and their NNN shells depleted, are mainly due to the presence of Sr ions, suggesting that dopant-vacancy interactions are the responsible for the organization of vacancies around host cations. A similar effect is observed for Ga cations; in singly and co-doped systems, the 6-coordinated NN, the 24-coordinated NNN and the 30-coordinated NNNN sites are slightly depleted, as vacancies tend to aggregate around Mg ions, which could potentially facilitate ionic conduction around such ions, as vacancies are not necessarily trapped. In ac-$LaGaO_3$ systems, on the other hand, there is no tendency to vacancy ordering around Ga(III), as the B-site dopant and hence dopant-vacancy interactions are not present in the structure. Therefore, even though the presence of dopants is paramount for good ionic conductivity, as they are responsible for the introduction of oxygen vacancies into the system, doping will strongly impact the location of vacancies in the system, with dopant-vacancy interactions negatively affecting the ionic conductivity, as the obtained σ values for ac-$LaGaO_3$ systems are significantly higher than those calculated for LSG, LGM and LSGM.

The oxide ion sublattice in ac-$LaGaO_3$

The number of oxygen vacancies surrounding another vacancy in orthorhombic ac-$LaGaO_{3-\delta}$ systems at 1073 K was also calculated through the integration of the RDF peaks, and is presented in Table 5.18. The calculated results for the rhombohedral system follow the same trends discussed here and are presented in Table A.27 (see Appendix).

Similarly to that which was observed for singly and co-doped systems, vacancy ordering occurs, as vacancies are trying to avoid each other due to their effective positive charge. As a result, the 2nd, 4th and 5th shells are overpopulated, while the 1st, 3rd and 6th shells are depleted. In singly and co-doped systems, the number of vacancies at a given shell was observed to increase with vacancy concentration, regardless of such shell being depleted or not. Accordingly, the number of vacancies at the depleted 6th shell in ac-$LaGaO_3$ systems was expected to increase with vacancy content, as more vacancies are being added to the system. However, a slightly different behaviour was observed, and the number of vacancies in the 6th shell decreases for $2\delta \geq 0.30$, i.e. for higher vacancy concentrations the 6th shell gets even more depleted, indicating that the more vacancies are present within the system, the more ordered they become. To confirm such behaviour, a 7th coordination shell, representing O-O bond distances between 7.6 and 8.0 Å, was also analysed, with its sites getting more populated as concentration goes up. Hence, the sites surrounding the 6th coordination shell get more populated as vacancy concentration goes up, resulting in an increased depletion of the 6th shell, confirming that oxygen vacancies are indeed more ordered in ac-$LaGaO_3$ systems. These results suggest that vacancy ordering occurs despite of dopant identity and gets more intense at higher vacancy concentrations when dopant effects are neglected, which might be responsible for the ionic conductivity drop observed at $2\delta \geq 0.30$. Such heightened ordering is not observed in singly and co-doped samples, as dopant-vacancy interactions can also affect the vacancy-vacancy long range arrangement.

The analysis of the local structure around A-, B- and oxygen sites suggests that, in real systems, dopant-vacancy interactions might have a higher influence on ionic conductivity values than vacancy ordering, since ac-$LaGaO_3$ systems, in which dopant-vacancy interactions are neglected, possess considerably higher σ values than LSG, LGM and LSGM. Furthermore, the maximum in ionic conductivity in ac-$LaGaO_3$ is achieved at higher vacancy concentrations when compared to real systems, indicating that dopant-vacancy interactions are also responsible for a lower maxima in LSG, LGM or LSGM.

Table 5.18 – Number of vacancies surrounding another oxygen vacancy in orthorhombic (*Pbnm*) ac-$LaGaO_{3-\delta}$ systems with 2δ = 0.15, 0.20, 0.25, 0.30, 0.35, 0.40, 0.45 and 0.50, at 1073 K. O-O corresponds to a random distribution of vacancies where no defect ordering has occurred.

	2δ	**1st**	**2nd**	**3rd**	**4th**	**5th**	**6th**	**7th**
O-O	**0.15**	0.201	0.027	0.754	0.259	0.204	0.844	0.278
	0.20	0.266	0.035	0.997	0.342	0.270	1.115	0.367
	0.25	0.330	0.044	1.239	0.426	0.335	1.385	0.456
	0.30	0.394	0.053	1.477	0.508	0.400	1.652	0.544
	0.35	0.457	0.061	1.714	0.589	0.464	1.917	0.631
	0.40	0.519	0.069	1.946	0.668	0.526	2.176	0.717
	0.45	0.579	0.077	2.171	0.746	0.587	2.429	0.800
	0.50	0.638	0.085	2.394	0.822	0.648	2.678	0.882
vac-vac	**0.15**	0.125	0.050	0.309	0.412	0.435	0.336	0.425
	0.20	0.168	0.088	0.410	0.500	0.580	0.446	0.683
	0.25	0.215	0.128	0.436	0.673	0.652	0.500	0.668
	0.30	0.318	0.147	0.514	0.783	0.655	0.433	0.921
	0.35	0.376	0.225	0.480	0.858	0.929	0.238	1.116
	0.40	0.486	0.214	0.708	1.034	1.029	0.173	1.503
	0.45	0.796	0.172	1.070	1.136	1.235	0.127	1.876
	0.50	0.923	0.268	1.498	0.984	1.030	0.142	1.658

5.6 Conclusions

A DIPole Polarizable Ion Model (DIPPIM) force field was parametrized from DFT data to predict the ionic conduction behaviour of orthorhombic (*Pbnm*) and rhombohedral (*R3c*) LSGM. The parametrization of the IP was done using a force-matching procedure, in which the forces, stresses and dipoles calculated by the interatomic potential were fitted to DFT values using the SCAN functional; hence, such force field possess *ab initio* quality. This methodology significantly improves the transferability of the IP in comparison to the force fields available in literature to study $LaGaO_3$-based systems, which were empirically derived to reproduce specific experimental properties [11, 280, 281] and are composed of parameters extracted from different sources. As a result, the IP derived in this thesis can be used to study different crystallographic phases and thermodynamic states of $LaGaO_3$

systems, such as surfaces and grain boundaries, for example. A total objective function of 0.24 was obtained, indicating the good quality of the IP. DIPPIM underestimated the thermal expansion coefficients of orthorhombic and rhombohedral $LaGaO_3$, with the description of the thermal expansion of the orthorhombic phase being better than that of the rhombohedral structure. DIPPIM also yields lattice parameters within ~1% of experimental results, and volumes with deviation lower than 2.5%.

A classical molecular dynamics study of the bulk properties of $La_{1-x}Sr_xGa_{1-y}Mg_yO_{3-\delta}$ was performed, with total dopant concentrations ranging from 5 to 50 mol%. To the best of our knowledge, this is the first theoretical study comprehensively and systematically investigating a range of dopant concentrations and temperatures, using the same methodology and hence obtaining consistent results. Experimentally, Huang *et al.* [74] is the only study to present a complete set of experimental ionic conductivities for 5 mol% $\leq x, y \leq$ 30 mol%. However, the reliability of their results can be questioned as their obtained σ values are considerably higher than the other available literature results, with more than 70% of their samples presenting secondary phase formation. For singly and co-doped systems, ionic conductivity was observed to increase with dopant content until reaching its maximum value for samples with a total dopant concentration of about 20 mol% (LSG20, LGM20 and LSGM1010), and decreasing after that. This is a result of oxygen vacancies repelling each other due to their effective positive charge, being ordered throughout the lattice and somewhat trapped in systems with higher dopant content. Such vacancy ordering occurs more intensely in systems with higher dopant concentration, leading to the observed decrease in ionic conductivity.

LGM systems were observed to possess higher σ values than LSG at the same dopant content, indicating that the dopant-vacancy interactions might be different in the two systems; oxygen vacancies are predicted to be trapped at NNN sites to Sr ions, as the NN and NNNN coordination shells around the A-site cation are depleted. The local coordination around Mg ions is different; all NN, NNN and NNNN coordination shells around the B-site cation are overpopulated in comparison to a random distribution of vacancies; hence, vacancies are not trapped, as they are free to move among the overpopulated shells, which has a positive effect on the ionic conductivity values. As a result, Mg-doping is presumably more effective than Sr-substitution for the improvement of ionic conduction properties via a vacancy mechanism. Experimentally, Sr-doping is used to improve ionic conduction

properties, with Mg being added to the system mainly for the purpose of lattice expansion, which increases the solubility limit of Sr. Our results, however, show that Mg-doping yields higher ionic conductivity values and less dopant-vacancy interactions, and for the first time show how differently vacancy ordering occurs around A- and B-site dopants. Despite vacancy trapping being directly influenced by dopant identity, vacancy ordering seems to occur regardless of which dopant is present in the system, as it is observed to happen for LSG, LGM, LSGM and ac-$LaGaO_3$ samples. The analysis of the local structure around A-, B- and oxide-ion sites in ac-$LaGaO_3$ systems suggests that, in real systems, dopant-vacancy interactions have a stronger influence than vacancy ordering on ionic conductivity values.

The calculated ionic conductivities for singly doped systems are in good agreement with the available experimental data; DIPPIM σ values are slightly higher, although this is likely due to the presence of secondary phases in experimental systems. For co-doped systems, comparison to experiment was not as straightforward; there is a large variation on the available experimental data on diffusion coefficients, ionic conductivities and activation energies of diffusion due to the different synthesis conditions (synthetic method, sintering times and temperatures) used, the variety of grain sizes, sample densities and the presence of impurities or secondary phases.

Chapter 6
Defect properties of $La_2NiO_{4+\delta}$, a potential IT-SOFC cathode

6.1 Introduction

The Ruddlesden-Popper (RP) series of layered oxides are perovskite-related materials with general formula $A_{n+1}B_nO_{3n+1}$. The first members of the series (n = 1) possess K_2NiF_4-type structures (Section 1.5.2), consisting of perovskite (ABO_3) and rock salt (AO) layers, intercalated along the *c*-axis, which results in strong anisotropic properties. One example of RP oxide with n = 1 is $La_2NiO_{4+\delta}$, which has attracted attention as a potential cathode material for IT-SOFCs. Its mixed ionic and electronic conduction properties expand the possible active areas for the oxygen reduction reaction beyond the triple-phase-boundary [329], as outlined in Section 1.1. Furthermore, lanthanum nickelate presents good catalytic activity to the ORR [6] and is compatible with commonly used electrolyte materials, such as Sr- and Mg-doped $LaGaO_3$ (LSGM) [330] and Gd-doped ceria (CGO) [329].

Lanthanum nickelate's K_2NiF_4-type structure, consisting of LaO rocksalt layers separating $LaNiO_3$ perovskite blocks, is presented in Figure 6.1a. Within a LaO layer with ideal La-O bond distances, La atoms would be 5.15 Å apart along the *a* and *b* directions. Similarly, the distance between Ni atoms in a NiO_2 layer (the middle part of the perovskite block) with ideal Ni-O bond distances would be 5.83 Å [331]. In this RP oxide, LaO and NiO_2 layers are intergrown and thus will have the same dimensions, which results in the stretching of first and compression of the latter, creating structural strain. One way of alleviating this tension is to rotate the NiO_6 octahedra, lowering the structural symmetry from tetragonal to orthorhombic. The addition of interstitial oxygen atoms to the lattice is another way of releasing such stress; it increases the oxidation state of Ni(II) to Ni(III) as charge compensating mechanism, effectively reducing nickel's ionic radius [331] from 0.69 to 0.56 Å [26]. At the same time, the ionic radius of La ions is increased (from 1.22 Å to 1.27 Å [26]), since the addition of an interstitial oxygen increases their coordination number from 9 to 10. $La_2NiO_{4+\delta}$ easily accommodates excess lattice oxygen and displays a large range of oxygen over-stoichiometries ($0.00 < \delta < 0.25$) as a result [332]. In air, the amount

of excess oxygen in the undoped material is around 0.14 per formula unit, decreasing down to 0.04 with increasing temperature [332]. Samples with $\delta = 0.18$ can be easily synthesized under 1 atm of oxygen [333].

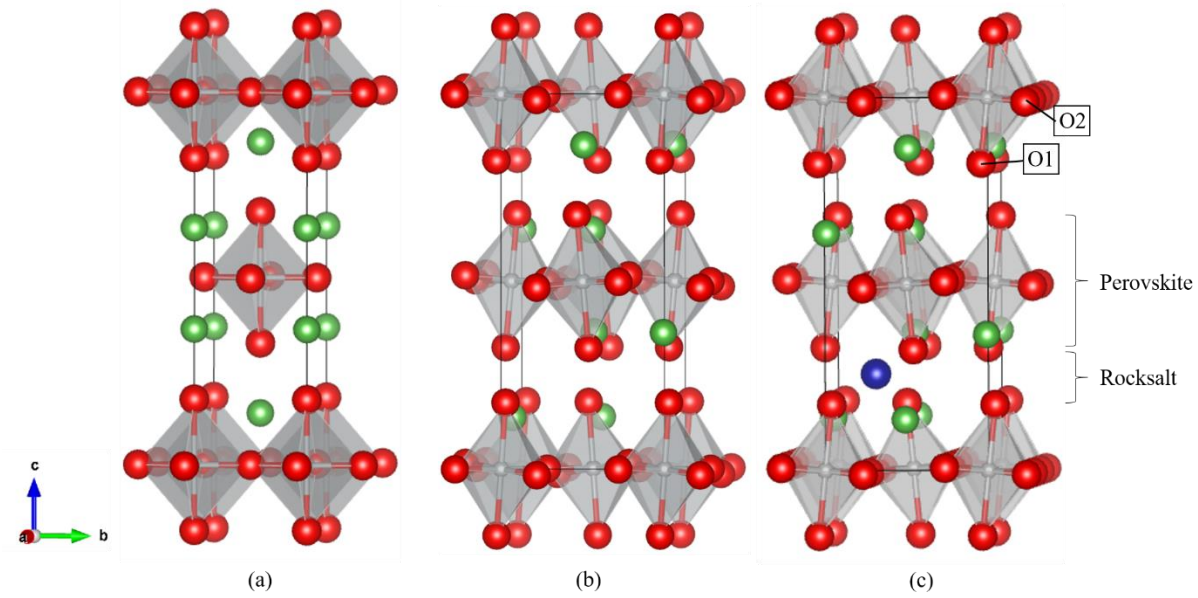

Figure 6.1 – La_2NiO_4 (a) tetragonal *I4/mmm*, (b) *P42/ncm* and (c) orthorhombic *Bmab* unit cell structures. La ions presented in green, Ni ions in light grey, O ions in red and an O interstitial in blue at the (¼, ¼, ¼) position.

Brown [331] used a bond valence model to predict the phase transformations in stoichiometric La_2NiO_4, and determined that two structural transitions should be expected with decreasing temperature; from tetragonal (space group *I4/mmm*) to orthorhombic (space group *Bmab*) at 780 K, and from orthorhombic to tetragonal (space group *P42/ncm*) at 80 K [331]. These three crystal structures are shown in Figure 6.1, with La ions in green, Ni ions in light grey and O ions in red. Figure 6.1 also distinguishes between axial and equatorial oxygen atoms in the NiO_6 octahedra, which will be referred to as O1 and O2, respectively, in this chapter. Experimentally, there are conflicting reports describing the material's structural transitions, mainly due to the wide range of observed oxygen stoichiometries and their influence on structural properties [334]. At high temperatures, the material indeed assumes a tetragonal *I4/mmm* structure, regardless of oxygen content, and transitions to orthorhombic at lower temperatures, with the space group depending on the oxygen stoichiometry. Jorgensen *et al*. [333] observed at room temperature the existence of *Bmab* and *Fmmm* orthorhombic phases for lower ($0.00 < \delta < 0.02$) and higher ($0.13 < \delta < 0.18$)

oxygen content, respectively. For intermediate oxygen content (δ = 0.07), the material separated into two phases – an oxygen-rich *Fmmm* region, and an oxygen-poor, nearly stoichiometric, *Bmab* region [333]. In the absence of an oxidizing atmosphere, the transition from the *I4/mmm* tetragonal to the nearly stoichiometric ($\delta \approx 0.00$) *Bmab* orthorhombic phase takes place at 780 K [335]. For higher oxygen partial pressures, the transition from the *I4/mmm* tetragonal to the over-stoichiometric *Fmmm* orthorhombic phase occurs approximately 423 K [336]. Therefore, both temperature and oxygen content influence $La_2NiO_{4+\delta}$ crystal structure, with higher temperatures yielding a tetragonal phase, and lower temperatures resulting in orthorhombic structures, which in turn, vary depending on oxygen content. Regarding the material's low temperature structures, some studies confirm the transition between *Bmab* orthorhombic and *P42/ncm* tetragonal structures at 56 K [337], while other reports show the low temperature symmetry change to be between two orthorhombic phases with *Bmab* and *Pccn* space groups at 74 K [334]. These low temperature phases, however, are not relevant for SOFC operation.

While in conventional perovskite- and fluorite-structured materials ionic conduction takes place mainly via a vacancy mechanism, in RP oxides ionic transport occurs primarily through the diffusion of interstitial oxygen ions [12], preferentially within the rocksalt layers [329]. Over-stoichiometric oxygen is incorporated at the (¼, ¼, ¼) interstitial lattice site [332–334,336,338], as shown in Figure 6.1c, located at the centre of a pseudo-tetrahedron composed of La atoms. The addition of an oxygen interstitial displaces four nearby oxygen atoms, located at the apical positions of the [NiO_6] octahedra, by approximately 0.5 Å [333,336], tilting the octahedra and hence favouring an orthorhombic distortion.

A few different charge compensating mechanisms for excess oxygen uptake have been suggested. Force-field calculations on the formation and migration of point defects were performed to propose the existence of both O^{2-} (O_i'') and O^- (O_i') as interstitial species, which could either result in the generation of charge compensating electron holes localized solely on Ni cations (Equations 6.1 and 6.2, in Kröger-Vink notation), oxidizing Ni(II) to Ni(III), or in the formation of electron holes localized on both nickel and oxygen sites (Equations 6.3 and 6.4) [339].

$$\frac{1}{2}O_2 + Ni_{Ni}^X \rightarrow O_i' + Ni_{Ni}^\bullet \tag{6.1}$$

$$\frac{1}{2}O_2 + 2Ni_{Ni}^X \rightarrow O_i'' + 2Ni_{Ni}^\bullet \tag{6.2}$$

$$\frac{1}{2}O_2 + 2O_O^X \rightarrow O_i' + 2O_O^\bullet \quad (6.3)$$

$$\frac{1}{2}O_2 + 2Ni_{Ni}^X \rightarrow O_i'' + Ni_{Ni}^\bullet + O_O^\bullet \quad (6.4)$$

The mechanisms presented in Equations 6.1 and 6.2 were suggested to occur for low δ values, while Equations 6.3 and 6.4 were proposed for higher δ. Hence, the material would possess distinct average nickel oxidation states depending on which charge compensation mechanism took place, which in turn depends on the magnitude of δ. Experimentally [340], X-ray absorption spectroscopy of the near-edge region (XANES) reveals that nickel's oxidation state indeed lies between (II) and (III), with a value of +2.24 for δ = 0.12 at room temperature, suggesting that interstitial oxygen uptake is charge-compensated solely by the formation of electron holes located on Ni (Equation 6.2), disproving the mechanisms suggested in Equations 6.1, 6.3 and 6.4. A reduction in the average oxidation state was observed to occur with increasing temperature, indicating the presence of less Ni(III) as a result of oxygen interstitials being released from the structure; average oxidation states of +2.15 (in air) and +2.08 (in nitrogen) were measured at 973 K, corresponding to estimated δ values of 0.08 and 0.04, respectively [340].

Neutron powder diffraction experiments show that stoichiometric lanthanum nickelate is G-type antiferromagnetically ordered at room temperature, with three-dimensional Néel temperature (T_N) of ~330 K [335,341,342]. The in-plane arrangement of magnetic moments consists of nearest-neighbour Ni(II) ions being oppositely polarized, with spins oriented along the *a* axis ([100] direction) [343,344]. Changes in oxygen stoichiometry influence not only La_2NiO_4 structural features, but also its magnetic and transport properties; increasing δ results in a decrease on the material's T_N [345].

The main drawback to the application of lanthanum nickelate as cathode is its low electronic conductivity (σ), with a wide range σ values being reported due to the variety of methods, sintering temperatures, oxygen partial pressures and conditions under which the material is synthesized, which affects its microstructure, oxygen stoichiometry and hence charge carrier concentration [346]. Maximum conductivity is reached at approximately 673 K, with lower σ values reported for the stoichiometric material (32 S cm^{-1} [346] and 56 S cm^{-1} [347] at 673 K) in comparison to oxygen-rich phases (82 S cm^{-1} for $La_2NiO_{4.15}$ at 673 K [336] and $La_2NiO_{4.30}$ at 694 K [348]). Still, suitable electrode candidates should possess σ > 100 S cm^{-1} at SOFC operation temperatures [329].

Below 673 K, the material presents thermally activated electronic conduction, i.e., σ increases with rising temperature, likely occurring via hopping of *p*-type charge carriers between Ni(II) and Ni(III) ions [336,347,349]. The smaller electronic conductivity values observed for samples with lower interstitial oxygen content confirms that electron holes are the predominant carriers for lanthanum nickelates [350]. The high temperature regime (above 673 K) is characterized by a change in the electrical conductivity behaviour; σ decreases with increasing temperature [336,347]. Electron conduction in La_2NiO_4 has been described as anisotropic and a result of electron hopping along O-Ni-O bonds, with its largest component attributed to the Ni-O axial bonds in the [NiO_6] octahedron [336,340,351]. Neutron powder diffraction results suggest that Ni-O1 (axial distances along *c* direction) interatomic distances contract with temperature, reaching a minimum value at 673 K, followed by an increase at higher temperatures. Hence, the transition between the low (thermally activated) and high temperature conduction regimes can be associated with the contraction/expansion of Ni-O1 bonds, with higher conductivities being achieved for shorter bond lengths [336].

Transport properties can be enhanced through aliovalent A- and B-site doping ($La_{2-x}A_xNi_{1-y}B_yO_{4+\delta}$). Changes on the equatorial Ni-O distances, for example, can be achieved through B-site doping, which could lead to improvement (smaller B-site dopants) or deterioration (larger B-site cations) of electrical conduction properties, due to changes in the electron hole activation energy. Electronic conduction changes can also be related to variations in the electron holes concentration, while changes in ionic transport properties are mainly associated to interstitial oxygen content [352].

Charge compensation for A-site substitution (A = Ca(II), Sr(II), Ba(II)) can be ionic, forming an oxygen vacancy (and hence decreasing oxygen content), or electronic, generating electron holes. Therefore, the addition of oxygen interstitials is not the only way to increase charge carrier concentration in these materials and improve electronic conduction [103–105,353]. The electronic conductivity of $La_{2-x}Sr_xNiO_{4+\delta}$ increases with dopant content ($0.0 < x < 0.5$), from 30 S cm^{-1} at 673 K for the undoped sample, to 50 S cm^{-1} in $La_{1.8}Sr_{0.2}NiO_{4+\delta}$ and 70 S cm^{-1} in $La_{1.5}Sr_{0.5}NiO_{4+\delta}$ [332,350]. Increased Sr concentration also leads to a decrease in interstitial oxygen content ($\delta = 0.14$ for $La_2NiO_{4.14}$, $\delta = 0.11$ for $La_{1.8}Sr_{0.2}NiO_{4.11}$ and $\delta = 0.05$ for $La_{1.5}Sr_{0.5}NiO_{4.05}$) due to the formation of oxygen vacancies, which are

immediately occupied by the nearest interstitial oxygen. Hence, A-site doping can potentially deteriorate ionic conductivity due to a decrease in the number of charge carriers. Despite the oxygen loss, samples with $x < 0.5$ remained over-stoichiometric in the 273-1273 K range [350]. Sr-doping also decreases the transition between the low and high temperature electronic conduction regimes, from 673 K ($x = 0.0$) to 20 K ($x = 1.2$) [345].

Similarly to Sr-substitution, Ca-doping ($0.0 < x < 0.5$) increases electronic conductivity, which reaches a maximum at ~623 K for all $La_{2-x}Ca_xNiO_{4+\delta}$ samples, and decreases the amount of oxygen in the structure through the formation of oxygen vacancies ($La_2NiO_{4.13}$, $La_{1.9}Ca_{0.1}NiO_{4.09}$, $La_{1.8}Ca_{0.2}NiO_{4.04}$, $La_{1.7}Ca_{0.3}NiO_{4.01}$) [329]. The best electronic conductivity results are achieved for $x = 0.3$; for higher Ca concentrations ($x = 0.4$ and 0.5) secondary phases (CaO and NiO) are formed, deteriorating transport properties [329]. An electrical conductivity of 111 S cm^{-1} was achieved at 973 K for $La_{1.7}Ca_{0.3}NiO_{4+\delta}$ (vs. 70 S cm^{-1} for the undoped sample) [329], turning the Ca-doped material into a suitable candidate for electrode applications in SOFCs.

Despite the observed oxygen loss in Ca-doped samples, deterioration of ionic conduction was not observed for samples with $x = 0.1$ and $x = 0.2$; a slight elongation of La-O bond distances (~0.03 Å) is observed with doping, facilitating oxide-ion migration within the LaO layers and decreasing the activation energy for oxide-ion migration (from 1.02 eV in the undoped sample to 0.87 eV in $La_{1.8}Ca_{0.2}NiO_{4.01}$) as a result [329]. Calcium, being a +2 dopant, will have a weaker pull on the oxygen ions surrounding it when compared to La(III), which may result in an increased charge carrier mobility. The ionic conductivity of $La_{1.7}Ca_{0.3}NiO_{4.01}$ does not improve in comparison to the undoped sample, as the substantial decrease in oxygen content might surpass the effects of the lower charged dopant on oxygen mobility [329]. Therefore, Ca-doping can improve both ionic and electronic transport properties for concentrations around 10 and 20 mol%. When comparing systems containing the same amount (15 mol%) of either Ca(II), Sr(II) or Ba(II), the maximum conductivity value of 85 S cm^{-1} at 973 K was obtained for the Ca-doped nickelate. Sr- and Ba-doped samples presented similar values of ~70 S cm^{-1}, while the undoped system possessed $\sigma = 65$ S cm^{-1} at the same temperature [351].

B-site doping with transition metals can also modify transport properties; however, the charge compensation mechanism will change depending on the most stable oxidation state of the B-site metal. For trivalent dopants, for example, it can occur either ionically or

electronically, resulting in excess oxygen or an extra electron, respectively. The generation of excess oxygen would lead to improvements in ionic conduction properties through an increase in the number of mobile oxygen ions.

Despite improvements on ionic conduction, B-site substitution usually decreases the concentration of B-site cations capable of contributing to a *p*-type hopping electronic conduction mechanism [332,352] and deteriorates the mobility of electron holes in the material, which in turn depends on the stability of the trivalent dopant cation with respect to its divalent form. Iron co-doping on $La_{1.9}Sr_{0.1}Ni_{1-y}Fe_yO_{4+\delta}$, for example, decreases electronic conductivity from 89 S cm^{-1} (y = 0.02) to 69 S cm^{-1} (y = 0.10) at 700 K with increasing Fe content. This is a result of an increased stabilization of Fe(III) with respect to its divalent form and to Ni(III) in Sr-doped samples; Fe preferably assumes its trivalent state as observed in $LaSrFeO_4$, which acts as an electron hole trap and decreases the concentration of Ni(II)/Ni(III) available to contribute to electron transport [1]. The same is observed in $La_{1.6}Ca_{0.4}Ni_{1-y}Fe_yO_{4+\delta}$; increasing Fe content decreases the electronic conductivity from ~95 S cm^{-1} (y = 0.10) to ~55 S cm^{-1} (y = 0.20) at 700 K [352], and increases the activation energy for electron hole transport from 9.26 kJ mol^{-1} (y = 0.10) to 11.64 kJ mol^{-1} (y = 0.20). As expected from an ionic charge compensation mechanism, Fe-doping increases the oxygen content (δ) in the Ca-substituted samples from 0.03 in $La_{1.6}Ca_{0.4}NiO_{4+\delta}$ to 0.04 and 0.09 in $La_{1.6}Ca_{0.4}Ni_{1-y}Fe_yO_{4+\delta}$ with y = 0.10 and 0.20, respectively [352].

When $La_{1.5}Sr_{0.5}NiO_{4+\delta}$ is doped with 20mol% of Fe or Co, the Co-doped sample possess less excess oxygen ($La_{1.5}Sr_{0.5}Ni_{1.8}Co_{0.2}O_{4.03}$ and $La_{1.5}Sr_{0.5}Ni_{1.8}Fe_{0.2}O_{4.06}$) and higher electrical conductivities than the Fe-substituted material (~ 87 S cm^{-1} and ~70 S cm^{-1} at 750 K for Co- and Fe-doped samples, respectively). While Fe is predominantly in its +3 form, cobalt possess an average oxidation state between +2 and +3 (the concentrations of Co(II) and Co(III) were determined to be 0.08 and 0.12, respectively) [3]. Hence, the charge compensation mechanisms for the two dopants with distinct average oxidation states will not be the same, resulting in more oxygen loss and less deterioration in the electronic conduction with Co-doping, since less Co(III) ions are available to act as electron hole traps in comparison to Fe(III).

Cu-doping ($La_{1.6}Ca_{0.4}Ni_{1-y}Cu_yO_{4+\delta}$ with y = 0.10, 0.20 and 0.30), on the other hand, would have different outcomes due to Cu distinct oxidation states (+1 and +2) when compared to Fe or Co, which are preferably divalent or trivalent. Cu-doping decreases

oxygen content (δ) from 0.03 when y = 0.00 to 0.02 when y = 0.10. For higher y values, the material is oxygen deficient ($La_{1.6}Ca_{0.4}Ni_{0.8}Cu_{0.2}O_{3.99}$ and $La_{1.6}Ca_{0.4}Ni_{0.7}Cu_{0.3}O_{3.98}$). The lower average oxidation state of Cu (between +1 and +2, with Mossbauer spectroscopy confirming a higher concentration of Cu(II) cations) in comparison to Ni (between +2 and +3) allows charge compensation through the formation of oxygen vacancies, as observed for lower valence A-site dopants. Cu(II) is also a d^8 metal, which favours square planar coordination and hence would favourably form oxygen vacancies to achieve such geometry. Electron conductivity values still decrease with Cu-doping, from ~130 S cm^{-1} (y = 0.10) to ~105 S cm^{-1} (y = 0.20) and ~100 S cm^{-1} (y = 0.30), due to the resulting decrease in the concentration of nickel ions with copper substitution. However, the activation energy for hole transport remains practically unchanged with increasing Cu concentration (7.13 kJ mol^{-1}, 7.12 kJ mol^{-1} and 7.05 kJ mol^{-1} for y = 0.10, 0.20 and 0.30, respectively), as copper do not form hole trapping states [352].

A- and B-site doping have been shown to affect the material's transport properties in different ways, and usually a trade-off between ionic and electronic conductivity needs to be achieved. In this chapter, PBEsol+U and HSE06 calculations are carried out to investigate the potential effects of A- (Ca (II), Sr (II), Ba(II)) and B-site (Co(III), Fe(III) and Mn(III)) doping on the ionic and electronic conductivity of stoichiometric orthorhombic (*Bmab*) La_2NiO_4. The thermodynamic stability of the orthorhombic phase was investigated, while the defect chemistry of the material was evaluated through the investigation of preferable compensation mechanisms (ionic or electronic) upon doping and the calculation of defect formation energies. The binding energies between dopants and their charge compensating defects were also calculated to predict which dopants would be detrimental to conduction properties. Transition level diagrams were then used to investigate the origin of charge carriers in the material. All properties were evaluated under a range of chemical environments, allowing comparison to experimentally obtained results. This work aims to suggest which dopants would yield the biggest improvements to the material's MIEC properties aiming IT-SOFC cathode applications.

6.2 Methodology

DFT+U calculations using the PBEsol [78] functional were carried out with VASP [146,354,355]. PBEsol is a revised version of the PBE functional, developed to provide a

better description of the equilibrium properties of solids, especially lattice parameters and bond distances. A plane wave basis set was used to describe valence electrons, while projector augmented wave (PAW) pseudopotentials were used to describe the interactions between core (La:[Kr], Ni:[Ar], O:[He], Co:[Ar], Fe:[Ar], Mn:[Ne,$3s^2$], Ca:[Ne], Sr:[Ar,$3d^{10}$], Ba:[Kr,$4d^{10}$]) and valence electrons [181,182]. The ionic and electronic convergence criteria were set to 0.005 eV $Å^{-1}$ and 10^{-6} eV, respectively, with a plane-wave cut-off energy of 400 eV. VESTA [212] was used to perform visual and structural analysis of the systems.

The self-interaction error is a problem to be considered when simulating materials containing transition metals with partially filled *d* shells; the SIE favours the partial occupation of *d* states, when in fact these electrons have a highly localised nature. In La_2NiO_4, a *p*-type conductor, the main contributors to the valence band are Ni 3*d* and O 2*p* states, with standard DFT predicting hole states to be delocalised over all Ni and O atoms, instead of promoting the oxidation of Ni(II) to Ni(III). To improve the description of the electronic properties of this RP oxide, a +*U* correction of 5.3 eV was applied to Ni 3*d* states using the Dudarev approach [86]. This value was chosen based on the work of Rohrbach *et al.* [203], who investigated the influence of +*U* corrections (0-9 eV) on the electronic and magnetic structure of NiO. This +*U* correction was then used in other work involving GGA+*U* calculations [356–360] to investigate a range of properties, such as the lattice constant, bulk modulus, band gap and magnetic moment, yielding results that were in excellent agreement to experimental data. In this work, a +*U* correction of 5.5 eV was also applied to O 2*p* states to correct any SIE associated with them. Previous studies have shown that an SIE correction needs to be applied on O 2*p* states in LDA and GGA calculations [361–365], especially when modelling oxygen-derived *p*-type defect states. Keating *et al*. [366] used a Koopmans-like procedure [362,363] to calculate U_{O2p} = 5.5 eV as the optimal correction to overcome the SIE, with higher values being observed to overstabilize electron holes in CeO_2. To the best of our knowledge, no previous computational study on La_2NiO_4 have applied +*U* corrections to O states. Finally, a +*U* value of 4 eV was applied on transition metal dopants, to ensure the localisation of Co(III), Fe(III) and Mn(III) 3*d* states. Similar +*U* values were previously reported for PBE+*U* [200,201,204–206] calculations. Single point HSE06 [367] calculations were carried out in the optimized PBEsol+*U* systems, to counteract DFT SIE and overcome any band gap issues, and hence determine which

approach superiorly describes the geometry, electronic structure and defect chemistry of the investigated material. Hybrid calculations were performed with a 400 eV planewave cut-off and electronic convergence criteria of 10^{-6} eV.

The orthorhombic (*Bmab*, space group 64) La_2NiO_4 unit cell was structurally optimized considering lattice constants ranging from 96% to 102% of experimental values and under the constraint of constant volume with atomic positions and cell shape being allowed to change. The equilibrium cell volume was determined after fitting the resulting energy-volume curve to the Murnaghan [243] equation of state, minimising errors associated with Pulay stress and plane-wave DFT calculations on volume change due to the incompleteness of the finite basis set [244] (Section 3.2.4).

Defect calculations were performed in a 3x3x1 unit cell expansion, resulting 252 atoms. This supercell size was chosen to ensure a minimum distance of 13 Å between defects in the investigation of A- and B-site doping (and the possible charge compensation mechanisms), and hence minimize defect-defect interactions.

Defect formation energies were calculated from the defect calculations and the chemical potential of the species, according to Equation 3.3. A- (A = Ca(II), Sr(II), Ba(II)) and B-site (B = Co(III), Fe(III), Mn(III)) aliovalent doping of La_2NiO_4 were investigated, with ionic and electronic charge compensation mechanisms being examined. A-site substitution with divalent dopants can result in the formation of one oxygen vacancy for every two dopants introduced (ionic compensation) or one electron hole localised on a Ni site (electron compensation), promoting the oxidation of Ni(II) to Ni(III). These processes are described in Equations 6.5 and 6.6, respectively, using Kroger-Vink notation, where M represents the divalent dopant.

$$2La_{La}^{X} + 2M_{E}^{X} + O_{O}^{X} \rightarrow 2La_{E}^{X} + 2M'_{La} + V_{O}^{\bullet\bullet} + \frac{1}{2}O_2 \quad (6.5)$$

$$La_{La}^{X} + M_{E}^{X} + Ni_{Ni}^{X} \rightarrow La_{E}^{X} + M'_{La} + Ni_{Ni}^{\bullet} \quad (6.6)$$

B-site substitution with trivalent dopants can be charge compensated by the formation of an oxygen interstitial for every two dopants introduced (ionic mechanism) or of an electron localised on Ni (electronic compensation), as in Equations 6.7 and 6.8, respectively, where M is the trivalent dopant. B-site dopants were tested in their high and low spin states, with the same or opposite spin as the Ni cations they replaced (the most stable configurations are reported here).

$$2Ni_{Ni}^{X} + 2M_{E}^{X} + \frac{1}{2}O_2 \rightarrow 2Ni_{E}^{X} + 2M_{Ni}^{\bullet} + O_{i}^{''} \quad (6.7)$$

$$Ni_{Ni}^{X} + M_{E}^{X} \rightarrow Ni_{E}^{X} + M_{Ni}^{\bullet} + Ni_{Ni}^{'} \quad (6.8)$$

6.2.1 Chemical Potentials

The elemental chemical potentials (required to calculate defect formation energies in Equation 3.3) were calculated relative to the formation energy of the pure stoichiometric La_2NiO_4 system, and to the limiting conditions determined by the formation of competing phases (La_2O_3, NiO, $La_3Ni_2O_7$ and $La_4Ni_3O_{10}$), using the Chemical Potential Limits Analysis Program (CPLAP) [252], as outlined in Section 3.2.6.3. CPLAP sets the sum of the chemical potentials to be equal to the formation energies of the compounds, generating a set of linear equations (Equations 6.9-6.13), which can be solved to determine the intersection points of the thermodynamic stability field of the RP oxide. Therefore, the software calculates the range of elemental chemical potentials ($\Delta\mu_{La,}$ $\Delta\mu_{Ni,}$ $\Delta\mu_{O}$) within which the *Bmab* phase is thermodynamically stable.

$$\Delta H_f(La_2NiO_4) = 2\Delta\mu_{La} + \Delta\mu_{Ni} + 4\Delta\mu_{O} \quad (6.9)$$

$$\Delta H_f(La_2O_3) \leq 2\Delta\mu_{La} + 3\Delta\mu_{O} \quad (6.10)$$

$$\Delta H_f(NiO) \leq \Delta\mu_{Ni} + \Delta\mu_{O} \quad (6.11)$$

$$\Delta H_f(La_3Ni_2O_7) \leq 3\Delta\mu_{La} + 2\Delta\mu_{Ni} + 7\Delta\mu_{O} \quad (6.12)$$

$$\Delta H_f(La_4Ni_3O_{10}) \leq 4\Delta\mu_{La} + 3\Delta\mu_{Ni} + 10\Delta\mu_{O} \quad (6.13)$$

The oxygen chemical potential obtained from CPLAP can then be used to calculate the chemical potential for the divalent or trivalent dopants, M (Equations 6.14 and 6.15, respectively).

$$\Delta H_f(MO) = \Delta\mu_{M} + \Delta\mu_{O} \quad (6.14)$$

$$\Delta H_f(M_2O_3) = 2\Delta\mu_{M} + 3\,\Delta\mu_{O} \quad (6.15)$$

The formation enthalpies (ΔH_f) were calculated from the difference between the DFT energy of a compound and the sum of the DFT elemental energies (e.g. metallic La and Ni, and molecular O_2), as exemplified in Equation 6.16.

$$\Delta H_f(La_2NiO_4) = E[La_2NiO_4] - 2\,E[La] - E[Ni] - 4\,E[O_2] \qquad (6.16)$$

Temperature effects are not considered when chemical potentials are calculated as outlined in Equations 6.9-6.16. The temperature and partial pressure dependence of the oxygen chemical potential, allowing its calculation for distinct chemical environments representing IT-SOFC operating conditions, is given by Equation 3.10 and outlined in Section 3.2.6.3. In this chapter, defect properties will be examined at the chemical potential environment corresponding to T = 700 K ($\Delta\mu_O$ = -0.78 eV, as presented in Table 3.1), representing the lower end of the IT range, with the *Bmab* orthorhombic to *I4/mmm* tetragonal transition occurring at higher temperatures.

6.2.2 Occupation Matrix Control

Even though the inclusion of a $+U$ correction to standard DFT methods encourages integer orbital occupation of *d* states, electron and electron hole localisation can still be problematic; these can get trapped in higher energy orbitals (local minima) instead of their true lowest energy configuration, resulting in an incorrect description of the ground state of a material. To address that problem and encourage correct orbital occupation, the occupation matrix control [368] was used when required, i.e., when systems did not get to their correct ground state when treated by standard PBEsol$+U$ calculations.

Occupation matrices are used to encourage a given orbital occupation by adjusting the potential as if the electrons were in a specific orbital, and hence encouraging the occupation of these states. Ni 3*d* orbitals are described by two 5x5 matrices, representing spin up and spin down states. Integer occupation of specific orbitals are encouraged by the matrix main diagonal elements, while the off-diagonal terms are used to alter the shape and rotation of the orbitals.

First, the system of interest is electronically and ionically optimized with the occupation matrix control turned on. This ensures that structural distortions resulting from specific orbital occupation are achieved. A second minimization is then performed on the optimised structure, starting from the previously calculated wavefunction information and with the occupation matrix control turned off. This step allows the obtained orbital states to minimize to more stable configurations, and hence for a meaningful DFT$+U$ energy to be

obtained. In this chapter, occupation matrix control was mainly used to ensure correct localisation of electron holes on Ni sites, and to evaluate the stability of systems with hole states positioned on distinct Ni cations.

6.3 Structural properties of La_2NiO_4

PBEsol+*U* calculations predict the orthorhombic *Bmab* structure to be slightly more stable than the tetragonal *I4/mmm* and the orthorhombic *Fmmm* phases, by only 0.01 eV. HSE06, on the other hand, calculates the *Bmab* phase to be 0.06 and 0.16 eV more stable than the *I4/mmm* and *Fmmm* phases, respectively. The *Bmab* structure will be used in this work for three main reasons besides its increased stability; first, such phase is thermodynamically stable in the lower end of the intermediate temperature SOFC operation range. Considering one of the main goals in the development of SOFCs is to lower the device's operating temperatures, the orthorhombic phase might be of increased interest in the future when compared to the tetragonal one. Furthermore, the transition from *Bmab* orthorhombic to *I4/mmm* tetragonal occurs at 770 K [335], while the change from *Fmmm* orthorhombic to *I4/mmm* tetragonal occurs at 423 K [336]. Hence, the only stable orthorhombic phase at SOFC operation temperatures (673 to 1273 K) is the *Bmab* one. In addition, experimentally, the *Fmmm* phase possess considerably more excess oxygen than the *Bmab* phase, while the main aim of this study is to investigate the defect properties of the stoichiometric material. Table 6.1 presents the equilibrium structural parameters of the *Bmab* orthorhombic unit cell of stoichiometric La_2NiO_4, obtained after fitting the PBEsol+*U* and HSE06 energy-volume curves to the Murnaghan equation of state (as outlined in Section 3.2.4), along with experimental data [333] for comparison.

HSE06 provides a better description of lattice vectors and cell volume than PBEsol+*U*, except for the *b* lattice vector, which is overestimated by 1.43%. Still, the lattice parameters calculated by both methods are in good agreement with experimental values. The symmetry independent fractional coordinates *x*, *y* and *z* calculated with PBEsol+*U* are in better agreement with neutron powder diffraction results. The deviation from experiment of the HSE06 fractional coordinates might be related to the overestimation of the *b* lattice vector. Overall, HSE06 also provides a better description of interatomic distances. However, the orthorhombic distortion of the structure predicted by PBEsol+*U*, closely related to the

Ni-O2-Ni angle, is in better agreement with experimental results, with a deviation of 0.67% from the experimental value, while HSE06 underestimates the angle by 1.58%. It is important to note that DFT calculates structural parameters at 0 K, while the experimental results presented here [333] were obtained at 295 K. Hence, some deviation was already expected. Still, both PBEsol+*U* and HSE06 values are in good agreement with experimental observations.

Table 6.1 – Structural properties of *Bmab* stoichiometric La_2NiO_4, obtained from PBEsol+*U* and HSE06 calculations and experiment [333,335]. O1 and O2 are the oxygen atoms in the axial and equatorial positions of the NiO_6 octahedra, respectively, according to Figure 6.1. The symmetry independent fractional coordinates are given by *x*, *y* and *z*. The percent deviation of calculated parameters with respect to experimental results is given in parenthesis.

Lattice Parameter		**PBEsol+*U***	**HSE06**	**Exp.** [333]
a (Å)		5.387 (-1.45%)	5.457 (-0.16%)	5.466
b (Å)		5.486 (-0.85%)	5.612 (1.43%)	5.533
c (Å)		12.459 (-0.76%)	12.501 (-0.43%)	12.555
V ($Å^3$)		368.18 (-3.02%)	382.82 (0.83%)	379.66
La	*x*	0.0000 (0.00%)	0.0000 (0.00%)	0.0000
	y	-0.0103 (-4.04%)	-0.0138 (39.39%)	-0.0099
	z	0.3639 (0.08%)	0.3635 (0.38%)	0.3636
Ni	*x* = *y* = *z*	0.0000 (0.00%)	0.0000 (0.00%)	0.0000
O1	*x*	0.0000 (0.00%)	0.0000 (0.00%)	0.0000
	y	0.0397 (+9.07%)	0.0542 (48.90%)	0.0364
	z	0.1759 (-1.90%)	0.1784 (-0.50%)	0.1793
O2	*x* = *y*	0.2500 (0.00%)	0.2500 (0.00%)	0.2500
	z	-0.0092 (-5.75%)	-0.0147 (68.96%)	-0.0087
Ni-O1 (Å)		2.202 (-2.61%)	2.251 (-0.44%)	2.261
Ni-O2 (Å)		1.926 (-1.18%)	1.965 (0.82%)	1.949
Ni-O2-Ni (°)		173.17 (0.67%)	169.29 (-1.58%)	172.01
La-O1 (Å) - across LaO layer		2.358 (+1.46%)	2.345 (0.90%)	2.324
- within $LaNiO_3$ layer		2.744 (-1.61%)	2.788 (-0.04%)	2.789
- within $LaNiO_3$ layer		2.517 (-2.02%)	2.480 (-3.46%)	2.569
La-O2 (Å) - within $LaNiO_3$ layer		2.521 (-0.67%)	2.524 (-0.55%)	2.538
		2.612 (-1.58%)	2.681 (1.02%)	2.654
O1-O1 (Å) - across LaO layer		3.294 (0.34%)	3.319 (1.10%)	3.283
		3.306 (0.58%)	3.328 (1.25%)	3.287
O2-O2 (Å)		2.694 (-1.43%)	2.728 (-0.18%)	2.733
		2.752 (-0.94%)	2.830 (1.87%)	2.778
O1-O2 (Å) - within NiO_6 octahedra		2.942 (-1.31%)	2.982 (0.03%)	2.981

6.4 Electronic and magnetic properties of La_2NiO_4

PBEsol+*U* and HSE06 calculations predict the G-type antiferromagnetic configuration of Ni cations on La_2NiO_4 to be more stable than the ferromagnetic state by 0.12 eV and 0.14 eV, respectively, in agreement with experimental observations [335,341–344].

The electronic structure of the *Bmab* phase of stoichiometric La_2NiO_4 was investigated, and the main valence and conduction band features were compared to experimental results. The calculated band structures calculated with PBEsol+*U* and HSE06 are presented in Figure 6.2, with the top of the valence band set as 0 eV.

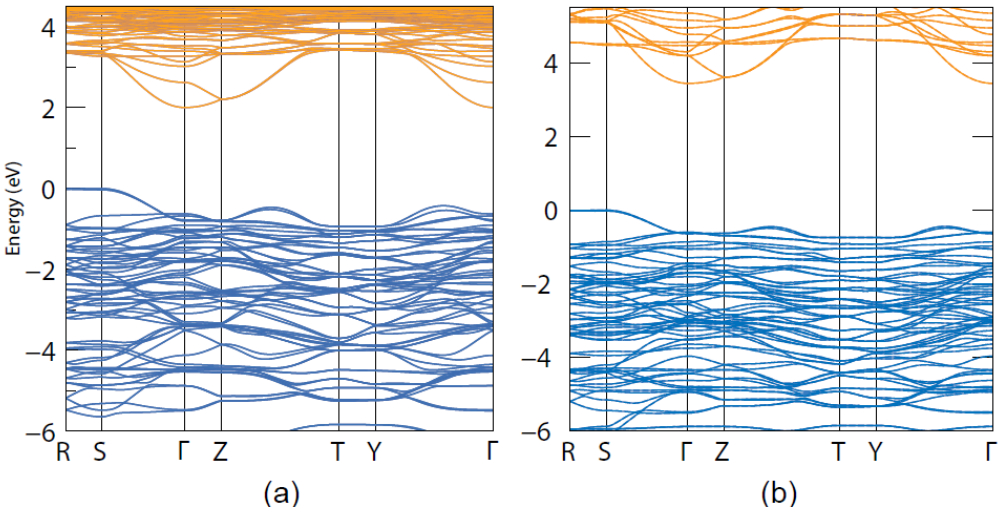

Figure 6.2 – Electronic band structure of orthorhombic (*Bmab*) La_2NiO_4, calculated with (a) PBEsol+*U* and (b) HSE06, plotted using the sumo package [246]. Valence band and conduction band are given in blue and orange, respectively. The valence band maximum is set to zero.

Similar features are observed in the electronic band structures obtained from both methods (Figure 6.2). PBEsol+*U* calculates the valence band maximum to be located at (0.00, 0.50, 0.03), immediately before the high symmetry point S (0.00, 0.50, 0.00). The conduction band minimum is located at Γ (0.00, 0.00, 0.00), resulting in an indirect band gap of 2.00 eV and a direct band gap of 2.63 eV at Γ. Higher band gap values are calculated with HSE06; the valence band maximum is located exactly at the high symmetry point S and the conduction band minimum is located at Γ, yielding an indirect band gap of 3.44 eV and a direct band gap of 4.05 eV at Γ. Experimental studies predict a charge excitation band gap

of at least 4 eV from valence band photoemission spectra [36,369], electron energy loss spectroscopy [370] and oxygen K-edge X-ray absorption [341]. Hence, HSE06 values are in much better agreement with experiment.

The calculated electronic density of states of *Bmab* La_2NiO_4 is presented in Figure 6.3. For both PBEsol+*U* and HSE06, the main feature of the valence band, which goes from 0 to approximately -6 eV, is dominated by O 2*p* and Ni 3*d* orbitals, with a small contribution from La states. These results are in agreement with the main feature in the material's valence-band photoemission spectra [370], which is shown in Figure 6.4 for comparison. Figure 6.4a shows the valence band XPS spectrum of $La_{1.85}Sr_{0.15}NiO_4$ [370]. According to the authors, the XPS spectrum of pure La_2NiO_4 is practically identical to the one presented in Figure 6.4a, apart from the Sr 4*p* feature observed at ~18 eV. In Figure 6.4b, the comparison between the UPS spectra of $La_{2-x}Sr_xNiO_4$ with varying *x*, indeed shows that the main valence band feature between 0 and 6 eV does not change significantly upon Sr-doping.

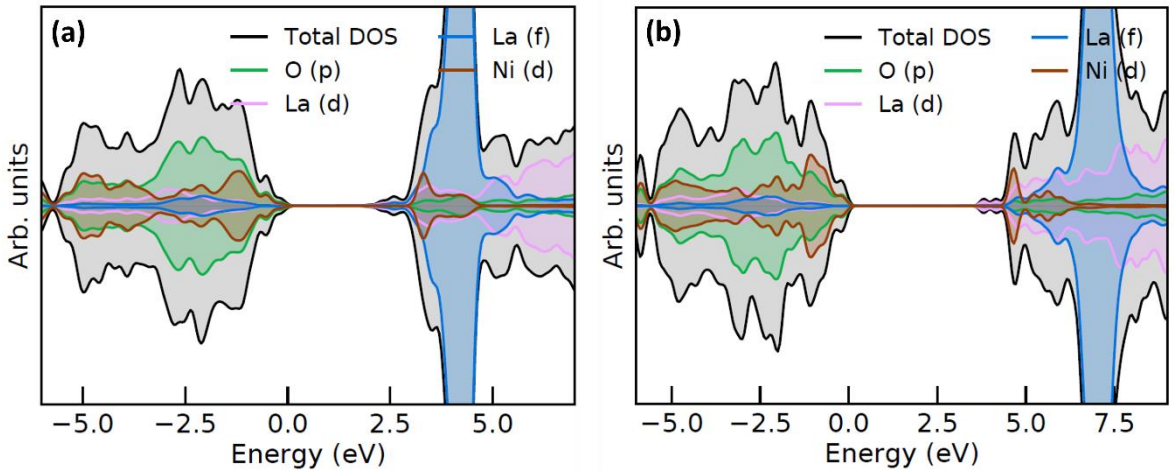

Figure 6.3 – Total and partial electronic density of states (EDOS) of orthorhombic (*Bmab*) La_2NiO_4 calculated with (a) PBEsol+*U* and (b) HSE06, plotted using the sumo package [246]. The valence band maximum is set to zero. O *p*, Ni *d*, La *d* and La *f* states are given in green, brown, pink and blue, respectively. The total EDOS is given in black.

The conduction band obtained from PBEsol+*U* and HSE06 calculations is mainly formed of La 4*f* orbitals, with some La 5*d*, Ni 3*d* and O 2*p* contributions. Bremsstrahlung isochromat spectroscopy (BIS) shows that unoccupied states consist of one intense La 4*f* feature, with a La 5*d* shoulder close to the CBM [370], as presented in Figure 6.4c, with the height of the La 4*f* feature at approximately 9 eV being proportional to the La concentration

in the material. Even though PBEsol+*U* predicts the existence of an intense La 4*f* feature in the conduction band, its position at approximately 4 eV above the Fermi level, is very different from what is observed in experiment, where La 4*f* states are located around 9 eV above the Fermi energy. Such discrepancy reflects the smaller band gap size calculated by this method in comparison to experiment. HSE06 results, on the other hand, yield a larger band gap, with the intense La 4*f* feature reaching its maximum at around 7 eV above the Fermi level, much closer to experimental observations. Therefore, HSE06 provides a better description of the electronic structure of the material. Still, as La_2NiO_4 is a *p*-type conductor, both PBEsol+*U* and HSE06 seem adequate to study its defect chemistry, as the valence band, relevant for *p*-type conduction, is well described by the two methods.

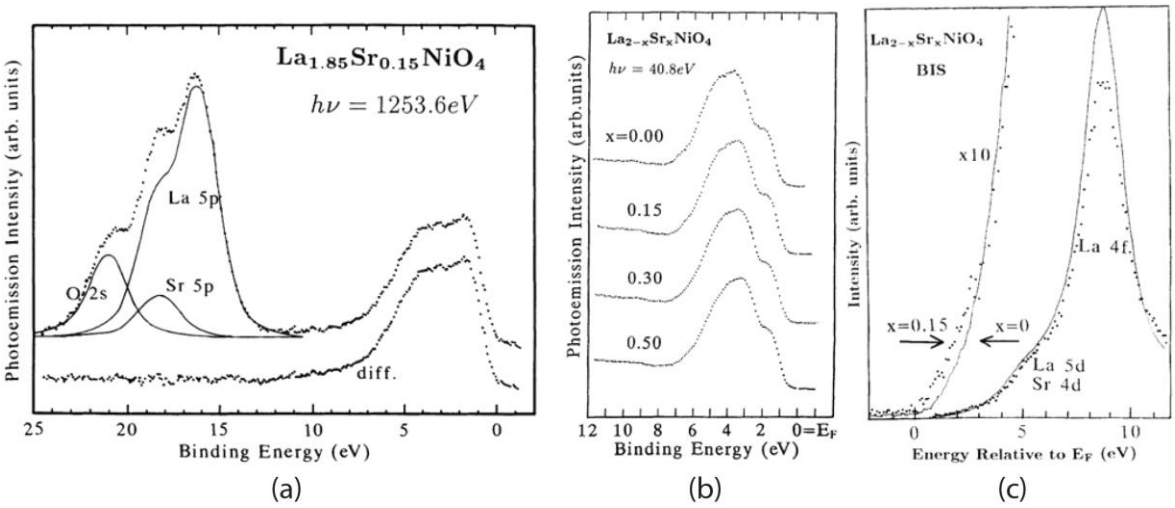

Figure 6.4 – (a) Valence band XPS spectrum of $La_{1.85}Sr_{0.15}NiO_4$ and, (b) UPS spectra of $La_{2-x}Sr_xNiO_4$ for x = 0.00, 0.15, 0.30 and 0.50 and (c) BIS spectra of La_2NiO_4 and $La_{1.85}Sr_{0.15}NiO_4$. Reproduced from Eisaki, H. *et al*. Electronic Structure of $La_{2-x}Sr_xNiO_4$ studied by photoemission and inverse-photoemission spectroscopy. *Phys. Rev. B* **45**, 12513-12521 (1992) [370].

The orbital projected band structures calculated from PBEsol+*U* and HSE06 results, presented in Figures 6.5 and 6.6, respectively, confirm that the valence band is primarily composed by Ni 3*d* and O 2*p* states, with oxygen states (mainly O2) being the main contributors at the VBM. Unoccupied states consist essentially of La 5*d* and 4*f* orbitals, with the first being the principal contributor to the CBM. The main difference between PBEsol+*U* and HSE06 results is the intensity of the La *f* contribution at the top of conduction band, as

observed in the EDOS in Figure 6.3. There is little overlap between La and O states, the main contributors to the CB and VB, respectively, indicating the occurrence of electron-charge transfer (and the charge transfer character of the band gap), and revealing the ionic character of the La-O interaction, in agreement to experimental results [36,341,369,370]. The interaction between Ni 3*d* and O 2*p* orbitals along the valence band indicates orbital mixing and hence some covalent character to the Ni-O bonds.

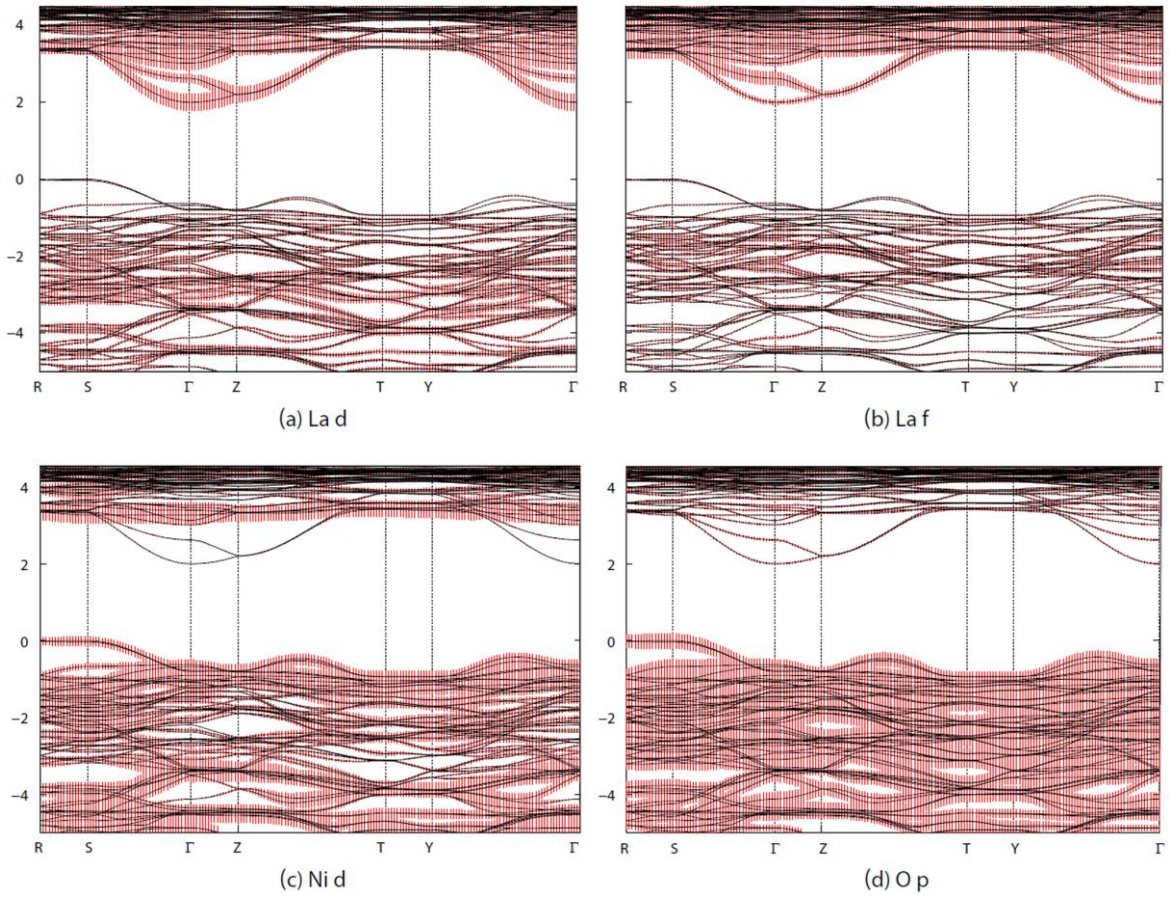

Figure 6.5 – Orbital project band structures of *Bmab* stoichiometric La_2NiO_4 calculated with PBEsol+*U* to investigate the mixing of (a) La *d*, (b) La *f*, (c) Ni *d* and (d) O *p* states in the electronic structure of the RP oxide.

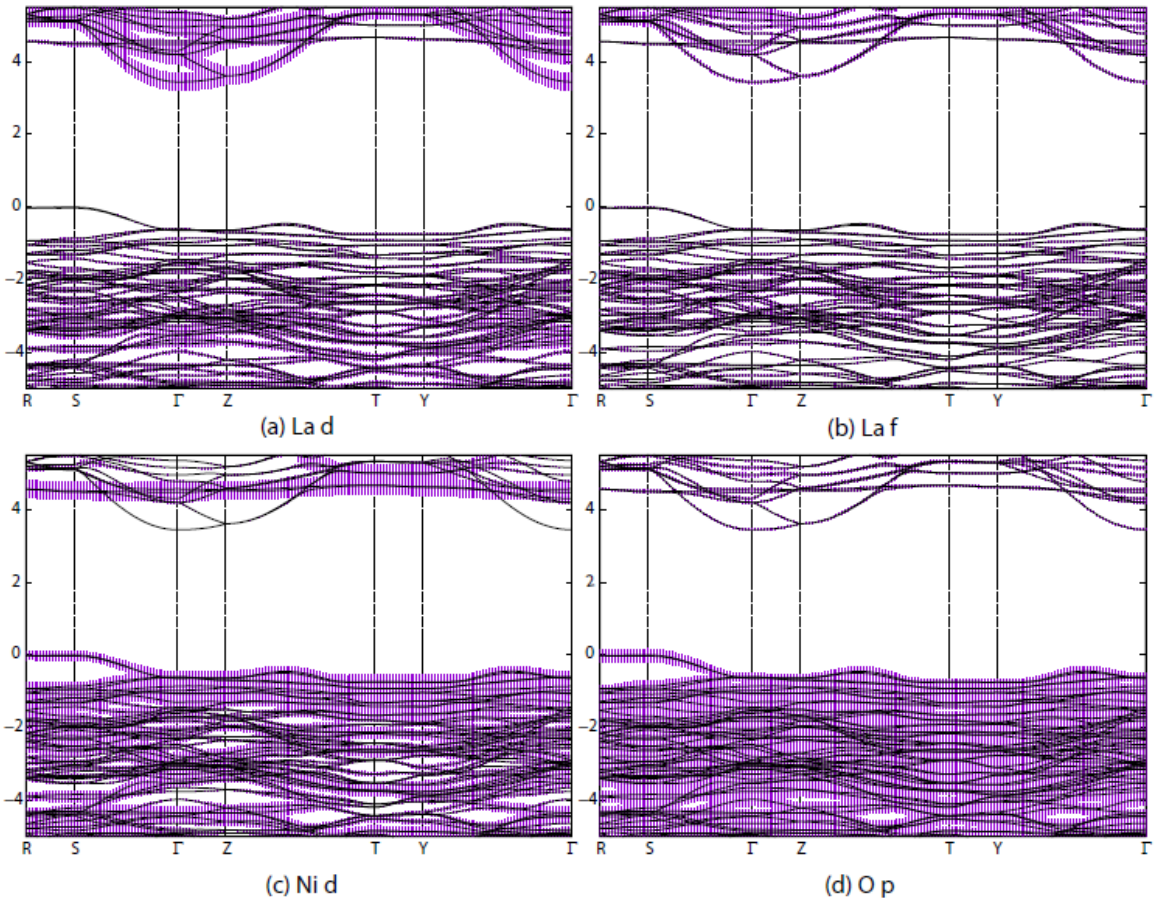

Figure 6.6 – Orbital project band structures of *Bmab* stoichiometric La_2NiO_4 calculated with HSE06 to investigate the mixing of (a) La *d*, (b) La *f*, (c) Ni *d* and (d) O *p* states in the electronic structure of the RP oxide.

6.5 Formation enthalpies of La_2NiO_4 and competing phases

The formation enthalpies of stoichiometric La_2NiO_4 and its competing phases (La_2O_3, NiO, $La_3Ni_2O_7$ and $La_4Ni_3O_{10}$), calculated from the elemental energies (as in Equation 6.16) using PBEsol+*U* and HSE06, with and without the inclusion of corrections to the over-binding of an oxygen molecule [371–373] (calculated as -0.60 eV for PBEsol+*U* and -0.17 eV for HSE06), are listed in Table 6.2, along with experimental results for comparison. All Ni-containing phases were predicted to preferably have an antiferromagnetic ordering of the Ni ions.

Table 6.2 – Formation enthalpies (eV) of La_2NiO_4 and its secondary phases from PBEsol+*U* and HSE06 results, with or without corrections to the over-binding of an O_2 molecule (-0.60 eV for PBEsol+U and -0.17 eV for HSE06). Values in bold are the closest to experimental results for a given functional, with their percent deviation given in parenthesis.

Phase	PBEsol+*U*	PBEsol+*U* (O correction)	HSE06	HSE06 (O correction)	Exp. (eV)
La_2NiO_4	-18.90 (10.3%)	**-21.32 (-1.2%)**	**-21.27 (-0.9%)**	-21.95 (-4.2%)	-21.08 [374]
La_2O_3	-16.09 (13.4%)	**-17.90 (3.6%)**	-18.08 (2.6%)	**-18.60 (-0.2%)**	-18.57 [240]
NiO	**-2.74 (-10.1%)**	-3.34 (-34.2%)	**-3.23 (-29.8%)**	-3.40 (-36.6%)	-2.49 [375], -2.44 [376]
$La_3Ni_2O_7$	-29.97 (11.2%)	**-34.20 (-1.3%)**	**-33.64 (0.3%)**	-34.84 (-3.2%)	-33.76 [374]
$La_4Ni_3O_{10}$	-40.69 (12.0%)	**-46.74 (-1.1%)**	**-45.60 (1.4%)**	-47.31 (-2.3%)	-46.24 [374]

For PBEsol+*U* calculations, the formation energies including the correction to the over-binding of O_2 are in better agreement with literature results. The formation enthalpies of La_2NiO_4, $La_3Ni_2O_7$ and $La_4Ni_3O_{10}$ are underestimated by approximately 1%, while the calculated value for La_2O_3 is overestimated by 3.6%. The largest error is in the calculation of the formation enthalpy of NiO; PBEsol+*U* severely underestimate its value (by 10.1%) and the use of an oxygen correction further increases this underestimation to 34.2%. It is important to note the challenges associated to the calculation of DFT formation energies; the overbinding of the O_2 molecule, for example, typically observed in LDA and GGA calculations [372,373,377], introduces systematic errors when calculating the formation enthalpies of oxides. Furthermore, uncompensated SIE can also introduce errors to the DFT total energies, which are more significant in the case of transition metals and their localised *d* states. Here, we tried to correct such errors by adding +*U* corrections to both Ni 3*d* and O 2*p* states. The +*U* value of 5.3 eV applied to Ni 3*d* states was fitted to reproduce the electronic and magnetic structure of NiO [203], since such corrections are used to encourage correct *d* orbital occupation. PBEsol+*U* calculations predict each Ni ion to have a magnetic moment of 1.696 μ_B, in excellent agreement with experimentally reported results (1.7-1.9 μ_B [378–380]), indicating the suitability of this +*U* correction. However, to correctly reproduce experimental formation energies, a different +*U* value would be necessary. Yu *et al*. [381] carried out PBE+*U* calculations with U_{Ni3d} = 0, 4.3 and 5.3 eV and obtained heats of formation of -1.00, -2.64 and -3.05 eV, respectively, suggesting that formation enthalpies strongly depend on the magnitude of +*U*.

For HSE06, most values (Table 6.2) are in closer agreement to experimental results when the O_2 correction is not considered. The formation energy of La_2NiO_4 is underestimated by 0.9%, while La_2O_3, $La_3Ni_2O_7$ and $La_4Ni_3O_{10}$ have their values overestimated by 2.6%, 0.3% and 1.4%, respectively. HSE06 also fails to accurately calculate the formation enthalpy of NiO, which is underestimated by ~30% in comparison to the experimental value. However, as HSE06 calculations are very computationally expensive and a relatively big unit cell (64 atoms) is necessary to correctly describe the antiferromagnetic arrangement of Ni ions in NiO, single point HSE06 calculations were performed on the optimized PBEsol+*U* NiO system, i.e. no volume optimization was carried out using HSE06. As a result, the obtained formation energies might carry some error from the volume optimization carried out with PBEsol+*U*.

6.6 Thermodynamic stability field of stoichiometric La_2NiO_4

The thermodynamic stability of La_2NiO_4 has been previously evaluated under a range of temperatures (305 K to 1673 K) and oxygen partial pressures (10^{-25} to 1 atm), through the calculation of the Gibbs free energy of the material's possible decomposition reactions from experimental thermodynamic data [38,382]. Its decomposition into La_2O_3 and higher order $La_{n+1}Ni_nO3_{n+1}$ phases, such as $La_3Ni_2O_7$ and $La_4Ni_3O_{10}$, was found to be thermodynamically favourable in the 300-1373 K range at $p(O_2)$ = 0.2 atm [38]. It has also been suggested that the decomposition of La_2NiO_4 into La_2O_3 and NiO is thermodynamically favourable at temperatures below 850 K regardless of oxygen partial pressure [382]. Therefore, La_2NiO_4 is kinetically stable; despite the thermodynamic favourability of its decomposition reactions, the material can still be obtained experimentally, and its complete decomposition is not observed. The reason why the material's decomposition is not experimentally observed is still not fully understood; its decomposition reactions might possess a very low rate determining step or surface passivation mechanisms might take place [38].

The chemical potential limits determining the region of thermodynamic stability for stoichiometric La_2NiO_4 defined by the formation of its competing phases, were calculated using CPLAP [252] for PBEsol+*U*, HSE06 and experimental formation enthalpies, and are presented in Figure 6.7. Despite the material's apparent thermodynamically instability, the experimental formation energies (Table 6.2) considered here yield a very narrow

thermodynamic stability field, as they were extracted from different sources [240,374,375]; the material is calculated to be stable by only 0.019 eV. PBEsol+*U* results suggest that the material is thermodynamically stable. HSE06 results, on the other hand, predict the material to be thermodynamically unstable by 0.04 eV, in agreement with previous studies [38,382]. The HSE06 thermodynamic stability field presented in Figure 6.8b was obtained by adjusting the calculated hybrid-DFT energy by 0.04 eV.

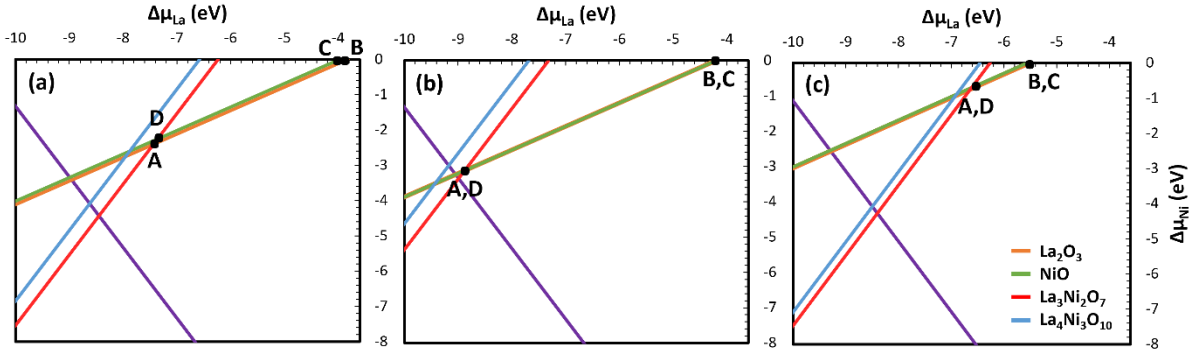

Figure 6.7 – Region of stability for La_2NiO_4 spanned by $\Delta\mu_{La}$ and $\Delta\mu_{Ni}$ obtained from the formation energies calculated using (a) PBEsol+*U* (b) HSE06 and (c) experimental results. A-D are the intersection points of the stability field determined by the limits set by the competing phases.

The coloured lines in Figure 6.7 represent the limits of the La_2NiO_4 stability field, set by the formation energies of the RP oxide and its competing phases. A-D are the intersection points defining the region of thermodynamic stability for this system. For HSE06, point A practically coincides with point D, while B is virtually the same as C, since the stability field was calculated for the exact energy value at which the material becomes stable. Lower hybrid-DFT energies would separate those points, increasing the width of the thermodynamic stability field. The oxygen, lanthanum and nickel chemical potentials and the competing phases in each of the intersection points of the stability field of La_2NiO_4, calculated from PBEsol+*U*, HSE06 and experimental results, are presented in Table 6.3 and will be used to calculate the material's defect properties under different chemical environments.

Table 6.3 – Elemental chemical potentials (in eV) for O, La and Ni, and competing phases at the A-D intersection points of the thermodynamic stability field of La_2NiO_4 (Figure 6.8), determined by the formation of its competing phases.

Competing Phases		PBEsol+U			HSE06			Experiment		
		$\Delta\mu_O$	$\Delta\mu_{La}$	$\Delta\mu_{Ni}$	$\Delta\mu_O$	$\Delta\mu_{La}$	$\Delta\mu_{Ni}$	$\Delta\mu_O$	$\Delta\mu_{La}$	$\Delta\mu_{Ni}$
A	La_2O_3, $La_3Ni_2O_7$	-1.01	-7.44	-2.41	-0.11	-8.88	-3.12	-1.77	-6.63	-0.74
B	La_2O_3	-3.42	-3.82	0.00	-3.23	-4.20	0.00	-2.51	-5.52	0.00
C	NiO	-3.34	-3.97	0.00	-3.23	-4.20	0.00	-2.49	-5.56	0.00
D	$La_3Ni_2O_7$, NiO	-1.09	-7.36	-2.26	-0.11	-8.88	-3.12	-1.79	-6.61	-0.70

The oxygen chemical potential values representing SOFC operating conditions, which vary from -0.65 to -1.17 eV in the 600-1000 K range (as outlined in Section 3.2.6.3 and presented in Table 3.1), fall within the stability field calculated by HSE06, as shown in Figure 6.8, but outside PBEsol+*U* and experimental stability fields. The La and Ni chemical potential values calculated from HSE06 results under IT-SOFC operating conditions ($600 < T < 800$K and $p(O_2) = 0.21$ atm) are listed in Table 6.4. While the main focus of this chapter is to calculate La_2NiO_4 defect properties under IT-SOFC conditions (Table 6.4), HSE06 chemical potential limits will also be used, to investigate how the defect chemistry of the material would vary under O-rich (intersection point A with $\Delta\mu_O = -0.11$ eV) and O-poor (intersection point B with $\Delta\mu_O = -3.23$ eV) chemical environments.

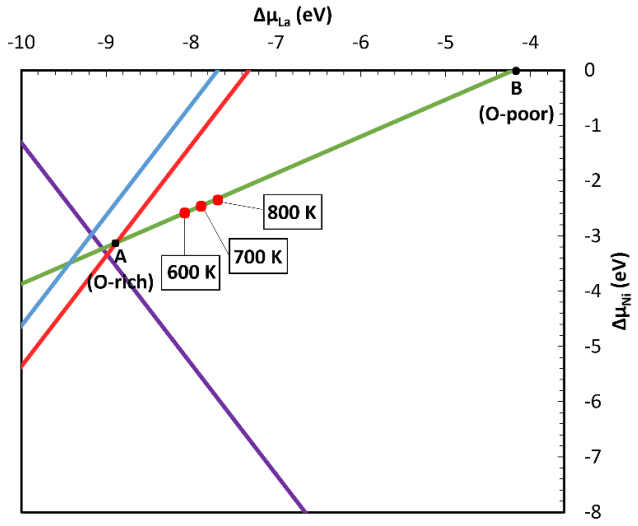

Figure 6.8 – Region of stability for La_2NiO_4 spanned by $\Delta\mu_{La}$ and $\Delta\mu_{Ni}$ obtained from the formation energies calculated using HSE06. A and B are the intersection points of the stability field determined by the limits set by the competing phases, corresponding to O-rich ($\Delta\mu_O$ = -0.11 eV) and O-poor ($\Delta\mu_O$ = -0.11 eV) conditions, respectively. Chemical potential environments related to IT-SOFC operating conditions (600 < T < 800 K, listed in Table 6.4) are in red.

Table 6.4 – Elemental chemical potentials (in eV) for O, La and Ni corresponding to IT-SOFC operating conditions (600 < T < 800 K), calculated from HSE06 results.

T (K)	$\Delta\mu_{La}$	$\Delta\mu_{Ni}$	$\Delta\mu_O$
600	-8.07	-2.58	-0.65
700	-7.87	-2.45	-0.78
800	-7.69	-2.33	-0.90

6.7 Oxygen defects in La_2NiO_4

Experimentally, oxygen interstitials are observed to be the dominant intrinsic defect in La_2NiO_4 systems [332]. In this section, PBEsol+U and HSE06 calculations are performed to investigate oxygen defect (vacancies and interstitials) formation. The formation energies of oxygen vacancies ($V_{O1}^{\bullet\bullet}$ and $V_{O2}^{\bullet\bullet}$) and oxygen interstitials (O_i'') in La_2NiO_4, under O-rich, O-poor and IT-SOFC operating conditions were calculated from Equation 3.3, to determine

which oxygen defects are predicted as the most stable by PBEsol+*U* and HSE06 in different chemical environments. Equation 3.3 can be rewritten as Equations 6.17 and 6.18 for an oxygen vacancy and an oxygen interstitial, respectively. E^D and E^P are the calculated energies of the defective and pure La_2NiO_4 systems, and $(E_{O_2} + \Delta\mu_{O_2})$ is the oxygen chemical potential. The obtained formation energies, E_f, are listed in Table 6.5. The introduction of an oxygen vacancy or an oxygen interstitial were charge compensated by two electrons or two holes, respectively, localised on Ni ions.

$$E_f(V_O^{\bullet\bullet}) = (E^D - E^P) + \frac{1}{2}(E_{O_2} + \Delta\mu_{O_2}) \quad (6.17)$$

$$E_f(O_i'') = (E^D - E^P) - \frac{1}{2}(E_{O_2} + \Delta\mu_{O_2}) \quad (6.18)$$

Table 6.5 – Formation energies of oxygen vacancies and interstitials (in eV) in La_2NiO_4 under O-rich, O-poor and IT-SOFC operating conditions (600-800 K, with $p(O_2)$ = 0.21 atm and p^o = 1 atm), calculated from PBEsol+*U* and HSE06 results. Each defect was charge compensated by the introduction of two electrons (for oxygen vacancies) or two holes (for oxygen interstitials) localized on Ni atoms.

Conditions	**$\Delta\mu_O$ (eV)**	**PBEsol+*U***			**HSE06**		
		E($V_{O1}^{\bullet\bullet}$)	**E($V_{O2}^{\bullet\bullet}$)**	**E(O_i'')**	**E($V_{O1}^{\bullet\bullet}$)**	**E($V_{O2}^{\bullet\bullet}$)**	**E(O_i'')**
O-rich (A)	-0.11	5.74	4.70	-0.44	5.35	4.11	-0.69
O-poor (B)	-3.23	2.62	1.57	2.68	2.23	0.99	2.43
600 K	-0.65	5.20	4.15	0.10	4.81	3.57	-0.15
700 K	-0.78	5.07	4.02	0.23	4.68	3.44	-0.02
800 K	-0.90	4.95	3.90	0.35	4.56	3.32	0.10

PBEsol+*U* and HSE06 predict $V_{O2}^{\bullet\bullet}$ to be more stable than $V_{O1}^{\bullet\bullet}$ by 1.05 and 1.24 eV, respectively, in agreement with experimental reports [339,383]. From PBEsol+*U* calculations, the formation energies of oxygen vacancies are higher than 1.5 eV under all analysed chemical potential environments, and hence these defects are unlikely to form or will be present in very low concentrations. HSE06 yield slightly lower defect formation enthalpies, with $V_{O2}^{\bullet\bullet}$ being likely to form under O-poor environments (E($V_{O2}^{\bullet\bullet}$) = 0.99 eV). However, O-poor conditions correspond to an extremely low oxygen chemical potential, which is not going to be achieved under SOFC operation.

The introduction of $V_{O1}^{\bullet\bullet}$ in the axial position of the NiO_6 octahedron causes significant elongation of the opposite axial Ni-O bond, which goes from 2.20 Å in the bulk structure to 2.62 Å, due to the displacement of the nickel cation towards the vacancy. When $V_{O2}^{\bullet\bullet}$ is introduced in an equatorial position, no significant displacement of the nickel cations occurs. An elongation of the opposite Ni-O equatorial bond occurs (from 1.92 Å to 2.04 Å), but is less significant than what was observed for $V_{O1}^{\bullet\bullet}$. These results suggest that the enhanced stability of $V_{O2}^{\bullet\bullet}$ might be due to the fact that the inclusion of a vacancy at the O2 site causes less structural distortion when compared to the O1 site. Furthermore, O1 and O2 experience distinct chemical environments in the RP structure – while the first oxygen is located at the edge of the perovskite/rocksalt layers, the latter is located within the perovskite block, further away from the region where oxide-ion transport via an interstitialcy mechanism occurs, resulting in increased stability. Electrons arising from charge compensation are preferably located on nickel cations that are in a nearest neighbour position to the oxygen vacancy, i.e., within the same [NiO_6] octahedra.

The defect formation energies listed in Table 6.5 suggest that oxygen interstitials are the dominant defect in this RP oxide, with negative formation energies under some chemical potential conditions. In fact, HSE06 predicts its formation to be spontaneous under all analysed chemical potential environments, except for the unrealistic O-poor conditions, in agreement with the experimental observation of oxygen excess [332]. O_i'' is located within a tetrahedron formed by La cations, with La-O distances of 2.34 Å. Oxygen interstitials are calculated to be less stable than vacancies only under O-poor environments, which are not relevant for SOFC operation.

6.8 Aliovalent A- and B-site doping in La_2NiO_4

Aliovalent doping and its influence on the conduction properties of La_2NiO_4 was evaluated by performing two types of calculations. A first set of defect calculations was carried out by introducing a single charged defect (either a dopant or its charge compensating defect) within the simulation cell, assuming a uniform background charge to maintain overall charge neutrality. The formation energies of these isolated charged defects were combined, yielding charge neutral defect energies. These combined isolated defects represent systems where the dopants and their charge compensating defects are far away from each other. In a

second set of calculations, neutral defect clusters were considered, in which the dopant and its charge compensating defects are located within the same simulation cell. Neutral defect clusters represent La_2NiO_4 systems in which dopants and their charge compensating defects are relatively close to each other. The binding energy between dopants and their charge compensating defect was then calculated from the difference between the formation energies of charged isolated defects and neutral defect clusters, indicating whether the clustered or isolated defects are more likely to be present in the material, i.e. if defects are stabilised when they are close to or far away from each other.

Dopants were introduced to the A- and B-sites of the La_2NiO_4 (A = Ca(II), Sr(II), Ba(II), and B = Fe(III), Mn(III), Co(III)), considering both ionic and electronic compensation mechanisms. A-site doping with divalent metals can result in the formation of an oxygen vacancy ($2A'_{La} + V_O^{\bullet\bullet}$, in Kröger-Vink notation, where A is the divalent A-site dopant), or an electron hole localized on a Ni atom ($A'_{La} + Ni_{Ni}^{\bullet}$), as presented in Equations 6.5 and 6.6, respectively. Similarly, B-site doping with trivalent metals can generate an oxygen interstitial ($2B_{Ni}^{\bullet} + O_i''$, where B is the trivalent B-site dopant) or an electron, also localized on Ni ($B_{Ni}^{\bullet} + Ni'_{Ni}$), as in Equations 6.7 and 6.8. Defect formation energies were evaluated under distinct chemical potential environments, representing O-poor, O-rich and IT-SOFC operating conditions. The La, Ni, O and dopant chemical potentials considered are listed in Table 6.6.

Table 6.6 – Chemical potentials of La, Ni, O and the analysed A- (Ca(II), Sr(II), Ba(II)) and B-site (Co(III), Fe(III), Mn(III)) dopants (in eV), corresponding to O-poor, O-rich and IT-SOFC conditions (T = 700 K, $p(O_2)$ = 0.21 atm and p^o = 1 atm)

Conditions	**$\Delta\mu_{La}$**	**$\Delta\mu_{Ni}$**	**$\Delta\mu_{O}$**	**$\Delta\mu_{Sr}$**	**$\Delta\mu_{Ca}$**	**$\Delta\mu_{Ba}$**	**$\Delta\mu_{Fe}$**	**$\Delta\mu_{Mn}$**	**$\Delta\mu_{Co}$**
A (O-rich)	-8.88	-3.12	-0.11	-5.65	-6.12	-5.16	-4.48	-5.09	-3.44
B (O-poor)	-4.20	0.00	-3.23	-2.53	-2.99	-2.04	0.20	-0.41	1.24
600 K	-8.07	-2.58	-0.65	-5.11	-5.57	-4.62	-3.67	-4.28	-2.63
700 K	-7.87	-2.45	-0.78	-4.98	-5.44	-4.49	-3.48	-4.09	-2.43
800 K	-7.69	-2.33	-0.90	-4.86	-5.32	-4.37	-3.30	-3.91	-2.25

6.8.1 Combined isolated defects

6.8.1.1 A-site dopants

Tables 6.7 and 6.8 present the defect formation energies for the different combinations of isolated defects in A-site doped La_2NiO_4 calculated from PBEsol+*U* and HSE06 results, respectively, considering both ionic and electronic charge compensation mechanisms. The possible defect combinations presented in Tables 6.7 and 6.8 are written in Kröger-Vink notation. A-site dopants were introduced in the La_2NiO_4 supercell in a formal charge state of -1, while oxygen vacancies were added to the system with a +2 charge states. The combination of these charged cells results in charge-neutral defects and represent systems in which charge compensating defects are far away from dopants.

There is no variation among the calculated defect formation energies for ionically charge compensated A-site doping under distinct chemical potential environments (e.g. HSE06 calculations predict a formation energy of 2.83 eV for the $2Ca'_{La} + V^{\bullet\bullet}_{O1}$ defect under all three chemical environments). This is a result of ionic charge compensation generating oxygen-containing defects (either vacancies or interstitials). Hence, $\Delta\mu_{La}$, $\Delta\mu_A/\Delta\mu_B$ and $\Delta\mu_O$ are necessary to calculate the defect formation energies (as in Equation 3.3), with changes in the La and O chemical potentials being balanced by changes in the dopant chemical potential. For defects generated from electronic charge compensation (holes or electrons), only $\Delta\mu_{La}$ and $\Delta\mu_A/\Delta\mu_B$ are included in the calculation, resulting in distinct values for the different chemical environments.

Table 6.7 – Formation energies (in eV) of the combined isolated defects in A-site doped La_2NiO_4, calculated from PBEsol+*U* results under distinct chemical potential environments, considering both ionic and electronic charge compensation mechanisms. Considered defects are written in Kröger-Vink notation.

Defect	O-rich	O-poor	600 K	700 K	800 K
$2Ca'_{La} + V^{\bullet\bullet}_{O1}$	2.06	2.06	2.06	2.06	2.06
$2Ca'_{La} + V^{\bullet\bullet}_{O2}$	1.51	1.51	1.51	1.51	1.51
$2Sr'_{La} + V^{\bullet\bullet}_{O1}$	1.07	1.07	1.07	1.07	1.07
$2Sr'_{La} + V^{\bullet\bullet}_{O2}$	0.53	0.53	0.53	0.53	0.53
$2Ba'_{La} + V^{\bullet\bullet}_{O1}$	1.19	1.19	1.19	1.19	1.19
$2Ba'_{La} + V^{\bullet\bullet}_{O2}$	0.64	0.64	0.64	0.64	0.64
$Ca'_{La} + Ni^{\bullet}_{Ni}$	-0.69	0.87	-0.42	-0.36	-0.30
$Sr'_{La} + Ni^{\bullet}_{Ni}$	-1.18	0.38	-0.91	-0.85	-0.79
$Ba'_{La} + Ni^{\bullet}_{Ni}$	-1.13	0.43	-0.86	-0.79	-0.73

Table 6.8 – Formation energies (in eV) of the combined isolated defects in A-site doped La_2NiO_4, calculated from HSE06 results under distinct chemical potential environments, considering both ionic and electronic charge compensation mechanisms. Considered defects are written in Kröger-Vink notation.

Defect	O-rich	O-poor	600 K	700 K	800 K
$2Ca'_{La} + V^{\bullet\bullet}_{O1}$	2.83	2.83	2.83	2.83	2.83
$2Ca'_{La} + V^{\bullet\bullet}_{O2}$	2.02	2.02	2.02	2.02	2.02
$2Sr'_{La} + V^{\bullet\bullet}_{O1}$	2.04	2.04	2.04	2.04	2.04
$2Sr'_{La} + V^{\bullet\bullet}_{O2}$	1.23	1.23	1.23	1.23	1.23
$2Ba'_{La} + V^{\bullet\bullet}_{O1}$	2.34	2.34	2.34	2.34	2.34
$2Ba'_{La} + V^{\bullet\bullet}_{O2}$	1.53	1.53	1.53	1.53	1.53
$Ca'_{La} + Ni^{\bullet}_{Ni}$	-0.62	0.94	-0.35	-0.28	-0.22
$Sr'_{La} + Ni^{\bullet}_{Ni}$	-1.01	0.55	-0.74	-0.68	-0.62
$Ba'_{La} + Ni^{\bullet}_{Ni}$	-0.86	0.70	-0.59	-0.53	-0.47

When dopants are far away from each other, the ionic charge compensation of A-site dopants will preferably result in the formation of oxygen vacancies on the O2 site rather than the O1 site, in agreement to the results presented in Section 6.7. PBEsol+*U* and HSE06 predict the $2A'_{La} + V^{\bullet\bullet}_{O2}$ configuration to be 0.54 and 0.81 eV more stable than the $2A'_{La} + V^{\bullet\bullet}_{O1}$ systems, respectively. Still, electronic charge compensation ($A'_{La} + Ni^{\bullet}_{Ni}$) possesses lower formation energies than the ionic mechanisms and hence is more likely to occur, suggesting that aliovalent A-site doping can potentially enhance *p*-type conduction in the material. Both PBEsol+*U* and HSE06 predict the calculated formation energies to increase in the Sr(II) < Ba(II) < Ca(II) order. A-site doping with bigger cations than the host (the ionic radii are 1.216 Å for La(III), 1.18 Å for Ca(II), 1.31 Å for Sr(II) and 1.47 Å for Ba(II) [26]) can alleviate tensions arising from the mismatch of the intergrown LaO and NiO_2 layers in this RP oxide; LaO and NiO_2 layers are stretched and compressed, respectively, when intercalated in the material [331], and the stretching observed in the first can be facilitated through A-site doping, releasing part of the stress. Indeed, the A(II)-O bond distances increase in the dopant order Ca(II) < Sr(II) < Ba(II), with Ca(II)-O and Sr/Ba(II)-O distances being smaller and bigger than La(III)-O in the bulk material, respectively. Ba(II), however, is considerably bigger than the host La(III) and hence is probably larger than the ideal ionic radii for A-site dopants in this system. Even though the most energetically favourable defect combination under SOFC operating conditions was calculated to be $Sr'_{La} + Ni^{\bullet}_{Ni}$, electronic compensation yields negative formation energies for all three dopants, indicating that they are easily formed and can all potentially contribute to *p*-type electronic conduction in the material, in line with experimental observations [329,332,350]

6.8.1.2 B-site dopants

Tables 6.9 and 6.10 present the defect formation energies for the different combinations of isolated defects in B-site doped La_2NiO_4 calculated from PBEsol+*U* and HSE06 results, respectively, considering both ionic and electronic charge compensation mechanisms. B-site trivalent dopants were introduced in the La_2NiO_4 supercell in a formal charge state +1. Oxygen interstitials were added to the system with a -2 charge state. Similarly to what was observed for A-site dopants, there is no variation among the calculated defect formation energies for ionically charge compensated B-site doping under distinct

chemical potential environments (e.g. HSE06 calculations predict a formation energy of 0.98 eV for the $2Fe_{Ni}^{\bullet} + O_i''$ defect under all three chemical environments), for the same reasons outlined above.

Both PBEsol+*U* and HSE06 predict ionic compensation to be more favourable than the electronic mechanism, resulting in the creation of an oxygen interstitial, which can potentially improve the material's ionic conduction properties. The calculated defect formation energies increase in the Co(III) < Mn(III) < Fe(III) order. Similarly to what was observed for A-site dopants, this is a result of steric effects; Fe(III) and Mn(III) are preferably in a high spin configuration and have an ionic radius of 0.64 Å, and hence are similar in size to 6-coordinate Ni(II) (0.69 Å). Co(II), on the other hand, preferably assumes a low spin configuration and has ionic radius of 0.54 Å, facilitating the compression of the NiO_2 layer and releasing the tension arising from the mismatch between the LaO and NiO_2 layers' ideal sizes. Under SOFC operating conditions, PBEsol+*U* predicts all three dopants to possess negative formation energies and potentially contribute to oxide-ion conductivity. HSE06 calculations, on the other hand, yield a higher positive defect formation energy for the Fe-doped system (0.98 eV), suggesting that Fe-doping would be the less beneficial than Mn- or Co-substitution (-0.24 and -0.32 eV, respectively).

Table 6.9 – Formation energies (in eV) of the combined isolated defects in B-site doped La_2NiO_4, calculated from PBEsol+*U* results under distinct chemical potential environments, considering both ionic and electronic charge compensation mechanisms. Considered defects are written in Kröger-Vink notation.

Defect	O-rich	O-poor	600 K	700 K	800 K
$2Co_{Ni}^{\bullet} + O_i''$	-0.72	-0.72	-0.72	-0.72	-0.72
$2Fe_{Ni}^{\bullet} + O_i''$	-0.14	-0.14	-0.14	-0.14	-0.14
$2Mn_{Ni}^{\bullet} + O_i''$	-0.50	-0.50	-0.50	-0.50	-0.50
$Co_{Ni}^{\bullet} + Ni_{Ni}'$	1.52	-0.04	1.25	1.19	1.13
$Fe_{Ni}^{\bullet} + Ni_{Ni}'$	1.81	0.25	1.54	1.48	1.42
$Mn_{Ni}^{\bullet} + Ni_{Ni}'$	0.07	1.63	1.36	1.30	1.24

Table 6.10 – Formation energies (in eV) of the combined isolated defects in B-site doped La_2NiO_4, calculated from HSE06 results under distinct chemical potential environments, considering both ionic and electronic charge compensation mechanisms. Considered defects are written in Kröger-Vink notation.

Defect	O-rich	O-poor	600 K	700 K	800 K
$2Co_{Ni}^{\bullet} + O_i''$	-0.32	-0.32	-0.32	-0.32	-0.32
$2Fe_{Ni}^{\bullet} + O_i''$	0.98	0.98	0.98	0.98	0.98
$2Mn_{Ni}^{\bullet} + O_i''$	-0.24	-0.24	-0.24	-0.24	-0.24
$Co_{Ni}^{\bullet} + Ni_{Ni}'$	1.81	0.25	1.54	1.47	1.41
$Fe_{Ni}^{\bullet} + Ni_{Ni}'$	2.46	0.90	2.19	2.12	2.06
$Mn_{Ni}^{\bullet} + Ni_{Ni}'$	1.85	0.29	1.58	1.52	1.46

6.8.2 Neutral defect clusters

6.8.2.1 A-site doping

The formation energies of neutral defect clusters, in which dopants and charge compensating defects are combined within the same supercell, were obtained, and indicate the stability of these defects when they are located close to each other. Their binding energy can then be calculated from the difference between the formation energies of charged isolated defects (Tables 6.7 and 6.8) and neutral defect clusters. Tables 6.11 and 6.12 present the formation energies of neutral defect clusters obtained from PBEsol+*U* and HSE06 results, respectively, and the resulting binding energy (BE) values. Several defect-defect configurations were tested, with the more energetically favourable ones presented here. BE indicates whether the clustered (negative values) or isolated defects (positive values) are more likely to be present in the material.

Table 6.11 – Formation and binding energies (in eV) of the neutral defect clusters in A-site doped La_2NiO_4, calculated from PBEsol+*U* results, under distinct chemical potential environments, considering both ionic and electronic charge compensation mechanisms. Defects are written in Kröger-Vink notation.

Defect	O-rich	O-poor	600 K	700 K	800 K	BE
$2Ca'_{La} + V^{\bullet\bullet}_{O1}$	1.60	1.60	1.60	1.60	1.60	-0.46
$2Ca'_{La} + V^{\bullet\bullet}_{O2}$	1.37	1.37	1.37	1.37	1.37	-0.15
$2Sr'_{La} + V^{\bullet\bullet}_{O1}$	0.74	0.74	0.74	0.74	0.74	-0.33
$2Sr'_{La} + V^{\bullet\bullet}_{O2}$	0.53	0.53	0.53	0.53	0.53	0.00
$2Ba'_{La} + V^{\bullet\bullet}_{O1}$	0.55	0.55	0.55	0.55	0.55	-0.64
$2Ba'_{La} + V^{\bullet\bullet}_{O2}$	0.51	0.51	0.51	0.51	0.51	-0.14
$Ca'_{La} + Ni^{\bullet}_{Ni}$	-0.33	1.23	-0.06	0.00	0.06	0.36
$Sr'_{La} + Ni^{\bullet}_{Ni}$	-0.82	0.74	-0.55	-0.48	-0.42	0.36
$Ba'_{La} + Ni^{\bullet}_{Ni}$	-0.76	0.80	-0.49	-0.43	-0.37	0.36

Table 6.12 – Formation and binding energies (in eV) of the neutral defect clusters in A-site doped La_2NiO_4, calculated from HSE06 results, under distinct chemical potential environments, considering both ionic and electronic charge compensation mechanisms. Defects are written in Kröger-Vink notation.

Defect	O-rich	O-poor	600 K	700 K	800 K	BE
$2Ca'_{La} + V^{\bullet\bullet}_{O1}$	2.43	2.43	2.43	2.43	2.43	-0.40
$2Ca'_{La} + V^{\bullet\bullet}_{O2}$	1.76	1.76	1.76	1.76	1.76	-0.26
$2Sr'_{La} + V^{\bullet\bullet}_{O1}$	1.71	1.71	1.71	1.71	1.71	-0.33
$2Sr'_{La} + V^{\bullet\bullet}_{O2}$	1.27	1.27	1.27	1.27	1.27	0.04
$2Ba'_{La} + V^{\bullet\bullet}_{O1}$	1.70	1.70	1.70	1.70	1.70	-0.64
$2Ba'_{La} + V^{\bullet\bullet}_{O2}$	1.43	1.43	1.43	1.43	1.43	-0.10
$Ca'_{La} + Ni^{\bullet}_{Ni}$	0.50	2.06	0.77	0.83	0.89	1.13
$Sr'_{La} + Ni^{\bullet}_{Ni}$	0.12	1.68	0.39	0.45	0.51	1.12
$Ba'_{La} + Ni^{\bullet}_{Ni}$	0.27	1.83	0.54	0.60	0.66	1.13

Similarly to what was observed for combined isolated systems, the ionic charge compensation of A-site dopants will preferably result in the formation of oxygen vacancies on the O2 site. However, when defects are clustered, the difference between the formation energies of $V_{O1}^{\bullet\bullet}$ or $V_{O2}^{\bullet\bullet}$ defects is smaller (between 0.04 and 0.23 eV for PBEsol+*U*, and between 0.26 and 0.67 eV for HSE06). Still, electronic charge compensation is more likely to occur than the ionic mechanism, with $Sr_{La}' + Ni_{Ni}^{\bullet}$ being the most stable defect, followed by $Ba_{La}' + Ni_{Ni}^{\bullet}$ and $Ca_{La}' + Ni_{Ni}^{\bullet}$ as a result of steric effects. Under IT-SOFC operating conditions, PBEsol+*U* calculations result in negative formation energies for electronically compensated Sr(II) (-0.48 eV) and Ba(II) (-0.43 eV), and a value close to zero for Ca(II) (0.002 eV), suggesting that these defects are easily accepted into the lattice. Formation energies obtained from HSE06 calculations, on the other hand, are positive, but still small enough (0.83, 0.45 and 0.60 eV for Ca(II), Sr(II) and Ba(II), respectively). Most $2A_{La}' + V_O^{\bullet\bullet}$ defects possess negative binding energies, indicating greater stability of the defect cluster, while the positive values calculated for $A_{La}' + Ni_{Ni}^{\bullet}$ defects (approximately 0.36 eV and 1.13 eV for PBEsol+U and HSE06, respectively) suggest that if electronic charge compensation occurs, isolated defects will be more stable. These results confirm that A-site doping can potentially improve the *p*-type electronic conductivity in the material, due to the lower formation energy and positive binding energies of $A_{La}' + Ni_{Ni}^{\bullet}$ defects, suggesting that electron holes will not be trapped around the dopants.

6.8.2.2 B-site doping

The formation energies of neutral defect clusters of B-site dopants and their charge compensating defects calculated from PBEsol+*U* and HSE06 results are presented in Tables 6.13 and 6.14, respectively. Several defect-defect configurations were tested, with the more energetically favourable ones presented here. The binding energy of these defects, obtained by the difference in formation energy between charged isolated defects (Tables 6.9 and 6.10) and neutral defect clusters (Tables 6.13 and 6.14), is also presented, and indicates whether the clustered (negative values) or isolated defects (positive values) are more likely to be present in the material.

Table 6.13 – Formation and binding energies (in eV) of the neutral defect clusters in B-site doped La_2NiO_4, calculated from PBEsol+*U* results, under distinct chemical potential environments, considering both ionic and electronic charge compensation mechanisms. Defects are written in Kröger-Vink notation.

Defect	O-rich	O-poor	600 K	700 K	800 K	BE
$2Co_{Ni}^{\bullet} + O_i''$	-0.53	-0.53	-0.53	-0.53	-0.53	0.19
$2Fe_{Ni}^{\bullet} + O_i''$	-0.30	-0.30	-0.30	-0.30	-0.30	-0.16
$2Mn_{Ni}^{\bullet} + O_i''$	-0.40	-0.40	-0.40	-0.40	-0.40	0.10
$Co_{Ni}^{\bullet} + Ni_{Ni}'$	0.65	-0.91	0.38	0.32	0.26	-0.87
$Fe_{Ni}^{\bullet} + Ni_{Ni}'$	1.94	0.37	1.66	1.60	1.54	0.12
$Mn_{Ni}^{\bullet} + Ni_{Ni}'$	1.76	0.20	1.49	1.42	1.36	0.12

Table 6.14 – Formation and binding energies (in eV) of the neutral defect clusters in B-site doped La_2NiO_4, calculated from HSE06 results, under distinct chemical potential environments, considering both ionic and electronic charge compensation mechanisms. Defects are written in Kröger-Vink notation.

Defect	O-rich	O-poor	600 K	700 K	800 K	BE
$2Co_{Ni}^{\bullet} + O_i''$	-0.21	-0.21	-0.21	-0.21	-0.21	0.11
$2Fe_{Ni}^{\bullet} + O_i''$	0.69	0.69	0.69	0.69	0.69	-0.29
$2Mn_{Ni}^{\bullet} + O_i''$	-0.17	-0.17	-0.17	-0.17	-0.17	0.07
$Co_{Ni}^{\bullet} + Ni_{Ni}'$	2.29	0.73	2.02	1.95	1.89	0.48
$Fe_{Ni}^{\bullet} + Ni_{Ni}'$	3.04	1.48	2.77	2.70	2.64	0.58
$Mn_{Ni}^{\bullet} + Ni_{Ni}'$	2.44	0.88	2.17	2.11	2.05	0.59

For B-site dopants, ionic charge compensation with the formation of an oxygen interstitial occurs preferably than the electronic mechanism. Under SOFC operating conditions, PBEsol+*U* yields negative defect formation energies for all three dopants (-0.30, -0.40 and -0.53 eV for Fe(III) Mn(III) and Co(III), respectively), indicating that they would be easily accepted into the lattice, while HSE06 calculations result in a positive (but still low) value for Fe(III) (0.69 eV), suggesting that Fe-doping will be more difficult than Mn-

or Co-substitution. $2Mn_{Ni}^{\bullet} + O_i''$ and $2Co_{Ni}^{\bullet} + O_i''$ possess positive biding energies, inferring that isolated defects are more stable and hence no trapping of the oxygen interstitial around the dopant should occur, which is desirable for ionic conduction. $2Fe_{Ni}^{\bullet} + O_i''$, on the other hand, possess negative binding energies (-0.16 eV and -0.29 eV for PBEsol+U and HSE06, respectively), indicating the greater stability of the defect cluster, which is likely to inhibit ionic conductivity improvements resulting from increased oxygen interstitial content. These results suggest that Co(III) would be the most beneficial B-site dopant to the oxide-ion conduction in this material, due to its low formation energy (-0.53 and -0.21 eV for PBEsol+*U* and HSE06, respectively) and higher binding energy (0.19 and 0.11 eV for PBEsol+*U* and HSE06, respectively). Since Sr(II) and Co(III) were determined to be the most best A- and B-site dopants to improve electronic and ionic conduction in La_2NiO_4, future work will consider the defect chemistry of the co-doped system.

6.9 Thermodynamic transition levels in La_2NiO_4

To further investigate the potential contribution of intrinsic and extrinsic defects to *n*- or *p*-type conductivity in doped and undoped La_2NiO_4, the thermodynamic transition levels (Section 3.2.6.4) of each defect were calculated. The introduction of defects in the system can generate distinct charge states in the material's band gap; their thermodynamic transition level consists of the Fermi energy at which the defect changes its charge state. The stability of such defects (and their concentration, in the case of intrinsic impurities) can be examined by calculating their formation energies under distinct chemical potential environments. The origin of charge carriers can also be investigated; if a defect is a contributor to band-like *p*-type conductivity, for example, its first transition level should be located close to the valence band (VB), allowing holes to easily move from acceptor levels to the VB. Similarly, if a defect is to contribute to band-like *n*-type conductivity, its first transition level will be close to the conduction band (CB), allowing electrons to readily move from donor levels to the CB. The interception of the thermodynamic transition levels of two defects with opposite polarity suggests the occurrence of charge compensation; i.e. if both defects are present in the system, the Fermi level would be pinned at the point of intersection, hindering any band-like *p*- or *n*-type conductivity that could potentially arise from such impurities. In this section, the defect chemistry of La_2NiO_4 was examined through the

analysis of the transition levels between defect charged states, which were calculated from Equation 3.12.

6.9.1 Intrinsic defects

The formation energies of the different charge states and the transition levels of La vacancies (V_{La}''' in Kröger-Vink notation), Ni vacancies (V_{Ni}''), oxygen interstitials (O_i''), oxygen vacancies in both equatorial and apical sites ($V_{O1}^{\bullet\bullet}$ and $V_{O2}^{\bullet\bullet}$, respectively), and Ni cations with a localized electron hole ($Ni_{Ni}^{\bullet}$) were calculated as in Equations 3.4 and 3.12. Defects were considered to have between one and three charged states (q); the oxygen interstitial (p-type) can have q = 0, -1 and -2, while oxygen vacancies (n-type) can have q = 0, 1 and 2. For La and Ni vacancies, q = 0, -1, -2 and -3 were considered. For Ni(III), i.e., an oxidized Ni(II) cation containing an electron hole, only q = 0 (corresponding to Ni(II)) and q = 1 (corresponding to Ni(III)) were included.

The transition level diagrams in Figures 6.9 and 6.10 show the formation energy of intrinsic defects in La_2NiO_4 as a function of Fermi energy at the chemical potentials corresponding to O-rich, O-poor and IT-SOFC conditions (Table 3.1), obtained from PBEsol+U and HSE06 calculations, respectively. As the chemical potential of IT-SOFC conditions at 600, 700 and 800 K are close enough to yield transition level diagrams with similar features, only chemical potentials equivalent to 700 K will be analysed in this section. It is important to note that the O-rich and O-poor chemical potential limits are unrealistic; at 700 K, an oxygen chemical potential of -3.23 eV (O-poor limit) corresponds to an extremely low oxygen partial pressure in the order of 10^{-36} atm. An oxygen chemical potential of -0.11 eV (O-rich limit), on the other hand, corresponds to an extremely high oxygen partial pressure in the order of 10^{9} atm. Despite their unrealism, such conditions will be analysed to show the variability of defect properties between O-poor and O-rich atmospheres. Still, the chemical potentials equivalent to IT-SOFC operating conditions are the ones truly relevant for the material's operation as cathode.

Changes of slope correspond to the transition levels between charge states, with p- and n-type defects having negative and positive slopes, respectively. The formation energy of the neutral defects (q = 0), along with their first ionization levels ($\varepsilon(0/\pm1)$) calculated from PBEsol+U and HSE06 are presented in Table 6.15. There is a slight variation between the formation energy values of oxygen vacancies and oxygen interstitials presented in Tables

6.5 and 6.15, even though both correspond to charge neutral defects; the results presented in Table 6.5 were calculated from Equation 3.3, while the formation energies presented in this section, were calculated from Equation 3.4. In Equation 3.4, a correction term (E_{align}) is added to the formation energy, aligning the valence band maximum of the pure and defect systems. E_{align} is calculated using the SXDEFECTALIGN code by Freysoldt *et al.* [157], which calculates the interaction of a defect with its periodic images using a charge model and the dielectric constant matrix of the pure material, which in turn is obtained from Density Functional Perturbation Theory as implemented in VASP.

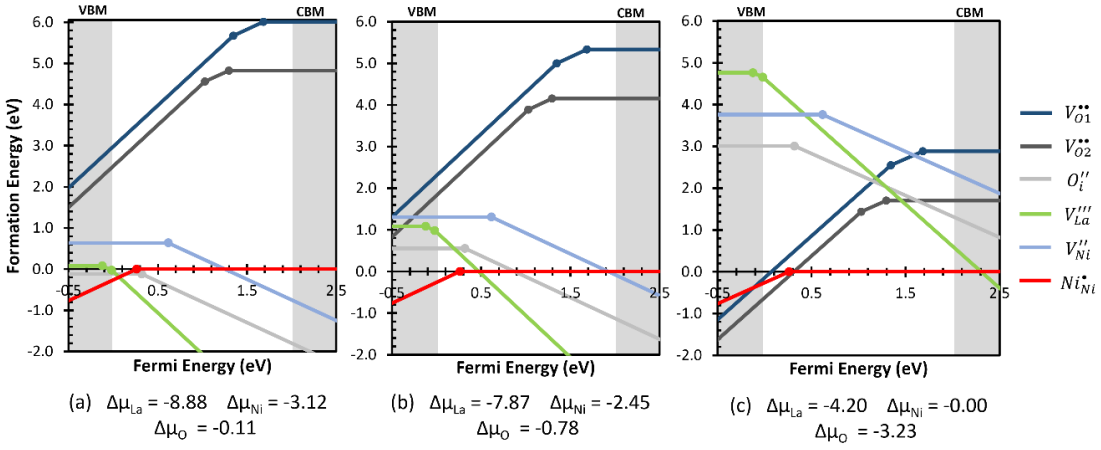

Figure 6.9 – Thermodynamic transition level diagrams of intrinsic defects in La_2NiO_4 under (a) O-rich, (b) IT-SOFC (T = 700 K and $p(O_2)$ = 0.21 atm) and (c) O-poor operating conditions, calculated from PBEsol+*U* results. Defects are given in Kröger-Vink notation. Valence and conduction band regions are represented by the shaded areas, with the band gap region between them.

All *p*-type defects have lower formation energies in O-rich conditions, while *n*-type defects have lower formation energies in O-poor environments, as expected. HSE06 calculations yield lower formation energies for all defects when compared to PBEsol+*U*. There are no formation energy values for $Ni_{Ni}^{\bullet}$ presented in Table 6.15, as electron holes localized on Ni ions naturally exist in La_2NiO_4.

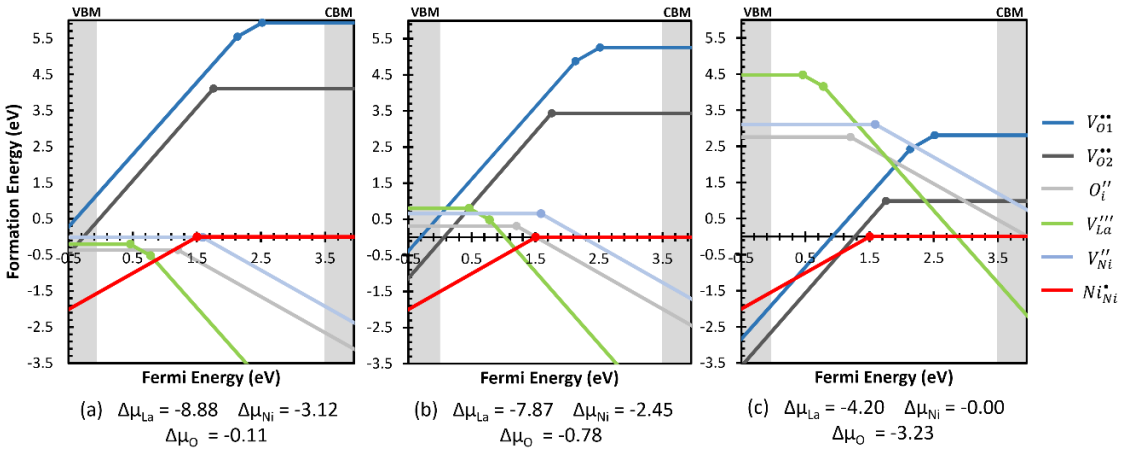

Figure 6.10 – Thermodynamic transition level diagrams of intrinsic defects in La_2NiO_4 under (a) O-rich, (b) IT-SOFC and (c) O-poor operating conditions, calculated from HSE06 results. Defects are given in Kröger-Vink notation. Valence and conduction band regions are represented by the shaded areas, with the band gap region between them.

Table 6.15 – Neutral defect formation energies (in eV) for intrinsic defects in La_2NiO_4 at the O-rich (A) and O-poor (B) limits, and under IT-SOFC operating conditions ($\Delta\mu_O$ = -0.78 eV, $\Delta\mu_{La}$ = -7.87 eV and $\Delta\mu_{Ni}$ = -2.45 eV, corresponding to T = 700 K and p(O_2) = 0.21 atm), along with their first ionization levels (in eV), calculated from PBEsol+*U* and HSE06 results.

Method	**Defect**	**Type**	**O-rich/La-, Ni-poor**	**IT-SOFC**	**O-poor/La-, Ni-rich**	**ε(0/±1)**
PBEsol+*U*	V_{La}'''	*p*-type	0.08	1.08	4.76	-0.12
	V_{Ni}''	*p*-type	0.64	1.31	3.76	0.62
	O_i''	*p*-type	-0.12	0.55	3.00	0.32
	$V_{O1}^{\bullet\bullet}$	*n*-type	6.01	5.34	2.89	1.68
	$V_{O2}^{\bullet\bullet}$	*n*-type	4.83	4.16	1.71	1.30
	$Ni_{Ni}^{\bullet}$	*n*-type	-	-	-	0.26
HSE06	V_{La}'''	*p*-type	-0.21	0.80	4.48	0.46
	V_{Ni}''	*p*-type	-0.02	0.66	3.11	1.59
	O_i''	*p*-type	-0.36	0.31	2.76	1.20
	$V_{O1}^{\bullet\bullet}$	*n*-type	5.93	5.26	2.81	2.52
	$V_{O2}^{\bullet\bullet}$	*n*-type	4.11	3.44	0.99	1.76
	$Ni_{Ni}^{\bullet}$	*n*-type	-	-	-	1.50

Under O-rich conditions, all examined defects, except for oxygen vacancies, have low formation energies and would be likely to form. While PBEsol+*U* calculates oxygen interstitials to have negative formation energies and hence form spontaneously, HSE06 predicts the spontaneous formation of both cation vacancies and oxygen interstitials. The calculated defect formation energies increase (and hence their stability decreases) in the order $O_i'' < V_{La}''' < V_{Ni}'' < V_{O2}^{\bullet\bullet} < V_{O1}^{\bullet\bullet}$ for both methods, indicating that under O-rich environments oxygen interstitials would be the dominating intrinsic defect.

Under O-poor limits, all intrinsic defects (except for $V_{O2}^{\bullet\bullet}$ as calculated by HSE06) possess formation energies higher than 1.5 eV and hence would not be expected to form. Hence, even at extremely low oxygen partial pressures, oxygen vacancies would still not exist in significant concentrations within the system. Under these conditions, the calculated defect formation energies increase in the order $V_{O2}^{\bullet\bullet} < V_{O1}^{\bullet\bullet} < O_i'' < V_{Ni}'' < V_{La}'''$, showing that in O-poor environments the formation of oxygen vacancies becomes more favourable (but still unlikely) than the formation of oxygen interstitials.

Under IT-SOFC conditions, cation vacancies and oxygen interstitials have low formation energies (< 1.5 eV) and hence would be likely to form. Both methods predict oxygen interstitials to be the most stable intrinsic defect, with formation energies 0.53 and 0.35 eV lower than the next most stable defect, respectively. The second most stable defect is predicted for be V_{La}''' by PBEsol+*U* and V_{Ni}'' by HSE06. The presence of lanthanum vacancies in La_2NiO_4 has been previously reported [335,384], but to a much lesser extent than oxygen interstitials. These results suggest that PBEsol+*U* provides a slightly better description of the materials intrinsic defect chemistry.

Defects with transition states close to the valence band maximum (VBM) and conduction band minimum (CBM) are likely to act as sources of band-like *p*- or *n*-type conductivity in the material. While formation energies depend on the chemical potential, the position of the transition levels does not. Among the analysed *p*-type impurities, PBEsol+*U* predicts V_{La}''' to be the only defect to possess a 0/-1 transition level before the VBM, and hence not contribute to band-like *p*-type conduction. HSE06 predicts V_{La}''' to have a 0/-1 transition level 0.46 eV above the VBM, which is probably not shallow enough to result in *p*-type conductivity. While HSE06 predicts all the remaining intrinsic defects to have transition levels located deep into the band gap, PBEsol+*U* calculates the 0/-1 transition level of O_i'' to be 0.32 eV above the VBM. As a result, the material's *p*-type conductivity can be

correlated to the presence of excess oxygen in the lattice. Among *n*-type defects, $V_{O1}^{\bullet\bullet}$ has shallow 0/+1 transition level 0.32 eV below the CBM; however, due to their high formation energies, oxygen vacancies would be unlikely to form or would be present in very low concentrations, not playing any significant effect. There is no significant charge compensation among intrinsic defects. The 0/+1 transition level of $Ni_{Ni}^{\bullet}$ represents where, in Fermi level terms, holes will be trapped by the Ni cations. The obtained results for both methods suggest that no band-like transport will occur, as the holes are trapped above the valence band, and that electron hole *p*-type conduction is likely to occur via a small polaron hopping mechanism, in agreement to experimental observations [336,347,349].

6.9.2 Extrinsic defects

The formation energies of the different charge states and the transition levels of A-site divalent dopants (Ca_{La}', Sr_{La}' and Ba_{La}') and B-site trivalent dopants ($Co_{Ni}^{\bullet}$, $Fe_{Ni}^{\bullet}$ and $Mn_{Ni}^{\bullet}$) were the calculated according to Equations 3.3 and 3.4. For the *p*-type A-site dopants, q = 0, -1 and -2 were considered, while for the *n*-type B-site dopants, more charge states (q = 0, 1, 2 and 3) were examined, since transition metals have more possible oxidation states. The transition level diagrams in Figures 6.11 and 6.12 show the formation energy of extrinsic neutral and charged defects in La_2NiO_4 as a function of Fermi energy at the chemical potentials corresponding to O-rich, O-poor and IT-SOFC conditions (700 K and $p(O_2)$ = 0.21 atm), obtained from PBEsol+*U* and HSE06 calculations, respectively. The calculated formation energy of the neutral defects (q = 0), along with their first ionization levels ($\varepsilon(0/\pm1)$) is presented in Table 6.16. The slight difference between the neutral defect formation energies presented here and in Section 6.8 is due to the inclusion of E_{align} to their calculation.

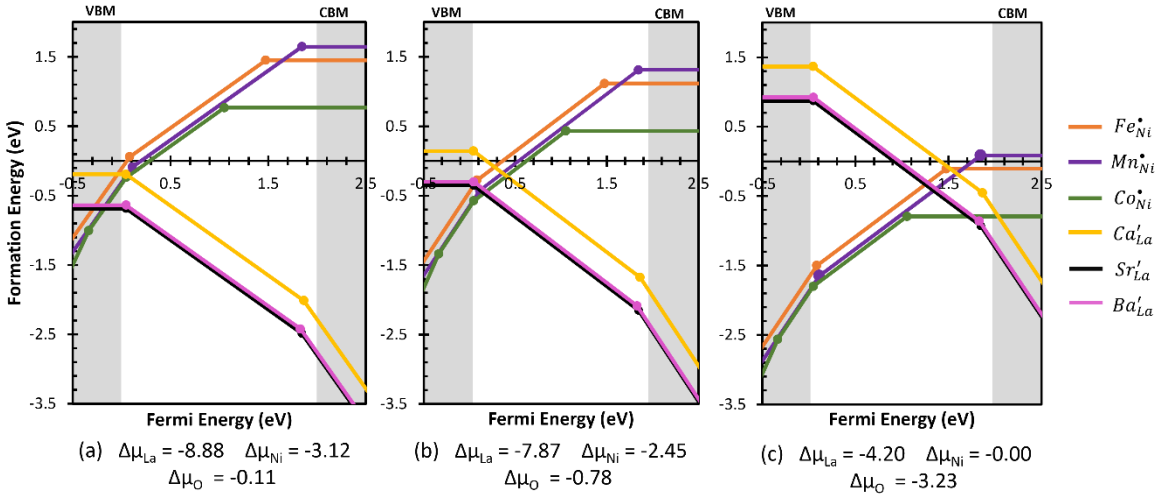

Figure 6.11 – Thermodynamic transition level diagrams of extrinsic defects in La_2NiO_4 under (a) O-rich, (b) IT-SOFC and (c) O-poor operating conditions, calculated from PBEsol+*U* results. Defects are given in Kröger-Vink notation. Valence and conduction band regions are represented by the shaded areas, with the band gap region between them.

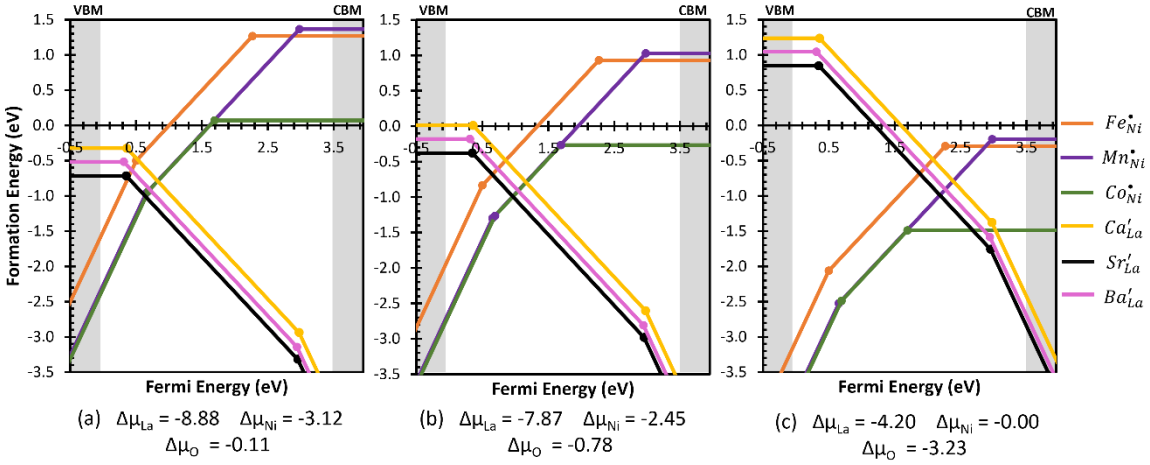

Figure 6.12 – Thermodynamic transition level diagrams of extrinsic defects in La_2NiO_4 under (a) O-rich, (b) IT-SOFC and (c) O-poor operating conditions, calculated from HSE06 results. Defects are given in Kröger-Vink notation. Valence and conduction band regions are represented by the shaded areas, with the band gap region between them.

Table 6.16 – Neutral defect formation energies (in eV) of extrinsic defects in La_2NiO_4 at the O-rich (A) and O-poor (B) limits, and under IT-SOFC operating conditions ($\Delta\mu_O$ = -0.78 eV, $\Delta\mu_{La}$ = -7.87 eV and $\Delta\mu_{Ni}$ = -2.45 eV, corresponding to T = 700 K and $p(O_2)$ = 0.21 atm), along with their first ionization levels (in eV), calculated from PBEsol+*U* and HSE06 results.

Method	**Defect**	**Type**	**O-rich/La-, Ni-poor**	**IT-SOFC**	**O-poor/La-, Ni-rich**	**$\varepsilon(0/\pm1)$**
PBEsol+*U*	Ca'_{La}	*p*-type	-0.19	0.14	1.37	0.04
	Sr'_{La}	*p*-type	-0.69	-0.35	0.87	0.04
	Ba'_{La}	*p*-type	-0.64	-0.30	0.92	0.05
	$Co^{\bullet}_{Ni}$	*n*-type	0.77	0.43	-0.79	1.05
	$Fe^{\bullet}_{Ni}$	*n*-type	1.45	1.12	-0.11	1.48
	$Mn^{\bullet}_{Ni}$	*n*-type	1.65	1.31	0.09	1.85
HSE06	Ca'_{La}	*p*-type	-0.33	0.01	1.24	0.36
	Sr'_{La}	*p*-type	-0.72	-0.38	0.85	0.35
	Ba'_{La}	*p*-type	-0.52	-0.18	1.04	0.31
	$Co^{\bullet}_{Ni}$	*n*-type	0.07	-0.27	-1.49	1.69
	$Fe^{\bullet}_{Ni}$	*n*-type	1.27	0.93	-0.30	2.27
	$Mn^{\bullet}_{Ni}$	*n*-type	1.36	0.80	-0.20	2.98

HSE06 calculations yield lower formation energies for all defects except Ba'_{La}, when compared to PBEsol+*U*. Under O-rich environments, A-site dopants (*p*-type defects) are calculated to have lower formation energies than B-site dopants (*n*-type defects), as expected. All A-site dopants have negative formation energies, suggesting that they are easily accepted into the lattice. PBEsol+*U* and HSE06 calculate formation energies to increase (and hence stability to decrease) in the order $Sr'_{La} < Ba'_{La} < Ca'_{La} < Co^{\bullet}_{Ni} < Fe^{\bullet}_{Ni} < Mn^{\bullet}_{Ni}$. Under O-rich environments, the *n*-type defects (B-site dopants) have lower (and negative) formation energies, with calculated values increasing in the order $Co^{\bullet}_{Ni} < Fe^{\bullet}_{Ni} < Mn^{\bullet}_{Ni} < Sr'_{La} < Ba'_{La} < Ca'_{La}$ for both methods. Under IT-SOFC conditions, among the analysed *p*-type defects, Sr'_{La} possesses the lowest formation energies, while $Co^{\bullet}_{Ni}$ is the *n*-type impurity to possess the lowest values. Under all analysed chemical environments, all A- and B-site dopants possess formation energies lower than 1.5 eV (except for $Mn^{\bullet}_{Ni}$ under O-rich

atmosphere as calculated by PBEsol+*U*), indicating the selected dopants would be easily accepted into the La_2NiO_4 lattice upon doping under a wide range of chemical environments.

The origin of charge carriers and the potential contribution of dopants to *p*- and *n*-type conductivity were also investigated. PBEsol+*U* calculates all A-site dopants to have very shallow 0/-1 transition levels (~0.05 eV above the VBM), suggesting their potential contribution to band-like *p*-type conduction. Experimentally, A-site dopants are observed to increase the material's electrical conductivity, but their *p*-type conduction mechanism has not been elucidated [329,332,350]. The contribution of A-site dopants to band conductivity occurs especially at O-richer environments, under which these defects are uncompensated. Under O-poor and IT-SOFC conditions, the intersection of the -1 state of Sr'_{La} and Ba'_{La} with the +1 state of $Fe^{\bullet}_{Ni}$ and $Mn^{\bullet}_{Ni}$ will cause pinning of the Fermi level at higher energies, hindering band-like *p*-type conduction in the co-doped material. The addition of B-site dopants in co-doped systems could then facilitate other conductivity mechanisms, such as small polaron hopping. Therefore, the mechanism of *p*-type conductivity in this material is sensitive to the oxygen chemical potential and can change in doped and co-doped systems. Among *n*-type defects, $Mn^{\bullet}_{Ni}$ has shallow 0/+1 transition level, 0.15 eV below the CBM, and hence its introduction could potentially deteriorate *p*-type conductivity by trapping electron holes, in line with experimental observations [329,352]. HSE06, on the other hand, predicts all A-site dopants to have their 0/-1 transition levels located deeper into the band gap, at approximately 0.3 eV above the VBM. Hence, they are unlikely to contribute to band-like *p*-type conduction. The same is observed for B-site dopants, which suggests that electron holes would not be trapped by these species. Under IT-SOFC conditions, the -1 charge state of all A-site dopants is compensated by the +1 states of B-site dopants, pinning the Femi level further into the band gap, indicating that no band-like *p*-type conduction would be observed in the co-doped material and alternative conduction mechanisms such as polaron hopping might be favoured. Therefore, even though PBEsol+*U* does not satisfactorily the thermodynamic stability of the material, it provides a better description of the extrinsic defect chemistry of A- and B-site doped La_2NiO_4, as it predicts A-site dopants to contribute to band-like *p*-type conductivity, and some B-site dopants ($Mn^{\bullet}_{Ni}$) to act as hole traps, hindering electronic conduction, in agreement to experimental observations [329,332,350,352].

6.10 Conclusions

The structural, electronic and defect properties of orthorhombic *Bmab* La_2NiO_4 have been investigated using PBEsol+*U* and HSE06 calculations. A +*U* correction was added to O 2*p* states (in addition to Ni 3*d* states) to try and correct the SIE, which has not been done in previous theoretical work. Both methods were shown to provide a good description of the structural parameters, magnetic properties and valence band features of the material. However, while PBEsol+*U* calculates indirect and direct band gaps of 2.00 eV and 2.63 eV, HSE06 results predict indirect and direct band gaps of 3.44 eV and 4.05 eV, in closer agreement to valence band photoemission spectroscopy [36,369], electron energy loss spectroscopy [370] and oxygen K-edge X-ray absorption measurements [341], which yield a charge excitation band gap of at least 4 eV. HSE06 also correctly predicts the material to be thermodynamically unstable, while PBEsol+*U* does not.

The stability of oxygen defects in La_2NiO_4 was also investigated, with both PBEsol+*U* and HSE06 predicting oxygen interstitials to be the dominant defect in the RP oxide. HSE06 calculations yield negative formation energies for interstitials under all relevant chemical potential environments, suggesting the spontaneous uptake of excess lattice oxygen, in agreement with experimental results. Both methods predict oxygen vacancies to be preferably located at the equatorial site ($V_{O2}^{\bullet\bullet}$) of the NiO_6 octahedron rather than in an axial position ($V_{O1}^{\bullet\bullet}$), as the introduction of oxygen defects at the O2 site causes less structural distortions. The observed results also reflect the distinct chemical environments experienced by O1 and O2 oxygens, which are located at the edge of the perovskite/rocksalt layers and within the perovskite block, respectively.

The potential effects of aliovalent A- (Ca(II), Sr(II) and Ba(II)) and B-site (Co(III), Fe(III), Mn(III)) doping on the ionic and electronic conduction properties of La_2NiO_4 were also studied. To the best of our knowledge, there is no comprehensive theoretical study in the literature systematically investigating a range of dopants. In this thesis, the use of the same methodology to analyse a range of different dopants yields consistent results and allows an appropriate comparison among dopants to determine which would be the most beneficial to MIEC properties. Furthermore, existing theoretical work does not take into consideration the material's defect properties under different chemical environments, hence their comparison to experiment is dubious. Here, this is done through the addition of chemical potential terms in the calculation of defect formation energies. A-site doping is

predicted to preferentially result in the formation of electron holes located at Ni sites through an electronic charge compensation mechanism. Sr-substitution yields the lowest defect formation energies, as it alleviates tensions arising from the mismatch of the intergrown LaO and NiO_2 layers in the RP oxide. Still, all analysed dopants possess low formation and binding energies and hence would be easily accepted into the lattice and should not act as hole traps. The analysis of the transition levels between different charge states obtained from PBEsol+*U* calculations indicate that A-site doping can enhance the material's *p*-type conductivity under IT-SOFC conditions, due to their shallow 0/-1 transition levels and low formation energies. However, these defects are compensated by the +1 state of B-site dopants, pinning the Fermi level at higher energies and suggesting that co-doping could hinder electrical conductivity or change its mechanism from band-like conduction to small polaron hopping. There is no previous theoretical study in literature analysing the transition level diagrams of this material; hence, in this thesis it is shown for the first time how co-doping, despite increasing the number of charge carriers in the system, can be detrimental to its conduction properties.

B-site doping is preferably charge compensated through an ionic mechanism, resulting in the generation of oxygen interstitials. Co-substitution yields the lowest defect formation energies due to steric effects and the release of stresses in the structure. Co(III) and Mn(III) have no tendency to trap oxygen interstitials around them and hence can potentially improve ionic conduction properties. Fe-doping, on the other hand, might lead to defect trapping, which is likely to inhibit ionic conductivity improvements resulting from increased oxygen interstitial content. According to PBEsol+*U* results, Mn-doping can potentially hinder *p*-type conductivity by trapping electron holes, due to its shallow 0/+1 transition level and low formation energy.

The obtained results suggest that Sr(II) and Co(III) would be the most beneficial dopants to the electronic and ionic conduction properties of the material, respectively. Current experimental work focus on the investigation of Sr(II) and Fe(III) co-doped systems [386-388]. In this thesis, in which a range of dopants is analysed and compared using the same methodology, Fe(III) was predicted to be detrimental to ionic conduction properties. Hence, it is then possible to suggest that a more thorough experimental investigation on Sr(II) and Co(III) co-doped systems is needed. Further theoretical work is also necessary to determine how Sr(II) and Co(III) co-doping would influence the defect chemistry and

conduction properties of the system, since A- and B-site doping have been shown to affect the material's transport properties in different ways. Experimentally, a trade-off between ionic and electronic conductivity usually has to be achieved.

Chapter 7

Conclusions and future work

7.1 Conclusions

In this thesis, two perovskite-based materials were investigated by means of first principles calculations and molecular dynamics simulations. Their defect chemistry and conduction properties were evaluated, aiming their application as electrolyte and cathode materials in intermediate temperature solid oxide fuel cells.

Firstly, DFT+*U* calculations were carried out to investigate the impact of thirteen divalent dopants (Ni(II), Sn(II), Mg(II), Zn(II), Co(II), Fe(II), Pt(II), Mn(II), Pd(II), Ca(II), Sr(II), Pb(II) and Ba(II)) in the defect chemistry and local structure of $LaGaO_3$. To the best of our knowledge, there is no previous theoretical study analysing the potential influence of a range of divalent dopants in the conduction properties of $LaGaO_3$ using density functional theory calculations. The systematic evaluation of dopants presented here makes it possible to rationalize the observed differences in the material's defect chemistry upon doping with distinct divalent cations. Such differences were related to steric factors, electronic effects and local structural distortions, which are difficult to be evaluated in such detail experimentally and were explained in depth in this thesis. The crystal and electronic structure of the perovskite were examined using the GGA PBE, the meta-GGA SCAN and the hybrid HSE06 functionals, to determine which method would provide the best description of the material's defect properties. The meta-GGA SCAN was observed to superiorly describe the geometry and electronic structure of the perovskite, and hence was used for defect calculations. Aliovalent doping in $LaGaO_3$ results in the creation of one charge compensating vacancy for every two divalent dopants introduced; the lowest energy structure for each doped system was calculated, with vacancies being observed to preferably occupy a nearest neighbour site to all dopants, as a result of Coulombic effects. Ba(II), the largest analysed dopant, was the only exception; vacancies are preferably located next-nearest-neighbour to it due to steric effects overcoming electrostatic effects. All dopants were tested in both La- and Ga-sites, to determine where they would preferentially lie; smaller dopants, with ionic radii up to 0.86 Å preferably occupy the perovskite's B-site,

while bigger dopants go to the A-site. Interestingly, Sn(II), which was expected to be a Ga-site dopant due to its small size (0.81 Å), presented a dual behaviour, being a Ga-site dopant under La-rich chemical environments, and a La-site dopant under Ga-rich atmospheres due to electronic effects. The doping energy was calculated for all dopants, to evaluate how easily they are accepted into the lattice and if there would be any tendency to dopant segregation upon their introduction. For A-site dopants, the magnitude of the doping energies was observed to be strictly related to dopant size, with Sr(II) and Ba(II) presenting the lowest values. Pb(II) presented the highest doping energy among the A-site dopants, as a result of its asymmetric electron density due to the formation of a sterically active "lone pair" of electrons. For B-site dopants, on the other hand, steric effects do not fully describe the variation of doping energy values; transition metals are not perfectly spherical due to their partially filled *d* orbitals; hence electronic structure effects also play a role. Fe(II) and Co(II) presented the lowest doping energies, while Sn(II), Pd(II) and Pt(II) presented the highest values. Sn(II) also possesses an asymmetric electron density due to lone pair formation, while Pd(II) and Pt(II) d^8 electron configuration favours square-planar (and not octahedral) coordination. The short- and long-range association energies were also calculated for each dopant, to evaluate their tendency to trap charge compensation vacancies around them in regions of uniform (high) or non-uniform (low) dopant concentration, respectively. Sr(II), Ca(II) and Ba(II) presented the lowest (and very similar) association energy values among the A-site dopants. For B-site dopants, distortions to the local structure introduced upon doping were observed to be strictly related to the magnitude of association energies. Such structural distortions are a result of steric and electronic effects, and of dopants trying to reach similar M(II)-O bond lengths and coordination environments to those observed in their native MO oxides. Pd(II), Sn(II) and Pt(II) were the dopants to introduce the most significant distortions to the perovskite lattice and hence presented the highest association energies, indicating that vacancies would likely be trapped around these dopants. Mg(II) and Ni(II), on the other hand, are the dopants to introduce the least amount of distortions, and hence present the lowest association energies. Mg(II) was predicted as the best Ga-site dopant aiming solid oxide electrolyte applications, due to its low doping energy associated to low short- and long-range association energies, suggesting it would be easily incorporated into the perovskite lattice and would not result in vacancy trapping. Co(II), Fe(II) and Zn(II) also possess comparatively low doping and association energies, and hence could be used as

dopants aiming cathode applications, as transition metal doping in $LaGaO_3$ has been reported to generate mixed ionic and electronic conduction. Among the A-site dopants, Sr(II) and Ba(II) should result in the greatest improvements to the ionic conduction properties of $LaGaO_3$. Therefore, this chapter provided fundamental understanding on the suitability of dopants to enhance the perovskite's ionic conductivity properties aiming IT-SOFC electrolyte applications. The results presented here suggest that co-doping of the A-site with Sr(II) and Ba(II) along with B-site doping with Mg(II) might be the most favourable strategy to improve ionic conduction properties, and should serve as a guide to future experimental work, which can evaluate quantities such as the solubility limits of the individual dopants and concentration effects on ionic conductivity and activation energies on such systems, for example.

As Sr(II) and Mg(II) are among the best dopants to improve $LaGaO_3$ ionic conduction properties according to DFT results, and the $La_{1-x}Sr_xGa_{1-y}O_{3-\delta}$ (LSGM) system attracts considerable interest from experimentalists as IT-SOFC electrolyte, a Dipole Polarizable Ion Model (DIPPIM) force field was parametrized from DFT data to predict the ionic conductivity behaviour of the LSGM perovskite in the 873-1273 K temperature range. This theoretical parametrization is an improvement from previous theoretical work, which relied on the empirical derivation of force fields to reproduce specific experimental properties, resulting in non-transferable IPs consisting of parameters extracted from difference sources. Here, a force-matching procedure to DFT data yields a force field of *ab initio* quality, which can in the future be used to study the different thermodynamic states of $LaGaO_3$, such as surfaces and interfaces (e.g. grain boundaries) which are technologically important for the further development of SOFCs. Our force field was fitted to forces, dipoles and stresses obtained from DFT (SCAN) calculations, with a total objective function of 0.24 being obtained, indicating the good quality of the IP. Molecular dynamics simulations were then carried out to investigate the ionic conductivity, activation energies of diffusion and local structure changes in singly- (LSG and LGM) and co-doped (LSGM) systems. There is no previous theoretical work in literature comprehensively and systematically analysing the influence of a wide range of dopant concentrations and temperatures on the ionic conduction properties of LSGM systems, using the same methodology and hence obtaining consistent results. A systematic theoretical investigation is also necessary to address the significant variation in the existing experimental data, with little agreement on the ionic conductivity

values of the LSGM system, due to the different synthesis conditions employed in distinct studies, and the resulting variety of grain sizes, sample densities, presence of impurities and secondary phases. DIPPIM results are in agreement with the lower end of experimental data. Experimental activation energies are usually higher, as the formation of secondary phases, not considered in the molecular dynamics simulations presented here, increases the barrier for oxide ion transport.

Ionic conductivity was observed to increase with dopant content, reaching its maximum value for samples with total dopant concentration of around 20 mol% (LSG20, LGM20 and LSGM1010), and decreasing after that. The observed ionic conductivity decrease is a result of dopant-vacancy and vacancy-vacancy interactions, which are more intense for higher dopant content. Vacancies repel each other due to their effective positive charge, and hence are ordered throughout the lattice, being trapped in systems with higher vacancy content. Strontium is predicted to trap vacancies in its second coordination shell; the distribution of oxygen vacancies at NN, NNN and NNNN sites around the A-site dopant were evaluated, with NN and NNNN shells being depleted and NNN sites being overpopulated with respect to a random distribution of vacancies. These results suggest that vacancies are trapped at NNN sites to Sr ions. Magnesium, on the other hand, has a different local coordination environment; dopant-vacancy interactions result in all the NN, NNN and NNNN coordination shells around the B-site dopant being overpopulated with respected to a random distribution of vacancies. As none of these coordination shells are depleted, vacancies are free to move among NN, NNN and NNNN sites, which might be beneficial to ionic conduction properties. In fact, LGM systems present higher ionic conductivity values than LSG samples at same dopant content, due to the distinct dopant-vacancy interactions observed in the two systems. Therefore, dopant-vacancy interactions are observed to depend on dopant identity. Vacancy ordering, on the other hand, is independent of dopant identity, as it occurs in LSG, LGM, LSGM and average cation $LaGaO_3$ systems, in which dopant effects are neglected. The analysis of the local structure in ac-$LaGaO_3$ and comparison of the obtained results with LSG, LGM and LSGM systems, revealed that dopant-vacancy interactions might have a stronger influence than vacancy ordering in ionic conduction properties. The magnitude of the activation energy of diffusion is also dopant dependent; Mg(II) is expected to introduce more lattice distortions due to its ionic radii; as a result, for the same dopant concentration, activation energies are bigger for LGM than for LSG. For

co-doped samples, a larger variation in activation energy was observed for varying Mg(II) (rather than Sr(II)) content. The preferred strategy of experimentalists is to rely on Sr-doping to enhance ionic conductivity; the main purpose of Mg addition is its resulting lattice expansion, aiming to increase the solubility limit of Sr. The results presented in this thesis show how differently vacancy ordering occurs around A- and B-site dopants, indicating that Mg-doping yields more significant ionic conductivity improvements and results in less dopant-vacancy interactions, indicating that experimental strategies should prioritize B-site doping in the perovskite.

Finally, the crystal and electronic structure, and the defect chemistry of A- and B-site doped La_2NiO_4, a potential IT-SOFC cathode, was also investigated using PBEsol+*U* and HSE06 calculations. While both methods provide a good description of the structural parameters, HSE06 superiorly describes the material's electronic structure (band gap and conduction band features), calculating indirect and direct band gaps of 3.44 eV and 4.05 eV, respectively, comparable to the experimentally measured charge excitation band gap of 4 eV, while PBEsol+*U* calculates indirect and direct band gap values of 2 eV and 2.63 eV. The stability of oxygen defects (vacancies and interstitials) was investigated, with oxygen interstitials being predicted to be the dominant defect in the material under all investigated chemical environments. The impact of A- and B-site doping on the ionic and electronic conduction properties of La_2NiO_4 was also evaluated. To the best of our knowledge, the work presented here is the first theoretical study systematically investigating the influence of a range of dopants in the material's defect chemistry, allowing an appropriate comparison among dopants to determine which would be the most beneficial to MIEC properties. A-site doping with Ca(II), Sr(II) and Ba(II) preferentially results in the formation of electron holes located at Ni sites (electron compensation mechanism), rather than the formation of oxygen vacancies (ionic compensation mechanism). All analysed A-site dopants present low formation enthalpies and binding energies, suggesting that they would be easily accepted into the lattice and would not act as hole traps. Sr-doping presents the lowest defect formation energies. B-site doping, on the other hand, is preferably charge compensated by the formation of oxygen interstitials (ionic mechanism), rather than the formation of an electron localized on Ni cations (electronic compensation). Co(II) doping presents the lowest defect formation energies. The calculation of binding energies indicate that Fe(III) has a tendency to trap oxygen interstitials, which could potentially inhibit any ionic conductivity

improvements arising from increased oxygen interstitial content. Co(III) and Mn(III), on the other hand, have no tendency to defect trapping. The thermodynamic transition levels of intrinsic and extrinsic defects in La_2NiO_4 were also calculated, aiming to evaluate the origin and mechanisms of *p*-type conductivity if the material. A-site doping is expected to enhance the material's *p*-type conduction under IT-SOFC conditions according to PBEsol+*U* results, as a result of their shallow 0/-1 transition levels. However, in co-doped systems, A-site defects are compensated by the +1 state of B-site dopants, pinning the Fermi level at higher energies and hindering band-like *p*-type conduction. Still, co-doping could lead to a change in the *p*-type conduction mechanism to small polaron hopping. Mn(II) is also predicted to hinder *p*-type conductivity due to its shallow 0/+1 transition level, which could lead to electron hole trapping. This study analyses the transition level diagrams of this material for the first time, revealing how co-doping, despite increasing the number of charge carriers in the system, can be detrimental to its conduction properties. The obtained results indicate that Sr(II) and Co(II) would be the most beneficial dopants to the electronic and ionic properties of La_2NiO_4, respectively. As A- and B-site doping affect the material's transport properties in different ways, a trade-off between ionic and electronic conductivity improvement needs to be achieved.

7.2 Future work

Co-doping (Ca/Sr and Ba/Sr) of the A-site in $LaGaO_3$ has been investigated by means of DFT calculations; it has been concluded that if the average size of the chosen dopants does not match the perovskite's ideal ionic radius, an average of the properties (doping and association energies) of the singly doped systems will be observed. If the average dopant size is close to the ideal radius, co-doping will then improve ionic conduction properties. Future work will also be carried out to determine the ideal ionic radius for B-site dopants; as Mg(II), Co(II), Fe(II) and Zn(II) were predicted to have low doping and association energies, different combination of B-site dopants will be tested to determine which would result in the greatest improvements for ionic conduction properties, aiming both electrolyte (where ionic conduction is paramount) and cathode (where mixed ionic-electronic conduction is key) applications.

As much of the research has focused on optimising the composition of doped-$LaGaO_3$ systems and evaluating its defect (dopant and vacancy) interactions, the limit of chemical optimisation in this field has been quickly approached. Therefore, to further improve its ionic conduction properties as an IT-SOFC electrolyte, mechanical optimisation routes can also be investigated. As there has been little theoretical investigation on the impact of surface terminations and strain on the oxide ion conductivity of LSGM, future work aims to use MD simulations with the DIPPIM force field derived in Chapter 5 to investigate structural parameters, ionic conductivity and activation energies for oxide diffusion at surfaces of LSGM systems for a range of dopant concentrations, temperatures and biaxial tensile strain levels. The obtained data will be compared to the bulk LSGM results presented in Chapter 5, providing an understanding of the influence of surfaces and strain on the perovskite's ionic conductivity aiming its application as electrolyte in IT-SOFCs.

The interface between two crystallites with distinct orientations is called a grain boundary (GB) and its structure and composition strongly affect the physicochemical properties of the material, as interfaces have unique chemistry when compared to the bulk. For example, defects and impurities that result from chemical doping can be segregated near the GBs, altering its local structure and hence significantly interfere in the ionic properties of polycrystalline solids. While most studies are performed to understand the structure of GBs focus on pure perovskites and on other materials that are commercially used as electrolytes, such as YSZ and doped ceria, there is a lack of understanding on the structure and composition of GBs in $LaGaO_3$. Therefore, the DIPPIM force field derived in Chapter 5 will be used to evaluate the mechanisms of dopant and vacancy segregation at GBs and how they affect the physicochemical properties of $LaGaO_3$, aiming to improve its application as IT-SOFC electrolyte. MD simulations will be carried out to understand the behaviour of impurities, defects and the influence of GBs on the ionic conductivity as a function of temperature and vacancy concentration. The obtained results can be compared to those of the corresponding surfaces, to evaluate if there is any tendency of vacancy or doping segregation at the grain boundary, which could potentially hinder ionic conductivity.

Finally, as Sr(II) and Co(III) were determined as the best A- and B-site dopants in La_2NiO_4, respectively, further work is necessary to determine how Sr(II) and Co(III) co-doping would influence the defect chemistry and conduction properties of the system, since A- and B-site doping have been shown to affect the material's transport properties in

different ways. The $Sr'_{La} + Co^{\cdot}_{Ni}$ cluster will be investigated, to evaluate the likelihood of its formation under IT-SOFC environments, and compared to the $Sr'_{La} + Fe^{\cdot}_{Ni}$ cluster, which is widely considered experimentally. After the most suitable combination of dopants have been determined, *ab initio* data will be generated, so the theoretical parametrization of a Dipole Ion Polarizable Ion Model can be carried out, to model oxygen interstitial diffusion in co-doped La_2NiO_4, with a range of dopant concentration and temperatures.

When interatomic potentials for both LSGM and La_2NiO_4 systems have been derived, the interfaces between LSGM and LNO can be generated to evaluate their effect on SOFC operation, i.e. to investigate oxygen and cation diffusion across the interface, or dopant/vacancy segregation at the interface, aiming the development of efficient cathode-electrolyte systems for IT-SOFC applications.

Appendix

Unrealistic dipole values were obtained from the Wannier analysis of the DFT data corresponding to the *Pbnm* and *Pm3m* phases containing a total dopant concentration of 50 mol%. From Figure A.1 (b) and (c), it is possible to observe that the calculated DFT dipoles cover a much wider range than expected (as presented in Figure A.1(a) for the *R3c* phase with same dopant content, in which Wannier analysis yielded the correct dipoles). This is most likely due to an error during Wannier analysis (and not on the DFT data itself), as the obtained forces and stresses for these frames are correct. Still, the dipole terms in the force field presented in Chapter 5 were fitted to the remaining 22 DFT frames with correct dipole terms. It is possible to observe in Figure A.1 (b) and (c) that the magnitude of FF dipoles, despite not matching the (inaccurate) Wannier results, are within a sensible range.

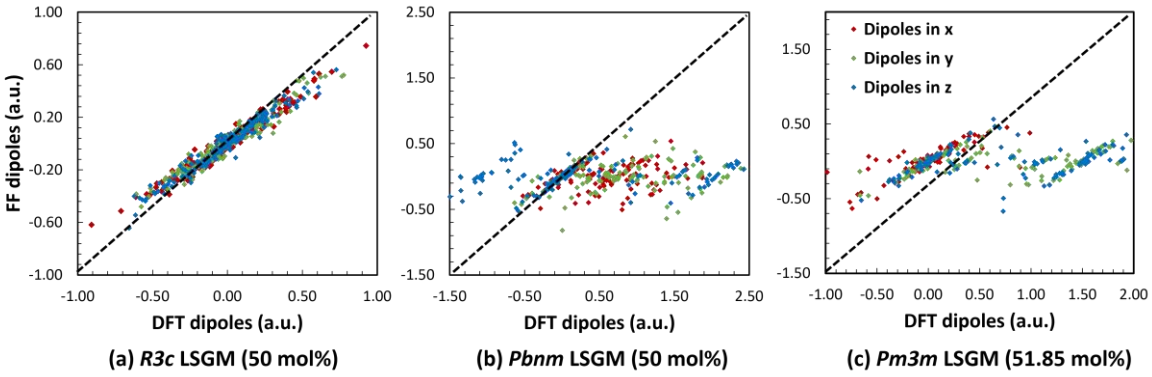

Figure A.1 – Comparison between dipoles (along the *x*, *y* and *z* axes) obtained calculated from DFT (Wannier analysis) and the DIPPIM force field, for the (a) *R3c*, (b) *Pbnm* and (c) *Pm3m* phases containing dopant concentration of 50 mol%. Despite the unrealistic values obtained from Wannier analysis for the *Pbnm* and *R3c* phases, the force field still calculates dipoles within a sensible range.

Tables A.1-A.4 show the calculated diffusion coefficients (from the linear fit of the MSD) and ionic conductivity (from the Nernst-Einstein Equation) for orthorhombic and rhombohedral LSG and LGM systems, for dopant concentrations ranging between 5 mol% and 25 mol%, and temperatures in the 873-1273 K interval. Errors are given as standard error.

Table A.1 – Calculated diffusion coefficients (D, in 10^{-8} cm^2 s^{-1}) and ionic conductivities (σ, in mS cm^{-1}) of orthorhombic (*Pbnm*) $La_{1-x}Sr_xGaO_{3-\delta}$, with x = 0.10, 0.15, 0.20, 0.25, 0.30, 0.35, at 873, 1073 and 1273 K. Values in bold are the highest obtained value for a given temperature.

	873 K		**1073 K**		**1273 K**	
x	**D (10^{-8} cm^2/s)**	**σ (mS/cm)**	**D (10^{-8} cm^2/s)**	**σ (mS/cm)**	**D (10^{-8} cm^2/s)**	**σ (mS/cm)**
0.10	**1.71±0.10**	**7.37±0.42**	8.82±0.03	37.916±0.12	23.61±1.14	100.92±4.88
0.15	1.70±0.47	7.25±2.00	8.99±0.65	38.337±2.79	27.15±0.95	115.07±4.01
0.20	1.50±0.09	6.69±0.40	**9.60±0.52**	**40.609±2.22**	**28.69±0.30**	**120.59±1.28**
0.25	1.22±0.15	5.13±0.63	8.83±0.35	37.022±1.48	27.68±1.75	115.36±7.29
0.30	0.84±0.06	3.50±0.24	6.59±0.08	27.384±0.33	26.93±0.30	111.18±1.22
0.35	0.94±0.02	3.90±0.08	6.11±0.19	25.152±0.80	24.63±0.56	100.79±2.29

Table A.2 – Calculated diffusion coefficients (D, in 10^{-8} cm^2 s^{-1}) and ionic conductivities (σ, in mS cm^{-1}) of rhombohedral (*R3c*) $La_{1-x}Sr_xGaO_{3-\delta}$, with x = 0.10, 0.15, 0.20, 0.25, 0.30, 0.35, at 873, 1073 and 1273 K. Values in bold are the highest obtained value for a given temperature.

	873 K		**1073 K**		**1273 K**	
x	**D (10^{-8} cm^2/s)**	**σ (mS/cm)**	**D (10^{-8} cm^2/s)**	**σ (mS/cm)**	**D (10^{-8} cm^2/s)**	**σ (mS/cm)**
0.10	**1.83±0.03**	**7.92±0.12**	**9.58±0.08**	**41.19±0.36**	24.25±0.48	103.68±2.03
0.15	1.31±0.22	5.60±0.95	8.80±0.35	37.53±1.47	26.37±2.76	111.78±11.68
0.20	1.41±0.02	5.98±0.10	9.39±0.01	39.72±0.02	28.37±0.57	119.26±2.40
0.25	1.50±0.25	6.34±1.06	8.76±0.18	36.71±0.77	**30.44±0.15**	**126.82±0.62**
0.30	1.29±0.08	5.38±0.34	7.93±0.12	32.94±0.49	28.38±1.91	117.20±7.88
0.35	0.94±0.08	3.90±0.32	7.00±0.42	28.83±1.74	27.02±1.02	110.55±4.18

Table A.3 – Calculated diffusion coefficients (D, in 10^{-8} cm^2 s^{-1}) and ionic conductivities (σ, in mS/cm) of orthorhombic (*Pbnm*) $LaGa_yMg_{1-y}O_{3-\delta}$, with y = 0.05, 0.10, 0.15, 0.20, 0.25, 0.30 and 0.35 at 873, 1073 and 1273 K. Values in bold are the highest for a given T.

	873 K		1073 K		1273 K	
x	**D (10^{-8} cm^2/s)**	**σ (mS/cm)**	**D (10^{-8} cm^2/s)**	**σ (mS/cm)**	**D (10^{-8} cm^2/s)**	**σ (mS/cm)**
0.05	1.04±0.19	4.50±0.83	6.68±0.60	28.84±2.57	15.93±0.12	68.47±0.50
0.10	1.50±0.06	6.47±0.26	8.92±0.24	38.14±1.02	25.51±1.08	108.61±4.58
0.15	**1.58±0.06**	**6.71±0.25**	**9.80±0.19**	**41.48±0.82**	28.65±0.66	120.71±2.76
0.20	1.36±0.17	5.71±0.71	9.74±0.14	40.85±0.61	32.83±0.32	136.99±1.32
0.25	1.46±0.16	6.10±0.68	9.13±0.42	37.91±1.76	**34.29±1.49**	**141.67±6.10**
0.30	0.84±0.04	3.47±0.15	7.01±0.24	28.83±1.01	31.06±0.44	127.06±1.77
0.35	0.92±0.15	3.76±0.60	9.43±0.20	30.28±8.06	27.57±0.48	111.75±1.96

Table A.4 – Calculated diffusion coefficients (D, in 10^{-8} cm^2 s^{-1}) and ionic conductivities (σ, in mS/cm) of rhombohedral (*R3c*) $LaGa_yMg_{1-y}O_{3-\delta}$, with y = 0.05, 0.10, 0.15, 0.20, 0.25, 0.30 and 0.35 at 873, 1073 and 1273 K. Values in bold are the highest obtained value for a given temperature.

	873 K		1073 K		1273 K	
x	**D (10^{-8} cm^2/s)**	**σ (mS/cm)**	**D (10^{-8} cm^2/s)**	**σ (mS/cm)**	**D (10^{-8} cm^2/s)**	**σ (mS/cm)**
0.05	1.19±0.11	5.15±0.46	6.25±0.25	26.99±1.06	16.78±0.50	72.15±2.14
0.10	1.32±0.18	5.66±0.78	9.56±0.78	40.92±0.34	25.31±0.30	107.76±1.27
0.15	1.15±0.24	4.90±1.10	**10.48±0.61**	**44.40±2.60**	30.04±0.26	126.60±1.11
0.20	**1.36±0.06**	**5.72±0.23**	9.38±0.13	39.37±0.55	32.14±1.32	134.09±5.49
0.25	1.08±0.03	4.50±0.14	9.66±1.03	40.14±4.27	32.85±0.28	135.71±1.14
0.30	1.14±0.03	4.69±0.11	9.18±0.34	37.74±1.38	33.74±2.96	137.98±12.03
0.35	0.80±0.05	3.27±0.22	8.36±1.25	34.06±5.09	**34.40±0.37**	**139.36±1.55**

Table A.5 and A.6 present the number of vacancies surrounding A-site and B-site cations in rhombohedral LSG and LGM systems, respectively. The number of vacancies located at NN, NNN and NNNN sites were calculated through the integration of the RDF peaks. Tables A.7 and A.8 present the number of oxygen vacancies surrounding another oxygen vacancy in six distinct coordination environments, for rhombohedral LSG and LGM, respectively.

Table A.5 – Number of oxygen vacancies surrounding A-site cations (La and Sr) in rhombohedral (*R3c*) $La_{1-x}Sr_xGaO_{3-\delta}$ (x = 0.10, 0.15, 0.20, 0.25, 0.30, 0.35) at 1073 K, occupying the nearest-neighbour (NN), next-nearest-neighbour (NNN) and next-next-nearest-neighbour (NNNN) positions. La-O corresponds to a random distribution of vacancies where no defect ordering has occurred.

x	**La-O**			**La-vac**			**Sr-vac**		
	NN	**NNN**	**NNNN**	**NN**	**NNN**	**NNNN**	**NN**	**NNN**	**NNNN**
# sites	12	24	24	12	24	24	12	24	24
0.10	0.199	0.399	0.395	0.206	0.344	0.391	0.132	0.890	0.449
0.15	0.302	0.603	0.597	0.322	0.482	0.600	0.182	1.278	0.609
0.20	0.399	0.798	0.790	0.435	0.616	0.802	0.250	1.519	0.771
0.25	0.501	1.004	0.992	0.562	0.771	1.013	0.313	1.688	0.966
0.30	0.603	1.209	1.194	0.689	0.886	1.214	0.399	1.942	1.191
0.35	0.700	1.403	1.386	0.809	1.011	1.412	0.495	2.118	1.386

Table A.6 – Number of oxygen vacancies surrounding a B-site cation (Ga or Mg) in rhombohedral (*R3c*) $LaGa_{1-y}Mg_yO_{3-\delta}$ (y = 0.05, 0.10, 0.15, 0.20, 0.25, 0.30, 0.35) at 1073 K, occupying the nearest-neighbour (NN), next-nearest-neighbour (NNN) and next-next-nearest-neighbour (NNNN) positions. Ga-O corresponds to a random distribution of vacancies where no defect ordering has occurred.

y	**Ga-O**			**Ga-vac**			**Mg-vac**		
	NN	**NNN**	**NNNN**	**NN**	**NNN**	**NNNN**	**NN**	**NNN**	**NNNN**
# sites	6	24	30	6	24	30	6	24	30
0.05	0.051	0.203	0.254	0.050	0.189	0.248	0.069	0.473	0.376
0.10	0.100	0.399	0.499	0.099	0.364	0.482	0.112	0.724	0.668
0.15	0.149	0.597	0.747	0.146	0.537	0.719	0.174	0.955	0.928
0.20	0.198	0.792	0.990	0.192	0.705	0.965	0.227	1.166	1.123
0.25	0.248	0.993	1.242	0.247	0.877	1.198	0.260	1.367	1.409
0.30	0.299	1.194	1.493	0.302	1.071	1.447	0.299	1.514	1.642
0.35	0.347	1.388	1.736	0.346	1.246	1.698	0.359	1.689	1.854

Table A.7 – Number of oxygen vacancies surrounding another oxygen vacancy in rhombohedral (*R3c*) $La_{1-x}Sr_xGaO_{3-\delta}$ (x = 0.10, 0.15, 0.20, 0.25, 0.30, 0.35) at 1073 K, occupying six different coordination shells. O-O corresponds to a random distribution of vacancies at the same temperature where no defect ordering has occurred.

x	O-O						vac-vac					
	1st	2nd	3rd	4th	5th	6th	1st	2nd	3rd	4th	5th	6th
0.10	0.136	0.018	0.502	0.192	0.281	0.552	0.052	0.068	0.228	0.290	0.281	0.256
0.15	0.205	0.027	0.759	0.291	0.388	0.835	0.069	0.082	0.340	0.486	0.388	0.416
0.20	0.271	0.036	1.004	0.385	0.511	1.105	0.111	0.119	0.444	0.514	0.511	0.525
0.25	0.341	0.046	1.261	0.483	0.628	1.388	0.149	0.143	0.490	0.657	0.628	0.647
0.30	0.410	0.055	1.518	0.582	0.731	1.671	0.208	0.188	0.614	0.760	0.731	0.795
0.35	0.476	0.064	1.763	0.675	0.836	1.940	0.286	0.232	0.727	0.827	0.836	0.919

Table A.8 – Number of oxygen vacancies surrounding another oxygen vacancy in rhombohedral (*R3c*) $LaGa_{1-y}Mg_yO_{3-\delta}$ (y = 0.05, 0.10, 0.15, 0.20, 0.25, 0.30, 0.35) at 1073 K, occupying six different coordination shells. O-O corresponds to a random distribution of vacancies where no defect ordering has occurred.

y	O-O						vac-vac					
	1st	2nd	3rd	4th	5th	6th	1st	2nd	3rd	4th	5th	6th
0.05	0.069	0.010	0.259	0.063	0.099	0.290	0.038	0.033	0.170	0.224	0.264	0.121
0.10	0.135	0.019	0.508	0.123	0.195	0.568	0.062	0.043	0.300	0.370	0.350	0.305
0.15	0.201	0.029	0.761	0.185	0.292	0.851	0.094	0.075	0.480	0.484	0.508	0.573
0.20	0.267	0.038	1.009	0.245	0.387	1.129	0.111	0.105	0.567	0.579	0.586	0.794
0.25	0.335	0.048	1.266	0.307	0.486	1.415	0.125	0.130	0.766	0.668	0.700	1.058
0.30	0.403	0.058	1.522	0.369	0.584	1.702	0.135	0.140	0.951	0.716	0.787	1.370
0.35	0.468	0.067	1.769	0.429	0.679	1.978	0.148	0.191	1.084	0.782	0.871	1.617

Tables A.9-A.16 present the calculated diffusion coefficients (from the linear fit of the MSD) and ionic conductivities (from the Nernst-Einstein equation) for LSGM systems. Each table reports diffusion coefficients and ionic conductivity values for a fixed x and varying y, i.e., there are separate tables for x = 0.10, 0.15, 0.20 and 0.25. Errors are given as standard error.

Table A.9 – Calculated diffusion coefficients (D, in 10^{-8} cm^2 s^{-1}) and ionic conductivities (σ, in mS/cm) of orthorhombic (*Pbnm*) $La_{0.9}Sr_{0.1}Ga_yMg_{1-y}O_{3-\delta}$ (x = 0.10), with y = 0.05, 0.10, 0.15, 0.20, 0.25 at 873, 1073 and 1273 K. Values in bold are the highest for a given T.

x = 0.10	873 K		1073 K		1273 K	
y	**D (10^{-8} cm^2/s)**	**σ (mS/cm)**	**D (10^{-8} cm^2/s)**	**σ (mS/cm)**	**D (10^{-8} cm^2/s)**	**σ (mS/cm)**
0.05	1.75±0.08	7.48±0.34	9.34±0.70	39.74±2.99	28.15±0.61	119.10±2.59
0.10	**1.84±0.18**	**7.78±0.75**	**10.22±0.13**	**43.02±0.56**	**31.15±1.17**	**130.44±4.91**
0.15	1.47±0.22	6.16±0.93	8.87±0.17	36.99±0.71	30.69±0.58	127.18±2.38
0.20	1.40±0.11	5.82±0.47	8.08±0.46	33.33±1.88	29.84±1.56	122.48±6.38
0.25	0.90±0.07	3.70±0.30	7.68±0.90	31.40±3.66	27.28±2.05	110.83±8.34

Table A.10 – Diffusion coefficients (D, in 10^{-8} cm^2 s^{-1}) and ionic conductivities (σ, in mS/cm) of orthorhombic (*Pbnm*) $La_{0.85}Sr_{0.15}Ga_yMg_{1-y}O_{3-\delta}$ (x = 0.15), with y = 0.05, 0.10, 0.15, 0.20, 0.25 at 873, 1073 and 1273 K. Values in bold are the highest for a given T.

x = 0.15	873 K		1073 K		1273 K	
y	**D (10^{-8} cm^2/s)**	**σ (mS/cm)**	**D (10^{-8} cm^2/s)**	**σ (mS/cm)**	**D (10^{-8} cm^2/s)**	**σ (mS/cm)**
0.05	**1.63±0.21**	**6.90±0.90**	8.72±0.19	36.81±0.81	28.53±1.49	119.73±6.24
0.10	1.50±0.01	6.32±0.04	**9.71±0.34**	**40.55±1.44**	**30.11±2.08**	**125.03±8.60**
0.15	1.29±0.14	5.35±0.58	8.19±0.44	33.86±1.83	28.32±0.13	116.37±0.52
0.20	0.95±0.02	3.92±0.08	7.40±0.85	30.27±3.49	25.58±0.19	104.09±0.79
0.25	0.87±0.31	3.56±1.27	7.00±0.10	28.35±0.37	23.86±0.56	96.07±2.24

Table A.11 – Calculated diffusion coefficients (D, in 10^{-8} cm^2 s^{-1}) and ionic conductivities (σ, in mS/cm) of orthorhombic (*Pbnm*) $La_{0.8}Sr_{0.2}Ga_yMg_{1-y}O_{3-\delta}$ (x = 0.20), with y = 0.05, 0.10, 0.15, 0.20, 0.25 at 873, 1073 and 1273 K. Values in bold are the highest D and σ for a given T.

x = 0.20	873 K		1073 K		1273 K	
y	**D (10^{-8} cm^2/s)**	**σ (mS/cm)**	**D (10^{-8} cm^2/s)**	**σ (mS/cm)**	**D (10^{-8} cm^2/s)**	**σ (mS/cm)**
0.05	**1.56±0.24**	**6.55±0.99**	8.50±0.01	35.57±0.01	26.92±0.34	111.96±1.40
0.10	1.53±0.10	6.38±0.39	**8.77±1.55**	**36.29±6.42**	**28.68±2.32**	**118.01±9.54**
0.15	1.18±0.03	4.88±0.10	6.33±0.61	25.95±2.49	26.37±0.92	107.40±3.70
0.20	1.09±0.10	4.45±0.41	6.69±0.58	27.14±2.35	23.61±1.17	95.14±4.75
0.25	0.74±0.10	3.01±0.40	7.00±0.65	28.32±2.62	21.98±2.19	87.66±8.74

Table A.12 – Calculated diffusion coefficients (D, in 10^{-8} cm^2 s^{-1}) and ionic conductivities (σ, in mS/cm) of orthorhombic (*Pbnm*) $La_{0.75}Sr_{0.25}Ga_yMg_{1-y}O_{3-\delta}$ (x = 0.25), with y = 0.05, 0.10, 0.15, 0.20, 0.25 at 873, 1073 and 1273 K. Values in bold are the highest for a given T.

x = 0.25	873 K		1073 K		1273 K	
y	**D (10^{-8} cm^2/s)**	**σ (mS/cm)**	**D (10^{-8} cm^2/s)**	**σ (mS/cm)**	**D (10^{-8} cm^2/s)**	**σ (mS/cm)**
0.05	**1.37±0.08**	**5.71±0.35**	**7.54±0.30**	**31.25±1.25**	**26.05±0.90**	**107.35±3.72**
0.10	1.27±0.20	5.23±0.84	6.50±0.22	26.66±0.92	25.31±1.34	103.22±5.48
0.15	0.79±0.03	3.24±0.12	6.06±0.30	24.61±1.20	21.05±1.66	84.93±6.72
0.20	0.88±0.03	3.56±0.11	6.03±0.61	24.22±2.47	21.96±1.79	87.67±7.23
0.25	0.99±0.11	3.95±0.43	4.92±0.92	19.56±3.65	18.27±0.88	72.13±3.41

Table A.13 – Calculated diffusion coefficients (D, in 10^{-8} cm^2 s^{-1}) and ionic conductivities (σ, in mS/cm) of rhombohedral (*R3c*) $La_{0.9}Sr_{0.1}Ga_yMg_{1-y}O_{3-\delta}$ (x = 0.10), with y = 0.05, 0.10, 0.15, 0.20, 0.25 at 873, 1073 and 1273 K. Values in bold are the highest for a given T.

x = 0.10	873 K		1073 K		1273 K	
y	**D (10^{-8} cm^2/s)**	**σ (mS/cm)**	**D (10^{-8} cm^2/s)**	**σ (mS/cm)**	**D (10^{-8} cm^2/s)**	**σ (mS/cm)**
0.05	1.53±0.45	6.54±1.94	9.47±0.31	**40.27±1.33**	27.68±0.26	117.09±1.12
0.10	1.74±0.14	**7.37±0.57**	9.34±0.80	39.35±3.38	29.75±0.52	124.61±2.18
0.15	1.61±0.13	6.75±0.55	8.79±0.63	36.63±2.64	29.29±0.37	121.39±1.57
0.20	1.40±0.23	5.81±0.97	8.93±0.68	36.85±2.78	30.95±0.64	**126.91±2.62**
0.25	1.06±0.17	4.36±0.69	7.55±0.39	30.85±1.60	28.46±1.02	115.59±4.13

Table A.14 – Calculated diffusion coefficients (D, in 10^{-8} cm^2 s^{-1}) and ionic conductivities (σ, in mS/cm) of rhombohedral (*R3c*) $La_{0.85}Sr_{0.15}Ga_yMg_{1-y}O_{3-\delta}$ (x = 0.15), with y = 0.05, 0.10, 0.15, 0.20, 0.25 at 873, 1073 and 1273 K. Values in bold are the highest for a given T.

x = 0.15	873 K		1073 K		1273 K	
y	**D (10^{-8} cm^2/s)**	**σ (mS/cm)**	**D (10^{-8} cm^2/s)**	**σ (mS/cm)**	**D (10^{-8} cm^2/s)**	**σ (mS/cm)**
0.05	1.41±0.10	5.99±0.42	8.62±1.29	36.37±5.43	29.82±2.02	**125.11±8.45**
0.10	1.84±0.19	**7.73±0.78**	10.43±0.90	**43.56±3.76**	29.64±1.81	123.03±7.50
0.15	1.54±0.11	6.38±0.46	8.56±1.25	35.37±5.16	29.31±1.13	120.40±4.63
0.20	1.35±0.24	5.56±0.99	7.65±0.67	31.30±2.74	28.45±1.71	115.70±6.92
0.25	1.02±0.07	4.15±0.30	6.48±0.03	26.25±0.11	24.02±2.22	97.54±9.79

Table A.15 – Calculated diffusion coefficients (D, in 10^{-8} cm^2 s^{-1}) and ionic conductivities (σ, in mS/cm) of rhombohedral (*R3c*) $La_{0.8}Sr_{0.2}Ga_yMg_{1-y}O_{3-\delta}$ (x = 0.20), with y = 0.05, 0.10, 0.15, 0.20, 0.25 at 873, 1073 and 1273 K. Values in bold are the highest D and σ for a given T.

x = 0.20	873 K		1073 K		1273 K	
y	**D (10^{-8} cm^2/s)**	**σ (mS/cm)**	**D (10^{-8} cm^2/s)**	**σ (mS/cm)**	**D (10^{-8} cm^2/s)**	**σ (mS/cm)**
0.05	1.26±0.02	**5.30±0.10**	8.44±0.07	35.33±0.27	30.34±2.54	**126.19±10.56**
0.10	1.07±0.09	4.47±0.36	8.63±0.39	**35.72±1.60**	29.15±0.73	119.95±2.99
0.15	1.04±0.24	4.28±1.00	7.37±0.04	30.22±0.16	29.15±2.52	118.76±10.25
0.20	1.26±0.01	5.16±0.03	6.41±0.21	25.99±0.84	24.18±2.06	97.46±8.25
0.25	0.81±0.11	3.27±4.44	5.80±0.20	23.30±0.80	22.73±0.12	90.69±0.53

Table A.16 – Calculated diffusion coefficients (D, in 10^{-8} cm^2 s^{-1}) and ionic conductivities (σ, in mS/cm) of rhombohedral (*R3c*) $La_{0.75}Sr_{0.25}Ga_yMg_{1-y}O_{3-\delta}$ (x = 0.25), with y = 0.05, 0.10, 0.15, 0.20, 0.25 at 873, 1073 and 1273 K. Values in bold are the highest D and σ for a given T.

x = 0.25	873 K		1073 K		1273 K	
y	**D (10^{-8} cm^2/s)**	**σ (mS/cm)**	**D (10^{-8} cm^2/s)**	**σ (mS/cm)**	**D (10^{-8} cm^2/s)**	**σ (mS/cm)**
0.05	1.12±0.09	4.65±0.39	8.38±0.66	**34.74±2.71**	29.31±0.46	**120.75±1.90**
0.10	1.46±0.40	**6.03±1.67**	7.44±0.49	30.52±2.01	26.99±0.01	110.05±0.05
0.15	0.87±0.01	3.56±0.01	7.43±0.19	30.16±0.75	24.89±0.16	100.38±0.67
0.20	0.99±0.06	3.98±0.26	6.17±0.21	24.78±0.85	22.59±0.83	90.14±3.33
0.25	0.80±0.01	3.19±0.03	5.37±0.21	21.38±0.85	19.94±0.25	78.76±0.96

Tables A.17-A.20 present the number of oxygen vacancies surrounding A- (La and Sr) and B-site (Ga and Mg) cations in orthorhombic and rhombohedral LSGM. The number of vacancies located at NN, NNN and NNNN sites was calculated through the integration of the RDF peaks. The number of vacancies surrounding another vacancy, an indicative of vacancy ordering, was also calculated taking into consideration six O-O bond distance intervals and is presented in Tables A.21 (orthorhombic LSGM) and A.22 (rhombohedral LSGM).

Table A.17 – Number of oxygen vacancies surrounding A-site cations (La or Sr) in orthorhombic (*Pbnm*) $La_{1-x}Sr_xGa_{1-y}Mg_yO_{3-\delta}$ (x = 0.10, 0.15, 0.20, 0.25 and y = 0.05, 0.10, 0.15, 0.20, 0.25) at 1073 K, occupying the nearest-neighbour (NN), next-nearest-neighbour (NNN) and next-next-nearest-neighbour (NNNN) positions. La-O corresponds to a random distribution of vacancies where no defect ordering has occurred.

x	*y*	La-O (Pbnm)			La-vac (*Pbnm*)			Sr-vac (*Pbnm*)		
		NN	NNN	NNNN	NN	NNN	NNNN	NN	NNN	NNNN
0.10	**0.05**	0.300	0.604	0.596	0.317	0.524	0.610	0.154	1.297	0.544
	0.10	0.398	0.802	0.790	0.416	0.711	0.805	0.253	1.594	0.783
	0.15	0.498	1.003	0.986	0.527	0.888	1.012	0.250	2.000	0.934
	0.20	0.600	1.209	1.188	0.637	1.077	1.230	0.298	2.351	1.058
	0.25	0.697	1.404	1.378	0.733	1.258	1.416	0.403	2.656	1.358
0.15	**0.05**	0.395	0.797	0.786	0.452	0.640	0.811	0.241	1.270	0.786
	0.10	0.498	1.003	0.988	0.567	0.823	1.025	0.302	1.535	0.982
	0.15	0.597	1.204	1.184	0.651	1.030	1.226	0.312	2.148	1.117
	0.20	0.696	1.402	1.378	0.754	1.194	1.431	0.385	2.535	1.292
	0.25	0.797	1.607	1.576	0.861	1.401	1.637	0.450	2.686	1.475
0.20	**0.05**	0.498	1.003	0.990	0.549	0.794	1.019	0.305	1.824	0.957
	0.10	0.599	1.207	1.189	0.667	1.008	1.220	0.345	1.979	1.185
	0.15	0.696	1.402	1.380	0.775	1.156	1.437	0.394	2.372	1.308
	0.20	0.797	1.607	1.578	0.894	1.345	1.631	0.428	2.617	1.549
	0.25	0.894	1.802	1.767	0.984	1.513	1.859	0.556	2.926	1.631
0.25	**0.05**	0.599	1.207	1.192	0.681	0.930	1.227	0.363	2.027	1.170
	0.10	0.696	1.402	1.381	0.794	1.096	1.416	0.406	2.287	1.368
	0.15	0.797	1.607	1.580	0.907	1.285	1.629	0.483	2.550	1.578
	0.20	0.894	1.802	1.769	1.015	1.472	1.834	0.540	2.748	1.757
	0.25	0.995	2.006	1.967	1.114	1.658	2.037	0.646	2.984	1.961

Table A.18 – Number of oxygen vacancies surrounding A-site cations (La or Sr) in rhombohedral (*R3c*) $La_{1-x}Sr_xGa_{1-y}Mg_yO_{3-\delta}$ (x = 0.10, 0.15, 0.20, 0.25 and y = 0.05, 0.10, 0.15, 0.20, 0.25) at 1073 K, occupying the nearest-neighbour (NN), next-nearest-neighbour (NNN) and next-next-nearest-neighbour (NNNN) positions. La-O corresponds to a random distribution of vacancies where no defect ordering has occurred.

x	*y*	La-O (*R3c*)			La-vac (*R3c*)			Sr-vac (*R3c*)		
		NN	**NNN**	**NNNN**	**NN**	**NNN**	**NNNN**	**NN**	**NNN**	**NNNN**
0.10	**0.05**	0.301	0.603	0.595	0.315	0.523	0.608	0.175	1.318	0.569
	0.10	0.400	0.802	0.790	0.423	0.709	0.807	0.188	1.627	0.769
	0.15	0.500	1.003	0.986	0.527	0.890	1.017	0.260	2.001	0.910
	0.20	0.603	1.209	1.187	0.635	1.083	1.226	0.316	2.318	1.100
	0.25	0.700	1.404	1.378	0.740	1.268	1.422	0.343	2.588	1.303
0.15	**0.05**	0.397	0.796	0.786	0.443	0.633	0.819	0.268	1.294	0.759
	0.10	0.500	1.003	0.988	0.563	0.837	1.022	0.322	1.510	0.993
	0.15	0.600	1.203	1.184	0.650	1.033	1.226	0.320	2.144	1.114
	0.20	0.699	1.402	1.377	0.754	1.220	1.433	0.391	2.410	1.265
	0.25	0.801	1.606	1.577	0.863	1.385	1.647	0.453	2.833	1.434
0.20	**0.05**	0.500	1.003	0.990	0.547	0.800	1.003	0.313	1.802	1.019
	0.10	0.602	1.207	1.190	0.672	0.981	1.231	0.327	2.090	1.139
	0.15	0.699	1.402	1.380	0.768	1.159	1.425	0.423	2.365	1.351
	0.20	0.801	1.606	1.579	0.880	1.343	1.640	0.486	2.369	1.528
	0.25	0.898	1.801	1.769	0.991	1.534	1.851	0.527	2.857	1.668
0.25	**0.05**	0.602	1.207	1.191	0.667	0.935	1.218	0.407	2.014	1.192
	0.10	0.699	1.402	1.381	0.785	1.132	1.416	0.443	2.204	1.393
	0.15	0.801	1.606	1.579	0.889	1.272	1.645	0.539	2.598	1.525
	0.20	0.898	1.801	1.768	1.007	1.498	1.827	0.575	2.702	1.776
	0.25	1.000	2.005	1.969	1.124	1.650	2.068	0.630	3.055	1.890

Table A.19 – Number of oxygen vacancies surrounding B-site cations (Ga or Mg) in orthorhombic (*Pbnm*) $La_{1-x}Sr_xGa_{1-y}Mg_yO_{3-\delta}$ (x = 0.10, 0.15, 0.20, 0.25 and y = 0.05, 0.10, 0.15, 0.20, 0.25) at 1073 K, occupying the nearest-neighbour (NN), next-nearest-neighbour (NNN) and next-next-nearest-neighbour (NNNN) positions. Ga-O corresponds to a random distribution of vacancies where no defect ordering has occurred.

x	*y*	Ga-O			Ga-vac			Mg-vac		
		NN	**NNN**	**NNNN**	**NN**	**NNN**	**NNNN**	**NN**	**NNN**	**NNNN**
0.10	**0.05**	0.150	0.602	0.753	0.150	0.576	0.744	0.151	1.082	0.918
	0.10	0.200	0.800	0.999	0.203	0.760	0.976	0.176	1.170	1.218
	0.15	0.250	1.000	1.247	0.254	0.931	1.221	0.230	1.396	1.415
	0.20	0.301	1.205	1.502	0.303	1.103	1.476	0.295	1.618	1.635
	0.25	0.350	1.400	1.742	0.359	1.277	1.685	0.323	1.771	1.945
0.15	**0.05**	0.199	0.794	0.994	0.207	0.762	0.974	0.157	0.999	1.140
	0.10	0.250	1.000	1.249	0.264	0.942	1.214	0.194	1.242	1.416
	0.15	0.300	1.200	1.497	0.310	1.119	1.469	0.242	1.658	1.681
	0.20	0.350	1.398	1.742	0.362	1.293	1.688	0.298	1.823	1.994
	0.25	0.400	1.601	1.993	0.410	1.477	1.930	0.366	1.963	2.205
0.20	**0.05**	0.250	1.000	1.252	0.251	0.969	1.241	0.226	1.589	1.444
	0.10	0.301	1.203	1.504	0.313	1.159	1.477	0.190	1.610	1.775
	0.15	0.350	1.398	1.745	0.363	1.319	1.699	0.274	1.845	2.032
	0.20	0.400	1.601	1.995	0.410	1.514	1.961	0.364	1.955	2.180
	0.25	0.449	1.796	2.234	0.476	1.674	2.177	0.370	2.170	2.469
0.25	**0.05**	0.301	1.203	1.506	0.307	1.170	1.490	0.195	1.835	1.811
	0.10	0.350	1.398	1.746	0.354	1.345	1.711	0.295	1.838	2.050
	0.15	0.400	1.601	1.997	0.416	1.531	1.957	0.316	2.006	2.290
	0.20	0.449	1.796	2.236	0.473	1.687	2.172	0.347	2.222	2.535
	0.25	0.500	1.999	2.487	0.511	1.848	2.428	0.456	2.433	2.701

Table A.20 – Number of oxygen vacancies surrounding B-site cations (Ga or Mg) in rhombohedral (*R3c*) $La_{1-x}Sr_xGa_{1-y}Mg_yO_{3-\delta}$ (x = 0.10, 0.15, 0.20, 0.25 and y = 0.05, 0.10, 0.15, 0.20, 0.25) at 1073 K, occupying the nearest-neighbour (NN), next-nearest-neighbour (NNN) and next-next-nearest-neighbour (NNNN) positions. Ga-O corresponds to a random distribution of vacancies where no defect ordering has occurred.

x	*y*	Ga-O			Ga-vac			Mg-vac		
		NN	**NNN**	**NNNN**	**NN**	**NNN**	**NNNN**	**NN**	**NNN**	**NNNN**
0.10	**0.05**	0.150	0.602	0.752	0.148	0.580	0.742	0.186	1.006	0.937
	0.10	0.200	0.799	0.999	0.205	0.751	0.983	0.149	1.238	1.158
	0.15	0.249	0.997	1.246	0.252	0.928	1.218	0.235	1.402	1.430
	0.20	0.300	1.200	1.500	0.315	1.112	1.449	0.247	1.574	1.737
	0.25	0.348	1.392	1.741	0.348	1.264	1.712	0.354	1.803	1.859
0.15	**0.05**	0.199	0.795	0.994	0.207	0.758	0.973	0.152	1.010	1.133
	0.10	0.250	0.999	1.249	0.267	0.936	1.213	0.184	1.267	1.433
	0.15	0.299	1.197	1.496	0.306	1.127	1.479	0.267	1.610	1.615
	0.20	0.348	1.392	1.740	0.363	1.300	1.711	0.292	1.791	1.896
	0.25	0.398	1.594	1.993	0.409	1.472	1.975	0.374	1.986	2.083
0.20	**0.05**	0.250	1.000	1.251	0.252	0.974	1.236	0.200	1.482	1.516
	0.10	0.301	1.203	1.503	0.306	1.152	1.483	0.251	1.658	1.704
	0.15	0.349	1.395	1.744	0.356	1.322	1.700	0.308	1.821	2.016
	0.20	0.399	1.595	1.995	0.417	1.503	1.967	0.332	1.985	2.142
	0.25	0.447	1.787	2.235	0.461	1.659	2.167	0.410	2.198	2.483
0.25	**0.05**	0.301	1.204	1.505	0.304	1.173	1.486	0.231	1.751	1.880
	0.10	0.349	1.396	1.745	0.361	1.339	1.727	0.242	1.910	1.943
	0.15	0.399	1.596	1.996	0.416	1.522	1.955	0.305	2.029	2.276
	0.20	0.447	1.787	2.234	0.477	1.675	2.169	0.330	2.266	2.564
	0.25	0.497	1.989	2.487	0.520	1.849	2.427	0.436	2.438	2.719

Table A.21 – Number of oxygen vacancies surrounding another oxygen vacancy in orthorhombic (*Pbnm*) and $La_{1-x}Sr_xGa_{1-y}Mg_yO_{3-\delta}$ (x = 0.10, 0.15, 0.20, 0.25 and y = 0.05, 0.10, 0.15, 0.20, 0.25) at 1073 K, occupying the nearest-neighbour (NN) and next-nearest-neighbour (NNN) positions. O-O corresponds to a random distribution of vacancies where no defect ordering has occurred.

x	*y*	O-O						vac-vac					
		1st	**2nd**	**3rd**	**4th**	**5th**	**6th**	**1st**	**2nd**	**3rd**	**4th**	**5th**	**6th**
0.10	**0.05**	0.205	0.027	0.767	0.264	0.208	0.858	0.076	0.081	0.310	0.477	0.501	0.401
	0.10	0.271	0.036	1.018	0.350	0.275	1.139	0.123	0.096	0.403	0.618	0.612	0.610
	0.15	0.339	0.045	1.271	0.437	0.344	1.421	0.172	0.117	0.503	0.719	0.697	0.800
	0.20	0.408	0.054	1.530	0.526	0.414	1.712	0.192	0.158	0.604	0.826	0.849	0.951
	0.25	0.473	0.063	1.775	0.610	0.480	1.985	0.233	0.189	0.746	0.850	0.910	1.209
0.15	**0.05**	0.270	0.036	1.013	0.348	0.274	1.133	0.205	0.096	0.378	0.468	0.550	0.458
	0.10	0.339	0.045	1.273	0.437	0.344	1.424	0.238	0.132	0.464	0.561	0.618	0.700
	0.15	0.407	0.054	1.526	0.524	0.413	1.706	0.193	0.153	0.610	0.800	0.793	0.917
	0.20	0.473	0.063	1.775	0.610	0.480	1.985	0.247	0.187	0.717	0.871	0.955	1.182
	0.25	0.541	0.072	2.031	0.698	0.549	2.271	0.315	0.201	0.812	0.993	1.019	1.222
0.20	**0.05**	0.340	0.045	1.276	0.438	0.345	1.427	0.170	0.160	0.491	0.719	0.756	0.732
	0.10	0.409	0.055	1.532	0.526	0.415	1.714	0.227	0.125	0.525	0.803	0.913	0.667
	0.15	0.474	0.063	1.778	0.611	0.481	1.989	0.245	0.197	0.679	0.897	0.921	1.048
	0.20	0.542	0.072	2.033	0.698	0.550	2.274	0.348	0.177	0.842	0.910	1.076	1.101
	0.25	0.607	0.081	2.277	0.782	0.616	2.546	0.392	0.229	0.962	1.021	1.123	1.515
0.25	**0.05**	0.409	0.055	1.535	0.527	0.415	1.717	0.254	0.199	0.563	0.820	0.787	0.779
	0.10	0.475	0.063	1.780	0.611	0.481	1.991	0.321	0.196	0.668	0.871	0.941	0.796
	0.15	0.543	0.072	2.035	0.699	0.550	2.276	0.413	0.193	0.760	0.941	1.105	0.920
	0.20	0.608	0.081	2.279	0.783	0.616	2.549	0.426	0.237	0.830	1.004	1.106	1.254
	0.25	0.676	0.090	2.534	0.870	0.685	2.834	0.466	0.256	1.033	1.037	1.127	1.461

Table A.22 – Number of oxygen vacancies surrounding another oxygen vacancy in rhombohedral (*R3c*) $La_{1-x}Sr_xGa_{1-y}Mg_yO_{3-\delta}$ (x = 0.10, 0.15, 0.20, 0.25 and y = 0.05, 0.10, 0.15, 0.20, 0.25) at 1073 K, occupying the nearest-neighbour (NN) and next-nearest-neighbour (NNN) positions. O-O corresponds to a random distribution of vacancies where no defect ordering has occurred.

x	*y*	O-O						vac-vac					
		1st	**2nd**	**3rd**	**4th**	**5th**	**6th**	**1st**	**2nd**	**3rd**	**4th**	**5th**	**6th**
0.10	**0.05**	0.205	0.027	0.767	0.264	0.208	0.858	0.059	0.079	0.349	0.486	0.414	0.473
	0.10	0.271	0.036	1.018	0.350	0.275	1.139	0.091	0.090	0.499	0.554	0.558	0.649
	0.15	0.339	0.045	1.271	0.437	0.344	1.421	0.112	0.130	0.602	0.678	0.655	0.903
	0.20	0.408	0.054	1.529	0.525	0.414	1.711	0.163	0.148	0.764	0.751	0.788	1.016
	0.25	0.473	0.063	1.775	0.610	0.480	1.985	0.164	0.222	0.938	0.767	0.902	1.481
0.15	**0.05**	0.270	0.036	1.013	0.348	0.274	1.133	0.146	0.104	0.480	0.471	0.470	0.647
	0.10	0.339	0.045	1.273	0.437	0.344	1.424	0.198	0.119	0.660	0.553	0.543	0.772
	0.15	0.407	0.054	1.525	0.524	0.413	1.706	0.151	0.141	0.726	0.798	0.710	0.966
	0.20	0.473	0.063	1.774	0.610	0.480	1.985	0.200	0.164	0.887	0.833	0.836	1.327
	0.25	0.542	0.072	2.032	0.698	0.550	2.273	0.201	0.208	1.115	0.903	0.943	1.677
0.20	**0.05**	0.340	0.045	1.275	0.438	0.345	1.426	0.159	0.138	0.552	0.683	0.625	0.731
	0.10	0.409	0.055	1.533	0.527	0.415	1.715	0.168	0.171	0.662	0.762	0.721	0.928
	0.15	0.474	0.063	1.778	0.611	0.481	1.989	0.208	0.182	0.790	0.895	0.820	1.093
	0.20	0.542	0.072	2.034	0.699	0.550	2.275	0.231	0.200	1.014	0.915	0.910	1.492
	0.25	0.607	0.081	2.278	0.783	0.616	2.548	0.259	0.243	1.203	1.028	1.023	1.704
0.25	**0.05**	0.409	0.055	1.535	0.527	0.415	1.717	0.213	0.179	0.685	0.749	0.739	0.885
	0.10	0.474	0.063	1.779	0.611	0.481	1.990	0.247	0.172	0.790	0.869	0.828	0.921
	0.15	0.543	0.072	2.035	0.699	0.550	2.276	0.294	0.210	0.965	0.946	0.945	1.300
	0.20	0.607	0.081	2.277	0.782	0.616	2.547	0.354	0.212	1.180	0.990	0.972	1.380
	0.25	0.676	0.090	2.536	0.871	0.686	2.837	0.313	0.253	1.363	1.068	1.097	1.929

Tables A.23 and A.24 present the calculated diffusion coefficients (from the linear fit of the MSD) and ionic conductivities (from the Nernst-Einstein equation) for orthorhombic and rhombohedral ac-$LaGaO_3$ systems. All errors are given as standard errors.

Table A.23 – Diffusion coefficients (D, in 10^{-8} cm^2 s^{-1}) and ionic conductivities (σ, in mS/cm) of orthorhombic (*Pbnm*) $LaGaO_{3-\delta}$, with 2δ = 0.15, 0.20, 0.25, 0.30, 0.35, 0.40, 0.45 and 0.50 at 873, 1073 and 1273 K. Values in bold are the highest σ for a given temperature.

	873 K		**1073 K**		**1273 K**	
2δ	**D (10^{-8} cm^2/s)**	**σ (mS/cm)**	**D (10^{-8} cm^2/s)**	**σ (mS/cm)**	**D (10^{-8} cm^2/s)**	**σ (mS/cm)**
0.15	3.28±0.18	13.78±0.74	23.09±0.52	96.57±2.15	53.75±2.75	223.54±11.42
0.20	3.60±0.80	14.39±3.32	**27.83±0.30**	**114.76±1.25**	66.48±0.76	272.53±3.12
0.25	**4.30±0.52**	**17.56±2.10**	27.56±0.14	111.99±0.59	76.30±2.32	308.13±9.37
0.30	3.93±0.03	15.85±0.13	26.02±0.68	104.17±2.71	**85.38±5.65**	**339.60±22.46**
0.35	2.04±0.01	8.09±0.04	19.10±0.50	75.34±1.97	73.92±1.11	289.68±4.38
0.40	2.02±0.19	7.92±0.72	16.43±0.12	63.83±0.43	63.73±1.16	245.96±4.52
0.45	1.64±0.20	6.32±0.75	12.86±3.00	49.13±11.52	51.34±1.26	195.09±4.79
0.50	1.37±0.26	5.16±1.00	9.02±0.53	33.89±1.97	36.82±6.20	137.53±23.28

Table A.24 – Diffusion coefficients (D, in 10^{-8} cm^2 s^{-1}) and ionic conductivities (σ, in mS/cm) of rhombohedral (*R3c*) $LaGaO_{3-\delta}$, with 2δ = 0.15, 0.20, 0.25, 0.30, 0.35, 0.40, 0.45 and 0.50 at 873, 1073 and 1273 K. Values in bold are the highest σ for a given temperature.

	873 K		**1073 K**		**1273 K**	
2δ	**D (10^{-8} cm^2/s)**	**σ (mS/cm)**	**D (10^{-8} cm^2/s)**	**σ (mS/cm)**	**D (10^{-8} cm^2/s)**	**σ (mS/cm)**
0.15	4.72±0.34	19.84±1.45	22.69±0.35	94.91±1.45	55.02±0.64	228.86±2.68
0.20	**5.10±0.69**	**21.16±2.86**	**27.07±0.48**	**111.65±1.96**	70.22±1.88	287.87±7.70
0.25	4.33±0.62	17.69±2.55	25.79±0.42	104.82±1.72	77.84±3.07	314.37±12.39
0.30	4.36±0.05	17.57±0.22	24.49±3.08	98.04±12.32	**82.11±1.64**	**326.66±6.57**
0.35	3.28±0.58	13.05±2.31	21.02±0.75	82.93±2.96	75.24±0.26	294.87±1.00
0.40	1.72±0.02	6.74±0.09	18.60±0.08	72.25±0.29	60.61±0.28	233.92±1.08
0.45	1.13±0.14	4.36±0.52	12.75±0.15	48.77±0.55	53.66±1.54	203.88±5.88
0.50	6.20±0.15	2.34±0.57	8.58±0.90	32.22±3.39	41.67±2.86	155.67±10.68

The number of oxygen vacancies surrounding La(III) and Ga (III) ions at NN, NNN and NNNN sites in orthorhombic and rhombohedral ac-$LaGaO_{3-\delta}$ systems at 1073 K,

calculated through the integration of the RDF peaks, are presented in Table A.25 and A.26. The number of oxygen vacancies surrounding another vacancy in rhombohedral ac-$LaGaO_{3-\delta}$ systems at 1073 K is presented in Table A.27.

Table A.25 – Number of oxygen vacancies surrounding a La and Ga ions in orthorhombic (*Pbnm*) ac-$LaGaO_{3-\delta}$ (2δ = 0.15, 0.20, 0.25, 0.30, 0.35, 0.40, 0.45 and 0.50) at 1073 K, occupying the nearest-neighbour (NN), next-nearest-neighbour (NNN) and next-next-nearest-neighbour (NNNN) positions. La-O and Ga-O correspond to a random distribution of vacancies where no defect ordering has occurred.

Cation	**2δ**	**La/Ga-O**			**La/Ga-vac**		
		NN	**NNN**	**NNNN**	**NN**	**NNN**	**NNNN**
La	**0.15**	0.294	0.593	0.585	0.301	0.605	0.613
	0.20	0.389	0.784	0.774	0.400	0.804	0.811
	0.25	0.484	0.975	0.961	0.500	1.005	1.010
	0.30	0.577	1.162	1.147	0.600	1.207	1.208
	0.35	0.669	1.348	1.330	0.700	1.408	1.409
	0.40	0.760	1.531	1.510	0.801	1.609	1.598
	0.45	0.848	1.708	1.685	0.901	1.809	1.764
	0.50	0.935	1.884	1.858	0.991	1.986	1.913
Ga	**0.15**	0.150	0.602	0.740	0.151	0.602	0.754
	0.20	0.200	0.800	0.978	0.200	0.801	1.002
	0.25	0.250	1.000	1.216	0.250	1.000	1.252
	0.30	0.300	1.200	1.450	0.300	1.201	1.502
	0.35	0.350	1.400	1.682	0.350	1.401	1.754
	0.40	0.400	1.600	1.909	0.400	1.602	2.007
	0.45	0.450	1.799	2.131	0.450	1.802	2.261
	0.50	0.500	1.999	2.349	0.494	1.978	2.488

Table A.26 – Number of oxygen vacancies surrounding a La and Ga ions in rhombohedral (*R3c*) ac-$LaGaO_{3-\delta}$ (2δ = 0.15, 0.20, 0.25, 0.30, 0.35, 0.40, 0.45 and 0.50) at 1073 K, occupying the nearest-neighbour (NN), next-nearest-neighbour (NNN) and next-next-nearest-neighbour (NNNN) positions. La-O and Ga-O correspond to a random distribution of vacancies where no defect ordering has occurred.

Cation	**2δ**	**La/Ga-O**			**La/Ga-vac**		
		NN	**NNN**	**NNNN**	**NN**	**NNN**	**NNNN**
La	**0.15**	0.150	0.602	0.740	0.148	0.575	0.754
	0.20	0.200	0.800	0.978	0.195	0.764	1.002
	0.25	0.250	1.000	1.215	0.243	0.956	1.252
	0.30	0.300	1.200	1.449	0.290	1.147	1.503
	0.35	0.350	1.400	1.681	0.336	1.339	1.754
	0.40	0.400	1.600	1.909	0.382	1.529	2.004
	0.45	0.450	1.800	2.130	0.426	1.705	2.238
	0.50	0.500	2.000	2.348	0.469	1.859	2.448
Ga	**0.15**	0.150	0.602	0.740	0.148	0.575	0.754
	0.20	0.200	0.800	0.978	0.195	0.764	1.002
	0.25	0.250	1.000	1.215	0.243	0.956	1.252
	0.30	0.300	1.200	1.449	0.290	1.147	1.503
	0.35	0.350	1.400	1.681	0.336	1.339	1.754
	0.40	0.400	1.600	1.909	0.382	1.529	2.004
	0.45	0.450	1.800	2.130	0.426	1.705	2.238
	0.50	0.500	2.000	2.348	0.469	1.859	2.448

Table A.27 – Number of oxygen vacancies surrounding another vacancy in rhombohedral (*R3c*) ac-$LaGaO_{3-\delta}$ (2δ = 0.15, 0.20, 0.25, 0.30, 0.35, 0.40, 0.45 and 0.50) at 1073 K, considering seven distinct coordination shells. O-O corresponds to a random distribution of vacancies where no defect ordering has occurred.

	2δ	**1st**	**2nd**	**3rd**	**4th**	**5th**	**6th**	**7th**
O-O	**0.15**	0.201	0.027	0.754	0.259	0.204	0.844	0.278
	0.20	0.266	0.035	0.997	0.342	0.270	1.115	0.367
	0.25	0.330	0.044	1.239	0.426	0.335	1.386	0.456
	0.30	0.394	0.053	1.477	0.508	0.400	1.653	0.544
	0.35	0.457	0.061	1.714	0.589	0.464	1.917	0.631
	0.40	0.519	0.069	1.946	0.668	0.526	2.176	0.717
	0.45	0.580	0.077	2.175	0.747	0.588	2.433	0.801
	0.50	0.638	0.085	2.392	0.822	0.647	2.676	0.881
vac-vac	**0.15**	0.134	0.036	0.262	0.416	0.424	0.343	0.403
	0.20	0.150	0.095	0.380	0.573	0.613	0.515	0.678
	0.25	0.155	0.122	0.513	0.655	0.663	0.477	0.593
	0.30	0.205	0.172	0.539	0.735	0.674	0.377	0.804
	0.35	0.269	0.216	0.493	0.878	0.870	0.278	1.550
	0.40	0.495	0.149	0.597	0.910	0.933	0.197	1.301
	0.45	0.759	0.187	0.962	1.031	0.992	0.120	1.339
	0.50	1.330	0.237	1.532	1.144	1.208	0.249	2.167

Bibliography

[1] Perera, F. Pollution from Fossil-Fuel Combustion is the Leading Environmental Threat to Global Pediatric Health and Equity: Solutions Exist. *Int. J. Environ. Res. Public Heal.* **15**, 16 (2017).

[2] Stambouli, A. B. & Traversa, E. Solid oxide fuel cells (SOFCs): a review of an environmentally clean and efficient source of energy. *Renew. Sust. Energy Rev.* **6**, 433–455 (2002).

[3] Minh, N. Q. Ceramic Fuel Cells. *J. Am. Ceram. Soc.* **76**, 563–588 (1993).

[4] Sood, K., Singh, K. & Pandey, O. P. Structural and electrical behavior of Ba-doped $LaGaO_3$ composite electrolyte. *J. Renew. Sustain. Energy* **6**, 063112 (2014).

[5] Singhal, S. C. Advances in solid oxide fuel cell technology. *Solid State Ionics* **135**, 305–313 (2000).

[6] Sharma, R. K. *et al.* Design of $La_{2-x}Pr_xNiO_{4+\delta}$ SOFC cathodes: a compromise between electrochemical performance and thermodynamic stability. *J. Mater. Chem. A* **5**, 1120–1132 (2017).

[7] Gavin, A. L. & Watson, G. W. Modelling oxygen defects in orthorhombic $LaMnO_3$ and its low index surfaces. *Phys. Chem. Chem. Phys.* **19**, 24636–24646 (2017).

[8] Sacanell, J. *et al.* Oxygen Reduction Mechanisms in Nanostructured $La_{0.8}Sr_{0.2}MnO_3$ Cathodes for Solid Oxide Fuel Cells. *J. Phys. Chem. C* **121**, 6533–6539 (2017).

[9] Drożdż, E., Łącz, A., Koleżyński, A., Mikuła, A. & Mars, K. Experimental and theoretical studies of structural and electrical properties of highly porous $Sr_{1-x}Y_xTiO_3$. *Solid State Ionics* **302**, 173–179 (2017).

[10] Biswas, M. & Sadanala, K. C. Electrolyte Materials for Solid Oxide Fuel Cell. *J. Powder Met. Min.* **2**, 10000117 (2013).

[11] Khan, M. S., Islam, M. S. & Bates, D. R. Dopant Substitution and Ion Migration in the $LaGaO_3$-based oxygen ion conductor. *J. Phys. Chem. B* **102**, 3099–3104 (1998).

[12] Tsvetkov, N., Lu, Q., Chen, Y. & Yildiz, B. Surface Chemistry and Non-Stoichiometry of $Nd_2NiO_{4+\delta}$ Epitaxial Thin Films with Different Orientation and Strain. *ECS Trans.* **57**, 1743–1752 (2013).

[13] Uchida, H., Arisaka, S. & Watanabe, M. High Performance Electrode for Medium-Temperature Solid Oxide Fuel Cells: Control of Microstructure of $La(Sr)CoO_3$ Cathodes with Highly Dispersed Pt Electrocatalysts. *J. Electrochem. Soc.* **149**, A13

(2002).

[14] Shao, Z. & Haile, S. M. A high-performance cathode for the next generation of solid-oxide fuel cells. *Nature* **431**, 170–173 (2004).

[15] Jacobson, A. J. Materials for Solid Oxide Fuel Cells. *Chem Mater.* **22**, 660–674 (2010).

[16] Ishihara, T. *Perovskite Oxide for Solid Oxide Fuel Cells*. (Springer, 2009).

[17] Hansen, J. B. Solid oxide electrolysis – a key enabling technology for sustainable energy scenarios. *Faraday Discuss.* **182**, 9–48 (2015).

[18] Jun, A., Ju, Y.-W. & Kim, G. Solid Oxide Electrolysis: concluding remarks. *Faraday Discuss.* **182**, 519–528 (2015).

[19] Minh, N. Q. & Mogensen, M. B. Reversible Solid Oxide Fuel Cell Technology for Green Fuel and Power Production. *Electrochem. Soc. Interface* **22**, 55–62 (2013).

[20] Gomez, S. Y. & Hotza, D. Current developments in reversible solid oxide fuel cells. *Renew. Sustain. Energy Rev.* **61**, 155–174 (2016).

[21] Chroneos, A., Yildiz, B., Tarancón, A., Parfitt, D. & Kilner, J. A. Oxygen diffusion in solid oxide fuel cell cathode and electrolyte materials: Mechanistic insights from atomistic simulations. *Energy Environ. Sci.* **4**, 2774–2789 (2011).

[22] Goodenough, J. B. Oxide-ion conductors by design. *Nature* **404**, (2000).

[23] Mogensen, M., Lybye, D., Bonanos, N., Hendriksen, P. V. & Poulsen, F. W. Factors controlling the oxide ion conductivity of fluorite and perovskite structured oxides. *Solid State Ionics* **174**, 279–286 (2004).

[24] Kim, D. J. Lattice Parameters, Ionic Conductivities, and Solubility Limits in Fluorite-Structure MO_2 oxide (M = Hf^{4+}, Zr^{4+}, Ce^{4+}, Th^{4+}, U^{4+}) Solid Solutions. *J. Am. Ceram. Soc.* **72**, 1415–1421 (1989).

[25] Marrocchelli, D., Bishop, S. R., Tuller, H. L. & Yildiz, B. Understanding chemical expansion in non-stoichiometric oxides: Ceria and Zirconia case studies. *Adv. Funct. Mater.* **22**, 1958–1965 (2012).

[26] Shannon, R. D. Revised Effective Ionic Radii and Systematic Studies of Interatomic Distances in Halides and Chalcogenides. *Acta Cryst.* **A32**, 751–767 (1976).

[27] Woodward, P. M. Octahedral Tilting in Perovskites. I. Geometrical Considerations. *Acta Cryst.* **B53**, 32–43 (1997).

[28] Figueiredo, F. M. L. & Marques, F. M. B. Electrolytes for solid oxide fuel cells.

WIREs Energy Environ. **2**, 52–72 (2012).

[29] De Souza, R. A. & Martin, M. An atomistic simulation study of oxygen-vacancy migration in perovskite electrolytes based on $LaGaO_3$. *Monatsh Chem.* **140**, 1011–1015 (2009).

[30] Gregori, G., Merkle, R. & Maier, J. Ion conduction and redistribution at grain boundaries in oxide systems. *Prog. Mater. Sci.* **89**, 252–305 (2017).

[31] Goldschmidt, V. M. Die Gesetze der Krystallochemie. *Naturwissenschaften* **14**, 477–485 (1926).

[32] Li, C., Soh, K. C. K. & Wu, P. Formability of ABO_3 perovskites. *J. Alloys Compd.* **372**, 40–48 (2004).

[33] Rao, C. N. R. Perovskites. in *Encyclopedia of Physical Science and Technology* (ed. Meyers, R. A.) 707–714 (Academic Press, 2003).

[34] Gauquelin, N., Weirich, T. E., Ceretti, M., Paulus, W. & Schroeder, M. Long-term structural surface modifications of mixed conducting $La_2NiO_{4+\delta}$ at high temperatures. *Monatshefte fur Chemie* **140**, 1095–1102 (2009).

[35] Zhou, Y., Lü, Z., Xu, S., Xu, D. & Wei, B. Investigation of a solid oxide fuel cells catalyst $LaSrNiO_4$: Electronic structure, surface segregation, and oxygen adsorption. *Int. J. Hydrogen Energy* **41**, 21497–21502 (2016).

[36] Ido, T., Magoshi, K., Eisaki, H. & Uchida, S. Optical study of the $La_{2-x}Sr_xNiO_4$ system: Effect of hole doping on the electronic structure of the NiO_2 plane. *Phys. Rev. B* **44**, 12094–12097 (1991).

[37] Upasen, S., Batocchi, P., Mauvy, F., Slodczyk, A. & Colomban, P. Protonation and structural/chemical stability of $Ln_2NiO_{4+\delta}$ ceramics vs. H_2O/CO_2: High temperature/water pressure ageing tests. *J. Alloys Compd.* **622**, 1074–1085 (2015).

[38] Wu, J., Pramana, S. S., Skinner, S. J., Kilner, J. A. & Horsfield, A. P. Why Ni is absent from the surface of $La_2NiO_{4+\delta}$? *J. Mater. Chem. A* **3**, 23760–23767 (2015).

[39] Railsback, J. & Barnett, S. A. Performance and stability of La_2NiO_4-infiltated oxygen electrodes during current switched life testing. *J. Power Sources* **395**, 1–7 (2018).

[40] Pintschovius, L. *et al.* Lattice dynamics of La_2NiO_4. *Phys. Rev. B* **40**, 2229–2238 (1989).

[41] Boumaza, S., Brahimi, R., Boudjellal, L., Belhadi, A. & Trari, M. Photoelectrochemical study of La_2NiO_4 synthesized using citrate sol gel method -

application for hydrogen photo-production. *J. Solid State Electrochem.* **24**, 329–337 (2020).

[42] Tan, Z., Heald, S. M., Cheong, S.-W., Cooper, A. S. & Moodenbaugh, A. R. Nature of hole doping in Nd_2NiO_4 and La_2NiO_4: Comparison with La_2CuO_4. *Phys. Rev. B* **47**, 12365–12368 (1993).

[43] Su, Y.-S., Kaplan, T. A. & Mahanti, S. D. Crystal Hartree-Fock calculations for La_2NiO_4 and La_2CuO_4. *Phys. Rev. B* **59**, 521–529 (1999).

[44] Kovalevsky, A. V. *et al.* Oxygen permeability, stability and electrochemical behavior of $Pr_2NiO_{4+\delta}$-based materials. *J. Electroceramics* **18**, 205–218 (2007).

[45] Montenegro-Hernández, A., Vega-Castillo, J., Mogni, L. & Caneiro, A. Thermal stability of $Ln_2NiO_{4+\delta}$ (Ln: La, Pr, Nd) and their chemical compatibility with YSZ and CGO solid electrolytes. *Int. J. Hydrogen Energy* **36**, 15704–15714 (2011).

[46] Railsback, J., Hughes, G., Mogni, L., Montenegro-Hernï¿½ndez, A. & Barnett, S. High-pressure performance of mixed-conducting oxygen electrodes: Effect of interstitial versus vacancy conductivity. *J. Electrochem. Soc.* **163**, F1433–F1439 (2016).

[47] Vashook, V., Zosel, J., Wen, T. L. & Guth, U. Transport properties of the $Pr_{2-x}Sr_xNiO_{4\pm\delta}$ ceramics with $x = 0.3$ and 0.6. *Solid State Ionics* **177**, 1827–1830 (2006).

[48] Nakamura, T., Yashiro, K., Sato, K. & Mizusaki, J. Oxygen nonstoichiometry and chemical stability of $Nd_{2-x}Sr_xNiO_{4+\delta}$. *J. Solid State Chem.* **182**, 1533–1537 (2009).

[49] Pikalov, S. M. *et al.* High-temperature behavior of calcium substituted layered neodymium nickelates. *J. Alloys Compd.* **801**, 558–567 (2019).

[50] Bogicevic, A. & Wolverton, C. Nature and Strength of Defect Interactions in Cubic Stabilized Zirconia. *Phys. Rev. B* **67**, 024106 (2003).

[51] Kilic, M. E. & Soon, A. Understanding the Enhancement of Ionic Transport in Heterogeneously Doped Zirconia by Heterointerface Engineering. *J. Phys. Chem. C* **122**, 22374–22388 (2018).

[52] Sun, M. & Huang, B. 'Energy Selection Channels' for High-Performance Electrolyte: Anion-Frenkel Defect Pair as Dominant Source for O Ion Conductions in Pyrochlore-type Lanthanide Hafnium Oxides SOFC. *Inorg. Chem.* **56**, 7975–7984 (2017).

[53] Valadez Huerta, G., Reus, L. & Kabelac, S. A Diffusivity Study of $(Sc_2O_3)_{0.1}(CeO_2)_{0.01}(ZrO_2)_{0.89}$ between 1100 and 1500 K at Zero Pressure with

Molecular Dynamics. *J. Chem. Eng. Data* **63**, 1955–1960 (2018).

[54] Badwal, S. P. S., Ciacchi, F. & Milosevic, D. Scandia-Zirconia Electrolytes for Intermediate Temperature Solid Oxide Fuel Cell Operation. *Solid State Ionics* **136**–**137**, 91–99 (2000).

[55] van Duin, A. C. T., Merinov, B. V., Jang, S. S. & Goddard, W. A. ReaxFF Reactive Force Field for Solid Oxide Fuel Cell Systems with Application to Oxygen Ion Transport in Yttria-Stabilized Zirconia. *J. Phys. Chem. A* **112**, 3133–3140 (2008).

[56] Lai, H. Y., Chan, Y. H. & Chen, C. K. Enhancement of ion conductivity for doped electrolytes in SOFC by MD modeling. *Comput. Mater. Sci.* **144**, 265–272 (2018).

[57] Chan, Y. H., Lai, H. Y. & Chen, C. K. Enhancing oxygen iron conductivity of 8YSZ electrolytes in SOFC by doping with Fe_2O_3. *Comput. Mater. Sci.* **147**, 1–6 (2018).

[58] Adamo, C. & Barone, V. Toward reliable density functional methods without adjustable parameters: The PBE0 model. *J. Chem. Phys.* **110**, 6158 (1999).

[59] Perdew, J. P., Ernzerhof, M. & Burke, K. Rationale for mixing exact exchange with density functional approximations. *J. Chem. Phys* **105**, 9982 (1996).

[60] Ricca, C., Ringuedé, A., Cassir, M., Adamo, C. & Labat, F. Conduction Mechanisms in Oxide-Carbonate Electrolytes for SOFC: Highlighting the Role of the Interface from First-Principles Modeling. *J. Phys. Chem. C* **122**, 10067–10077 (2018).

[61] Inaba, H. & Tagawa, H. Ceria-based solid electrolytes. *Solid State Ionics* **83**, 1–16 (1996).

[62] Zha, S., Xia, C. & Meng, G. Effect of Gd (Sm) doping on properties of ceria electrolyte for solid oxide fuel cells. *J. Power Sources* **115**, 44–48 (2003).

[63] Fu, Z. *et al.* Effects of Sm doping content on the ionic conduction of CeO_2 in SOFCs from first principles. *Appl. Phys. Lett.* **111**, (2017).

[64] Lucid, A. K., Keating, P. R. L., Allen, J. P. & Watson, G. W. Structure and Reducibility of CeO_2 Doped with Trivalent Cations. *J. Phys. Chem. C* **120**, 23430–23440 (2016).

[65] Koettgen, J. *et al.* Understanding the ionic conductivity maximum in doped ceria: Trapping and blocking. *Phys. Chem. Chem. Phys.* **20**, 14291–14321 (2018).

[66] Ahn, J. *et al.* Strain-Induced Tailoring of Oxygen-Ion Transport in Highly Doped CeO_2 Electrolyte: Effects of Biaxial Extrinsic and Local Lattice Strain. *ACS Appl. Mater. Interfaces* **9**, 42415–42419 (2017).

[67] Wungu, T. D. K., Sakaue, M., Aspera, S. M., Thuy, T. L. P., Alaydrus, M., Kasai, H. & Ishihara, T. First Principles Study on the Electronic Structure and Properties of Sr- and Mg-doped $LaGaO_3$. *ECS Trans.* **57**, 2715–2722 (2013).

[68] Ishihara, T., Matsuda, H. & Takita, Y. Doped $LaGaO_3$ Perovskite Type Oxide as a New Oxide Ionic Conductor. *J. Am. Chem. Soc.* **116**, 3801 (1994).

[69] Lee, D., Han, J. H., Chun, Y., Song, R. H. & Shin, D. R. Preparation and characterization of strontium and magnesium doped lanthanum gallates as the electrolyte for IT-SOFC. *J. Power Sources* **166**, 35–40 (2007).

[70] Huang, K. & Goodenough, J. B. A solid oxide fuel cell based on Sr- and Mg-doped $LaGaO_3$ electrolyte: the role of a rare-earth oxide buffer. *J. Alloys Compd.* **303**–**304**, 454–564 (2000).

[71] Huang, P. & Petric, A. Superior Oxygen Ion Conductivity of Lanthanum Gallate Doped with Strontium and Magnesium. *J. Electrochem. Soc.* **143**, 1644–1648 (1996).

[72] Traina, K., Henrist, C., Vertruyen, B. & Cloots, R. Dense $La_{0.9}Sr_{0.1}Ga_{0.8}Mg_{0.2}O_{2.85}$ electrolyte for IT-SOFCs: Sintering study and electrochemical characterization. *J. Alloys Compd.* **509**, 1493–1500 (2011).

[73] Wu, Y. C. & Lee, M. Z. Properties and microstructural analysis of $La_{1-x}Sr_xGa_{1-y}Mg_yO_{3-\delta}$ solid electrolyte ceramic. *Ceram. Int.* **39**, 9331–9341 (2013).

[74] Huang, K., Tichy, P. R. & Goodenough, J. B. Superior Perovskite oxide-ion conductor; Strontium- and Magnesium-doped $LaGaO_3$: I, Phase relationships and electrical properties. *J. Am. Chem. Soc.* **81**, 2565–2575 (1998).

[75] Islam, M. S. Computer modelling of defects and transport in perovskite oxides. *Solid State Ionics* **154**–**155**, 75–85 (2002).

[76] Gavin, A. L. & Watson, G. W. Modelling the electronic structure of orthorhombic $LaMnO_3$. *Solid State Ionics* **299**, 13–17 (2017).

[77] Perdew, J. P., Burke, K. & Ernzerhof, M. Generalized Gradient Approximation Made Simple. *Phys. Rev. Lett.* **77**, 3865–3868 (1996).

[78] Perdew, J. P., Ruzsinszky, A., Csonka, G. I., Vydrov, O. A., Scuseria, G. E., Constantin, L. A., Zhou, X. & Burke, K. Restoring the density-gradient expansion for exchange in solids and surfaces. *Phys. Rev. Lett.* **100**, 136406 (2008).

[79] Heyd, J., Scuseria, G. E. & Ernzerhof, M. Hybrid functionals based on a screened Coulomb potential. *J. Chem. Phys.* **118**, 8207 (2003).

[80] Becke, A. D. Density-Functional thermochemistry. III. The role of exact exchange. *J. Chem Phys.* **98**, 5648 (1993).

[81] He, J. & Franchini, C. Screened hybrid functional applied to $3d^0 \rightarrow 3d^8$ transition-metal perovskites $LaMO_3$ (M= Sc-Cu): influence of the exchange mixing parameter on the structural, electronic, and magnetic properties. *Phys. Rev. B* **86**, 235117 (2012).

[82] Kotomin, E., Evarestov, R., Mastrikov, Y. & Maier, J. DFT plane wave calculations of the atomic and electronic structure of $LaMnO_3$ (001) surface. *Phys. Chem. Chem. Phys.* **7**, 2346–2350 (2005).

[83] Gavin, A. L. & Watson, G. W. Defects in orthorhombic $LaMnO_3$-ionic: Versus electronic compensation. *Phys. Chem. Chem. Phys.* **20**, 19257–19267 (2018).

[84] Ahmad, E. A. *et al.* Thermodynamic stability of $LaMnO_3$ and its competing oxides: a hybrid density functional study of an alkaline fuel cell catalyst. *Phys. Rev. B* **84**, 085137 (2011).

[85] Ahmad, E. A., Mallia, G., Kramer, D., Kucernak, A. R. & Harrison, N. M. The stability of $LaMnO_3$ surfaces: a hybrid exchange density functional theory study of an alkaline fuel cell catalyst. *J. Mater. Chem. A* **1**, 11152–11162 (2013).

[86] Dudarev, S. L., Botton, G. A., Savrasov, S. Y., Humphreys, C. J. & Sutton, A. P. Electron-energy-loss spectra and the structural stability of nickel oxide: An LSDA+U study. *Phys. Rev. B* **57**, 1505–1509 (1998).

[87] Kotomin, E. A., Merkle, R., Mastrikov, Y. A., Kuklja, M. M. & Maier, J. The effect of (La,Sr)MnO_3 cathode surface termination on its electronic structure. *ECS Trans.* **77**, 67–73 (2017).

[88] Zhang, X. *et al.* Mechanism of chromium poisoning the conventional cathode material for solid oxide fuel cells. *J. Power Sources* **381**, 26–29 (2018).

[89] Jiang, S. P. A Comparison of O_2 Reduction Reactions on Porous (La,Sr)MnO_3 and (La,Sr)(Co,Fe)O_3 Electrodes. *Solid State Ionics* **146**, 1–22 (2002).

[90] Tietz, F., Haanappel, V. A. C., Mai, A., Mertens, J. & Stöver, D. Performance of LSCF Cathodes in Cell Tests. *J. Power Sources* **156**, 20–22 (2006).

[91] Taylor, F. H., Buckeridge, J. & Catlow, C. R. A. Screening Divalent Metals for A- and B-Site Dopants in $LaFeO_3$. *Chem. Mater.* **29**, 8147–8157 (2017).

[92] Oh, M. Y., Unemoto, A., Amezawa, K. & Kawada, T. Stability of $La_{0.6}Sr_{0.4}Co_{0.2}Fe_{0.8}O_{3-\delta}$ as SOFC Cathode. *J. Electrochem. Soc.* **159**, F659–F664

(2012).

[93] Simner, S. P., Anderson, M. D., Engelhard, M. H. & Stevenson, J. W. Degradation Mechanisms of La-Sr-Co-Fe-O_3 cathodes. *Electrochem. Solid-State Lett.* **9**, A478–A481 (2006).

[94] Oh, D., Gostovic, D. & Wachsman, E. D. Mechanism of $La_{0.6}Sr_{0.4}Co_{0.2}Fe_{0.8}O_3$ cathode degradation. *J. Mater. Res.* **27**, 1992–1999 (2012).

[95] Baumann, F. S., Fleig, J., Konuma, M., Starke, U. Habermeier, K. & Maier, J. Strong Performance Improvement of $La_{0.6}Sr_{0.4}Co_{0.8}Fe_{0.2}O_{3-\delta}$ SOFC Cathodes by Electrochemical Activation. *J. Electrochem. Soc.* **152**, A2074–A2079 (2005).

[96] Li, M. *et al.* Mechanism for the enhanced oxygen reduction reaction of $La_{0.6}Sr_{0.4}Co_{0.2}Fe_{0.8}O_{3-\delta}$ by strontium carbonate. *Phys. Chem. Chem. Phys.* **19**, 503–509 (2017).

[97] Chen, Y. *et al.* A highly active, CO_2-tolerant electrode for the oxygen reduction reaction. *Energy Environ. Sci.* **11**, 2458–2466 (2018).

[98] Koyama, M. & Ishimoto, T. First-principles study on oxygen reduction reaction over $La_{1-x}Sr_xCoO_{3-\delta}$. *ECS Trans.* **77**, 75–80 (2017).

[99] Wang, X. *et al.* An insight into the effects of transition metals on the thermal expansion of complex perovskite compounds: An experimental and density functional theory investigation. *Phys. Chem. Chem. Phys.* **20**, 17781–17789 (2018).

[100] Koo, J. Y. *et al.* Suppression of Cation Segregation in (La,Sr)$CoO_{3-\delta}$ by Elastic Energy Minimization. *ACS Appl. Mater. Interfaces* **10**, 8057–8065 (2018).

[101] Sun, C., Hui, R. & Roller, J. Cathode Materials for Solid Oxide Fuel Cells : A Review. *J. Solid. State Electrochem.* **14**, 1125–1144 (2009).

[102] Chroneos, A., Parfitt, D., Kilner, J. A. & Grimes, R. W. Anisotropic oxygen diffusion in tetragonal $La_2NiO_{4+\delta}$: Molecular dynamics calculations. *J. Mater. Chem.* **20**, 266–270 (2010).

[103] Sadykov, V. A. *et al.* Oxygen transport properties of Ca-doped Pr_2NiO_4. *Solid State Ionics* **317**, 234–243 (2018).

[104] Tropin, E., Ananyev, M., Porotnikova, N., Khodimchuk, A., Saher, S., Farlenkov, A., Kurumchin, E., Shepel, D., Antipov, E., Istomin, S. & Bouwmeester, H. Oxygen surface exchange and diffusion in $Pr_{1.75}Sr_{0.25}Ni_{0.75}$ $Co_{0.25}O_{4\pm\delta}$. *Phys. Chem. Chem. Phys.* **21**, 4779–4790 (2019).

[105] Pikalova, E. Y., Sadykov, V. A., Filonova, E. A., Eremeev, N. F., Sadovskaya, E. M., Pikalov, S. M., Bogdanovich, N. M., Lyagaeva, J. G., Kolchugin, A. A., Vedmid, L. B., Ishchenko, A. V. & Goncharov, V. B. Structure, oxygen transport properties and electrode performance of Ca-substituted Nd_2NiO_4. *Solid State Ionics* **335**, 53–60 (2019).

[106] Vashook, V. *et al.* Oxygen non-stoichiometry and electrical conductivity of $Pr_{2-x}Sr_xNiO_{4\pm\delta}$ with x = 0-0.5. *Solid State Ionics* **177**, 1163–1171 (2006).

[107] Istomin, S. Y. *et al.* Tuning the high-temperature properties of $Pr_2NiO_{4+\delta}$ by simultaneous Pr- and Ni-cation replacement. *RSC Adv.* **6**, 33951–33958 (2016).

[108] Li, S., Tu, H., Li, F., Anwar, M. T. & Yu, L. Investigation of $Nd_2Ni_{0.9}M_{0.1}O_{4+\delta}$ (M = Ni, Co, Cu, Fe, and Mn) cathodes for intermediate-temperature solid oxide fuel cell. *J. Alloys Compd.* **694**, 17–23 (2017).

[109] Miyoshi, S., Furuno, T., Sangoanruang, O., Matsumoto, H. & Ishihara, T. Mixed conductivity and oxygen permeability of doped Pr_2NiO_4-based oxides. *J. Electrochem. Soc.* **154**, 57–62 (2007).

[110] Bansod, M. B., Khandale, A. P., Kumar, R. V. & Bhoga, S. S. Crystal structure, electrical and electrochemical properties of Cu co-doped $Pr_{1.3}Sr_{0.7}NiO_{4+\delta}$ mixed ionic-electronic conductors (MIECs). *Int. J. Hydrogen Energy* **43**, 373–384 (2018).

[111] Ishihara, T., Miyoshi, S., Furuno, T., Sanguanruang, O. & Matsumoto, H. Mixed conductivity and oxygen permeability of doped Pr_2NiO_4-based oxide. *Solid State Ionics* **177**, 3087–3091 (2006).

[112] Hwang, B., Kwon, H., Ko, J., Kim, B. K. & Han, J. W. Density functional theory study for the enhanced sulfur tolerance of Ni catalysts by surface alloying. *Appl. Surf. Sci.* **429**, 87–94 (2018).

[113] Zhang, Y., Xu, X. & Yang, Z. The first principles study of the sulfur oxidation on Ni surface with H_2O. *J. Alloys Compd.* **741**, 1183–1187 (2018).

[114] Yoon, Y., Kim, H. & Lee, J. Enhanced catalytic behavior of Ni alloys in steam methane reforming. *J. Power Sources* **359**, 450–457 (2017).

[115] Lu, H., Hua, D., Iqabl, T., Zhang, X., Li, G. & Zhang, D. Molecular dynamics simulations of the coke formation progress on the nickel-based anode of solid oxide fuel cells. *Int. Commun. Heat Mass Transf.* **91**, 40–47 (2018).

[116] Han, Z., Yang, Z. & Han, M. Comprehensive investigation of methane conversion

over Ni(111) surface under a consistent DFT framework: Implications for anti-coking of SOFC anodes. *Appl. Surf. Sci.* **480**, 243–255 (2019).

[117] Kim, S. *et al.* Tailoring Ni-based catalyst by alloying with transition metals (M = Ni, Co, Cu, and Fe) for direct hydrocarbon utilization of energy conversion devices. *Electrochim. Acta* **225**, 399–406 (2017).

[118] Foresman, J. B. & Frisch, E. *Exploring Chemistry with Electronic Structure Methods*. (Gaussian, Inc, 1996).

[119] Cramer, C. J. *Essentials of Computational Chemistry*. (John Wiley & Sons, Ltd., 2004).

[120] Szabo, A. & Ostlund, N. S. *Modern Quantum Chemistry - Introduction to Advanced Electronic Structure Theory*. (Dover Publications, 1996).

[121] Hartree, D. R. The Wave Mechanics of an Atom with a Non-Coulomb Central Field. Part I. Theory and Methods. *Math. Proc. Cambridge Philos. Soc.* **24**, 89–110 (1928).

[122] Hartree, D. R. The Wave Mechanics of an Atom with a Non-Coulomb Central Field. Part II. Some Results and Discussion. *Math. Proc. Cambridge Philos. Soc.* **24**, 111–132 (1928).

[123] Hartree, D. R. The Wave Mechanics of an Atom with a non-Coulomb Central Field. Part III. Term Values and Intensities in Series in Optical Spectra. *Math. Proc. Cambridge Philos. Soc.* **24**, 426–437 (1928).

[124] Hohenberg, P. & Kohn, W. Inhomogeneous Electron Gas. *Phys. Rev.* **136**, B864 (1964).

[125] Leach, A. R. *Molecular Modelling - Principles and Applications*. (Pearson Education Limited, 1996).

[126] Kohn, W. & Sham, L. J. Self-Consistent Equations Including Exchange and Correlation Effects. *Phys. Rev.* **140**, A1133–A1138 (1965).

[127] Perdew, J. P., Chevary, J. A., Vosko, S. H., Jackson, K. A., Pederson, M. R., Singh, D. J. & Fiolhais, C. Atoms, molecules, solids, and surfaces: Applications of the generalized gradient approximation for exchange and correlation. *Phys. Rev. B* **46**, 6671 (1992).

[128] Tao, J. & Perdew, J. P. Climbing the Density Functional Ladder: Nonempirical Meta-Generalized Gradient Approximation Designed for Molecules and Solids. *Phys. Rev. Lett.* **91**, 146401 (2003).

[129] Sun, J., Remsing, R. C., Zhang, Y., Sun, Z., Ruzsinszky, A., Peng, H.,Yang, Z., Paul, A., Waghmare, U., Wu, X., Klein, M. L. & Perdew, J. P. Accurate first-principles structures and energies of diversely bonded systems from an efficient density functional. *Nat. Chem.* **8**, 831–836 (2016).

[130] Terakura, K., Oguchi, T., Williams, A. R. & Kübler, J. Band theory of insulating transition-metal monoxides: Band-structure calculations. *Phys. Rev. B* **30**, 4734 (1984).

[131] Petit, T., Morel, B., Lemaignan, C., Pasturel, A. & Bigot, B. Cohesive properties of UO_2. *Philos. Mag. B* **73**, 893–904 (1996).

[132] Castell, M. R., Muggelberg, C., Briggs, G. A. D. & Goddard, D. T. Scanning tunneling microscopy of the UO_2 (111) surface. *J. Vac. Sci. Technol. B* **14**, 966–969 (1996).

[133] Dudarev, S. L., Botton, G. A., Savrasov, S. Y., Humphreys, C. J. & Sutton, A. P. Electron-energy-loss spectra and the structural stability of nickel oxide: An LSDA+U study. *Phys. Rev. B* **57**, 1505–1509 (1998).

[134] Salanne, M. *et al.* Including many-body effects in models for ionic liquids. *Theor. Chem. Acc.* **131**, 1–16 (2012).

[135] Madden, P. A. & Wilson, M. 'Covalent' Effects in 'Ionic' Systems. *Chem. Soc. Rev.* **25**, 339–350 (1996).

[136] Madden, P. A., Heaton, R., Aguado, A. & Jahn, S. From first-principles to material properties. *J. Mol. Struct. Theochem.* **771**, 9–18 (2006).

[137] Wilson, M., Madden, P. A., Pyper, N. C. & Harding, J. H. Molecular dynamics simulations of compressible ions. *J. Chem. Phys.* **104**, 8068–8081 (1996).

[138] Castiglione, M. J., Wilson, M. & Madden, P. A. Polarization effects in the simulation of lead (II) fluoride. *J. Phys. Condens. Matter* **11**, 9009–9024 (1999).

[139] Lucid, A. K. Computational Modelling of Solid Oxide Electrolytes and their Interfaces for Energy Applications, PhD Thesis. (Trinity College Dublin, 2018).

[140] Ewald, P. P. Die Berechnung Optischer und Elektrostatischer Gitterpotentiale. *Ann. Phys.* **369**, 253–287 (1921).

[141] Toukmaji, A. Y. & A., B. J. J. Ewald Summation Techniques in Perspective: a Survey. *Comp. Phys. Comm.* **95**, 73–92 (1996).

[142] Tang, K. T. & Toennies, J. P. An improved simple model for the van der Waals

potential based on universal damping functions for the dispersion coefficients. *J. Chem. Phys.* **80**, 3726 (1984).

[143] Tang, K. T. & Toennies, J. P. The van der Waals potentials between all the rare gas atoms from He to Rn. *J. Chem Phys.* **118**, 4976–4983 (2003).

[144] J̌emmer, P., Wilson, M., Madden, P. A. & Fowler, P. W. Dipole and quadrupole polarization in ionic systems: Ab initio studies. *J. Chem. Phys.* **111**, 2038–2049 (1999).

[145] Kresse, G. & Furthmüller, J. Efficiency of *ab initio* total energy calculations for metals and semiconductors using a plane-wave basis set. *Comput. Mater. Sci.* **6**, 15–50 (1996).

[146] Kresse, G. & Furthmüller, J. Efficient iterative schemes for ab initio total-energy calculations using a plane-wave basis set. *Phys. Rev. B* **54**, 11169–11186 (1996).

[147] Kresse, G. & Hafner, J. *Ab initio* molecular-dynamics simulation of the liquid-metal–amorphous-semiconductor transition in germanium. *Phys. Rev. B* **49**, 14251–14269 (1994).

[148] Cherry, M., Islam, M. S. & Catlow, C. R. A. Oxygen Ion Migration in Perovskite-Type Oxides *J. Sol. State Chem.* **118**, 125–132 (1995).

[149] Jensen, F. *Introduction to Computational Chemistry*. (John Wiley & Sons, 2007).

[150] Baldereschi, A. Mean-Value Point in the Brillouin Zone. *Phys. Rev. B* **7**, 5212–5215 (1973).

[151] Kratzer, P. & Neugebauer, J. The Basics of Electronic Structure Theory for Periodic Systems. *Front. Chem.* **7**, 106 (2019).

[152] Monkhorst, H. J. & Pack, J. D. Special points for Brillouin-zone integrations. *Phys. Rev. B* **13**, 5188–5192 (1976).

[153] Kresse, G. & Joubert, D. From ultrasoft pseudopotentials to the projector augmented-wave method. *Phys. Rev. B* **59**, 1758–1775 (1999).

[154] Blöchl, P. E. Projector augmented-wave method. *Phys. Rev. B* **50**, 17953–17979 (1994).

[155] Murnaghan, F. D. The Compressibility of Media under Extreme Pressures. *Proc. Natl. Acad. Sci.* **30**, 244–247 (1944).

[156] Bradley, D. & Cracknell, A. *The Mathematical theory of Symmetry in Solids: Representation Theory for Point Groups and Space Groups*. (Oxford Classic Texts,

1972).

[157] Freysoldt, C., Neugebauer, J. & de Walle, C. G. Fully *Ab Initio* Finite-Size Corrections for Charged-Defect Supercell Calculations. *Phys. Rev. Lett.* **102**, 16402 (2009).

[158] Chase, M. W. *NIST-JANAF Thermochemical Tables*. (American Chemical Society, 1998).

[159] Allen, M. P. & Tildesley, D. J. *Computer Simulations of Liquids*. (Oxford Univeristy Press, 1987).

[160] Verlet, L. Computer 'Experiments' on Classical Fluids. I. Thermodynamical Properties of Lennard-Jones Molecules. *Phys. Rev.* **159**, 98–103 (1967).

[161] Hockney, R. W. Potential calculation and some applications. *Methods Comput. Phys.* **9**, 135–211 (1970).

[162] Swope, W. C., Andersen, H. C., Berens, P. H. & Wilson, K. R. A computer simulation method for the calculation of equilibrium constants for the formation of physical cluster of molecules: application to small water clusters. *J. Chem Phys.* **76**, 637–649 (1982).

[163] Kim, S. Issues on the choice of a proper time step in molecular dynamics. *Phys. Procedia* **53**, 60–62 (2014).

[164] Burbano, M. Computer Modelling of metal oxides, PhD thesis. (Trinity College Dublin, 2014).

[165] Nosé, S. & Klein, M. L. Constant-temperature–constant-pressure molecular-dynamics calculations for molecular solids: Application to solid nitrogen at high pressure. *Mol. Phys.* **50**, 1055 (1983).

[166] Nosé, S. A molecular dynamics method for simulations in the canonical ensemble. *Mol. Phys.* **52**, 255–268 (1984).

[167] Hoover, W. G. Canonical dynamics: Equilibrium phase-space distributions. *Phys. Rev. A* **31**, 1695–1697 (1985).

[168] Martyna, G. J., Tuckerman, M. E. & Klein, M. L. Nosé–Hoover chains: The canonical ensemble via continuous dynamics. *J. Chem Phys.* **97**, 2635 (1992).

[169] Martyna, G. J., Tobias, D. J. & Klein, M. L. Constant pressure molecular dynamics algorithms. *J. Chem. Phys.* **101**, 4177–4189 (1994).

[170] Frenkel, D. & Smit, B. *Understanding Molecular Simulation - From Algorithms to*

Applications. (Academic Press, 1996).

[171] Callister, W. D. & Rethwish, D. G. *Materials Science and Engineering - An introduction*. (John Wiley & Sons, 2010).

[172] Smart, L. & Moore, E. *Solid State Chemistry, an Introduction*. (Stanley Thornes, 1995).

[173] Cheng, C. H., Lee, S. F. & Hong, C. W. Ionic dynamics of an intermediate-temperature yttria-doped-ceria electrolyte. *J. Electrochem. Soc.* **154**, E158–E163 (2007).

[174] Ogisu, K. *et al.* Electronic Band Structures and Photochemical Properties of La-Ga-based Oxysulfides. *J. Phys. Chem. C* **112**, 11978–11984 (2008).

[175] Burbano, M., Nadin, D., Marrocchelli, D., Salanne, M. & W., W. G. No Title. *Phys. Chem. Chem. Phys.* **16**, 8320–8331 (2014).

[176] Norby, T. Fast oxygen ion conductors - from doped to ordered systems. *J. Mater. Chem.* **11**, 11–18 (2001).

[177] Savioli, J. & Watson, G. W. Computational modelling of solid oxide fuel cells. *Curr. Opin. Electrochem.* **21**, 14–21 (2020).

[178] Fu, Q., Xu, X., Peng, D., Liu, X. & Meng, G. Preparation and electrochemical characterization of Sr- and Mn-doped $LaGaO_3$ as anode materials for LSGM-based SOFCs. *J. Mater. Sci.* **38**, 2901–2906 (2003).

[179] Liu, X. *et al.* Impregnated nickel anodes for reduced-temperature solid oxide fuel cells based on thin electrolytes of doped $LaGaO_3$. *J. Power Sources* **222**, 92–96 (2013).

[180] Chen, F. & Liu, M. Study of transition metal oxide doped $LaGaO_3$ as electrode materials for LSGM-based solid oxide fuel cells. *J. Solid State Electrochem.* **3**, 7–14 (1998).

[181] Blöchl, P. E. Projector augmented-wave method. *Phys. Rev. B* **50**, 17953–17979 (1994).

[182] Kresse, G. & Joubert, D. From ultrasoft pseudopotentials to the projector augmented-wave method. *Phys. rev. B* **59**, 1758 (1999).

[183] Leonov, I. Metal-insulator transition and local-moment collapse in FeO under pressure. *Phys. Rev. B* **92**, 085142 (2015).

[184] Mazin, I. & Anisimov, V. Insulating gap in FeO: Correlations and covalency. *Phys. Rev. B - Condens. Matter Mater. Phys.* **55**, 12822–12825 (1997).

[185] Engelking, P. C. & Lineberger, W. C. Laser photoelectron spectrometry of FeO: Electron affinity, electronic state separations, and ground state vibrations of iron oxide, and a new ground state assignment. *J. Chem. Phys.* **66**, 5054–5058 (1977).

[186] Schrön, A. & Bechstedt, F. Magnetic anisotropy of FeO and CoO: The influence of gradient corrections on exchange and correlation. *J. Phys. Condens. Matter* **25**, 486002 (2013).

[187] Sarte, P. M. *et al.* Spin-orbit excitons in CoO. *Phys. Rev. B* **100**, 075143 (2019).

[188] Mackrodt, W. C. *et al.* Ab initio Hartree-Fock calculations of CaO, VO, MnO and NiO. *Philos. Mag. A Phys. Condens. Matter, Struct. Defects Mech. Prop.* **68**, 653–666 (1993).

[189] Weaver, J. F. *et al.* Precursor-mediated dissociation of n-butane on a PdO (101) thin film. *Catal. Today* **160**, 213–227 (2011).

[190] Bruska, M. K., Czekaj, I., Delley, B., Mantzaras, J. & Wokaun, A. Electronic structure and oxygen vacancies in PdO and ZnO: Validation of DFT models. *Phys. Chem. Chem. Phys.* **13**, 15947–15954 (2011).

[191] Parmigiani, F. & Sangaletti, L. Fine structures in the X-ray photoemission spectra of MnO, FeO, CoO, and NiO single crystals. *J. Electron Spectros. Relat. Phenomena* **98**–**99**, 287–302 (2002).

[192] Pillo, T., Zimmermann, R., Steiner, P. & Hüfner, S. The electronic structure of PdO found by photoemission (UPS and XPS) and inverse photoemission (BIS). *J. Phys. Condens. Matter* **9**, 3987–3999 (1997).

[193] Holl, Y. *et al.* Electronic structure of PdO studied by photoemission (XPS, UPS). *Solid State Commun.* **32**, 1189–1192 (1979).

[194] Eder, R. Correlated band structure of NiO, CoO, and MnO by variational cluster approximation. *Phys. Rev. B* **78**, 115111 (2008).

[195] Kurmaev, E. Z. *et al.* Oxygen x-ray emission and absorption spectra as a probe of the electronic structure of strongly correlated oxides. *Phys. Rev. B - Condens. Matter Mater. Phys.* **77**, 1–5 (2008).

[196] Kuo, C. Y. *et al.* Challenges from experiment: electronic structure of NiO. *Eur. Phys. J. Spec. Top.* **226**, 2445–2456 (2017).

[197] Temesghen, W. & Sherwood, P. M. A. Analytical utility of valence band X-ray photoelectron spectroscopy of iron and its oxides, with spectral interpretation by

cluster and band structure calculations. *Anal. Bioanal. Chem.* **373**, 601–608 (2002).

[198] Briggs, D. & Fairley, N. Valence-band x-ray photoelectron spectroscopic studies of manganese and its oxides interpreted by cluster and band structure calculations. *Surf. Interface Anal.* **33**, 274–282 (2002).

[199] van Elp, J., Potze, R. H., Eskes, H., Berger, R. & Sawatzky, G. A. Electronic Structure of MnO. *Phys. Rev. B* **44**, 1530–1537 (1991).

[200] Chen, J., Wu, X. & Selloni, A. Electronic structure and bonding properties of cobalt oxide in the spinel structure Electronic structure and bonding properties of cobalt oxide in the spinel structure. *Phys. Rev. B* **83**, 245204 (2011).

[201] Meng, Y. *et al.* When Density Functional Approximations Meet Iron Oxides. *J. Chem. Theory Comput.* **12**, 5132–5144 (2016).

[202] Bengone, O., Alouani, M., Blöchl, P. & Hugel, J. Implementation of the projector augmented-wave LDA+U method: Application to the electronic structure of NiO. *Phys. Rev. B - Condens. Matter Mater. Phys.* **62**, 16392–16401 (2000).

[203] Rohrbach, G., Hafner, J. & Kresse, G. Molecular adsorption on the surface of strongly correlated transition-metal oxides: A case study for CO/NiO (100). *Phys. Rev. B - Condens. Matter Mater. Phys.* **69**, 1–13 (2004).

[204] Mosey, N. J., Liao, P. & Carter, E. A. Rotationally invariant *ab initio* evaluation of Coulomb and exchange parameters for DFT+U calculations. *J. Chem. Phys.* **129**, 1–13 (2008).

[205] Franchini, C., Podloucky, R., Paier, J., Marsman, M. & Kresse, G. Ground-state properties of multivalent manganese oxides: Density functional and hybrid density functional calculations. *Phys. Rev. B - Condens. Matter Mater. Phys.* **75**, 1–11 (2007).

[206] Wang, L., Maxisch, T. & Ceder, G. Oxidation energies of transition metal oxides within the GGA+U framework. *Phys. Rev. B* **73**, 195107 (2006).

[207] Pickett, W., Erwin, S. & Ethridge, E. Reformulation of the method for a local-orbital basis. *Phys. Rev. B* **58**, 1201–1209 (1998).

[208] Jiang, H., Gomez-Abal, R. I., Rinke, P. & Scheffler, M. First-principles modeling of localized d states with the GW@LDA+U approach. *Phys. Rev. B - Condens. Matter Mater. Phys.* **82**, 1–16 (2010).

[209] Trimarchi, G. & Binggeli, N. Structural and electronic properties of $LaMnO_3$ under pressure: An *ab initio* LDA+U study. *Phys. Rev. B* **71**, 035101 (2005).

[210] Xu, Z., Joshi, Y. V., Raman, S. & Kitchin, J. R. Accurate electronic and chemical properties of 3*d* transition metal oxides using a calculated linear response *U* and a DFT+*U* method. *J. Chem. Phys.* **142**, 1–7 (2015).

[211] Cococcioni, M. & de Gironcoli, S. Linear respones approach to the calculation of the effective interaction parameters in the LDA+*U* method. *Phys. Rev. B* **71**, 35105 (2005).

[212] Momma, K. & Izumi, F. VESTA 3 for three-dimensional visualization of crystal, volumetric and morphology data. *J. Appl. Cryst.* **44**, 1272–1276 (2011).

[213] Gautam, G. S. & Carter, E. A. Evaluating transition-metal oxides within DFT-SCAN and SCAN+*U* frameworks for solar thermochemical applications. *Phys. Rev. Mater.* **2**, 095401 (2018).

[214] Franchini, C., Podloucky, R., Paier, J., Marsman, M. & Kresse, G. Ground-state properties of multivalent manganese oxides: Density functional and hybrid density functional calculations. *Phys. Rev. B* **75**, 1–11 (2007).

[215] Olivia Y. Long, Gopalakrishnan Sai Gautam, E. A. C. Evaluating optimal *U* for 3*d* transition-metal oxides within the SCAN+*U* framework. *Phys. Rev. Mater.* **4**, 045401 (2020).

[216] Sirajuddeen, M. M. S. *et al.* A DFT+*U* study to report magnetic phase transition, electronic properties and half metallic ferromagnetism in palladium oxide using Hubbard method. *Mater. Chem. Phys.* **241**, 122263 (2020).

[217] Bennett, J. W. *et al.* A systematic determination of hubbard *U* using the GBRV ultrasoft pseudopotential set. *Comput. Mater. Sci.* **170**, 109137 (2019).

[218] Rodl, C., Fuchs, F., Furthmuller, J. & Bechstedt, F. Quasiparticle Band Structures of the antiferromagnetic transition metal oxides MnO, FeO, CoO and NiO. *Phys. Rev. B* **79**, 235114 (2009).

[219] Gillen, R. & Robertson, J. Accurate screened exchange LDA band structures for transition metal monoxides MnO, FeO, CoO and NiO. *J. Phys. Condens. Matter* **25**, 165502 (2013).

[220] Seriani, N., Harl, J., Mittendorfer, F. & Kresse, G. A first-principles study of bulk oxide formation on Pd (100). *J. Chem. Phys.* **131**, (2009).

[221] Lipton, D. & Jacobs, R. L. The Density of States and Magnetic Parameters for Transition Metals. *J. Phys. C Met. Phys. Suppl.* **3**, S389 (1970).

[222] Uddin, J., Peralta, J. E. & Scuseria, G. E. Density functional theory study of bulk platinum monoxide. *Phys. Rev. B - Condens. Matter Mater. Phys.* **71**, 1–7 (2005).

[223] Sawatzky, G. A. & Allen, J. W. Magnitude and origin of the band gap in NiO. *Phys. Rev. Lett.* **53**, 2339–2342 (1984).

[224] Hufner, S., Osterwalder, J., Riesterer, T. & Hulliger, F. Photoemisson and Inverse Photoemission Spectroscopy of NiO. *Solid State Commun.* **52**, 793 (1984).

[225] Sasi, B. *et al.* Preparation of Transparent and Semiconducting NiO Films. *Vacuum* **68**, 149 (2002).

[226] Newman, R. & Chrenko, R. M. Optical Properties of Nickel Oxide. *Phys. Rev.* **114**, 1507 (1959).

[227] Rey, E., Kamal, M., Miles, R. B. & Royce, B. S. The Semiconductivity and Stability of Palladium Oxide. *J. Mater. Sci.* **13**, 812 (1978).

[228] Nilsson, P. O. & Shivaraman, M. S. Optical Properties of PdO in the range of 0.5-5.4 eV. *J. Phys. C Solid State Phys.* **12**, 1423 (1979).

[229] Okamoto, H. & Aso, T. Formation of Thin Films of PdO and their Electric Properties. *Jpn. J. Appl. Phys.* **6**, 779 (1967).

[230] Iskenderov, R. N., Drabkin, I. A., Emel'yanova, L. T. & Ksendzov, Y. M., *Sov. Phys. Solid State* **10**, 2031 (1969).

[231] Drabkin, I. A., Emel'yanova, L. T., Iskenderov, R. N. & Ksendzov, Y. M., *Sov. Phys. Solid State* **10**, 2428 (1969).

[232] Huffman, D. R., Wild, R. L. & Shinmei, J. Optical Absorption Spectra of Crystal-Field Transitions in MnO. *Chem. Phys.* **50**, 4092 (1969).

[233] Bowen, H. K., Adler, D. & Auker, B. H. Electrical and Optical Properties of FeO. *Solid State Chem.* **12**, 355 (1975).

[234] Powell, R. J. & Spicer, W. E. Optical Properties of NiO and CoO. *Phys. Rev. B* **2**, 2182 (1970).

[235] Hufner, S. & Wertheim, G. K. Estimates of the Coulomb Correlation Energy from X-ray and Photoemission data. *Phys. Rev. B* **7**, 5086 (1973).

[236] van Elp, J. *et al.* Electronic Structure of CoO, Li-doped CoO and $LiCoO_2$. *Phys. Rev. B* **44**, 6090 (1991).

[237] Seriani, N., Jin, Z., Pompe, W. & Ciacchi, L. C. Density functional theory study of platinum oxides: From infinite crystals to nanoscopic particles. *Phys. Rev. B* -

Condens. Matter Mater. Phys. **76**, 1–10 (2007).

[238] Savytskii, D. *et al.* Low-temperature structural and Raman studies on rare-earth gallates. *Phys. Rev. B* **68**, 024101 (2003).

[239] Howard, C. J. & Kennedy, B. J. The orthorhombic and rhombohedral phases of $LaGaO_3$ - a neutron powder diffraction study. *J. Phys. Condens. Matter* **11**, 3229 (1999).

[240] Kuncewicz-Kupczyk, W. *et al.* Vaporization Studies of the La_2O_3–Ga_2O_3 System. *J. Am. Ceram. Soc.* **85**, 2299–2305 (2004).

[241] Åhman, J., Svensson, G. & Albertsson, J. A Reinvestigation of β-Gallium Oxide. *Acta Crystallogr. Sect. C* **52**, 1336–1338 (1996).

[242] Kasunič, M., Meden, A., Škapin, S. D., Suvorov, D. & Golobič, A. Order–disorder of oxygen anions and vacancies in solid solutions of La_2TiO_5 and $La_4Ga_2O_9$. *Acta Crystallogr. Sect. B* **65**, 558–566 (2009).

[243] Murnaghan, F. D. The compressibility of media under extreme pressures. *Proc. Natl. Acad. Sci. U. S. A.* **30**, 244–247 (1944).

[244] Allen, J. P., Scanlon, D. O., Parker, S. C. & Watson, G. W. Tin Monoxide: Structural Prediction from First Principles Calculations with van der Waals Corrections. *J. Phys. Chem. C* **115**, 19916–19924 (2011).

[245] Luo, B. *et al.* Electronic, dielectric and optical properties of orthorhombic lanthanum gallate perovskite. *J. Alloys Compd.* **708**, 187–193 (2017).

[246] Ganose, A. M., Jackson, A. J. & Scanlon, D. O. sumo: Command-line tools for plotting and analysis of periodic ab initio calculations. *J. Open Source Softw.* **3**, 717 (2018).

[247] Slater, P. R., Irvine, J. T. S., Ishihara, T. & Takita, Y. High Temperature Neutron Powder Diffraction Study of the Oxide Ion Conductor $La_{0.9}Sr_{0.1}Ga_{0.8}Mg_{0.2}O_{2.85}$. *J. Sol. Stat. Chem.* **139**, 135–143 (1998).

[248] Knight, K. S. Low temperature thermoelastic and structural properties of $LaGaO_3$ perovskite in the Pbnm phase. *J. Solid State Chem.* **194**, 286–296 (2012).

[249] Taylor, D. Thermal expansion data: III Sesquioxides, M_2O_3, with the corundum and the A-, B- and C-M_2O_3 structures. *Trans. J. Br. Ceram. Soc.* **83**, 92–98 (1984).

[250] Yamane, H., Ogawara, K., Omori, M. & Hirai, T. Phase Transition of Rare-Earth Aluminates ($RE_4Al_2O_9$) and Rare-Earth Gallates ($RE_4Ga_2O_9$). *J. Am. Ceram. Soc.* **78**,

2385–2390 (1995).

[251] Jackson, A. MCTOOLS - plot-cplap-ternary. https://github.com/ajjackson/mctools/ (2017).

[252] Buckeridge, J., Scanlon, D. O., Walsh, A. & Catlow, C. R. A. Automated procedure to determine the thermodynamic stability of a material and the range of chemical potentials necessary for its formation relative to competing phases and compounds. *Comp. Phys. Comm.* **185**, 330–338 (2014).

[253] Kim, D. J. Lattice Parameters, Ionic Conductivities, and Solubility Limits in Fluorite-Structure MO_2 Oxide [M = Hf^{4+}, Zr^{4+},Ce^{4+}, Th^{4+}, U^{4+}] Solid Solutions. *J. Am. Ceram. Soc.* **72**, 1415–1421 (1989).

[254] Watson, G. W. The origin of the electron distribution in SnO. *J. Chem. Phys.* **114**, 758 (2001).

[255] Walsh, A. & Watson, G. W. Electronic structures of rock salt, litharge and herzenbergite SnO by density functional theory. *Phys. Rev. B* **70**, 235114 (2004).

[256] Walsh, A. & Watson, G. W. The origin of the stereochemically active Pb(II) lone pair: DFT calculations on PbO and PbS. *J. Solid State Chem.* **178**, 1422–1428 (2005).

[257] Walsh, A. & Watson, G. W. Influence of the anion on lone pair formation in Sn(II) monochalcogenides: A DFT study. *J. Phys. Chem. B* **109**, 18868–18875 (2005).

[258] Kehoe, A. B., Scanlon, D. O. & Watson, G. W. Role of Lattice Distortions in the Oxygen Storage Capacity of Divalently Doped CeO_2. *Chem. Mater.* **23**, 4464–4468 (2011).

[259] Scanlon, D. O., Morgan, B. J. & Watson, G. W. The origin of the enhanced oxygen storage capacity of $Ce_{(1-x)}(Pd/Pt)_{(x)}O$. *Phys. Chem. Chem. Phys.* **13**, 4279–4284 (2011).

[260] Mansour, A. N. & Melendres, C. A. Analysis of X-ray Absorption Spectra of Some Nickel Oxycompounds Using Theoretical Standards. *J. Phys. Chem. A* **102**, 65–81 (1998).

[261] Moore Jr., W. J. & Pauling, L. The crystal structures of the tetragonal monoxides of lead, tin, paladium and platinum. *J. Am. Chem. Soc.* **63**, 1392–1394 (1941).

[262] Yoshida, S. Fundamental Properties of Wide Bandgap Semiconductors. in *Wide Bandgap Semiconductors* (eds. Takahashi, K., Yoshikawa, A. & Sandhu, A.) 35 (Springer-Verlag Berlin Heidelberg, 2007).

[263] Seetawan, U. *et al.* Effect of Calcinations Temperature on Crystallography and Nanoparticles in ZnO Disk. *Mater. Sci. Appl.* **2**, 1302–1306 (2011).

[264] Redman, M. J. & Steward, E. G. Cobaltous Oxide with the Zinc Blende/Wurtzite-type Crystal Structure. *Nature* **193**, 867 (1962).

[265] Wu, Z. Y. *et al.* Characterization of iron oxides by x-ray absorption at the oxygen K edgeusing a full multiple-scattering approach. *Phys. Rev. B* **55**, 2570 (1997).

[266] Wyckoff, R. W. G. *Crystal Structures*. (Interscience, 1964).

[267] Nayak, S. K. & Jena, P. Equilibrium Geometry, Stability, and Magnetic Properties of Small MnO Clusters. *J. Am. Chem. Soc.* **121**, 644–652 (1999).

[268] Keating, J., Sankar, G., Hyde, T., Kohara, S. & Ohara, K. Elucidation of structure and nature of the PdO-Pd transformation using in situ PDF and XAS techniques. *Phys. Chem. Chem. Phys.* **15**, 8555 (2013).

[269] Parker, S. F. *et al.* Characterization of Hydrous Palladium Oxide: Implications for Low-Temperature CArbon Monoxide Oxidation. *J. Phys. Chem. C* **114**, 14164–14172 (2010).

[270] Pedersen, A. & Luisier, M. Lithiation of Tin Oxide: A computational study. *ACS Appl. Mater. Interfaces* **6**, 22247–22263 (2014).

[271] Dholabhai, P. P., Adams, J. B., Crozier, P. A. & Sharma, R. In search of enhanced electrolyte materials: A case study of doubly doped ceria. *J. Mater. Chem.* **21**, 18991–18997 (2011).

[272] Dikmen, S., Aslanbay, H., Dikmen, E. & Şahin, O. Hydrothermal preparation and electrochemical properties of Gd^{3+} and Bi^{3+}, Sm^{3+}, La^{3+}, and Nd^{3+} codoped ceria-based electrolytes for intermediate temperature-solid oxide fuel cell. *J. Power Sources* **195**, 2488–2495 (2010).

[273] Sha, X. *et al.* Study on La and Y co-doped ceria-based electrolyte materials. *J. Alloys Compd.* **428**, 59–64 (2007).

[274] Omar, S., Wachsman, E. D. & Nino, J. C. Higher ionic conductive ceria-based electrolytes for solid oxide fuel cells. *Appl. Phys. Lett.* **91**, 89–92 (2007).

[275] Van Herle, J., Seneviratne, D. & McEvoy, A. J. Lanthanide co-doping of solid electrolytes: AC conductivity behaviour. *J. Eur. Ceram. Soc.* **19**, 837–841 (1999).

[276] Guan, X., Zhou, H., Liu, Z., Wang, Y. & Zhang, J. High performance Gd^{3+} and Y^{3+} co-doped ceria-based electrolytes for intermediate temperature solid oxide fuel cells.

Mater. Res. Bull. **43**, 1046–1054 (2008).

[277] Butler, V., Catlow, C. R. A., Fender, B. E. F. & Harding, J. H. Dopant ion radius and ionic conductivity in cerium dioxide. *Solid State Ionics* **8**, 109–113 (1983).

[278] Hayashi, H., Sagawa, R., Inaba, H. & Kawamura, K. Molecular dynamics calculations on ceria-based solid electrolytes with different radius dopants. *Solid State Ionics* **131**, 281–290 (2000).

[279] Kilner, J. A. Fast Anion Transport in Solids. *Solid State Ionics* **8**, 201–207 (1983).

[280] Yamamura, Y. *et al.* Materials design of perovskite-based oxygen ion conductor by molecular dynamics method. *Solid State Ionics* **160**, 93–101 (2003).

[281] Kilo, M. *et al.* Modeling of cation diffusion in oxygen ion conductors using molecular dynamics. *Solid State Ionics* **175**, 823–827 (2004).

[282] Buzlukov, A. *et al.* Vacancy ordering and oxygen dynamics in oxide ion conducting $La_{1-x}Sr_xGa_{1-x}Mg_xO_{3-x}$ ceramics: ^{71}Ga, ^{25}Mg and ^{17}O NMR. *J. Solid State Chem.* **184**, 36–43 (2011).

[283] Lybye, D., Poulsen, F. W. & Mogensen, M. Conductivity of A- and B-site doped $LaAlO_3$, $LaGaO_3$, $LaScO_3$ and $LaInO_3$ perovskites. *Solid State Ionics* **128**, 91–103 (2000).

[284] Sammes, N. M., Tompsett, G. A., Phillips, R. J. & Cartner, A. M. Characterisation of doped-lanthanum gallates by X-ray diffraction and Raman spectroscopy. *Solid State Ionics* **111**, 1–7 (1998).

[285] Zheng, F., Bordia, R. K. & Pederson, L. R. Phase constitution in Sr and Mg doped $LaGaO_3$ system. *Mater. Res. Bull.* **39**, 141–155 (2004).

[286] Kharton, V. V *et al.* Ionic conductivity of La(Sr)Ga(Mg,M)$O_{3-\delta}$ (M = Ti, Cr, Fe, Co, Ni): effects of transition metal dopants. *Solid State Ionics* **132**, 119–130 (2000).

[287] Feng, M. & Goodenough, J. B. A superior oxide-ion electrolyte. *Eur. J. Solid State Inorg.Chem.* **31**, 663–672 (1994).

[288] Huang, K. & Goodenough, J. B. Wet Chemical Synthesis of Sr- and Mg-Doped $LaGaO_3$, a Perovskite-Type Oxide-Ion Conductor. *J. Solid State Chem.* **136**, 274–283 (1998).

[289] Slater, P. R., Irvine, J. T. S., Ishihara, T. & Takita, Y. The structure of the oxide ion conductor $La_{0.9}Sr_{0.1}Ga_{0.8}Mg_{0.2}O_{2.85}$ by powder neutron diffraction. *Solid State Ionics* **107**, 319–323 (1998).

[290] Chen, T. & Fung, K. Comparison of dissolution behavior and ionic conduction between Sr and/or Mg doped $LaGaO_3$ and $LaAlO_3$. *J. Power Sources* **132**, 1–10 (2004).

[291] Chen, T.-Y. & Fung, K.-Z. Phase Stability and Conductivity of Doped $LaGaO_3$ and $LaAlO_3$ Solid Electrolytes. *Proc. Electrochem. Soc. PV* **16**, 403–412 (2001).

[292] Kilner, J. A. & Brook, R. J. A study of oxygen ion conductivity in doped non-stoichiometric oxides. *Solid State Ionics* **6**, 237–252 (1982).

[293] Huang, K., Feng, M. & Goodenough, J. B. Sol-gel synthesis of a new oxide-ion conductor Sr- and Mg-Doped $LaGaO_3$ perovskite. *Journal of the American Ceramic Society* vol. 79 1100–1104 (1996).

[294] Blanc, F., Middlemiss, D. S., Gan, Z. & Grey, C. P. Defects in Doped $LaGaO_3$ Anionic Conductors: Linking NMR Spectral Features, Local Environments, and Defect Thermodynamics. *J. Am. Chem. Soc.* **133**, 17662–17672 (2011).

[295] Ishihara, T., Kilner, J. A., Honda, M. & Takita, T. J. Oxygen Surface Exchange and Diffusion in the New Perovskite Oxide Ion Conductor $LaGaO_3$. *J. Am. Chem. Soc.* **119**, 2747 (1997).

[296] Drennan, J. *et al.* Characterisation, conductivity and mechanical properties of the oxygen-ion conductor $La_{0.9}Sr_{0.1}Ga_{0.8}Mg_{0.2}O_{3-x}$. *J. Mater. Chem.* **7**, 79 (1997).

[297] Islam, M. S. & Davies, R. A. Atomistic study of dopant site-selectivity and defect association in the lanthanum gallate perovskite. *J. Mat. Chem.* **14**, 86–93 (2004).

[298] Mostofi, A. A. *et al.* wannier90: A tool for obtaining maximally-localised Wannier functions. *Comput. Phys. Commun.* **178**, 685–699 (2008).

[299] Wannier, G. H. The structure of electronic excitation levels in insulating crystals. *Phys. Rev.* **52**, 191–197 (1937).

[300] Cloizeaux, J. Des. Orthogonal orbitals and generalized wannier functions. *Phys. Rev.* **129**, 554–566 (1963).

[301] Marzari, N. & Vanderbilt, D. Maximally localized generalized Wannier functions for composite energy bands. *Phys. Rev. B* **56**, 12847–12865 (1997).

[302] Santos, C. H. S., Goncalves, M. S. & Hernandez-Figueroa, H. E. Designing novel photonic devices by bio-inspired computing. *IEEE Photonics Technol. Lett.* **22**, 1177–1179 (2010).

[303] Santos, C. H. S. Parallel and bio-inspired computing applied to analyze microwave

and photonic metamaterial structures, PhD thesis (University of Campinas, 2010).

[304] Johnson, S. G. The NLopt nonlinear-optimization package.

[305] Nelder, J. A. & Mead, R. A simplex method for function minimization. *Comput. J.* **7**, 308–313 (1965).

[306] Fletcher, R. & Powell, M. J. D. A rapidly convergent descent method for minimization. *Comput. J.* **6**, 163–168 (1964).

[307] Davidon, W. C., Laboratory, A. N. & Comission, U. S. A. E. *Variable metric method for minimization*. (1959).

[308] James, F. *MINUIT Function Minimization and Error Analysis*. Reference Manual, Version 94.1

[309] Dimitrov, V. & Sakka, S. Electronic oxide polarizability and optical basicity of simple oxides. *J. Appl. Phys.* **79**, 1736–1740 (1996).

[310] Slater, J. C. & Kirkwood, J. G. The van der waals forces in gases. *Phys. Rev.* **37**, 682–697 (1931).

[311] Fowler, P. W., Harding, J. H. & Pyper, N. C. The polarizabilities and dispersion coefficients for ions in the solid group IV oxides. *J. Phys. Condens. Matter* **6**, 10593–10606 (1994).

[312] Mahan, G. D. van der Waals coefficient between closed shell ions. *J. Chem. Phys.* **76**, 493 (1982).

[313] Pauling, L. The Theoretical Prediction of the Physical Properties of Many-Electron Atoms and Ions: Mole Refraction, Diamagnetic Susceptibility, and Extension in Space. *Proc. Roy. Soc.* **A114**, 181–211 (1927).

[314] Klimeš, J. & Michaelides, A. Perspective: Advances and challenges in treating van der Waals dispersion forces in density functional theory. *J. Chem. Phys.* **137**, 120901 (2012).

[315] Grimme, S. Semiempirical GGA-type density functional constructed with a long-range dispersion correction. *J. Comput. Chem.* **27**, 1787–1799 (2006).

[316] Marti, W., Fischer, P., Altorfer, F., Scheel, H. J. & Tadin, M. Crystal structures and phase transitions of orthorhombic and rhombohedral $RGaO_3$ (R = La, Pr, Nd) investigated by neutron powder diffraction. *J. Phys. Condens. Matter* **127**, 127–135 (1994).

[317] Ruggiero, A. & Ferro, A. Ortogalliti di elementi delle terre rare. *Atti della Accad. Naz.*

Dei Lincei, Cl. Di Schi. Fis. Mat. E Nat. Rend. Ser. **8**, 48–50 (1954).

[318] Vasylechko, L., Senyshyn, A. & Bismayer, U. *Chapter 242: Perovskite-Type Aluminates and Gallates*. *Handbook on the Physics and Chemistry of Rare Earths* vol. 39 (Elesvier B.V., 2009).

[319] Senyshyn, A., Ehrenberg, H., Vasylechko, L., Gale, J. D. & Bismayer, U. Computational study of $LnGaO_3$ (Ln = La-Gd) perovskites. *J. Phys. Condens. Matt.* **17**, 6217–6234 (2005).

[320] Gotte, A., Hermansson, K. & Baudin, M. Molecular dynamics simulations of reduced CeO_2: bulk and surfaces. *Surf. Sci.* **552**, 273–280 (2004).

[321] Gotte, A., Spangberg, D., Hermansson, K. & Baudin, M. Molecular dynamics study of oxygen self-diffusion in reduced CeO_2. *Solid State Ionics* **178**, 1421–1427 (2007).

[322] Grimes, R., Busker, G., McCoy, M. A., Chroneos, A., Kilner, J. A. and Chen, S. The Effect of Ion Size on Solution Mechanism and Defect Cluster Geometry. *Berichte der Bunsen-Gesellschaft* **101**, 1204–1210 (1997).

[323] Nomura, K. & Tanase, S. Electrical conduction behavior in $(La_{0.9}Sr_{0.1})M(III)O_{3-\delta}$ (M(III) = Al, Ga, Sc, In and Lu) perovskites. *Solid State Ionics* **98**, 229–236 (1997).

[324] Huang, P. & Petric, A. Superior Oxygen Ion Conductiviiy of Lanthanum Gallate. *J. Electrochem. Soc.* **143**, 1644–1648 (1996).

[325] Goodenough, J. B. Oxide-Ion Electrolytes. *Annu. Rev. Mater. Res.* **33**, 91–128 (2003).

[326] Li, S. & Bergman, B. Doping effect on secondary phases, microstructure and electrical conductivities of $LaGaO_3$ based perovskites. *J. Eur. Ceram. Soc.* **29**, 1139–1146 (2009).

[327] Stevenson, J. W., Armstrong, R., Mccready, D. E., Pederson, L. R. & Weber, W. J. Processing and Electrical Properties of Alkaline Earth-Doped Lanthanum Gallate. *J. Electrochem. Soc.* **144**, 3613–3620 (1997).

[328] Shi, M. *et al.* Synthesis and characterization of Sr- and Mg-doped $LaGaO_3$ by using glycine – nitrate combustion method. *J. Alloys Compd.* **425**, 348–352 (2006).

[329] Shen, Y., Zhao, H., Liu, X. & Xu, N. Preparation and electrical properties of Ca-doped $La_2NiO_{4+\delta}$ cathode materials for IT-SOFC. *Phys. Chem. Chem. Phys.* **12**, 15124–15131 (2010).

[330] Skinner, S. J. Evaluation of $La_2Ni_{1-x}Co_xO_{4\pm\delta}$ as a SOFC Cathode Material. *ECS Proc. Vol.* **2003**–**07**, 552–560 (2003).

[331] Brown, I. D. Modelling the structures of La_2NiO_4. *Zeitschrift fur Krist.* **199**, 255–272 (1992).

[332] Kharton, V. V., Viskup, A. P., Naumovich, E. N. & Marques, F. M. B. Oxygen ion transport in La_2NiO_4-based ceramics. *J. Mater. Chem.* **9**, 2623–2629 (1999).

[333] Jorgensen, J. D., Dabrowski, B., Pei, S., Richards, D. R. & Hinks, D. G. Structure of the interstitial oxygen defect in $La_2NiO_{4+\delta}$. *Phys. Rev. B* **40**, 2187–2199 (1989).

[334] Paulus, W. *et al.* Neutron diffraction studies of stoichiometric and oxygen intercalated La_2NiO_4 single crystals. *Solid State Sci.* **4**, 565–573 (2002).

[335] Rodríguez-Carvajal, J., Fernández-Díaz, M. T. & Martinez, J. L. Neutron diffraction study on structural and magnetic properties of La_2NiO_4. *J. Phys. Condens. Matter* **3**, 3215–3234 (1991).

[336] Aguadero, A. *et al.* In situ high temperature neutron powder diffraction study of oxygen-rich $La_2NiO_{4+\delta}$ in air: Correlation with the electrical behaviour. *J. Mater. Chem.* **16**, 3402–3408 (2006).

[337] Burriel, R., Castro, M. & Saez-Puche, R. Calorimetric study of the structural and magnetic ordering in R_2NiO_4 (R = La, Pr and Nd). *Pure Appl. Chem.* **67**, 1825–1830 (1995).

[338] Tranquada, J. M. *et al.* Oxygen intercalation, stage ordering, and phase separation in $La_2NiO_{4+\delta}$ with $0.05< \delta <0.11$. *Phys. Rev. B* **50**, 6340–6351 (1994).

[339] Minervini, L., Grimes, R. W., Kilner, J. A. & Sickafus, K. E. Oxygen migration in $La_2NiO_{4+\delta}$. *J. Mater. Chem.* **10**, 2349–2354 (2000).

[340] Woolley, R. J., Illy, G. N., Ryan, M. P. & Skinner, S. J. In situ determination of the nickel oxidation state in $La_2NiO_{4+\delta}$ and $La_4Ni_3O_{10-\delta}$ using X-ray absorption near-edge structure. *J. Mater. Chem.* **21**, 18592 (2011).

[341] Kuiper, P. *et al.* Unoccupied density of states of $La_{2-x}Sr_xNiO_{4+\delta}$ studied by polarization-dependent x-ray-absorption spectroscopy and bremsstrahlung isochromat spectroscopy. *Phys. Rev. B* **44**, 4570–4575 (1991).

[342] Saleem, M., Mishra, A. & Varshney, D. Structural, transport and collosal dielectric properties of A-site substituted La_2NiO_4. *Mater. Res. Express* **6**, 026304 (2018).

[343] Aeppli, G. & Buttrey, D. J. Magnetic correlations in La_2NiO_4. *Phys. Rev. Lett.* **61**, 203–206 (1988).

[344] Pardo, V., Botana, A. S. & Baldomir, D. Strain effects to optimize the thermoelectric

properties of hole-doped $La_2NiO_{4+\delta}$ via ab initio calculations. *Phys. Rev. B* **87**, 125148 (2013).

[345] Takeda, Y. *et al.* Crystal Chemistry and Physical Properties of $La_{2-x}Sr_xNiO_4$ ($0 < x < 1.6$). *Mat. Res. Bull.* **25**, 293–306 (1990).

[346] Zhou, N., Chen, G. Ã., Zhang, H. J. & Zhou, C. Synthesis and transport properties of La_2NiO_4. *Phys. B* **404**, 4150–4154 (2009).

[347] Gervais, F. & Odier, P. Plasmon Behaviour at the 'Semiconductor-Metal' transition in La_2NiO_4 and $La_2Ni_2O_7$. *Solid State Commun.* **56**, 371–374 (1985).

[348] Kolchugin, A. A. *et al.* Structural, electrical and electrochemical properties of calcium-doped lanthanum nickelate. *Solid State Ionics* **288**, 48–53 (2016).

[349] Bassat, J. M., Gervais, F., Odier, P. & Loup, J. P. Anisotropic Transport Properties of La_2NiO_4 Single Crystals. *Mater. Sci. Eng.* **B3**, 507–514 (1989).

[350] Vashook, V. V. *et al.* Oxygen nonstoichiometry and electrical conductivity of the solid solutions $La_{2-x}Sr_xNiO_y$ ($0 \leq x < 0.5$). *Solid State Ionics* **110**, 245–253 (1998).

[351] Kol'chugin, A. A., Pikalova, E. Y., Bogdanovich, N. M., Bronin, D. I. & Filonova, E. A. Electrochemical Properties of Doped Lantanum-Nickelate-Based Electrodes. *Russ. J. Electrochem.* **53**, 826–833 (2017).

[352] Gilev, A. R., Kiselev, E. A., Zakharov, D. M. & Cherepanov, V. A. Effect of calcium and copper-iron co-doping on defect-induced properties of La_2NiO_4-based materials. *J. Alloys Compd.* **753**, 491–501 (2018).

[353] Wahyudi, O. *et al.* Growth of high quality single crystals of strontium doped (Nd,Pr)-nickelates, $Nd_{2-x}Sr_xNiO_{4+\delta}$ and $Pr_{2-x}Sr_xNiO_{4+\delta}$. *CrystEngComm* **17**, 6278–6285 (2015).

[354] Kresse, G. & Hafner, J. *Ab initio* molecular dynamics simulation of the liquid-metal-amorphous-semiconductor transition in germanium. *Phys. Rev. B* **49**, 14251–14271 (1994).

[355] Kresse, G. & Furthmüller, J. Efficiency of *ab initio* total energy calculations for metals and semiconductors using a plane-wave basis set. *Comput. Mater. Sci.* **6**, 15–50 (1996).

[356] Lee, H. D., Magyari-Köpe, B. & Nishi, Y. Model of metallic filament formation and rupture in NiO for unipolar switching. *Phys. Rev. B - Condens. Matter Mater. Phys.* **81**, 1–4 (2010).

[357] Park, S. *et al.* Interaction and ordering of vacancy defects in NiO. *Phys. Rev. B* **77**, 134103 (2008).

[358] Rohrbach, A., Hafner, J. & Kresse, G. Ab initio study of the (001) surfaces of hematite and chromia: Influence of strong electronic correlations. *Phys. Rev. B* **70**, 125426 (2004).

[359] Ferrari, A. M., Pisani, C., Cinquini, F., Giordano, L. & Pacchioni, G. Cationic and anionic vacancies on the NiO(110) surface: DFT+*U* and hybrid functional density functional theory calculations. *J. Chem. Phys.* **127**, 174711 (2007).

[360] Cinquini, F. *et al.* Electronic structure of NiO/Ag(100) thin films from DFT+*U* and hybrid functional DFT approaches. *Phys. Rev. B* **74**, 165403 (2006).

[361] Lany, S. & Zunger, A. Polaronic hole localization and multiple hole binding of acceptors in oxide wide-gap semiconductors. *Phys. Rev. B* **80**, 085202 (2009).

[362] Morgan, B. J. & Watson, G. W. Polaronic trapping of electrons and holes by native defects in anatase TiO_2. *Phys. Rev. B - Condens. Matter Mater. Phys.* **80**, 233102 (2009).

[363] Nolan, M. & Watson, G. W. Hole localization in Al doped silica: A DFT+*U* description. *J. Chem. Phys.* **125**, 144701 (2006).

[364] Morgan, B. J. & Watson, G. W. Intrinsic n-type defect formation in TiO_2: A comparison of rutile and anatase from GGA+*U* calculations. *J. Phys. Chem. C* **114**, 2321–2328 (2010).

[365] Scanion, D. O. *et al.* Surface sensitivity in lithium-doping of MgO: A density functional theory study with correction for on-site coulomb interactions. *J. Phys. Chem. C* **111**, 7971–7979 (2007).

[366] Keating, P. R. L., Scanlon, D. O., Morgan, B. J., Galea, N. M. & Watson, G. W. Analysis of Intrinsic Defects in CeO_2 Using a Koopmans-Like GGA+ U Approach. *J. Phys. Chem. C* **116**, 2443–2452 (2012).

[367] Heyd, J., Scuseria, G. E. & Ernzerhof, M. Hybrid functionals based on a screened Coulomb potential. *J. Chem. …* **118**, 8207–8215 (2003).

[368] Allen, J. P. & Watson, G. W. Occupation matrix control of *d*- and *f*-electron localisations using DFT + U. *Phys. Chem. Chem. Phys.* **16**, 21016–21031 (2014).

[369] Maiti, K., Mahadevan, P. & Sarma, D. D. Evolution of electronic structure with dimensionality in divalent nickelates. *Phys. Rev. B - Condens. Matter Mater. Phys.*

59, 12457–12470 (1999).

[370] Eisaki, H. *et al.* Electronic Structure of $La_{2-x}Sr_xNiO_4$ studied by photoemission and inverse-photoemission spectroscopy. *Phys. Rev. B* **45**, 12513–12521 (1992).

[371] Gunnarsson, O. & Jones, R. O. Total-energy differences: Sources of error in local-density approximations. *Phys. Rev. B* **31**, 7588 (1985).

[372] Hammer, B., Hansen, L. B. & Norskov, J. K. Improved adsorption energetics within density-functional theory using revised Perdew-Burke-Ernzerhof functionals. *Phys. Rev. B* **59**, 7413 (1999).

[373] Patton, D. C., Porezag, D. V & Pederson, M. R. Simplified generalized-gradient approximation and anharmonicity: Benchmark calculations on molecules. *Phys. Rev. B* **55**, 7454–7459 (1997).

[374] Zinkevich, M., Solak, N., Nitsche, H., Ahrens, M. & Aldinger, F. Stability and thermodynamic functions of lanthanum nickelates. *J. Alloy. Compd.* **438**, 92–99 (2007).

[375] Hemingway, B. S. Thermodynamic properties for bunsenite, NiO, magnetite, Fe_2O_4, and hematite, Fe_2O_3, with comments on selected oxygen buffer reactions. *Am. Mineral.* **75**, 781–790 (1990).

[376] Boyle, B. J., King, E. G. & Conway, K. C. Heats of formation of nickel and cobalt oxides (NiO and CoO) of combustion calorimetry. *J. Am. Chem. Soc.* **76**, 3835–3837 (1954).

[377] Jones, R. O. & Gunnarsson, O. The density functional formalism, its applications and prospects. *Rev. Mod. Phys.* **61**, 689–746 (1989).

[378] Roth, W. L. Magnetic structures of MnO, FeO, CoO and NiO. *Phys. Rev.* **110**, 1333 (1958).

[379] Cheetham, A. K. & Hope, D. A. O. Magnetic ordering and exchange effects in the antiferromagnetic solid solutions $Mn_xNi_{1-x}O$. *Phys. Rev. B* **27**, 6964 (1983).

[380] Fender, B. E. F., Jacobson, A. J. & Wedgewood, F. A. Covalency Parameters in MnO, α-MnS, and NiO. *J. Chem. Phys.* **48**, 990 (1968).

[381] Yu, J., Rosso, K. M. & Bruemmer, S. M. Charge and ion transport in NiO and aspects of Ni oxidation from first principles. *J. Phys. Chem. C* **116**, 1948–1954 (2012).

[382] Zinkevich, M. & Aldinger, F. Thermodynamic analysis of the ternary La-Ni-O system. *J. Alloys Compd.* **375**, 147–161 (2004).

[383] Xie, W., Lee, Y. L., Shao-Horn, Y. & Morgan, D. Oxygen Point Defect Chemistry in Ruddlesden-Popper Oxides $(La_{1-x}Sr_x)_2MO_{4\pm\delta}$ (M = Co, Ni, Cu). *J. Phys. Chem. Lett.* **7**, 1939–1944 (2016).

[384] Choisnet, J., Bassat, J. M., Pilliere, H., Odier, P. & Leblanc, M. A re-investigation of the crystal structure of La_2NiO_4: Non stoichiometry and 'LaO' layers. *Solid State Commun.* **66**, 1245–1249 (1988).

[385] Burbano, M., Carlier, D., Boucher, F., Morgan, B. J. & Salanne, M. Sparse Cyclic Excitations Eplain the Low Ionic Conductivity of Stoichiometric $Li_7La_3Zr_2O_{12}$ *Phys. Rev. Lett.* **116**, 135901 (2016).

[386] Gilev, A. R., Kiselev, E. A. & Cherepanov, V. A. Bulk Oxygen Diffusion and Surface Exchange Limitations on $La_{2-x}Sr_xNi_{1-y}Fe_yO_{4+\delta}$ *KnE Materials Science*, 24-31 (2018).

[387] Benloucif, R., Nguyen, N., Greneche, J. M & Raveau, B. $La_{2-x}Sr_xNi_{1-y}Fe_yO_{4+\delta}$: Relationships between oxygen non-stoichiometry and magnetic and electron transport properties *J. Phys. Chem. Sol.* **52**, 381-387 (1991).

[388] Whittingham, A. W. H., Liu, X. & Smith, R. D. L. How Cation Substitutions Affect the Oxygen Reduction Reaction on $La_{2-x}Sr_xNi_{1-y}Fe_yO_{4+\delta}$ *The European Society Journal for Catalysis* **14**, e202101684 (2022).